

Dissertation

submitted to the
Combined Faculties for the Natural Sciences and for Mathematics
of the Ruperto-Carola-University of Heidelberg, Germany
for the degree of
Doctor of Natural Sciences

put forward by
Julia Maria Anne Repp
born in Trier, Germany

Date of oral examination: Oktober 31, 2012

The setup of the high-precision Penning-
trap mass spectrometer PENTATRAP
and first production studies
of highly charged ions

Referees: Prof. Dr. Klaus Blaum

PD Dr. Yuri Litvinov

Abstract: The five-Penning-trap mass spectrometer PENTATRAP is a novel high-precision experiment located at the Max-Planck-Institut für Kernphysik, Heidelberg. PENTATRAP aims for an accuracy of up to a few parts in 10^{12} for mass ratios of long-lived highly charged nuclides up to uranium. A physics program for PENTATRAP includes, e.g., measurements of Q -values of relevant β -transitions for neutrino physics, stringent tests of quantum electrodynamics in extreme electromagnetic fields, and a test of special relativity. Thanks to a multi-trap configuration various fast measurement schemes comprising simultaneous frequency measurements can be applied. Further main features of PENTATRAP are highly sensitive cryogenic non-destructive detection systems and the access to highly charged ions via the small PENTATRAP-EBIT and the Heidelberg-EBIT.

In the context of the present thesis, the assembly of this world-wide unique facility was started and was considerably put forward. The ion transport and capture in the Penning-traps was simulated and a multitude of operational test, e.g., the investigation of the magnetic field of the superconducting magnet were performed. A magnetic field compensation system and the instrumentally challenging cryogenic translation and tilt system were built up and characterized. Furthermore, the highly tolerated Penning traps were designed, built and assembled. The first installation of the cryogenic assembly including the first cabling of the Penning traps finally allowed the first cool down of the experiment. Moreover, the successful installation of the PENTATRAP-EBIT was performed and the first production of highly charged rhenium and osmium ions which are required for Q -value measurements was demonstrated and optimized.

Zusammenfassung: Das Fünf-Penningfallen-Massenspektrometer PENTATRAP ist ein neues Hochpräzisions-Experiment, welches am Max-Planck-Institut für Kernphysik in Heidelberg ansässig ist. Das Ziel von PENTATRAP ist es Massenverhältnisse von langlebigen und hochgeladenen Nukliden bis hin zu Uran mit einer Genauigkeit von bis zu einigen 10^{-12} zu bestimmen. Die physikalischen Anwendungsgebiete umfassen Messungen des Q -Wertes von relevanten β -Übergängen in der Neutrino-physik, zwingende Tests der Quantenelektrodynamik in starken elektromagnetischen Feldern und ein Test der speziellen Relativitätstheorie. Dank des Mehrfallenaufbaus können verschiedene Messschemata, die gleichzeitige Frequenzmessungen umfassen, angewendet werden. Weitere Hauptmerkmale von PENTATRAP sind hochsensitive, kryogene, nichtdestruktive Detektionssysteme und der Zugang zu hochgeladenen Ionen über die kleine PENTATRAP-EBIT und die Heidelberg-EBIT.

Im Rahmen der vorliegenden Arbeit startete der Aufbau dieser weltweit einzigartigen Anlage und wurde wesentlich vorangebracht. Der Ionttransport und der Einfang in die Penningfallen wurde simuliert und eine Vielzahl von Funktionstests, wie z.B. die Untersuchung des Magnetfeldes des supraleitenden Magneten, durchgeführt. Ein Magnetfeldkompensationssystem und die technologisch anspruchsvolle kryogene Justagevorrichtung wurden aufgebaut und charakterisiert. Darüber hinaus wurden die hoch tolerierten Penningfallen konstruiert, hergestellt und aufgebaut. Die Montage des gesamten kryogenen Aufbaus, welche die Verkabelung der Penningfallen beinhaltete, ermöglichte ein erstes Abkühlen des Experiments. Abschließend konnte die PENTATRAP-EBIT erfolgreich in Betrieb genommen und die erste Produktion von hochgeladenen Rhenium- und Osmium-Ionen, die für Q -Wert-Messungen von Interesse sind, demonstriert werden.

Contents

1	Introduction	1
2	Penning-trap mass spectrometry	7
2.1	The ideal Penning trap	7
2.2	The real Penning trap	10
2.2.1	The quadrupolar trapping potential	11
2.2.2	Magnetic field imperfections	13
2.3	Ion manipulation	14
2.3.1	Ion excitation	14
2.3.2	Ion cooling	16
2.4	Ion detection	17
3	The electron beam ion trap	25
3.1	Mode of operation	26
3.2	The electron beam	28
3.3	The ion cloud	30
3.4	Interaction of the ion cloud with the electron beam	32
3.4.1	Collision processes within the EBIT	32
3.4.2	Heating and escape of the ions	35
3.4.3	Rate equation	36
4	The PENTATRAP mass spectrometer	39
4.1	Ion sources	39
4.2	Transfer beamline and beam diagnostics	41
4.3	Superconducting magnet system	43
4.4	The cryogenic assembly	45
4.5	Penning traps	48
4.6	Ion detection	50
4.7	The highly stable voltage source	50
4.8	The control system	51
4.9	Measurement procedure	52
5	Simulations	55
5.1	Operating principles of SIMION [®]	55
5.2	Ion injection into the drift tube	56
5.3	Ion injection into the trap stack	59
5.3.1	Examination of the electrostatic potential	60
5.3.2	Investigation of the time of flight	62

5.4	The ion transport between the traps	65
5.4.1	Possible timing schemes	65
5.4.2	Variation of the ramping times	67
5.4.3	Introduction of imperfections	69
5.4.4	Choosing a shallow trap depth	70
5.4.5	Choosing a three-dimensional start distribution	70
6	Magnetic field investigations	73
6.1	The earth's magnetic field and investigations of distortions	73
6.2	The homogeneous magnetic field region	74
6.2.1	The warm-bore device for NMR measurements	75
6.2.2	Measurement of the magnetic field on-axis	79
6.2.3	Influence of the determined magnetic field inhomogeneities on the eigenfrequencies	80
6.2.4	Examination of the spatial homogeneity	84
6.2.5	Magnetization of the trap materials	85
6.3	Magnetic field measurements outside the Penning trap	86
7	Commissioning of PENTATRAP	89
7.1	The temperature stabilization of the laboratory	89
7.2	The fluxgate system for the stabilization of the magnetic field	91
7.2.1	Principle of operation and setup of the fluxgate system	91
7.2.2	Commissioning and characterization of the fluxgate system	94
7.2.3	Operating tests of the fluxgate system	96
7.3	The setup of the Penning-trap stack	99
7.3.1	The mechanical construction of the Penning traps	99
7.3.2	The manufacturing process of the Penning traps	101
7.3.3	Assembly of the Penning traps	105
7.4	The setup of the translation and tilt system	106
7.4.1	The mechanical construction of the translation and tilt system	106
7.4.2	Test of the translation and tilt system at room and cryogenic temperatures	108
7.5	First installation of the cryogenic part	113
7.5.1	Installation of the cryogenic components	113
7.5.2	First cabling of the Penning traps	115
7.6	First cool down of the experiment	117
8	The PENTATRAP-EBIT	121
8.1	The setup of the Dresden-EBIT3	121
8.1.1	The Wien filter	124
8.2	The measurement setup in the accelerator hall	125
8.3	First characterization of the EBIT parameters	127
8.4	Charge breeding of xenon ions	130
8.5	Rhenium and osmium ions for first β -decay measurements	133
8.6	Summary of the charge breeding studies	137
9	Conclusion and outlook	141

A	Geometry files and <i>LUA</i> codes	145
B	Technical drawings and photographs	150

List of Tables

2.1	Radii of the eigenmotions of some exemplary nuclides after axial side-band cooling.	23
4.1	Calculated charge breeding performance of the Heidelberg-EBIT. . .	41
4.2	Comparison of the Heidelberg-EBIT and the Dresden-EBIT3.	42
4.3	Magnetic susceptibilities of different materials at 4.2 K	46
4.4	Main trap parameters of a single trap	49
5.1	Parameters describing the ion bunch.	57
5.2	Results obtained for the ion transport introducing a time uncertainty.	70
6.1	Fit parameters of the magnetic field in the five traps.	82
6.2	Fit parameters of the magnetic field on the magnet's vertical axis. . .	88
7.1	Dimensions of the Penning-trap electrodes at 4.2 K and at 293 K. . .	101
7.2	Operating of the coni and the resulting movement of the trap.	110
8.1	Obtained calibration factors of the Wien filter.	130

List of Figures

2.1	Three-dimensional quadrupolar potential inside a Penning trap. . . .	8
2.2	Ion motion in a Penning trap.	9
2.3	Energy level diagram of a charged particle stored in a Penning trap. .	10
2.4	Sketch of a hyperboloidal and cylindrical Penning trap.	11
2.5	Example of excitations in a five-electrode Penning trap.	15
2.6	Conversion from pure magnetron into pure cyclotron motion.	16
2.7	Basic idea of the image current detection.	18
2.8	Sketch of the single particle detection in a cylindrical Penning trap .	19
2.9	Absolute value of the impedance and phase for a parallel LC circuit. .	20
2.10	Noise spectrum superimposed with a peak and dip signal.	21
3.1	Operation principle of an EBIT	27
3.2	Three-dimensional potential in an EBIT	27
3.3	Ionization energies	28
3.4	Brillouin and Herrmann radius	29
3.5	Electron current density	30
3.6	Space charge potential	31
3.7	Radiative and dielectronic recombination	34
3.8	Evolution of charge states	37
3.9	Evaporative cooling	37
4.1	Layout of the experimental setup.	40
4.2	Photograph of the beam diagnostic system.	43
4.3	Photograph and sectional view of the PENTATRAP magnet.	43
4.4	Temperature dependence of the magnetic susceptibility of copper. . .	44
4.5	Exploded assembly-drawing of the cryogenic assembly and photograph	45
4.6	Thermal conductivity of materials used at PENTATRAP.	47
4.7	Photograph of the Penning-trap assembly.	48
4.8	Schematic of the five-trap setup and magnetic field along the axis. . .	49
4.9	Sketch of a proposed cryogenic detection and excitation system. . . .	51
4.10	Proposed measurement scheme of first choice.	53
5.1	Geometry used in the simulations.	56
5.2	Bunch parameters for different drift tube voltages	58
5.3	Sketch of the ion injection principle.	59
5.4	Exemplary electrostatic potential used for ion injection into the traps.	61
5.5	Influence of the fastening plate on the electric potential	62
5.6	Potential at the position where the ion enters the first Penning trap. .	63

5.7	Distortion of the Penning-trap potential by the drift tube.	63
5.8	Timing scheme of the pulsed drift tube.	64
5.9	Simulated data for the capture of the ion bunch.	64
5.10	Sketch of the timing scheme used for the simulation of the ion transport.	66
5.11	Shape of the electric potential during the transport.	67
5.12	Axial energy gain depending on the chosen ramping time.	68
5.13	Axial and radial energy gain depending on the tilting angle.	69
6.1	Vertical earth magnetic field measured in the laboratory	74
6.2	Environmental influences on the magnetic field in the laboratory. . . .	75
6.3	Dewar made of fiber glass epoxy.	76
6.4	Temperature decrease inside the warm-bore	79
6.5	Axial magnetic field of the superconducting magnet.	80
6.6	Frequency shift of ω_c due to B_2 for the double-dip technique.	82
6.7	Frequency shift of ω_+ due to B_1 and B_2 for the double-dip technique.	83
6.8	Spatial homogeneity in a cylinder with 2.5 mm radius.	84
6.9	Spatial homogeneity in a cylinder with 5 mm radius	85
6.10	Trap geometry used for Suszi and simulated data.	86
6.11	Magnetic field on axis through the magnet's bore.	87
6.12	Fringe field of the superconducting magnet	88
7.1	Sketch of the temperature stabilization system in the laboratory. . . .	90
7.2	Temperature behavior in the laboratory and calculated Allan deviation	91
7.3	Signal shapes of the fluxgate detection principle.	92
7.4	Sketch and photograph of the ring-core fluxgate	93
7.5	Sketch of the magnetic stabilization system.	93
7.6	Simplified block diagram of the complete fluxgate stabilization system.	94
7.7	Measured characteristics of the Helmholtz coil pair.	96
7.8	Technical drawing of the gimbal-mounted fluxgate.	97
7.9	Location in the laboratory and photograph of the fluxgate system. . .	98
7.10	Setup for determining the compensation factor and measured values.	98
7.11	Thermal expansion of copper and sapphire.	100
7.12	Sketch of the Penning trap defining the parameters for which the thermal shrinkage was calculated.	100
7.13	Circularity of the sapphire ring and photomicrograph.	102
7.14	Surface detachment due to acid cleaning and photomicrographs. . . .	103
7.15	Photomicrographs of the surfaces at the different processing steps. . .	104
7.16	Photographs of the laser welded trap pins.	105
7.17	Photograph of a finished electrode and view inside the Penning trap.	106
7.18	Photographs of the translation and tilt system.	107
7.19	Sketch of the working principle of the translation and tilt stage. . . .	108
7.20	Experimental setup used for testing the translation and tilt system. .	109
7.21	Coordinate system and locations of the coni.	109
7.22	Evaluated camera picture and thermal expansion of the materials. . .	110
7.23	Results of the translation and tilt system's functionality at 293 K. . .	111
7.24	Results of the translation and tilt system's functionality at 77 K. . .	112
7.25	Photographs of the feedthrough flange.	114
7.26	Photographs of the charcoal absorbers.	115

7.27	Photographs of the cabled Penning traps and the final setup.	116
7.28	Photographs of oxygen ice in the magnet and the ice removal tool. . .	118
7.29	Photographs of the first lowering of the experiment in the magnet. . .	118
8.1	Photograph of the cathode, the drift tubes and the collector.	122
8.2	Electrode arrangement and potentials at the Dresden-EBIT3.	122
8.3	Photograph of the Dresden-EBIT3 setup.	123
8.4	Sketch of the gas connection used for the production of metal ions. .	124
8.5	Photographs of the Wien filter.	125
8.6	Photograph of the PENTATRAP setup in the accelerator hall.	126
8.7	Sketch of the beamline and location of the detectors.	126
8.8	Sketch of the detection setup and the signal processing steps.	127
8.9	Characteristics of the cathode in use at the Dresden-EBIT3.	128
8.10	Wien filter scans of argon ions for different confinement times.	129
8.11	Assignment of the Wien filter voltage to the mass-to-charge ratio. . .	129
8.12	Example of a residual gas spectrum.	131
8.13	Wien filter scans of xenon ions for different confinement times.	131
8.14	The evolution of charges states of ^{132}Xe	132
8.15	Measured charge balance of argon and oxygen ions.	133
8.16	Gas inlet of natural abundant osmocene into the EBIT.	135
8.17	Studies to optimize the creation of highly charges osmium ions.	136
8.18	The evolution of charges states of ^{187}Re	136
8.19	Time-of-flight spectra of differently charged rhenium ion bunches . . .	137
8.20	Highest attained charge states of osmium and rhenium ions.	138
8.21	Summary of the charge breeding studies.	139
8.22	Addressable mass-to-charge ratios in the Penning trap.	139
A.1	Geometry file used for the SIMION [®] simulations (part 1)	146
A.2	Geometry file used for the SIMION [®] simulations (part 2)	147
A.3	Lua code for pulsing down the drift tube (part 1).	148
A.4	Lua code for pulsing down the drift tube (part 2).	149
B.1	Assembly drawing of the translation and tilt stage.	151
B.2	Assembly drawing of the Penning-trap stack	152
B.3	Technical drawing of the sapphire ring.	153
B.4	Technical drawing of the ring electrode.	154
B.5	Technical drawing of the correction electrode.	155
B.6	Technical drawing of the lower endcap electrode.	156
B.7	Technical drawing of the upper endcap electrode.	157
B.8	Photographs of gold and silver plated Penning-trap components. . . .	158
B.9	Photograph of the gold plated Penning-trap electrodes.	158

Chapter 1

Introduction¹

The mass of a nuclide is an important parameter in many fields of physics and reflects all forces acting in the nucleus [2, 3, 4]. The necessary relative uncertainty of the mass measurement depends on the physics being investigated. For example, mass measurements of short-lived radionuclides with a relative uncertainty of $\delta m/m \approx 10^{-7}$ - 10^{-8} suffice to test different nuclear mass models [5, 6, 7] and the determined mass values serve as input parameters for astrophysical calculations [8, 9, 10]. Relative uncertainties of $\leq 10^{-8}$ are required for tests of fundamental interactions and their symmetries, e.g., to test the conserved vector current (CVC) hypothesis and the unitarity of the Cabibbo-Kobayashi-Maskawa (CKM) quark-mixing matrix, see e.g. [11, 12]. Stringent tests of charge-, parity-, and time-reversal (CPT) symmetry in the baryon sector demand uncertainties of better than 10^{-11} in the comparison of charge-to-mass ratios [13]. Especially tests of quantum electrodynamics (QED) or some aspects of special relativity require a determination of mass ratios with an accuracy of up to few parts in 10^{12} [14, 15, 16].

Penning traps are nowadays the most suitable devices for high-precision mass measurements of nuclides. The mass is determined via the measurement of the free-space cyclotron frequency (see later Eq. (2.2)) of an ion with its specific charge-to-mass ratio stored in a homogeneous magnetic field. Frequencies can generally be measured with a very high precision. Therefore, relating a mass measurement to a frequency measurement is advantageous. The most accurate mass measurements with light and stable atoms and molecules in closed systems have been achieved with a relative mass uncertainty of below 10^{-11} by van Dyck *et al.* (UW-PTMS, Washington, USA) [17, 18] and Pritchard *et al.* (MIT-TRAP, Massachusetts, USA) [19]. The MIT-TRAP moved to FSU (Florida, USA), where Myers *et al.* performed mass measurements with an accuracy of few 10^{-11} on, e.g., ^{32}S and ^{28}Si , respectively, mainly limited by magnetic field fluctuations [20, 21].

The choice of a higher charge state of the ion generally is of benefit, since the cyclotron frequency scales with the charge state and the experimental precision of the mass measurement can be improved. A well-proven source for highly charged ions is the electron beam ion trap (EBIT). A first proof of the confinement of highly charged ions produced by an EBIT in a Penning trap was carried out in 1994 at RETRAP employing the Livermore-EBIT [22]. At present, direct access to highly charged stable ions and an accuracy of a few 10^{-10} in the mass determination are solely

¹Parts of the introduction are taken from the author's paper [1].

provided by the SMILETRAP Penning trap facility [23, 24]. SMILETRAP was the first mass spectrometer which had direct access to highly charged stable ions which were created at the electron beam ion source CRYISIS [25]. At present SMILETRAP II [26], which will be connected to the S-EBIT [27], is under construction to provide access to higher charge states. Recently, the TITAN facility [28] carried out high-precision mass measurements on highly charged short-lived radionuclides [29], where the highly charged ions are produced at the TITAN-EBIT [30]. Both experiments use the time-of-flight ion cyclotron resonance measurement technique [31].

In contrary to SMILETRAP and TITAN, the high-precision Penning-trap experiment PENTATRAP will determine mass ratios by storing only a single nuclide in the Penning trap and detecting it non-destructively via an image-current detection technique [32]. PENTATRAP aims for accuracies of up to a few parts in 10^{12} for highly charged long-lived and heavy nuclides up to uranium. To enable these ultra-high accuracies, PENTATRAP employs a highly sensitive cryogenic detection system. Moreover, it is the first Penning-trap experiment which uses a stack of five Penning traps. Employing five traps it is guaranteed that both the measurement of the frequency ratio and the particle preparation can be done fast. This is indispensable, since the effect of magnetic field fluctuations and drifts generally increases with time.

The mass ratios measured at PENTATRAP will contribute among others to a determination of neutrino properties [4]. The discovery of neutrino oscillations has showed that the neutrino has a nonzero rest mass [33]. Absolute mass values from other experiments are required, since in the oscillation experiments only squared neutrino mass differences can be obtained. A goal of PENTATRAP is to contribute to determinations of the electron neutrino and electron antineutrino masses by means of measuring the Q -values of relevant β -transitions.

The Q -value is defined as the energy difference between the initial and final nuclide and is determined by measuring the frequency ratio of both nuclides. Taking into account that frequency ratios of ions and not atoms are measured, the Q -value can be determined for, e.g., the β^- -decay by

$$\begin{aligned} \frac{Q}{c^2} &= M(Z, A) - M(Z + 1, A) \\ &= M(Z, A)^{q+} \left(1 - \frac{\nu_c(M(Z, A)^{q+})}{\nu_c(M(Z + 1, A)^{q+})} \right) + \frac{\Delta E_B}{c^2}, \end{aligned} \quad (1.1)$$

where ΔE_B is the difference of the total binding energies and c is the speed of light. $M(Z, A)$ and $M(Z + 1, A)$ are the masses of the neutral atoms in the initial and final states, respectively, and the measured cyclotron frequencies of the q -fold charged ions are $\nu_c(M(Z, A)^{q+})$ and $\nu_c(M(Z + 1, A)^{q+})$, respectively. Z is the atomic number and A the mass number. The total uncertainty of the Q -value is dominated by the uncertainty of the frequency ratio and the calculated uncertainty of ΔE_B and not by the uncertainty of $M(Z, A)^{q+}$. This is due to the fact that the frequency ratio is close to one, because the mother and the daughter nuclides are isobars.

The most prominent experiment dedicated to the determination of the electron antineutrino mass is the KATRIN experiment [34]. Here, the electron energy spectrum of the tritium β^- -decay will be analyzed. The shape near the end point depends on the absolute value of the neutrino mass. For the analysis a precise determination of the Q -value of the decay is helpful. The present value was obtained by

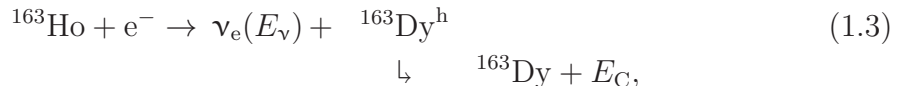
[35] and a further improvement down to a precision of 30 meV is planned at another Penning trap experiment here in Heidelberg [36]. Compared to measurements in the field of cosmology, KATRIN has the advantage that the electron antineutrino mass is determined model-independently. The aim of KATRIN is to improve the present best model-independent value of the electron antineutrino mass of about $2.0 \text{ eV}/c^2$ [37, 38] to $0.2 \text{ eV}/c^2$ (90 %c.l.) [39].

In this field, a further radioactive process under investigation is the β^- -decay of rhenium



The two isotopes ^3H and ^{187}Re meet the demand of a low end-point energy in the beta-spectrum, which is required to maximize the sensitivity of the experiments. For tritium the end-point-energy is 18.6 keV and for rhenium it is 2.47 keV [40]. In contrary to the KATRIN project, which employs a tritium source outside the spectrometer for the detection of the β -electron energy spectrum, the MARE project [41] uses an alternative approach to determine the electron antineutrino mass in the rhenium β^- -decay. Here, the rhenium β -source is placed inside the detector, which consists of an array of rhenium based thermal microcalorimeters [41]. A sub-eV sensitivity of the total energy, except the one of the neutrino, released in the decay is planned. Here, PENTATRAP aims to contribute by measuring the Q -value of ^{187}Re and ^{187}Os with a precision of much better than 1 eV. Both, the calorimetric measurement and the Q -value determined by high-precision Penning-trap mass spectrometry might enable one to probe the neutrino mass at a sub-eV level [39].

Another application of PENTATRAP is to contribute to the determination of an upper limit of the electron neutrino mass. For this purpose, the electron capture (EC) process of holmium [42]



where E_C is the de-excitation energy of dysprosium, is investigated. The choice of holmium can be explained by having a look at the total energy Q_ν of the neutrino

$$Q_\nu = E_\nu + m_\nu c^2 = Q_{\text{EC}} - E_{\text{B},i}, \quad (1.4)$$

with E_ν and m_ν the kinetic energy and the rest mass of the neutrino, respectively, and $E_{\text{B},i}$ the binding energy of the captured electron. The recoil energy of the nucleus is negligible ($< 2 \cdot 10^{-5} \text{ eV}$) [42]. The Q_{EC} -value of the capture process as well as the difference $Q_{\text{EC}} - E_{\text{B},i}$ should be as small as possible in order to have a small Q_ν -value and thus a higher contribution of the rest mass of the neutrino. By far the best candidate with a small Q_{EC} -value of 2.56 keV is ^{163}Ho [43]. PENTATRAP aims to measure the Q_{EC} -value with an accuracy of better than 1 eV. In combination with cryogenic microcalorimetry [44], which aims to determine the end point of the total de-excitation spectrum with an accuracy of $< 1 \text{ eV}$, the present limit of the electron neutrino mass of about 200 eV is planned to be improved by three orders of magnitude. The de-excitation spectrum consists of a couple of peaks having Breit-Wigner shapes. The peaks occur when the ionization energy of the respective electron orbital is equal to $Q_{\text{EC}} - E_\nu$. It should be noted that the MARE collaboration is considering the possibility to investigate also the electron capture

of ^{163}Ho . It is worth mentioning that the search for new EC candidates is still ongoing including nuclides with excited daughter states [4]. Moreover, Penning-trap Q -value measurements of resonant double-electron capture processes can help to find new candidates for microcalorimetric measurements in order to investigate whether neutrinos are Majorana or Dirac particles [45].

Further applications for PENTATRAP are stringent tests of quantum electrodynamics in the regime of extreme electromagnetic fields. Here, the determination of binding energies of highly charged ions is planned. The total binding energy of the electrons of a q -fold charged ion with mass $M(Z, A)^{q+}$ is given as

$$\sum_{i=1}^q E_{\text{B},i}(Z, A) = (M(Z, A)^{q+} - M(Z, A) + q \cdot m_e)c^2, \quad (1.5)$$

where m_e is the electron mass and $M(Z, A)$ is the atomic mass of the atom. It is planned to measure the mass of the same isotope for different charge states. Thus, numerous electron binding energies in the atom can be obtained by calculating the mass difference of ions whose charge state differ by one. As discussed in [46] a lack of measured binding energies in highly charged ions is existing and, e.g., theory models show a discrepancy for the calculated values between Pb^{14+} and Pb^{36+} . A prospect would be the determination of the binding energy of the last remaining $1s$ electron in highly charged ^{208}Pb at the level of better than 1 eV to determine QED contributions. The planned accuracy would exceed the present precision of X-ray spectroscopy [47] by at least a factor of three.

The high-precision mass measurements of PENTATRAP can also contribute to tests of fundamental symmetries and constants, e.g., to a direct test of the mass-energy relationship $E = Mc^2$ of special relativity. Here, PENTATRAP aims for an accuracy of a few eV in the determination of mass differences. Such tests are based on the comparison of the speed of light c_γ with the limiting velocity of a massive particle c_m , whereby the quantity $1 - c_m/c_\gamma$ is determined. Generally, a transition is used where a mass difference ΔM is converted into electromagnetic radiation with frequency ν_γ . The experimental relation is given by

$$\Delta M c_m^2 = h\nu_\gamma = \frac{hc_\gamma}{\lambda}, \quad (1.6)$$

where λ is the wavelength and h the Planck constant. A first experiment was carried out by Greene *et al.* comparing the electron and positron masses with their annihilation energy [48]. The emitted photon wavelength was measured by curved crystal γ -ray spectrometry and the electron and positron masses were known from trap experiments. A second more recent experiment was related to the thermal neutron capture of a nuclide. Highly accurate measurements of the atomic mass difference of the mother and the daughter nuclides were performed [16]. In combination with the detection of the released γ -energy by crystal-diffraction spectrometry a test of Einstein's formula was carried out. A combined value considering the results of the investigated nuclides sulfur and silicon of $1.4(4.4) \cdot 10^{-7}$ was obtained [16]. The error was limited by the uncertainty of the γ -ray measurement.

The PENTATRAP experiment is currently being built at the Max-Planck-Institut für Kernphysik in Heidelberg. The starting point of this thesis was at the early

experimental design phase of the project, where, e.g., the preparations of the specifications for the engineering design office were made. Main results obtained within the work presented here are the commissioning of this technically challenging experiment, including the characterization of the superconducting magnet, the setup of the Penning trap stack to the point of the first cool down of the experiment in the cryogenic environment of the magnet. Furthermore, the setup of the small EBIT at PENTATRAP was carried out and the production of highly charged rhenium and osmium ions for the above mentioned β -transition studies was demonstrated.

This thesis is structured as follows: The basic principles of Penning-trap mass spectrometry including the detection principles will be summarized in Chap. 2. A main intention of this thesis was the commissioning and the characterization of the small PENTATRAP-EBIT as well as first charge breeding investigations. Therefore, the basic working principles of an EBIT and the processes occurring in it are addressed in Chap. 3. The novel design of the PENTATRAP experiment and its specific features comprising the exploration of different measurement schemes are outlined in Chap. 4. Simulations of the ion injection into the Penning-trap stack and the ion transport between two traps are addressed in Chap. 5 followed by the presentation and the discussion of the first magnetic field investigations at PENTATRAP in Chap. 6. Chap. 7 covers the commissioning and testing of this instrumentally challenging experiment such as performance tests of the temperature stabilization of the laboratory and the magnetic field compensation system. Furthermore, the assembly of the highly tolerated Penning traps, the installation of the cryogenic translation and tilt system and the complete cryogenic assembly, the cabling of the Penning traps and the first cooling down of the experiment are presented. Finally, Chap. 8 deals with the commissioning of the PENTATRAP-EBIT and the successful production of highly-charged osmium and rhenium ions dedicated to first measurements related to β -decay studies. In Chap. 9, the thesis is concluded with a summary and future prospects.

Chapter 2

Principles of high-precision Penning-trap mass spectrometry

The centerpiece used in the PENTATRAP experiment is the Penning trap. It enables a storage of charged particles in three dimensions. The basic concept was developed in the nineteen-thirties by Frans M. Penning [49] for the implementation of a vacuum gauge. John R. Pierce first described the Penning trap 1949 [50] and particular experimental development was done later by Hans G. Dehmelt. Together with Wolfgang Paul, Dehmelt was awarded the Nobel Prize in Physics in 1989 for the development of the ion trap technique [51, 52]. Nowadays Penning traps are widely used and deployed in many fields of physics [2, 4]. Particularly for high-precision mass measurements of nuclides they are powerful devices, since they take advantage of relating a mass determination to a frequency measurement, which generally can be realized with very high precision.

In the following the ideal Penning trap (Sec. 2.1), the real Penning trap (Sec. 2.2), ion manipulation principles (Sec. 2.3) and, finally, the ion detection principles (Sec. 2.4) with regard to the planned ultra high-precision measurements at PENTATRAP are presented.

2.1 The ideal Penning trap

The storage of a charged particle in an ideal Penning trap is realized through a superposition of a strong homogeneous static magnetic field for radial and a weak electrostatic quadrupolar field for axial confinement with respect to the magnetic field [53]. A superposition of both fields is required, since Earnshaws' theorem [54], which is understood today as a direct consequence of Maxwell's equations, implies the impossibility to store charged particles only with a static electric or magnetic field. The magnetic field pointing in axial direction $\vec{B} = B \cdot \hat{z}$ forces the ion with charge q and velocity \vec{v} due to the Lorentz-force

$$\vec{F} = q\vec{v} \times \vec{B} \quad (2.1)$$

into a circular cyclotron motion in a plane perpendicular to \vec{B} . Thus, confinement in radial direction is provided and the ion of mass m moves at the free cyclotron frequency

$$\omega_c = \frac{q}{m} B. \quad (2.2)$$

Confinement in the axial direction is provided by an additional electrostatic quadrupole potential

$$V(z, \rho) = V_0 C_2 \left(z^2 - \frac{1}{2} \rho^2 \right), \quad (2.3)$$

where V_0 is the trapping voltage and the parameter C_2 is a specific coefficient which is dependent on the trap geometry, and therefore characterizing the geometrical dimension of the potential. A three-dimensional quadrupolar potential is shown in Fig. 2.1. The equation of motion leads to three differential equations whose solutions

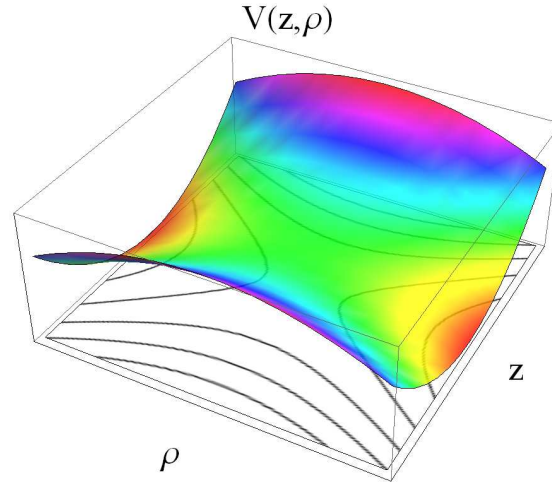


Figure 2.1: Three-dimensional quadrupolar potential inside a Penning trap and projected contour plot in the ρz -plane.

yield a superposition of three uncoupled oscillations [53]. The resulting ion motion is shown in Fig. 2.2. In the axial direction the ion performs a harmonic motion with the axial frequency

$$\omega_z = \sqrt{\frac{q}{m} 2V_0 C_2}. \quad (2.4)$$

The radial motion is a superposition of two circular motions, a fast one at the reduced cyclotron frequency ω_+ and a slow one at the magnetron frequency ω_- . The frequencies ω_{\pm} are given by

$$\omega_{\pm} = \frac{1}{2} \left(\omega_c \pm \sqrt{\omega_c^2 - 2\omega_z^2} \right). \quad (2.5)$$

A bound periodic motion is only possible if the three eigenmotions ω_z , ω_+ and ω_- are real numbers. The square-root in Eq. (2.5) must therefore be a real number which leads to a condition for a stable confinement of a charged particle in a Penning trap

$$\frac{|q|}{m} > 4 \frac{|V_0 C_2|}{B^2}. \quad (2.6)$$

Meaning physically that the magnetic force must be strong enough to hold the particle against the radial electric force on the circular orbit. The magnitudes of the eigenfrequencies are generally ordered such that

$$\omega_- < \omega_z < \omega_+. \quad (2.7)$$

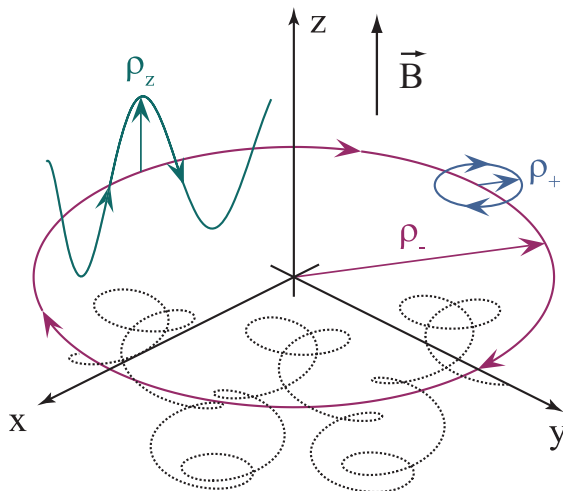


Figure 2.2: Sketch of the complete ion motion in a Penning trap (dashed line), which is a superposition of three modes with amplitudes ρ_+ , ρ_- and ρ_z .

In first order approximation the magnetron motion is found to be independent of the particles mass

$$\omega_- = \frac{C_2 U_0}{B} \quad (2.8)$$

and therefore only depends on the electromagnetic fields. Moreover the following useful relations are valid in an ideal Penning trap:

$$\omega_c = \omega_+ + \omega_- \quad (2.9)$$

and

$$\omega_z^2 = 2\omega_+ \omega_- . \quad (2.10)$$

The invariance theorem [53] gives the relation between the free-space cyclotron frequency and the three eigenfrequencies, which is

$$\omega_c^2 = \omega_z^2 + \omega_+^2 + \omega_-^2, \quad (2.11)$$

and is even valid in the case of elliptic imperfections of the electrical field and misalignments between the electric and magnetic field axis. A measurement of all three frequencies thus results in a determination of the ion's mass (see Eq. (2.2)).

It should be mentioned that the three eigenmotions in an ideal Penning trap can be treated in a quantum-mechanical way as well. Thereby the independent eigenmotions are covered as quantized harmonic oscillators. The total energy for a spinless stored particle can be expressed as

$$E = \hbar\omega_+ \left(n_+ + \frac{1}{2} \right) + \hbar\omega_z \left(n_z + \frac{1}{2} \right) - \hbar\omega_- \left(n_- + \frac{1}{2} \right) = E_+ + E_z + E_-, \quad (2.12)$$

where n_+ , n_z and n_- are the quantum numbers and E_+ , E_z and E_- the energies of the respective modes. The energy levels are shown in Fig. 2.3. The magnetron motion is a metastable motion, since increasing the magnetron number lowers the energy. The expression for the magnetron energy is given by [53]

$$E_- = \underbrace{\frac{1}{2}m\omega_-^2\rho_-^2}_{\text{kinetic energy}} - \underbrace{\frac{1}{2}m\omega_z^2\rho_-^2}_{\text{potential energy}}, \quad (2.13)$$

which clarifies, since $\omega_-^2 \ll \omega_z^2$, that the magnetron energy is dominated by the potential energy with respect to the ring electrode. Therefore, increasing the quantum number n_- and thus increasing the magnetron radius leads to a loss of energy. In general the magnetron motion is stable as long as no additional energy is added. Since the interaction of the magnetron mode with the surrounding is generally very low, the storage time is considerably longer than common experimental observation and measuring times.

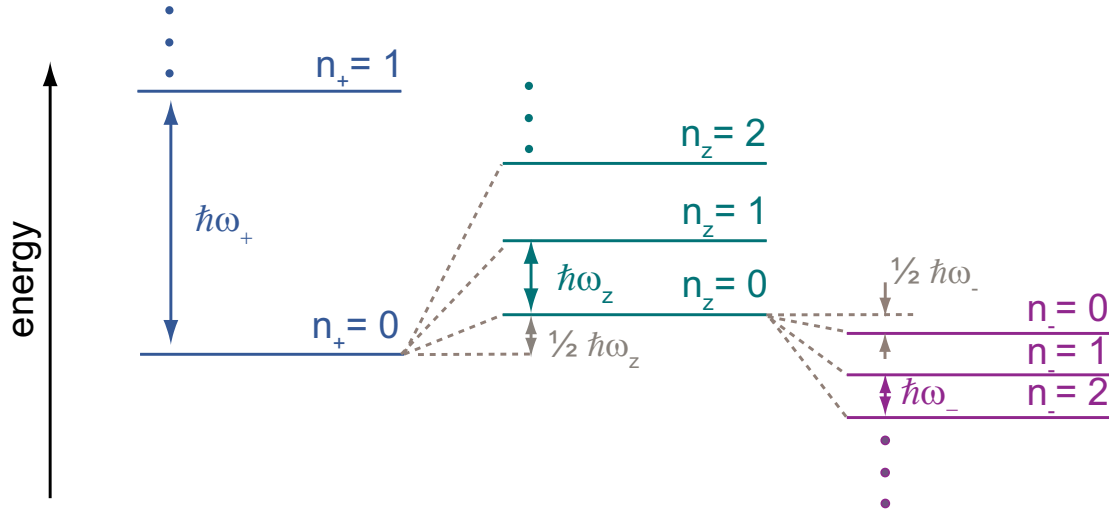


Figure 2.3: Shown are the energy levels of a charged particle stored in an ideal Penning trap. The quantized harmonic oscillators have quantum numbers n_i with $i = \{+, z, -\}$ corresponding to the eigenfrequencies ω_+ , ω_z and ω_- . The magnetron motion is metastable has a negative contribution to the total energy. The spacing between the energy levels is not at right scale.

2.2 The real Penning trap

So far an ideal Penning trap was theoretically described. In the laboratory, the Penning trap commonly is an arrangement of gold-plated high-purity copper electrodes placed in a strong magnetic field of a superconducting magnet. Up to now perfect trapping potentials were considered, but in the experiment deviations from the ideal field configuration are unavoidable. Electric and magnetic field imperfections will change the ion motion and make the motional frequencies energy dependent, which results in a shift of the eigenfrequencies and a modification of the detection signals. Additionally, the shape of the detection signal can be broadened, which depends on the timescales of the nonlinear fluctuations. Especially in the field of high-precision Penning-trap mass measurements this field imperfections must be well understood to counteract them. The field imperfections mentioned above are to some extent under experimental control. This is not the case for the relativistic mass effect [53], which also leads to a coupling and shifting of the eigenfrequencies.

2.2.1 The quadrupolar trapping potential

In general several things have influence on the electric field in a Penning trap, e.g., geometric imperfections such as the finite length of the electrode surfaces, the segmentation of electrodes for excitation and detection as well as manufacture tolerances and truncation by assembling the parts of the Penning trap [53]. Another influence will be due to the image charge fields created by the ions in a Penning trap [55] and the Coulomb interaction between different ions stored in one trap [56]. Both effects lead to a shift of the free cyclotron frequency which is independent of the ion mass and linear in the ion charge. Moreover, the supply voltages of the Penning trap are not ideal and patch potentials on the electrode surfaces can be present (see Sec. 7). The trapping potentials applied at adjacent traps can additional influence each other and the ions stored in each of these traps can interact with each other.

Experimentally the three-dimensional quadrupolar potential near the trap center can be created e.g. by electrodes formed as hyperbolas of revolution (Fig. 2.4(a)) or as a cylindrical trap structure (Fig. 2.4(b)) [57]. Cylindrical structures are often used due to their easier manufacturing and free access to the trap center for particle loading. Such a real trap cannot produce a pure quadrupolar potential, but the geometry of the trap can be chosen in such a way that a compensated trap is designed [58]. Therefore, correction or compensation electrodes are added to the Penning-trap setup. The compensation of the traps provides a harmonic electric potential in the trap's central regions by tuning the applied voltages. To this end the tuning ratio (TR), which is the ratio of the correction and the ring voltage, must be tuned in such a way, that the leading anharmonic terms of the potential vanish. Experimentally the optimum tuning ratio is found when the axial frequency is invariant under changes in the axial energy. Varying the tuning ratio usually will change C_2 and therefore the axial oscillation frequency of the particle. Thus, the detection signals move away from the resonance frequency of the detection system (see Sec. 2.4), which would require changing the ring voltage. Therefore, it is favorable

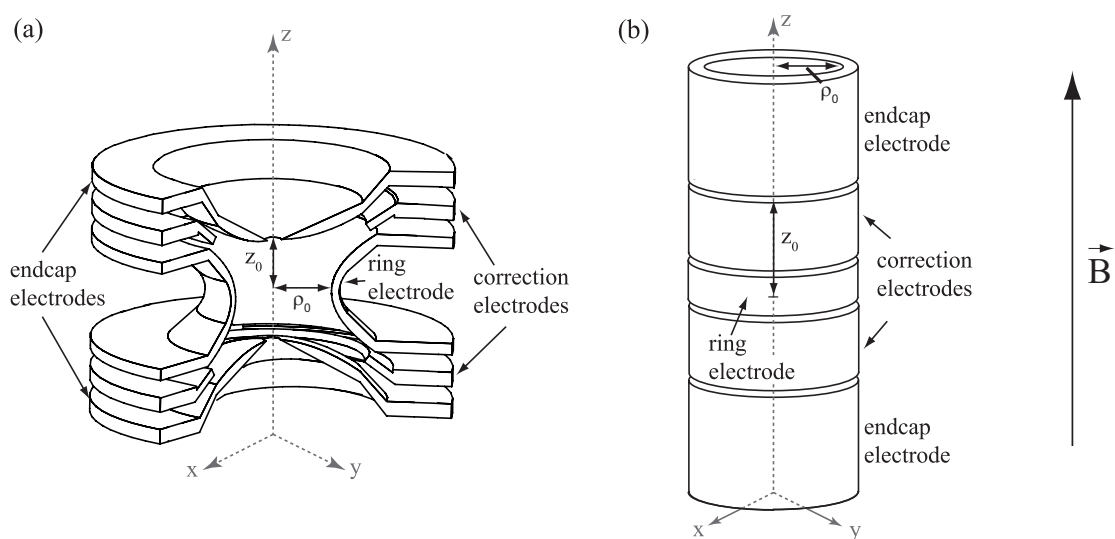


Figure 2.4: Sketch of a five-electrode hyperboloidal (a) and cylindrical (b) Penning trap consisting of ring, correction and endcap electrodes. The correction electrodes are added to create a compensated and orthogonal trap.

to choose the trap geometry such that also an orthogonalized trap is obtained [58] making C_2 ideally independent to the TR and hence less sensitive to the correction voltage. Therewith the needed accuracy of the correction voltage is minimized as well.

Commonly the electrostatic potential of a Penning trap can be expressed through a Taylor expansion [59, 60], and the influence of the electric field coefficients on the ion modes can be determined as done for the cylindrical trap in [58]. A multipole expansion of the potential of the form

$$\Phi(\rho, z) = V_0 \sum_{i=0}^{\infty} C_i (\rho^2 + z^2)^{i/2} P_i \left(\frac{z}{\sqrt{\rho^2 + z^2}} \right), \quad (2.14)$$

with the Legendre polynomials P_i , is done in [53] to determine the difference between this potential and the pure quadrupolar potential mentioned in Eq. (2.3) and therewith the frequency shifts of the eigenfrequencies. The multipole order is characterized by the expansion coefficients C_i , which are also calculated for a cylindrical trap in [57, 58] and in [61] for a multiple trap setup. In case of mirror symmetry (symmetry under the reflection $z \rightarrow -z$), odd terms can be neglected. The shifts of the eigenfrequencies which occur due to the anharmonic potential are calculated in [53, 62] and can be written for the first perturbation order in a matrix form

$$\begin{pmatrix} \Delta\omega_+/\omega_+ \\ \Delta\omega_z/\omega_z \\ \Delta\omega_-/\omega_- \end{pmatrix} = \frac{3C_4}{qV_0C_2^2} \begin{pmatrix} \frac{1}{4}(\omega_z/\omega_+)^4 & -\frac{1}{2}(\omega_z/\omega_+)^2 & -(\omega_z/\omega_+)^2 \\ -\frac{1}{2}(\omega_z/\omega_+)^2 & 1/4 & 1 \\ -(\omega_z/\omega_+)^2 & 1 & 1 \end{pmatrix} \begin{pmatrix} E_+ \\ E_z \\ E_- \end{pmatrix}. \quad (2.15)$$

It is therefore important to tune the correction term C_4/C_2^2 to small values to minimize these shifts. Note, E_- is defined as $E_- = -\hbar\omega_-(n_- + 1/2)$ (see Eq. (2.12)). Considering expansion terms till $i = 6$ the axial energy dependent shift of the axial frequency is

$$\frac{\Delta\omega_z}{\omega_z} = \frac{3}{4} \left(\frac{C_4}{C_2^2} + \frac{5}{4} \frac{C_6}{C_2^3} \left(\frac{E_z}{qV_0} \right) \right) \frac{E_z}{qV_0}. \quad (2.16)$$

The effect on the cyclotron frequency follows from Eq. (2.11) and can be calculated as

$$\frac{\Delta\omega_c}{\omega_c} = \left(\frac{\omega_+}{\omega_c} \right)^2 \cdot \frac{\Delta\omega_+}{\omega_+} + \left(\frac{\omega_z}{\omega_c} \right)^2 \cdot \frac{\Delta\omega_z}{\omega_z} + \left(\frac{\omega_-}{\omega_c} \right)^2 \frac{\Delta\omega_-}{\omega_-}.$$

The anharmonic oscillation leads moreover to an asymmetric shape of the detection signal. A description of the experimental application of tuning the trap by means of the anharmonic signal shape can be found in [60].

In case of distorted mirror symmetry, which occurs, e.g., for patch potentials at the electrode surfaces (see Sec. 7.3) or for asymmetrically biased endcaps, the asymmetric terms of the Taylor expansion are needed to completely describe the electrostatic potential. The main contribution to the asymmetric potential V_A is governed by the coefficients C_1 and C_3 . Due to V_A the center of the ion motion is shifted by [53]

$$z_e = -\frac{1}{2} \frac{V_A C_1}{V_0 C_2}, \quad (2.17)$$

which can be used to move the ion and to measure the magnetic field at various positions in the trap, and the axial frequency is shifted by

$$\frac{\Delta\omega_z}{\omega_z} = \frac{3}{4} \frac{C_1 C_3}{C_2^2} \left(\frac{V_A}{V_0} \right)^2. \quad (2.18)$$

2.2.2 Magnetic field imperfections

Magnetic field inhomogeneities are present due to an imperfect shimming of the finite length solenoid magnet, magnetization of the trap electrodes and the magnetization of the materials used in the ion-trap apparatus. The strength of the magnetization depends on the magnetic susceptibilities of the materials in use (see Tab. 4.3). As result of these inhomogeneities the ion's motion is perturbed which leads to energy-dependent frequency shifts and a broadening of the width of the detection signal. Frequency shifts and modulation effects due to solenoidal magnetic field inhomogeneities are discussed in [63]. The effect of magnetic field inhomogeneities in our experiment are of particular relevance in Chap. 6.

Brown and Gabrielse have derived the relationship between the quantity and location of magnetic material near the center of a trap and the resulting magnetic field perturbation [53]. This perturbation $\Delta B(\rho, z)$, where ρ and z are cylindrical coordinates, can be expressed as the gradient of a skalar potential $\Psi(\rho, z)$ which satisfies the Laplace equation. A multipole expansion of $\Psi(\rho, z)$ in powers of z

$$\Psi(\rho, z) = - \sum_{l=1}^{\infty} l^{-1} B_{l-1} (\rho^2 + z^2)^{l/2} P_l \left(\frac{z}{\sqrt{\rho^2 + z^2}} \right) \quad (2.19)$$

leads to

$$\begin{aligned} \Delta B(\rho, z) &= \sum_{l=0}^{\infty} B_l (\rho^2 + z^2)^{l/2} \left[P_l \left(\frac{z}{\sqrt{\rho^2 + z^2}} \right) \hat{z} - (l+1)^{-1} P_l^1 \left(\frac{z}{\sqrt{\rho^2 + z^2}} \right) \hat{\rho} \right] \\ &= B_0 \hat{z} + B_1 \left[z \hat{z} - \frac{1}{2} \rho \hat{\rho} \right] + B_2 \left[\left(z^2 - \frac{1}{2} \rho^2 \right) \hat{z} - \rho z \hat{\rho} \right] + \dots \end{aligned} \quad (2.20)$$

with the expansion coefficients B_l , the Legendre polynomials $P_l(z/(\rho^2 + z^2))$ and the associated Legendre polynomials $P_l^1(z/(\rho^2 + z^2))$. The leading and most important nonuniform field perturbation is given by the magnetic bottle term B_2 , which causes an energy dependent frequency shift. A compilation of magnetic susceptibilities for materials used at PENTATRAN is given in Chap. 4. For the experimental determination of B_2 and the calculated influence on the ion's frequencies see Chap. 6. Further theoretical treatment in this context can be found in text books such as, e.g., [64]. The resulting frequency shift of the three eigenfrequencies can be written for the first perturbation order in a matrix form as well [53]:

$$\begin{pmatrix} \Delta\omega_+/\omega_+ \\ \Delta\omega_z/\omega_z \\ \Delta\omega_-/\omega_- \end{pmatrix} = \frac{1}{m\omega_z^2 |B|} \begin{pmatrix} -(\omega_z/\omega_+)^2 & 1 & 2 \\ 1 & 0 & -1 \\ 2 & -1 & -2 \end{pmatrix} \begin{pmatrix} E_+ \\ E_z \\ E_- \end{pmatrix}. \quad (2.21)$$

Another process which leads to a change in the magnetic field is based on the fact that the current running through the superconducting coils of the magnet decreases

steadily due to the so-called flux creep phenomenon [65]. Therefore measurements of the cyclotron frequencies of ions with well-known masses will be done over a period of time to check this effect [66]. Further, fluctuations of the level and pressure in the liquid helium vessels of the magnet cause a change in the magnetic permeability of the materials used in the magnet (see Chap. 4).

Unavoidal imperfections, such as tilted axes of the electric and magnetic potential with respect to each other or deviations of the trap surface from the ideal form, alter the quadratic terms in the electrostatic potential. The eigenfrequencies are then functions of two misalignment angles (θ, φ) and a harmonic distortion factor ϵ [67]: $\bar{\omega}_+(\theta, \varphi, \epsilon)$, $\bar{\omega}_z(\theta, \varphi, \epsilon)$ and $\bar{\omega}_-(\theta, \varphi, \epsilon)$. The magnetic field and the electrostatic potential at lowest order are also described by θ , φ and ϵ and are given by

$$B = B \sin \theta \cos \varphi \hat{x} + B \sin \theta \sin \varphi \hat{y} + B \cos \theta \hat{z} \quad (2.22)$$

and

$$V = V_0 C_2 \left(z^2 - \frac{1}{2} (x^2 + y^2) - \frac{1}{2} \epsilon (x^2 - y^2) \right) + \dots \quad (2.23)$$

To optimize the misalignment angle θ the axial frequency

$$\bar{\omega}_z^2 \approx \omega_z^2 \left(1 - \frac{3}{2} \theta^2 \right) \quad (2.24)$$

is maximized for a fixed trapping voltage. This ideally will make θ zero. For several high-precision hyperboloidal traps θ is adjusted to $|\theta| < 10^{-3}$ [68]. The adjustment system used at PENTATRAP for this procedure is presented in Chap. 7. Another possibility to characterize θ and ϵ is by measuring the eigenfrequencies and use the relation

$$\frac{9}{4} \theta^2 - \frac{1}{2} \epsilon^2 \approx \frac{2\bar{\omega}_- \bar{\omega}_+}{\bar{\omega}_z^2} - 1. \quad (2.25)$$

Thereby $|\epsilon| \leq 10^{-3}$ is determined for high-precision hyperboloidal traps [68]. To first order these effects are not relevant and the invariance theorem will be anyhow valid when substituting the eigenfrequencies in Eq. (2.11) by $\bar{\omega}_+(\theta, \varphi, \epsilon)$, $\bar{\omega}_z(\theta, \varphi, \epsilon)$ and $\bar{\omega}_-(\theta, \varphi, \epsilon)$.

2.3 Ion manipulation

A good control over the manipulation of the ion's motion is indispensable to perform high-precision mass measurements. In the following the principles of excitation, coupling and the cooling of different eigenmodes are presented.

2.3.1 Ion excitation

Applying a resonant dipolar electric rf field to a Penning trap enables a change of the quantum number of one of the three eigenmodes (see Eq.(2.12)) of the trapped particle. This allows one to increase the amplitude of motion, which is relevant for detection or for elimination of unwanted ions. Due to the almost mass independence of the magnetron motion, an excitation at ω_- will affect all ions stored inside the

trap. In contrast, a dipolar excitation at ω_+ or ω_z affects only ions with a certain mass-to-charge ratio. For a dipolar excitation in the radial x -direction a field of the shape

$$\vec{E}_x = \frac{V_d}{d} \cdot \cos(\omega_{\text{rf}}t - \phi_{\text{rf}}) \cdot \hat{x} \quad (2.26)$$

can be applied at an electrode segment of a splitted correction electrode (see Fig. 2.5(a)). Here V_d is the rf voltage amplitude, d a characteristic trap dimension, ω_{rf} the excitation frequency and ϕ_{rf} the phase offset. This electrode segment can be used for applying an axial dipolar excitation as well.

A coupling of two modes is achieved by applying a quadrupolar electric rf field at the right frequency [69]. Here it is possible to transfer energy from one mode to another. Quadrupolar excitation is done at the sum or the difference of two eigenfrequencies. The excitation can be done with two rf fields at the drive frequency ω_{rf} , which are applied with the same phase at two electrode segments of different, rotated by 90° against each other, correction electrodes (see Fig. 2.5(b)). A possible quadrupolar field for coupling the axial and the radial modes ($\omega_{\text{rf}} = \omega_+ - \omega_z$ or $\omega_{\text{rf}} = \omega_z + \omega_-$) is created by

$$\vec{E}_x = \frac{2V_q}{d^2} \cdot \cos(\omega_{\text{rf}}t - \phi_{\text{rf}}) \cdot z \cdot \hat{x} \quad (2.27)$$

$$\vec{E}_z = \frac{2V_q}{d^2} \cdot \cos(\omega_{\text{rf}}t - \phi_{\text{rf}}) \cdot x \cdot \hat{z}. \quad (2.28)$$

Here, V_q is the applied rf voltage amplitude for the creation of the quadrupolar field. A quadrupolar excitation at $\omega_{\text{rf}} = \omega_+ + \omega_-$ for coupling the radial modes can be realized with this electrode configuration as well. Figure 2.6 shows the conversion of a primary pure magnetron motion into a pure cyclotron motion due to an excitation with an azimuthal quadrupolar field at the sum frequency. The radial kinetic energy

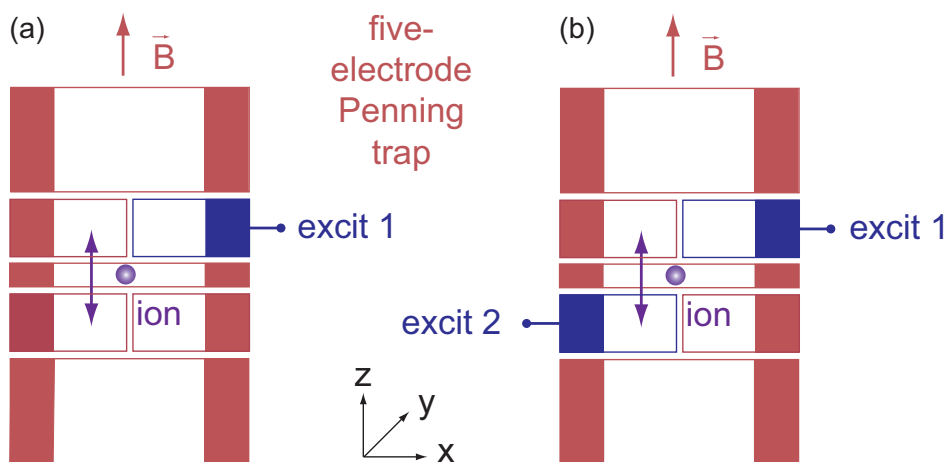


Figure 2.5: Example of excitations in a five-electrode Penning trap. Excitation 1 (excit 1) can be used for either an axial dipolar or a radial dipolar excitation (a). In combination with excitation 2 (excit 2) a quadrupolar coupling of the eigenfrequencies can be realized (b). It is worth mentioning that in configuration (a) the rf field contains quadrupolar components as well but they are small compared to configuration (b).

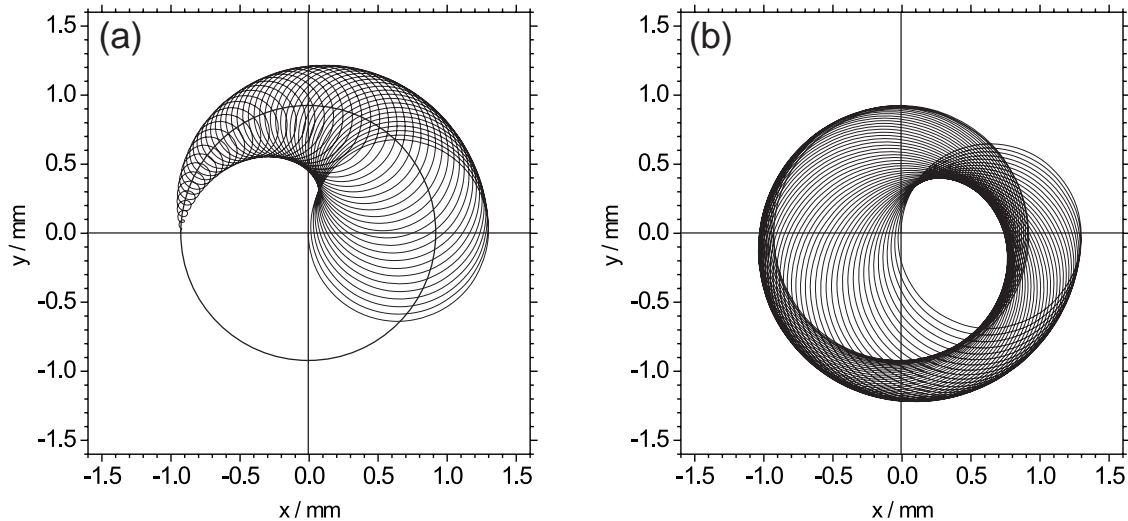


Figure 2.6: Conversion from pure magnetron into pure cyclotron motion under a quadrupolar excitation at $\omega_{rf} = \omega_+ + \omega_-$. The first part of the conversion is shown in part (a) the second half in part (b). The center of the cross characterizes the trap center. Picture taken from [2].

is related to the modified cyclotron amplitude and changes periodically. A variety of different excitation schemes employing different electrodes are possible and an overview is given in [70]. Recently, there have been a number of studies on the octupolar excitation [71, 72], which is till now not planned at PENTATRAP.

2.3.2 Ion cooling

For high-precision experiments using Penning traps excellent control over the motional amplitudes is essential. Frequency shifts due to magnetic and electric field imperfections generally increase with larger distance from the trap center, which implies the necessity of small ion orbits. Moreover, the ion transport is simplified due to the decreased emittance. Commonly cooling of an atom means increasing the phase space density. Consequently cooling in a Penning trap means a reduction of the motional amplitudes and in a quantum mechanical sense a reduction of the quantum numbers (see Fig. 2.3). In order to enable cooling and not to infringe Liouville's theorem [73] outer interactions are needed. For a non-destructive single particle detection a cryogenic environment and ultra-high vacuum conditions are realized in the experiment. Thus, loss mechanisms like collisions with the rest gas or radiative energy loss generally are suppressed. In setups like PENTATRAP a damping of the ion motion is realized via a connected external circuit. An overview of techniques applied in various fields of Penning-trap spectrometry can be found in [2, 74]. In the following the general principles of cooling the respective eigenmode are outlined. In Sec. 2.4 they are further discussed in the context with the ion detection principles.

Damping of the axial frequency can be accomplished via a tuned axial circuit. Thereby a minimal energy of $E_z = k_B T_C$ can be realized, with T_C the temperature of the tuned circuit which is near the ambient temperature (in our case ≈ 4 K). A reduction of the motional amplitude of the magnetron mode is realized by adding energy to this mode, since a smaller quantum number and radius corresponds to an

increase of the magnetron energy, as the decrease of the kinetic energy is exceeded by the increase of potential energy (see Eq. (2.13)). Note, the magnetron radius is generally larger than the motional radii in the other modes (see Fig. 2.2). A procedure for damping the magnetron motion can be, e.g., a coupling to the axial motion, which is called sideband cooling [69]. Therefore a quadrupolar coupling field at frequency $\omega_{\text{rf}} = \omega_z + \omega_-$ is applied. However, with the maximal axial sideband cooling only a minimum achievable average magnetron energy of [53]

$$k_{\text{B}}T_- = \langle E_- \rangle = -\frac{\omega_-}{\omega_z} \langle E_z \rangle = -\frac{\omega_-}{\omega_z} k_{\text{B}}T_z, \quad (2.29)$$

with T_z and T_- the temperature of the axial and magnetron oscillation, respectively, can be achieved. With Eq. (2.13) the corresponding magnetron radius ρ_- can be calculated. Shining $\omega_{\text{rf}} = \omega_+ - \omega_z$ to the trap the modified cyclotron motion is cooled via a coupling to the axial motion.

Moreover, it is possible to perform cooling via a tuned circuit on $\nu_+ = \omega_+/2\pi$. The advantage of cooling via coupling to the cyclotron motion is that very low cooling limits (see frequency relation given in Eq. (2.7))

$$T_z = \frac{\langle E_z \rangle}{k_{\text{B}}} = \frac{\omega_z}{\omega_+} \frac{\langle E_+ \rangle}{k_{\text{B}}} = \frac{\omega_z}{\omega_+} T_+ \quad (2.30)$$

and

$$T_- = \frac{\langle E_- \rangle}{k_{\text{B}}} = -\frac{\omega_-}{\omega_+} \frac{\langle E_+ \rangle}{k_{\text{B}}} = -\frac{\omega_-}{\omega_+} T_+, \quad (2.31)$$

with T_+ the temperature of the modified cyclotron motion, can be realized, but with the disadvantage of typically very slow cooling rates [53].

2.4 Ion detection

Two basic principles, the destructive time-of-flight ion-cyclotron-resonance (TOF-ICR) detection technique [31, 75] and the non-destructive Fourier-transform ion-cyclotron resonance (FT-ICR) detection technique [32, 76] are used in the field of Penning-trap mass spectrometry. To perform mass-ratio measurements with relative uncertainties of 10^{-11} and below, it is mandatory to measure the eigenfrequencies of a single stored ion non-destructively via the image-current detection technique. It will be used at PENTATRAP and in the following the detection principles which are employed, the resulting experimental constraints and the specific measurement methods to determine the free cyclotron frequency with ultra-high accuracy at PENTATRAP are outlined.

As can be seen by means of Eq. (2.17), which gives the variation of the cyclotron frequency as a function of the variation of the ion's eigenfrequencies, the axial and the magnetron frequency are sufficient to be measured by a factor $(\nu_z/\nu_c)^2$ and $(\nu_-/\nu_c)^2$ less precise than the reduced cyclotron frequency. These factors depend on the charge-to-mass ratio of the measured ion, which implies that the required precision generally decreases with the charge state of the ion. The eigenfrequencies of, e.g., $^{187}\text{Os}^{45+}$ are at a magnetic field of 7 T and a trapping voltage of $V_0 = -20.45$ V $\nu_+ = 25.86$ MHz, $\nu_- = 6.96$ kHz and $\nu_z = 600$ kHz. In order to measure ν_c with a

precision of a few parts in 10^{12} , one has to measure ν_+ , ν_z and ν_- with a relative precision of about 10^{-12} , 10^{-9} and 10^{-5} , respectively. Consequently, a main challenge is to achieve the necessary precision in the determination of ν_+ . Moreover, to keep the required absolute precision as low as possible a strong magnetic field of 7 T is chosen.

The basic idea of the image current detection is shown in Fig. 2.7(a). An ion oscillating between two infinitely extended parallel conducting plates, which are connected by an impedance $Z(\omega)$, causes a temporal change of the image charges induced on the plates [77]. This model can be extended by substituting the conducting plates by finite Penning-trap electrodes. Thus, as a result of the ions' oscillation, image currents I

$$I = \frac{q}{d} 2\pi\nu_i \rho_i \quad (2.32)$$

are induced in the trap electrodes, where ν_i is the respective eigenfrequency and ρ_i is the corresponding motional amplitude. d is a characteristic length defined by the geometry of the trap. This so-called effective electrode distance [78] can be calculated for axial or radial signal pick up using the equations given, e.g., in [60]. Typically the induced currents I are in the fA range. These tiny currents can be detected with highly sensitive detection systems, which are connected to the trap electrodes. Since the Penning-trap electrodes have a capacitance to ground C_t a purely high ohmic resistor cannot be used, since it would be bypassed by the trap capacitance which is in the pF range. Therefore, the detection system, technically based on [76], employs a tank circuit that consists of an inductor L and the system's total capacitance C (see Fig. 2.8). The total capacitance $C = C_t + C_c + C_p$ is given by the trap capacitance C_t , the capacitance of the coil C_c and other parasitic capacitances C_p . In Fig. 2.9(a) the absolute value of the complex impedance of the tank circuit is shown. At the tank circuit's resonance frequency

$$2\pi\nu_0 = \frac{1}{\sqrt{LC}}, \quad (2.33)$$

the effective resistance is purely real (see Fig. 2.9(b)) and has its maximum value of

$$R_{\text{res}} = 2\pi\nu_0 QL. \quad (2.34)$$

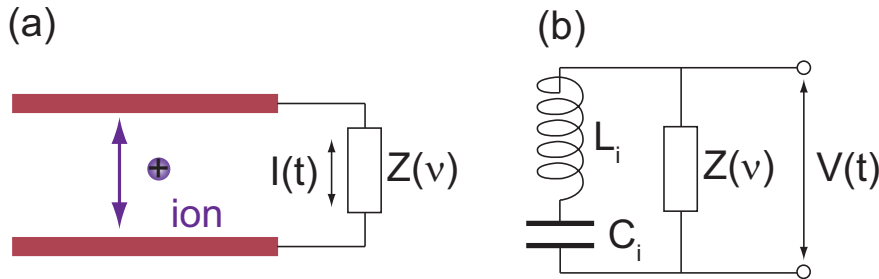


Figure 2.7: The image current detection can be illustrated by the ion moving between two parallel conducting plates which are connected by a high impedance $Z(\nu)$ (a). As a result of the ions' oscillation image currents are induced. In thermal equilibrium with the tank circuit, the ion movement can be modelled as a series LC circuit (b) formed by the inductance L_i and capacitance C_i . The tiny image current causes a voltage drop $V(t)$.

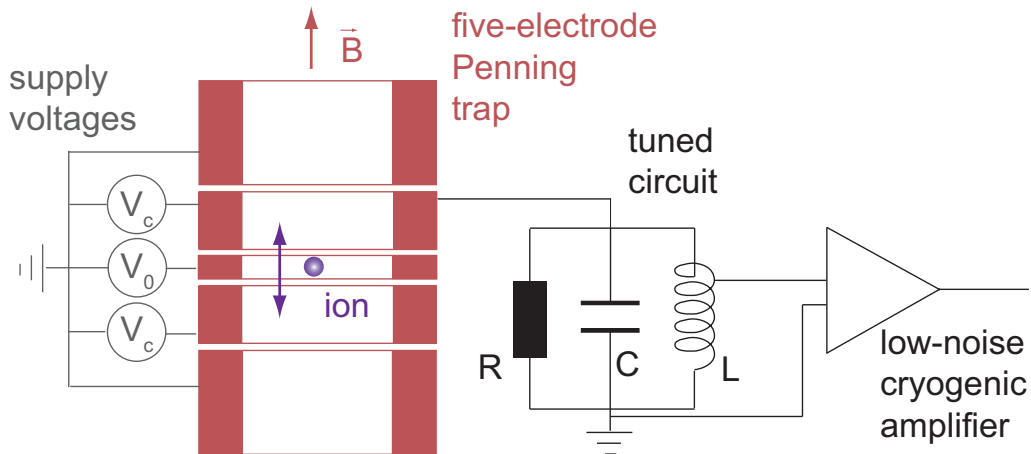


Figure 2.8: Sketch of the single particle detection in a five-electrode cylindrical Penning trap. The ion is oscillating in the trap. In this example a correction electrode of the Penning trap is connected to a parallel LCR tank circuit. Subsequent the signal is fed to a low-noise cryogenic amplifier with high ohmic input. For details see text.

A perfect parallel LC circuit would have infinite resistance on resonance, but due to resistive and dielectric losses, the resistance on resonance is finite. The quality factor Q of the tank circuit is given as (see Fig. 2.9(a))

$$Q = \frac{R_{\text{res}}}{2\pi\nu_0 L} = \frac{\nu_0}{\Delta\nu}. \quad (2.35)$$

Tuning the resonance frequency of the detector to the eigenfrequency of the particle, the tiny image current I causes a voltage signal

$$V = R_{\text{res}} I, \quad (2.36)$$

which is amplified by an ultra low-noise amplifier and analyzed with an FFT spectrum analyzer.

In order to work at high signal-to-noise ratios, the whole trap system is operated at cryogenic temperatures (4 K). In this environment, superconducting alloys (NbTi) can be used for the axial inductors, which leads to high quality factors [79]. Furthermore, at 4 K the equivalent input noise density e_n of the amplifiers is reduced, e.g., at PENTATRAP e_n amounts to approximately $700 \text{ pV/Hz}^{1/2}$ for the axial amplifier at $\nu_0 = 600 \text{ kHz}$ [80]. For a description of the noise matching of the amplifier see, e.g., [60].

In case the eigenmotion is not in thermal equilibrium with the tank circuit, the excess energy is dissipated in the resistance of the circuit, which results in a voltage drop across the tank circuit (see Fig. 2.10(a)). The noise spectrum of the resonator is superimposed with a peak at the eigenfrequency with maximum peak amplitudes for $\nu_0 = \nu_i$. When coupled to the detection system, the particle cools resistively to the ambient temperature of the detection system [32] with a cooling time constant

$$\tau = \frac{m}{q^2} \frac{d^2}{R_{\text{res}}}. \quad (2.37)$$

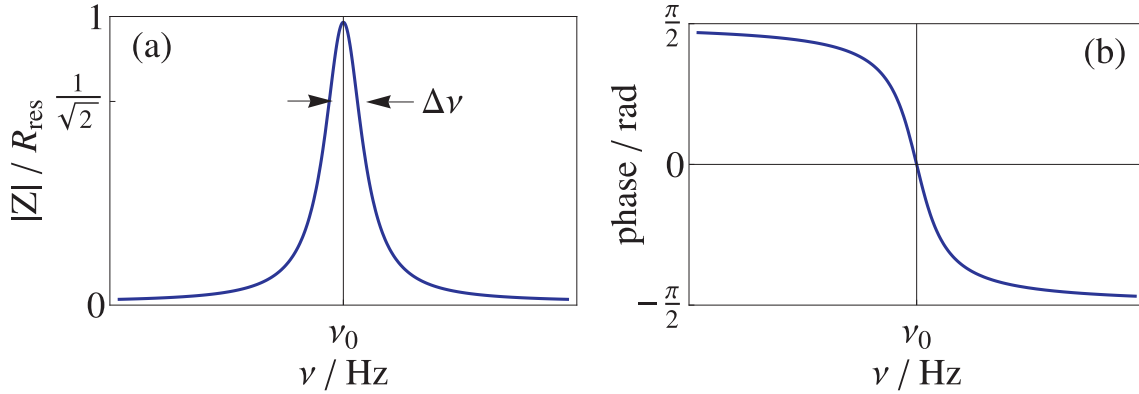


Figure 2.9: (a) Absolute value of the complex impedance $Z(\nu)$. The full width at $R_{\text{res}}/\sqrt{2}$ is $\Delta\nu$ and defines the quality factor Q . (b) Shown is the phase of $Z(\nu)$. The impedance is purely real at resonance, since for $\nu = \nu_0$ the phase is zero.

Depending on the electrode chosen for the axial signal pickup and for typical values of the loaded Q (see Eq. (2.35)), the estimated axial cooling constant at PENTATRAP ranges from a few seconds for low charged ions down to a few tens milliseconds for highly charged ions. The cooling time constant of the reduced cyclotron motion is estimated to range from a few minutes to a few seconds for highly and low charged ions, respectively. Thus, higher charge states are preferable because the measurement cycle can be kept shorter and the ions are confined to a smaller volume. Moreover, negative feedback cooling [81, 82] can be applied, whereby particle temperatures far below the ambient temperatures of the setup can be realized. The principle is based on the feedback of the properly amplified and phase shifted signal to the resonator.

When the ions are in thermal equilibrium with the detection circuit, which is in direct contact with the liquid helium at 4 K, they short out the thermal noise of the tuned circuit, and a dip occurs in the FFT spectrum with a minimum at the eigenfrequency of the particle [32] (see Fig. 2.10(b)). This is understandable because the ion motion can be modeled as a series LC circuit [81], which has zero impedance at its resonance frequency (see Fig. 2.7 (b)). An equivalent circuit model is described e.g. in [83]. The respective eigenfrequency ν_i of the trapped ion can be directly measured by determining the frequency of the minimum in the noise spectrum of the detection system (see Fig. 2.10(b)). In a frequency measurement, which is carried out detecting the noise dip, the trapped particle is at low temperatures, which corresponds to low amplitudes. Thus, the ion is less affected by electric and magnetic field errors. In general, the coupling of the ion motion to the thermal bath of the detection system leads to a broadening of the resonance curve [53, 84].

Due to the very narrow and commonly not resolvable noise dip of the modified cyclotron frequency ν_+ , the noise-dip detection technique is applied only to measure the axial frequency ν_z of the particle. The radial frequencies ν_+ and ν_- are measured indirectly via resonant sideband coupling [69]. Applying a radiofrequency drive signal with frequency $\nu_{\text{rf}} = \nu_{\pm} \mp \nu_z$ to the trap, a double-dip structure occurs in the thermal noise spectrum of the detector. By determining the frequencies of both dips, the modified cyclotron frequency ν_+ and the magnetron frequency ν_- , respectively, can be calculated as described in [69].

Another possible technique to measure the modified cyclotron frequency ν_+ uses

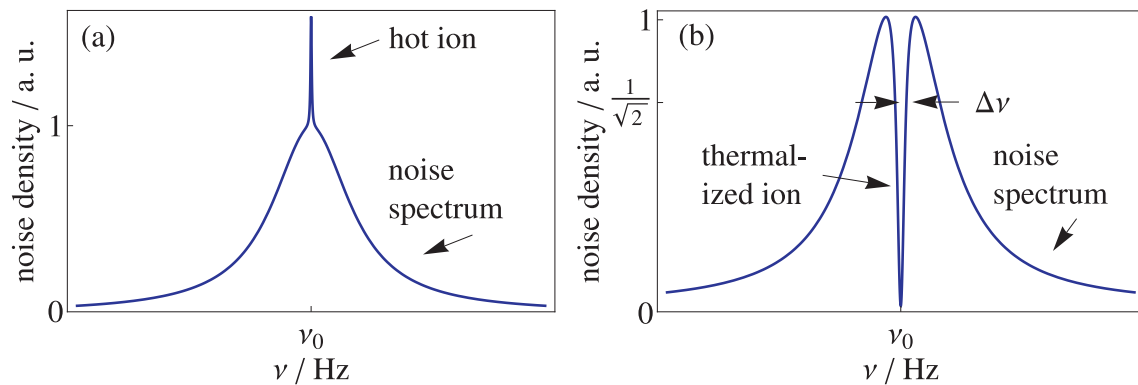


Figure 2.10: (a) Noise spectrum of the resonator superimposed with a peak at the eigenfrequency. The ion is not in thermal equilibrium with the tank circuit. Maximum peak amplitudes are obtained for $\nu_0 = \nu_i$. (b) Minimum in the noise spectrum of the detection system in case the ion is at thermal temperatures and $\nu_0 = \nu_i$. Note, for detection it is also possible to slightly detune ν_i . The pictures are not at right scale.

phase-sensitive detection. Compared to the double-dip detection technique it is faster [85] and therefore less sensitive to magnetic and electric field fluctuations. Furthermore, due to the direct detection of the phase, the dependence of ν_+ on fluctuations in the trap supply voltage is smaller. Phase fluctuations originating from the noise of the detection system are a limiting factor. They can only be minimized through longer measurement times or by increasing the signal-to-noise ratio. The latter can be achieved by an excitation of the particle's motional amplitudes. In this context, the use of highly charged ions is advantageous since lower amplitudes are needed to obtain a sufficient signal, and therefore the ion experiences less anharmonicities of the storage fields. Radii of the eigenmotions of some exemplary nuclides after axial sideband cooling are listed in Tab. 2.1.

A well-proven phase-sensitive method to measure the modified cyclotron frequency ν_+ with low uncertainty down to a level of 10^{-11} is the so-called Pulse-aNd-Phase (PNP) technique [86]. In this technique, the modified cyclotron motion of the pre-cooled ion is first excited to a fixed amplitude and starting phase. After a well-defined phase evolution time, a coupling pulse is applied that swaps the phase of the cyclotron and axial modes. The axial phase is measured as a function of the free phase evolution time. From this measurement the modified cyclotron phase can be determined. Finally, the knowledge of both, the modified cyclotron phase and the phase evolution time, leads to a determination of the modified cyclotron frequency.

For the ultra high-precision experiments with PENTATRAN, it is planned to apply a novel phase-sensitive technique introduced by S. Sturm *et al.* [87] for the measurements of ν_+ . Similar to the well-known PNP technique this Pulse 'N' Amplify, (PNA) technique allows the direct extraction of the phase information of the cyclotron motion from the digitized axial signal. In the PNA method, in contrast to the PNP method, cyclotron-to-axial-coupling is applied at the sum frequency, producing parametric amplification of the resulting axial motion. This allows cyclotron measurements with substantial smaller initial cyclotron amplitudes, in principle independent of the detector performance, hence reducing energy-dependent systematic

shifts. This allows a measurement of ν_+ with higher precision for a certain measurement time.

In order to achieve a single shot precision of $\Delta\nu_+/\nu_+ = 10^{-10}$ at $\nu_+ = 20$ MHz within a measurement time of 100 s, a phase jitter up to $\delta\phi = 72^\circ$ is acceptable. Thereby, the relative frequency jitter is connected to the phase jitter $\delta\phi$ by

$$\frac{\delta\nu_+}{\nu_+} = \frac{\delta\phi}{360^\circ\nu_+T_{\text{meas}}}, \quad (2.38)$$

where T_{meas} is the measurement time. It follows that the excitation energy, which defines the starting phase, should be 3.6 meV or converted into the particle's temperature 42 K for an initial temperature of, e.g., 4 K. It is worth mentioning that the measurement time depends on the magnetic field stability. A stabilization system is planned to achieve an overall temporal stability of the magnetic field of at least a few ten ppt per hour (see Chap. 4). Further discussion in the context of the anharmonic electrostatic potential is given in [61]. For a discussion addressing the magnetic bottle term B_2 see Chap. 6.

Concluding, the main experimental features to achieve the required precision are:

- a 4 K environment
- a stable magnet system
- fast measurement cycles to reduce the effect of magnetic noise
- a stable voltage source to achieve $\Delta\nu_z/\nu_z \leq 10^{-9}$ to measure ν_c on a 10^{-11} level by means of the PNA technique. Therefore, even when ν_z is taken as the average over many measurements, the ring voltage must be stable on a level of a few parts in 10^8 over a few minutes.

Keeping these requirements in mind, the experimental setup of PENTATRAP will be explained in Chap. 4.

Table 2.1: Trapping voltage V_0 and radii of the eigenmotions of some exemplary nuclides for a magnetic field of 7 T and a fixed axial frequency of 600 kHz. The radii were calculated for an axial energy of $E_z = k_B \cdot 4.2$ K and radial energies which were determined for an indirect axial sideband cooling (see Eq. 2.30 and Eq. 2.31). In the cooling limit the radial frequencies are equal. The radius of the axial frequency ρ_z is independent of the charge state of the nuclide, but the radii of the radial motions (ρ_+ and ρ_-) decrease with increasing charge state of the nuclide.

ion	V_0 / V	$\rho_{+,-} / \mu\text{m}$	$\rho_z / \mu\text{m}$
${}^4\text{He}^{1+}$	-19.69	5.24	35.05
${}^4\text{He}^{2+}$	-9.85	3.70	
${}^{40}\text{Ar}^{2+}$	-98.45	3.73	11.08
${}^{40}\text{Ar}^{18+}$	-10.94	1.23	
${}^{132}\text{Xe}^{7+}$	-92.83	1.99	6.10
${}^{132}\text{Xe}^{20+}$	-32.49	1.17	
${}^{132}\text{Xe}^{54+}$	-12.03	0.71	
${}^{208}\text{Pb}^{11+}$	-93.08	1.59	4.86
${}^{208}\text{Pb}^{20+}$	-51.19	1.17	
${}^{208}\text{Pb}^{40+}$	-25.60	0.83	
${}^{208}\text{Pb}^{82+}$	-12.49	0.58	

Chapter 3

The electron beam ion trap

A well-proven source for highly charged ions is the electron beam ion trap (EBIT), which was developed by Levine *et al.* [88, 89]. Its design is based on the electron beam ion source (EBIS) concept realized in Dubna by Donets *et al.* [90, 91]. An upgrade of the EBIT leading to higher energy operation, Super-EBIT [92], was developed at the Lawrence Livermore National Laboratory (LLNL). Such devices have delivered ions of up to Cf^{96+} [93, 94, 95]. In general, EBITs are all-purpose and comparatively flexible devices. They are deployed manifold to study the physics of highly charged ions [96], e.g., to analyze processes occurring inside the EBIT volume or to determine fundamental properties of the highly charged ions. Excellent beam quality, variable pulse lengths of the extracted ion bunch from μs to DC beams and UHV compability are additional advantages [97].

Based on the possibility of *in situ* observations of emitted X-rays from the highly charged ions a differentiation of EBIT and EBIS devices can be made. Including this feature differences in the magnet configuration and the trap length are resulting as will be discussed later. Nevertheless EBITs can be operated as ion traps or ion sources as well. Experiments employing the EBIT as a trap are, e.g., charge exchange [98], resonance spectroscopy [99], spectroscopy [100], lifetime [101] and photoionization [102] experiments. EBITs are today utilized as ion sources in the field of collision physics such as reaction microscopy [103], surface science [104] and in the case of high-precision Penning-trap mass spectrometry [29].

Generally mass measurements benefit from choosing higher charge states of the ion since the cyclotron frequency scales with q (see Eq. (2.2)) and the experimental precision can be improved. A first proof of the confinement of highly charged ions ($\text{Th}^{68+,72+}$ and Xe^{44+}) produced by an EBIT in a cryogenic Penning trap was carried out in 1994 by Schneider *et al.* with the Livermore EBIT using RETRAP [22]. The first mass spectrometer which had direct access to highly charged stable ions was the SMILETRAP Penning-trap facility [23, 24]. At SMILETRAP highly charged ions were created at the electron beam ion source CRYISIS [25] and accuracies of a few 10^{-10} in the mass determination were realized using the TOF-ICR detection technique (see Sec. 2.4). Currently SMILETRAP II [26] is under construction and will be connected to the S-EBIT [27]. With the new S-EBIT higher electron beam energies up to 260 keV will allow the creation of fully-ionized U^{92+} . Another mass spectrometer including an EBIT is the TITAN facility [28, 30]. For the first time TITAN recently carried out high-precision mass measurements on highly charged

short-lived radionuclides employing also the TOF-ICR measurement technique [29]. These experiments on radioactive nuclides with half-lives down to 65 ms and charge states up to 22+ were possible due to recent developments at the TITAN-EBIT [105].

In contrary to the above mentioned high-precision Penning-trap experiments, PENTATRAP will determine mass ratios by storing only a single highly charged long-lived nuclide in the Penning trap and detecting it non-destructively via the FT-ICR detection technique. Utilizing this technique, which requires a certain lifetime of the ion, accuracies of few parts in 10^{12} are aimed for. The PENTATRAP setup currently employs a small commercial room temperature Dresden-EBIT3 [106, 107, 108] and soon it will be connected to the Heidelberg-EBIT [109, 110, 111] to obtain highly charged long-lived ions up to uranium (see Chap. 8). Future prospects furthermore include plans to adapt the PENTATRAP mass spectrometer to the HITRAP facility [112] at the Helmholtzzentrum für Schwerionenforschung GSI, to have access to low-emittance beams of highly charged short-lived ions up to bare uranium with charge-specific kinetic energies in the range of $\text{meV}\cdot q$.

This chapter covers the basic working principles and processes occurring inside an EBIT, since a main intention of this thesis was the commissioning and the characterization of the Dresden-EBIT3 as well as the first charge breeding investigations for PENTATRAP. Section 3.1 introduces the principle of operation, Sec. 3.2 covers the properties of the electron beam, Sec. 3.3 the ion cloud and finally Sec. 3.4 the interaction of the ion cloud with the electron beam. An overview of the various collision processes in the trap is given and the rate equation of the time evolution of the charge states is presented.

3.1 Mode of operation

The operation principle of an EBIT is shown in Fig. 3.1. Ions are axially confined inside the trap volume by applying a voltage to the drift tubes. Radial confinement is achieved by a magnetically compressed monoenergetic electron beam in combination with the magnetic field itself. A sketch of the electrostatic potential is shown in Fig. 3.2. The electrons emitted from a cathode ionize the atoms sequentially by electron impact. The electron beam energy is defined by the potential difference applied between the cathode and the trap. Cryogenic temperatures ensure an ultra-high vacuum, which is necessary for reaching high charge states. In general, the magnetic field is realized by a superconducting magnet structure. Solenoids in a Helmholtz configuration together with small openings cut in the central electrode assure optical access to the trap volume to allow, e.g., for the investigation of emitted photons. In contrast, the magnetic field is created in an EBIS device by a single long solenoid and the lengths of the drift tubes are longer. Therefore, an EBIS allows to trap more charged particles in a given volume and to produce a higher flux of ions which both together leads to increased plasma instabilities [88]. To avoid these instabilities the shorter trap length of the EBIT compared to the EBIS is chosen. The shorter trap length additionally facilitates the creation of a highly magnetically compressed electron beam, which allows the EBIT to realize high electron densities and thus high ionization rates. Another main part of an EBIT is the electron collector, which ensures a stable collection of all electrons. The kinetic energy of the electron beam defines the maximum achievable charge state of an ion. Ionization

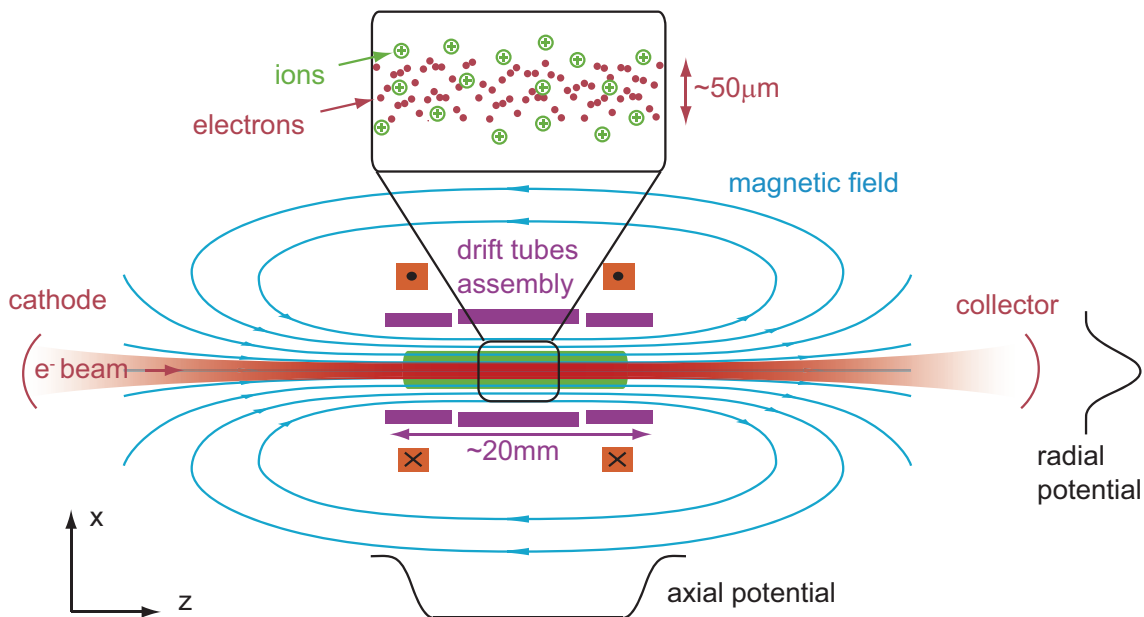


Figure 3.1: Operation principle of an EBIT. Ions are axially confined by the electrostatic potential of the drift tube assembly and radially by a magnetically compressed monoenergetic electron beam. The shape of the axial and radial trapping potentials are sketched. The electrons are emitted from a cathode and, after they ionized the atoms sequentially by electron impact, are collected at the collector. The numbers correspond to the Dresden-EBIT3 parameters. For details see text.

of an ion is generally possible in case the electron beam energy is higher than the ionization potential of the charge state of interest. For the creation of fully-ionized U^{92+} ionization energies higher than 130 keV are required. Atomic binding energies calculated by Rodrigues *et al.* [113] are shown in Fig. 3.3.

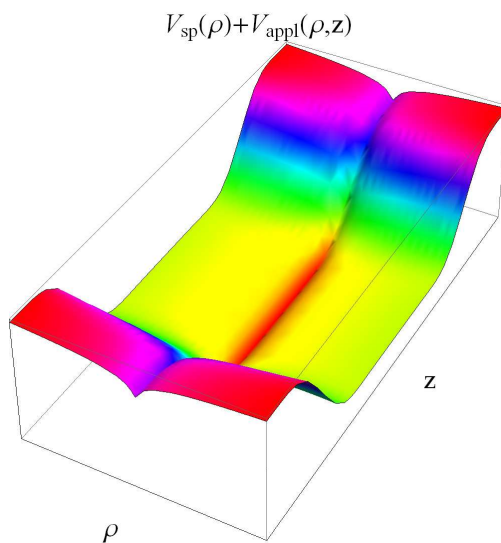


Figure 3.2: Sketch of the three-dimensional electrostatic potential in an EBIT. The ions are axially trapped by the potential applied to the drift tubes $V_{appl}(\rho, z)$ and radially by the negative space charge potential of the electron beam $V_{sp}(\rho)$.

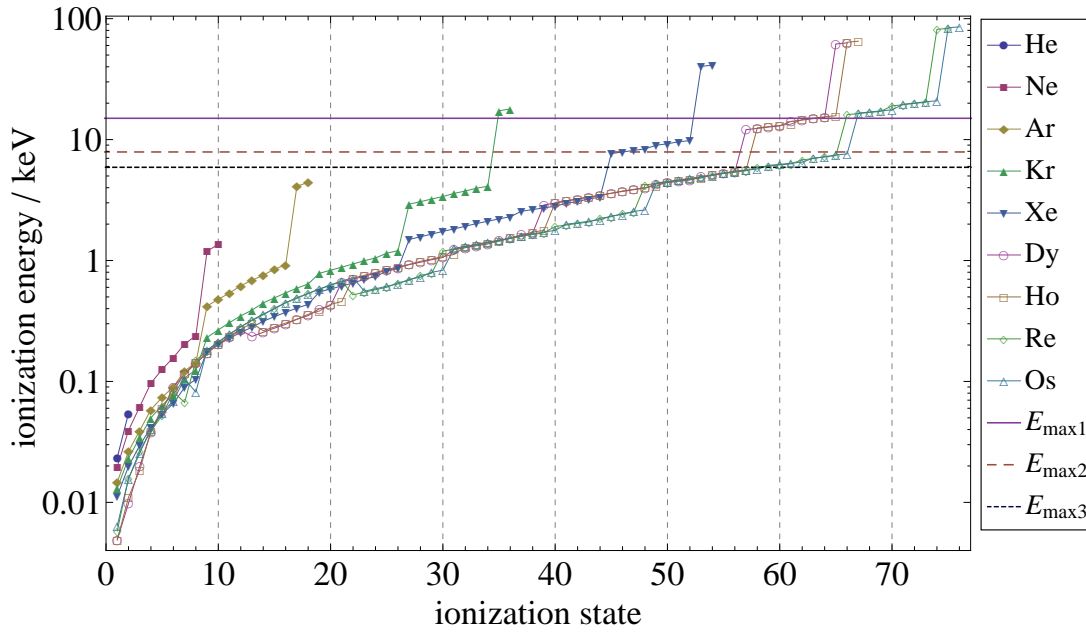


Figure 3.3: Ionization energies including those of ions which are produced with the Dresden-EBIT3 (see Chap. 8). The plotted values are taken from [113]. The line at $E_{\max 1}$ indicates the maximum beam energy realizable with the Dresden-EBIT3. The lines at $E_{\max 2} = 7.9$ keV and $E_{\max 3} = 5.9$ keV show the electron beam energies which have been chosen in the measurements done so far and presented in Chap. 8.

The time-scales of processes in an EBIT show a clear hierarchy. The motion in the trap occurs on the fastest time-scale (a few ns), thus the ion can explore the available phase-space before colliding with another ion. The collision frequencies (e.g. ion-ion collisions) are lower and occur on a time-scale in the order of a few 100 ns. Processes which change the charge states of the ions in the trap (e.g. electron impact ionization) are strongly dependent on the obtained charge state and range from microseconds to seconds. Finally, the cross field diffusion rate (see later) for highly charged ions can be considered fast enough (\approx ms) that the ions are already in their equilibrium spatial distribution.

3.2 The electron beam

The electron beam radius r_e in the trap region can be described in a simple model assuming zero temperature of the electrons at the cathode and zero magnetic field at the place of their emission. Assuming a laminar flow and a homogeneous axial magnetic field, r_e can be described by the Brillouin radius [114] r_B . It is given as

$$r_B = \sqrt{\frac{2m_e I_e}{\pi \epsilon_0 v_e e B^2}}, \quad (3.1)$$

with I_e the electron current, ϵ_0 the vacuum permittivity, v_e the electron velocity, B the magnetic field at the trap and m_e/e the electron's mass-to-charge ratio. Figure 3.4(a) shows the dependence of r_B on $\sqrt{I_e}$. The description of the electron beam

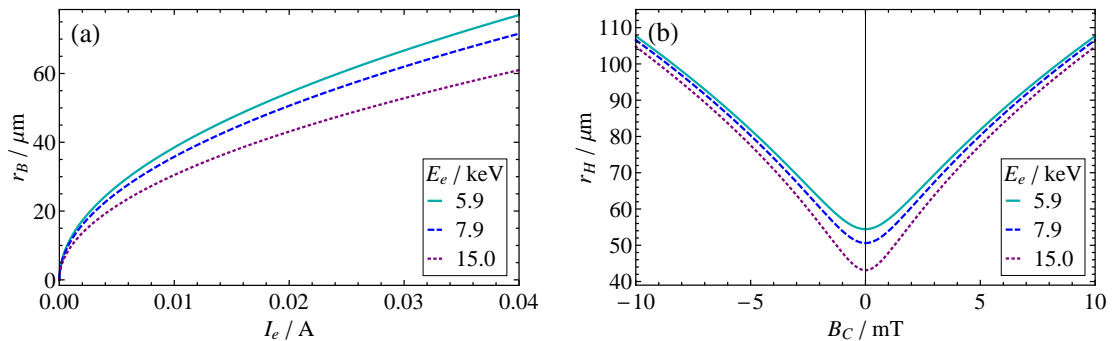


Figure 3.4: (a) Brillouin radius in dependence of the electron beam current I_e for different electron beam energies E_e at the trap. (b) Herrmann radius in dependence of the magnetic field at the cathode B_C shown for the same values of E_e . Here, I_e is chosen 20 mA. A cathode temperature of 2000 K and a radius of the cathode of 0.5 mm is considered. For both graphs the magnetic field at the trap is set to 0.25 T. The parameters are characteristic parameters of the Dresden-EBIT3 (see Chap. 8).

radius by Herrmann [115] is more realistic, since he considers finite temperature and magnetic field at the cathode and a non-laminar flow. The Herrmann radius

$$r_H = r_B \sqrt{\frac{1}{2} + \frac{1}{2} \sqrt{1 + 4 \left(\frac{8m_e k_B T_C r_C^2}{e^2 r_B^4 B^2} + \frac{B_C^2 r_C^4}{B^2 r_B^4} \right)}} \quad (3.2)$$

is defined as the radius through which 80% of the beam passes. Here, T_C and B_C are the temperature and the magnetic field at the cathode, r_C is the cathode radius and k_B the Boltzmann constant. Figure 3.4(b) shows the dependence of r_H on the magnetic field at the cathode for a fixed T_C . Knowing the electron beam radius, the electron current density, which directly depends on I_e , can be determined $j_e = I_e / (\pi r_e^2)$. Note, an increased I_e results in a larger beam radius as well. In order to illustrate the reduction of the current density due to magnetic and thermal influences at the cathode, the current density calculated via the Brillouin and Herrmann radius as a function of E_e is shown in Fig. 3.5(a). The effect of a non zero magnetic field at the cathode on j_e is shown in Fig. 3.5(b) for various electron beam currents and energies. Furthermore, the electron beam radius allows to derive the number density of electrons $N_e = I_e / (4\pi r_e^2 v_e e)$ in the trap.

The space charge of the electron beam causes a partial conversion of the kinetic energy of the electrons into potential energy. Thus, the effective interaction energy is reduced and the electrostatic potential experienced by the ions is [96]:

$$V(\rho, z) = V_{\text{sp}}(\rho) + V_{\text{appl}}(\rho, z) + V_{\text{corr}}(\rho, z). \quad (3.3)$$

Here, V_{sp} denotes the space charge potential of the electron beam, V_{appl} the voltage applied at the trap electrodes and V_{corr} is a correction voltage. The term V_{corr} considers changes in the charge distribution on the drift tube walls due to the electron beam. Contributions from the ions are not yet considered (see Sec. 3.3). For a cylindrically homogeneous electron beam with radius r_e the space charge potential

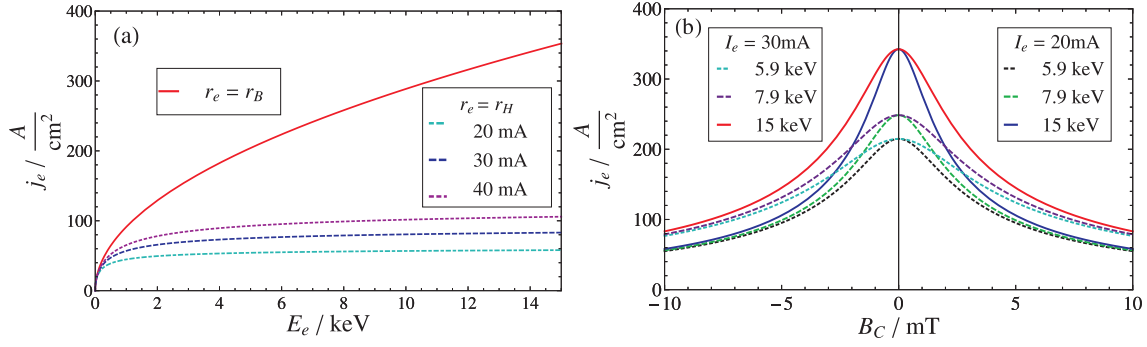


Figure 3.5: Calculated electron current density j_e in dependence of the electron beam energy E_e using the Brillouin radius (red solid line) and the Herrmann radius r_H (a). For the more realistic case of considering r_H , the current density is reduced due to a finite temperature (here $T_C = 2000\text{ K}$) and magnetic field (here $B_C = 10\text{ mT}$) at the cathode. For this case j_e is plotted for different electron beam currents. In (b) the current density is determined via the Herrmann radius. The dependence of j_e on B_C is shown for different electron beam currents and energies. The higher the magnetic field at the cathode the less the dependence of j_e on E_e . In both graphs r_C is set to 0.5 mm and B to 0.25 T . The obtained values agree with the value of $< 300\text{ A/cm}^2$ specified in [107].

can be derived with the first Maxwell equation (Gauss' law)

$$V_{\text{sp}}(\rho) = \begin{cases} V_0 \left(\frac{\rho}{r_e} \right)^2, & \text{if } \rho < r_e \\ V_0 \left(2 \ln \left(\frac{\rho}{r_e} \right) + 1 \right), & \text{if } \rho > r_e, \end{cases} \quad (3.4)$$

where

$$V_0(\rho) = \frac{I_e}{4\pi\epsilon_0 v_e}. \quad (3.5)$$

For a Gaussian electron beam profile, the potential can be expressed in a closed form [96, 116]. Figure 3.6 shows $V_{\text{sp}}(\rho)$ assuming a Gaussian profile for parameters used at the Dresden-EBIT3. The potential difference between the radius of interest and the drift tube radius leads to an energy shift at a given position in the electron beam.

3.3 The ion cloud

The Lagrangian of the trapped ions leads to the equations of motion (see e.g. [96]) and the complete effective potential experienced by the ion can be deduced

$$V_{\text{eff}}(\rho, z) = V(\rho, z) + \frac{eZB^2\rho^2}{8m} + \frac{P_\phi^2}{4meZ\rho^2}, \quad (3.6)$$

where $V(\rho, z)$ is given by Eq. (3.3), Z and m are the ion charge state and mass, respectively. A constant of motion is the generalized angular momentum P_ϕ . For highly charged ions oscillating inside the electron beam the curvature of the potential near its minimum is independent of P_ϕ . The ion movement can be described by an

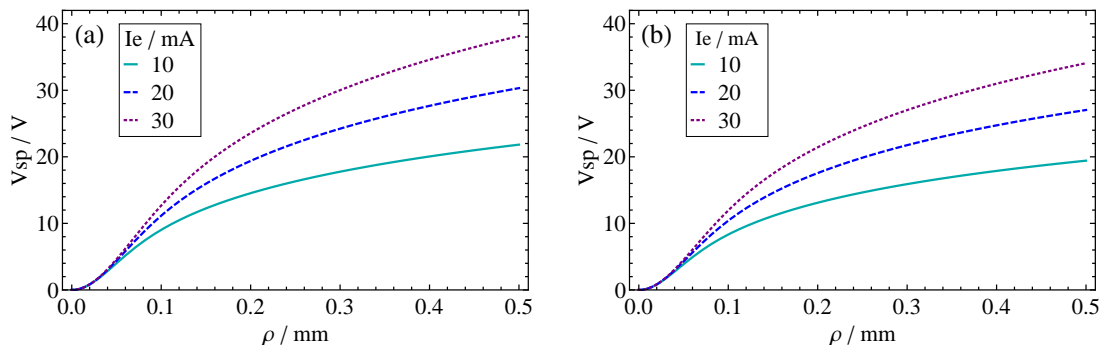


Figure 3.6: Space charge potential for 5.9 keV (a) and 7.9 keV (b) electron beam energy for various electron beam currents I_e . A Gaussian profile and the parameters $B = 0.25$ T, $r_C = 0.5$ mm, $T_C = 2000$ K and $B_C = 0$ were used. These graphs can be used to estimate the expected maximum space charge potential for the Dresden-EBIT3 in case B_C is zero. The more realistic case of $B_C \neq 0$ would require the knowledge of B_C , which is currently not known. An estimation of the reduction of V_{sp} can be done by means of Fig. 3.5.

axial ω_ϕ and a radial frequency ω_ρ , where the radial movement can be represented as a harmonic motion considering small deviations from the equilibrium value. In the case of trap imperfections such as misalignments, which would break the cylindrical symmetry, coupling of the radial and axial motions occur.

Once the ions are trapped, they arrange themselves within the radial space-charge potential of the electron beam mainly due to ion-ion interactions (see Sec. 3.4). A characteristic temperature T_i can be associated with the velocity components of the ions of charge state Z_i and can, furthermore, be associated with the spatial distribution of the ions. With the help of the Vlasov equation [117], which describes the fluid nature of plasmas, it can be shown that a Maxwellian distribution

$$f(t = \infty) = N_i \cdot \exp \left[-\frac{eZ_i V_{\text{eff}}(\rho, z)}{k_B T_i} \right] \quad (3.7)$$

describes the equilibrium spatial distribution of N_i ions of charge state i . Hence, the space-charge potential V_i can be numerically calculated and the potential $V_{\text{eff}}(\rho, z)$ can be extended by the potential of the space charge of all trapped charges

$$\tilde{V}(\rho, z) = V_{\text{eff}}(\rho, z) + \sum_i V_i(\rho, z). \quad (3.8)$$

The approach to the equilibrium spatial distribution of the ions is called cross-field diffusion. At this process two colliding ions can change their trajectories along different magnetic field lines, which would be otherwise not possible. Especially when the ions are once outside the electron beam this process is relevant to allow the ions to diffuse across the magnetic field lines. For more details see textbooks, e.g. [96]. Cross-field diffusion also helps to describe the magnetic trapping mode, when the electron beam is switched off.

3.4 Interaction of the ion cloud with the electron beam

There are a variety of processes inside the trap leading to an increase or decrease of the ion's charge state or to an ion loss. Nevertheless, a steady state is reached before the total charge of the electron beam is fully neutralized. Understanding the temporal dynamics of the ions of various charge states is essential to determine cross sections or to predict from known cross sections the behavior of the EBIT as is shown later. In this section the different creation and loss processes occurring in an EBIT which lead to a description of the evolution of the charge states are presented.

3.4.1 Collision processes within the EBIT

The ionization in an EBIT mainly proceeds by single steps via successive generation of ions from their neutral or a low charge state to their maximum charge state. The array of charge states including the processes involved is often illustrated as a 'staircase' (see e.g. [118]). The cross sections of ionization processes of higher order are in general a few orders of magnitude smaller than that for single ionization [119]. Furthermore, the double charge transfer between ion and neutral atom can be neglected when compared to the single charge transfer. In the following an overview of the complex range of collision processes in an EBIT is given.

Electron impact ionization (EI): It is the main process and most fundamental in atomic and molecular physics. The process of single ionization of a q -fold charged ion by electron impact can be written as:

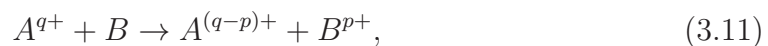


The cross sections for systems with only a few electrons left show a characteristic maximum near the double to threefold threshold energy. The minimum kinetic energy needed by the electron to perform EI defines the threshold energy. An empirical formula widely used to describe the cross section is the formula derived by Lotz [120]

$$\sigma_{i \rightarrow i+1}^{\text{EI}} = \sum_{j=1} \frac{a_{ij} q_{ij}}{E_e P_{ij}} \ln \left(\frac{E_e}{P_{ij}} \right) \{1 - b_{ij} \exp[-c_{ij} (E_e/P_{ij} - 1)]\}. \quad (3.10)$$

The parameters a_{ij} , b_{ij} and c_{ij} are constants. P_{ij} is the ionization potential and q_{ij} is the number of electrons in the j^{th} shell with the outer shell corresponding to $j=1$. The subshells are not considered. For a more comprehensive theory see [121].

Ion-Atom collisions: A collision process between an ion and an atom in which one or more electrons of the atom change to a bound state in the ion is called Charge eXchange (CX). For collision impact energies up to about 100 keV/u the cross section of CX dominates the one of atom- or ion-ionization [122]. The reaction equation is



where A is the q -fold positively charged ion which catches p electrons from the atom B . An approximation of the cross sections for the transfer of up to four electrons

in single collisions, with collision energies < 25 keV/amu, between multiply charged ions and neutral atoms and molecules by empirical scaling laws was done by Müller and Salzborn [123]. The cross section for charge exchange is given as

$$\sigma_{i \rightarrow i-1}^{\text{CX}} = 1.43 \cdot 10^{-12} \cdot Z_i^{1.17} \cdot P_0^{-2.76}, \quad (3.12)$$

where P_0 is the ionization potential of the neutral target. A classical description of one-electron capture in collisions between highly charged ions and atomic targets was first given by the Bohr-Lindhard model [124], which assumes that an electron can detach from an atom, if the Coulomb force of the approaching ion cancels the nuclear force of the atom. A further development of this model is the so-called classical over-barrier model [125]. The approaching ion deforms the Coulomb potential such that the ionic electron can move free in the unified potential. The classical-trajectory Monte-Carlo method [126] solves numerically the classical equations of motion of all particles involved in the collision considering the Coulomb interactions. Quantum mechanical solutions are obtained by close-coupling-methods. Here, the complete wave function of the electrons is expanded in a complete set of basis functions. The expansion coefficients are obtained from the Schrödinger equation. A comprehensive overview of the different models describing charge exchange processes is given in [127].

The rate describing the energy gain of the i th ionic species due to ion-ion collision with the j th ionic species is [128]

$$\left(\frac{d}{dt} (N_i k_B T_i) \right)_j^{\text{CX}} = 2\nu_{ij} N_i \frac{m_i}{m_j} \frac{k_B (T_j - T_i)}{(1 + m_i T_j / (m_j T_i))^{3/2}}. \quad (3.13)$$

Here, ν_{ij} is the Coulomb collision rate between the two species:

$$\nu_{ij} = \frac{4}{3} \sqrt{2\pi} N_j \left(\frac{Z_i Z_j e^2}{m_i} \right)^2 \cdot \left(\frac{m_i}{k_B T_i} \right)^{3/2} \ln \Lambda_{ij}, \quad (3.14)$$

where Λ_{ij} is the ion-ion Coulomb logarithm and N_i and N_j are the average ion densities. The Coulomb logarithm is the natural logarithm of the ratios of the maximum to minimum impact parameters.

Radiative recombination (RR): In this mechanism a free electron with kinetic energy E_e is captured into a vacant shell, which is in the example shown in Fig. 3.7(a) the L -shell associated with a binding energy E_B . Subsequently a photon with energy $h\nu = E_e + E_B$ is radiated. The reaction equation is



RR is the inverse process to photoionization. A simple model for the cross section of RR is derived by Kim and Pratt [129]

$$\sigma_{i \rightarrow i-1}^{\text{RR}} = \frac{16\pi}{3\sqrt{3}} \frac{\alpha I_H \lambda_e^2 Z_{\text{eff}}^2}{E_e} \ln \left(1 + \frac{Z_{\text{eff}}^2 I_H}{E_e (n_0)_{\text{eff}}^2} \right). \quad (3.16)$$

Here, α is the fine structure constant, I_H the ionization potential of the hydrogen atom and λ_e the electron Compton wavelength. An effective charge $Z_{\text{eff}} = (Z_0 + Z_i)/2$ as well as an effective quantum number

$$(n_0)_{\text{eff}} = n_0 + (1 - W_{n_0}) - 0.3 \quad (3.17)$$

is introduced, with n_0 being the valence shell number. The ratio between the number of unoccupied states and the total number of states in the valence shell n_0 is given by W_{n_0} . Another simple equation is given by Bethe and Salpeter [130, 131] describing the RR with bare ions. The cross section decreases with decreasing kinetic energy and is larger for the capture in a deeper vacant state.

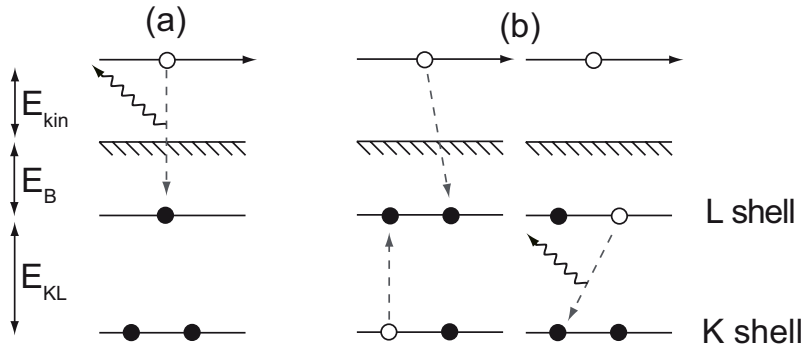


Figure 3.7: Schematic of a radiative (a) and dielectronic (b) recombination process. For details see text.

Dielectronic recombination (DR): An alternative mechanism to RR is known as dielectronic recombination. In this resonant process an electron is captured from the ion in case the energy equation $E_e + E_B = E_{\text{KL}}$, here E_{KL} is the energy difference between the L-shell and K-shell, is fulfilled (see Fig. 3.7(b)). The excess energy of the recombination is absorbed by a second ionic electron, which then occupies an excited state as well. In the simple sketch shown in Fig. 3.7(b) the electron captured in the L-shell can raise a K-shell electron to the L-shell. This intermediate state is commonly doubly excited and can decay either autoionizing and radiation free or can decay in the ground state completing the DR. Due to the resonant character, the cross section outside the resonance is close to zero.

Electron impact excitation (EE): This collision process is only referred to for completeness, since it is not essential to derive the charge balance in an EBIT. Rather, it is the basis for emission spectroscopy performed at an EBIT. In this mechanism a free electron impacts a bound electron releasing its energy and raising the bound electron to an excited state.

Ion-Ion collisions: In this collision mechanism the ions perform pure Coulomb scattering, since both collision partners are charged. Ion-ion collisions are responsible for a slow diffusion of the ions across the magnetic field lines, which is else not possible due to the conservation of the angular momentum. As a result of the long-range Coulomb force, the frequent ion-ion collisions provide both exchange of

energy between ions of one charge state and between ions of different charge states. Thus, a characteristic temperature can be assigned to ions of one charge state and hot ions can release energy to colder ions. Since the Coulomb collision frequencies for ionic species i and j have a $Z_i^2 Z_j^2$ dependence, the coupling between high charge states is strong and thus resulting in a fast energy transfer and similar temperatures. In summary, ion-ion collisions are responsible for the equipartitioning of the thermal energy.

3.4.2 Heating and escape of the ions

Before the rate equation of the evolution of charge states can be deduced, loss processes have to be considered. Without these loss processes, the total positive charge of the trapped ions would increase up to the maximum charge state given by the ionization potentials of the elements under consideration. To this end, the heating of the ions and the escape from the trap are introduced in the following.

Heating of the ions: The ions gain energy due to several heating processes, before the energy is thermalized by ion-ion collisions. The primary mechanism for heating the ions is via Coulomb collisions with the electron beam. The heating rate at which energy is transferred is calculated in [132]. It is evaluated by taking the speed distribution of the electron beam as delta function, and the speed distribution of the ions as a Maxwellian. In case the electron velocity is much higher than the ion velocity ($v_e \ll v_i$), the axial escape rate is

$$\frac{3}{2} \left(\frac{d}{dt} (N_i k_B T_i) \right)^{\text{Heat}} \approx N_i N_e \Upsilon \frac{m_e m_e}{m_i v_e}, \quad (3.18)$$

with

$$\Upsilon = 4\pi \left(\frac{Z_i e^2}{m_e} \right)^2 \ln \Lambda_i. \quad (3.19)$$

Λ_i is the electron-ion Coulomb logarithm for the i th ion. Another heating process is, e.g., the ionization heating resulting from ionization events in the fringes of the potential well.

Ion escape: The axial escape rate of ions from the trap assuming each charge state i to have a characteristic temperature T_i is given by Penetrante [133]

$$\frac{dN_i^{\text{aESC}}}{dt} = -N_i \nu_i \left(\frac{e^{-\omega_i}}{\omega_i} - \sqrt{\omega_i} (\text{erf}(\omega_i) - 1) \right), \quad (3.20)$$

where $\nu_i = \sum_j \nu_{ij}$ is the total Coulomb collision rate for collisions between charge i and all charges, ω_i is given as $\omega_i = (eZ_i V_{\text{at}} / k_B T_i)$ and $\text{erf}(\omega_i)$ is the Gauss error function. V_{at} is the axial trap depth. In [133] the rate of energy loss due to escaping ions is furthermore derived

$$\left(\frac{d}{dt} (N_i k_B T_i) \right)^{\text{aESC}} = - \left(\frac{2}{3} N_i \nu_i e^{-\omega_i} - \frac{dN_i^{\text{aESC}}}{dt} \right) k_B T_i. \quad (3.21)$$

Note, the complete escape rate (ESC) consists of the axial (aESC) and a radial (rESC) rate. The radial rate can be calculated using the potential given in Eq. (3.6) instead of V_{at} .

3.4.3 Rate equation

In order to describe the evolution of the ion densities the contributing rates must first be defined. Electron ionization and radiative recombination processes have average rates of the form

$$R_{i \rightarrow i+1}^{\text{EI}} = \frac{j_e}{e} \sigma_{i \rightarrow i+1}^{\text{EI}}(E_e) N_i f(r_e, r_i) \quad (3.22)$$

and

$$R_{i \rightarrow i-1}^{\text{RR}} = \frac{j_e}{e} \sigma_{i \rightarrow i-1}^{\text{RR}}(E_e) N_i f(r_e, r_i), \quad (3.23)$$

respectively. The overlap factor $f(r_e, r_i)$ considers the overlap in the volume between the electron beam and the ion density distribution. An estimation of this overlap or compensation factor is generally difficult, since the quantity and the exact distribution of the charge states must be known, which both depend on design and operational parameters of the EBIT. A possibility to approximate it is by using the ion characteristic radius r_i . An expression of r_i is given in [133]

$$r_i = \begin{cases} r_e \sqrt{\frac{k_B T_i}{e Z_i V(r_e)}}, & \text{if } e Z_i V(r_e) > k_B T_i \\ r_e \exp \left[\frac{1}{2} \left(\frac{k_B T_i}{e Z_i V(r_e)} - 1 \right) \right], & \text{if } e Z_i V(r_e) < k_B T_i. \end{cases} \quad (3.24)$$

Each charge exchange leads to the formation of a singly charged ion, therefore the rate is given as

$$R_{i \rightarrow i-1}^{\text{CX}} = N_0 N_i \sigma_{i \rightarrow i-1}^{\text{CX}}(\bar{v}_i) f(r_0, r_i). \quad (3.25)$$

Assuming a continuous injection of neutrals a source term

$$R_1^{\text{SC}} = \frac{j_e}{e} \sigma_{0 \rightarrow 1}^{\text{EI}}(E_e) N_0, \quad (3.26)$$

where N_0 is the neutral gas density, must be also considered. The full rate equation is then given by

$$\begin{aligned} \frac{dN_i}{dt} = & R_{i-1 \rightarrow i}^{\text{EI}} - (R_{i \rightarrow i+1}^{\text{EI}} + R_{i \rightarrow i-1}^{\text{RR}} + R_i^{\text{aESC}} + R_i^{\text{rESC}} + R_{i \rightarrow i-1}^{\text{CX}}) \\ & + (R_{i+1 \rightarrow i}^{\text{RR}} + R_{i+1 \rightarrow i}^{\text{CX}}). \end{aligned} \quad (3.27)$$

Numerical simulations can describe the charge state evolution in an EBIT and provide design parameters, e.g., by using the computer code called NSCB (Numerical Simulation of Charge Balance) [134]. In Fig. 3.8 the calculated evolution of the charge breeding of iron ions in the Heidelberg-EBIT is shown.

Furthermore, the equations (3.13), (3.18) and (3.21) lead to an expression of the evolution of the ion temperature

$$\begin{aligned} \frac{d}{dt} (N_i k_B T_i) = & \left(\frac{d}{dt} (N_i k_B T_i) \right)^{\text{Heat}} + \sum_j \left(\frac{d}{dt} (N_i k_B T_i) \right)_j^{\text{CX}} \\ & - \left(\frac{d}{dt} (N_i k_B T_i) \right)^{\text{aESC}} - \left(\frac{d}{dt} (N_i k_B T_i) \right)^{\text{rESC}}. \end{aligned} \quad (3.28)$$

In general, the temperature of one ion species increases for higher charge states. However, a high temperature causes the ion to spend less time in the electron beam leading to reduced overlap factors and ionization. Thus, a cooling mechanism is mandatory to achieve high charge states.

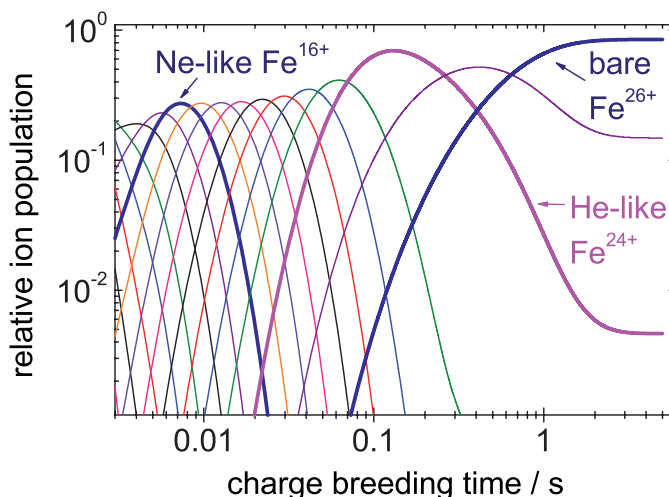


Figure 3.8: Calculated fraction of Fe ions in charge state $n+$ versus charge breeding time after injection into the Heidelberg-EBIT. An electron beam current of 500 mA and an electron/ion overlap of 0.1 are assumed. The electron beam energy is set to 20 keV. For charge breeding times greater than 2 s, 85% of the Fe ions are bare

Evaporative cooling: The cooling mechanism of choice in an EBIT is evaporative cooling. An upper limit of the temperature is given by the potential applied at the drift tubes. In case the hot ions gain enough energy to overcome the potential well, the high energy tail of the temperature distribution evaporates. The remaining energy is distributed through ion-ion collisions between the trapped ions. Making the potential well shallower the ions get cooler at the expense of ion number. Lower charge states leave generally the trap first, which is at first glance not intuitive, since the highly charged ions are the hot ones. For axial trapping the factor $eZ_i V_{\text{at}} / (k_B T_i)$ is, however, essential (see Eq. (3.7) and Eq. (3.24)) and which is large for highly charged ions. Bringing an additional light gas into the EBIT, highly charged ions can be effectively cooled (see Fig. 3.9). The equilibrium temperatures are typically limited to 0.1 to 0.4 $eZ_i V_{\text{at}}$ [118], which gives for, e.g., $V_{\text{at}} = 7.9$ kV and $Z_i = 50$ temperatures of $9 \cdot 10^6$ K to $37 \cdot 10^6$ K.

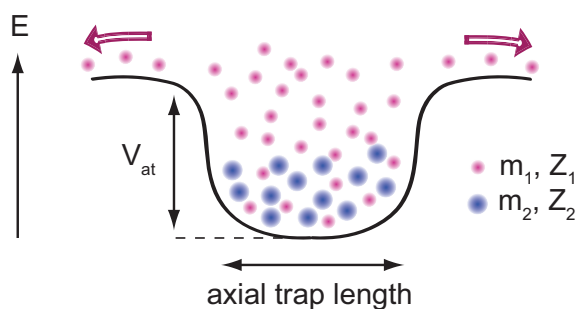


Figure 3.9: Sketch of an evaporative cooling process. Two ion species with charge states Z_1 and Z_2 and masses m_1 and m_2 , respectively, are stored in the EBIT volume. First, light ions with lower charge state, which are in this example ions with charge state Z_1 (red balls), leave the trap in axial direction. The ions with higher charge state Z_2 (blue balls) are still trapped. The remaining energy is transferred through ion-ion collisions and thus the ions with higher charge state are cooled.

Chapter 4

The PENTATRAP mass spectrometer

In this chapter the experimental setup of PENTATRAP¹ [1], which is installed at the Max-Planck-Institut für Kernphysik in Heidelberg, is presented. An overview of the experimental setup is shown in Fig. 4.1. The components of the mass spectrometer are discussed in the following.

4.1 Ion sources

As already discussed in Chap. 3, well-proven sources for highly charged ions are electron beam ion traps (EBITs). Therefore, highly charged long-lived and stable ions will be created by the small commercial room temperature Dresden-EBIT3 (see Chap. 8) with an additional Wien filter, and the Heidelberg-EBIT. The Dresden-EBIT3 with a maximum electron beam energy of about 15 keV and an electron beam current of about 50 mA is dedicated to the production of bare ions with nuclear charge numbers up to $Z = 30$. For elements with higher nuclear charge number, complete ionization is not possible. Thus, only ions up to helium- or neon-like charge states can be produced for medium- and high- Z elements, respectively. This ion source will be used for the commissioning of PENTATRAP and for the investigation of its performance. Moreover, this ion source can be used to produce ions for mass measurements with applications in the field of neutrino physics (see Chap. 8).

For physics applications which require extremely high charge states of long-lived and stable nuclides, e.g., bare or hydrogen-like lead or uranium, PENTATRAP will obtain ions from the Heidelberg-EBIT. Currently, the maximum electron beam energy of 100 keV allows a production of ions such as helium-like mercury Hg^{78+} [135] or hydrogenic barium Ba^{55+} , and stripping all electrons from elements up to krypton Kr^{36+} . For the extracted highly charged ion beam from the Heidelberg-EBIT, a beam emittance of $3 \cdot \pi \cdot \text{mm} \cdot \text{mrad}$ has been demonstrated, which meets the requirements for the transport through the PENTATRAP beamline and capture in the Penning traps (see Chap. 5). In Tab. 4.1, the calculated charge breeding performance of the Heidelberg-EBIT for some example ions at fixed electron beam energies is listed.

¹Parts of the following sections are taken from the author's paper [1].

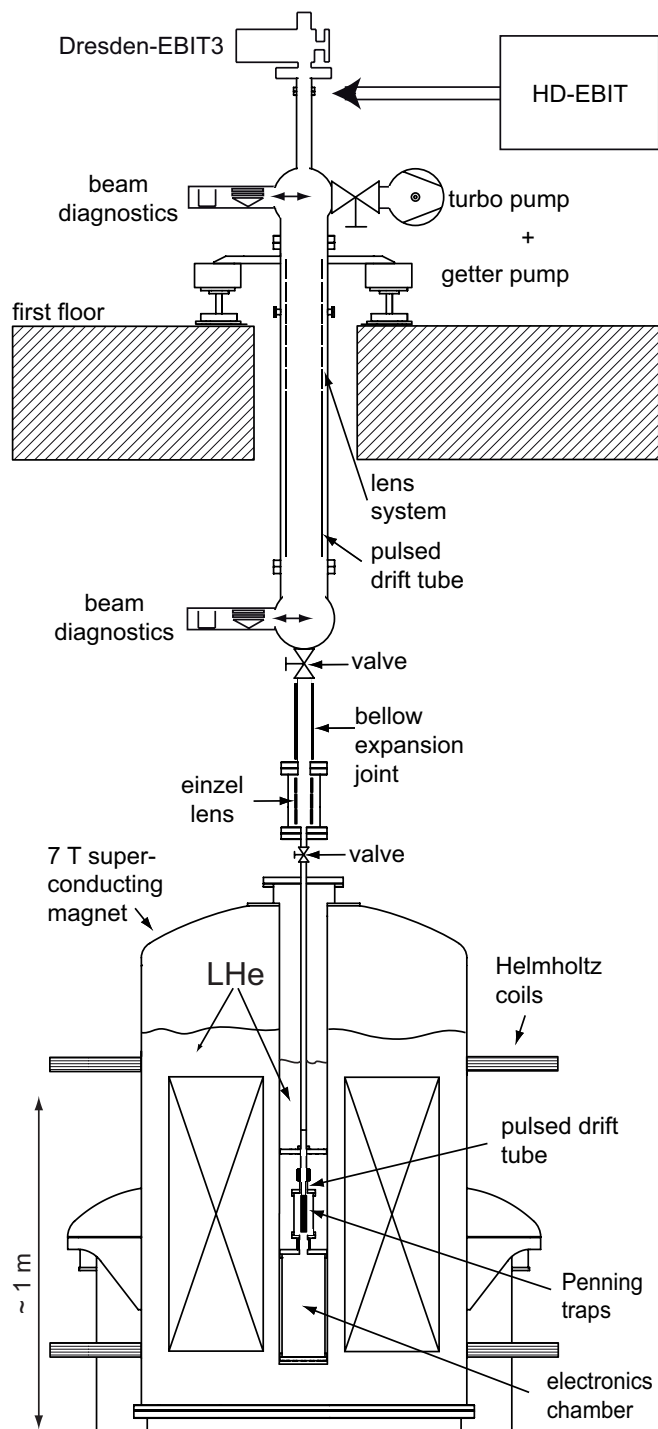


Figure 4.1: Layout of the experimental setup. Ions will be created by either a commercial electron beam ion trap (EBIT) or the Heidelberg-EBIT. The ions will pass the beamline towards the superconducting magnet, which is situated in a temperature-stabilized and pressure-regulated room in the basement. The beam diagnostic elements and the electrostatic lens system are shown. The cryogenic chambers for the trap tower and the detection electronics are placed inside the cold bore of the magnet.

Table 4.1: Calculated charge breeding performance of the Heidelberg-EBIT for different electron beam energies E_e . Parameters used for this calculation are an electron beam current of 500 mA and an electron/ion overlap of 0.1. For the definitions see Chap. 3. Here, t_{ion} and $C_{\text{trap}}^{40\%}$ are the ionization time and the trap capacity at 40 % compensation of the ions. In general, the trap capacity represents the number of positive charges in the trap.

ion	E_e (keV)	ions in charge state	t_{ion} (s)	$C_{\text{trap}}^{40\%}$
Ne ¹⁰⁺	5	60 %	0.016	$7.2 \cdot 10^7$
Ar ¹⁸⁺	20	60 %	0.19	$2.0 \cdot 10^7$
Kr ³⁴⁺	60	60 %	0.54	$6.1 \cdot 10^6$
Xe ⁵²⁺	120	60 %	3.0	$2.8 \cdot 10^6$
Pb ⁵⁴⁺	160	10 %	0.27	$3.9 \cdot 10^5$
Pb ⁷²⁺	160	10 %	1.7	$2.9 \cdot 10^5$
Pb ⁸⁰⁺	160	10 %	7.4	$2.6 \cdot 10^5$
Pb ⁸¹⁺	160	1 %	9.5	$2.6 \cdot 10^4$
Pb ⁸²⁺	160	0.1 %	17	$2.6 \cdot 10^3$

For the calculated charge state production of iron ions as a function of the charge breeding time in the Heidelberg-EBIT see Fig. 3.8 in Chap. 3. An upgrade of this device, planned for the near future, will enable the production of bare uranium.

A comparison of the Dresden-EBIT3 and the Heidelberg-EBIT is summarized in Tab. 4.2. The Heidelberg-EBIT is by far more powerful than the Dresden-EBIT3. Nevertheless the Dresden-EBIT3 is a compact device which is already installed and at which first successful tests had been carried out (see Sec. 8).

A future plan is to adapt the PENTATRAP mass spectrometer to the HITRAP facility [112] at the Helmholtzzentrum für Schwerionenforschung GSI. There, access to low-emittance beams of highly charged short-lived ions up to bare uranium with charge-specific kinetic energies of only a few meV·q will be provided.

4.2 Transfer beamline and beam diagnostics

An approximately 2 meter long ion beamline will interface the Dresden-EBIT3 ion source with the cryogenic part of the setup (see Fig. 4.1). It consists of a series of electrostatic einzel lenses, two pulsed drift tubes, drift regions and two diagnostics stations. The einzel lenses allow an efficient transport of the ions towards the magnet and match the ion beam emittance to the acceptance of the magnetic field. Two pulsed drift tubes are used for a reduction of the kinetic energy of the ions from a few kV·q down to few V·q to ensure, together with the lens system, an efficient injection of the ions into the magnetic field, and to enable a capture of the ions in the traps. The ion transport from the ion sources to the magnet, the injection into the magnetic field, and the capture of the ions into the traps have been simulated with the software package SIMION[®] [136] in order to optimize the voltage settings for an efficient transport. For an ion beam emittance of $3 \cdot \pi \cdot \text{mm} \cdot \text{mrad}$ and a kinetic

Table 4.2: Comparison of the Heidelberg-EBIT [135] and the Dresden-EBIT3 [107]. The commonly used electron beam energies as well as the maximum possible values are included. For the electron beam energy of the Heidelberg-EBIT the current possible operating value of 100 keV is given. With an upgrade electron beam energies up to 350 keV and electron beam currents up to 750 mA are aimed for [135]. For the Dresden-EBIT3 the theoretical maximum electron beam energy is given. So far we operated the EBIT at a maximum value of 7.9 keV. For the calculation of the electron beam density of the Dresden-EBIT3 see Chap. 3.

	Heidelberg-EBIT	Dresden-EBIT3
application	for high charge states of long-lived and stable nuclides	for commissioning of setup and first measurements
electron beam current	300 mA (max. 530 mA)	30 mA (max. 50 mA)
magnetic field	superconducting magnet 3 T-9 T	permanent SmCo magnet 0.25 T
electron beam energy	100 keV	15 keV
electron beam density	15000 A/cm ²	< 300 A/cm ²
drift tube length	40 mm-200 mm	20 mm
accessible charge states	up to Ba ⁶⁵⁺ and Hg ⁷⁸⁺ (bare uranium after upgrade)	bare ions up to $Z=30$ He- and Ne-like ions for medium and high Z -elements, respectively
status	connection to PENTATRAP under development	running and first successful tests

energy of $7 \text{ kV} \cdot q$, the efficiency of the simulated ion transport and injection into the magnetic field exceeds 90%. The efficiency of the ion capture in the traps is a few ten percent for an ion bunch of a few hundred nanoseconds length (see Chap. 5).

In order to monitor the ion beam transport, two movable diagnostic stations will be placed in the focal planes of the ion beamline. The first diagnostic station will be installed directly behind the Dresden-EBIT3 for a measurement and optimization of the ion beam parameters. The second diagnostic station will be mounted close to the entrance region of the magnet for monitoring the ion beam position and emittance right before the injection into the superconducting magnet. Figure 4.2 shows the beam diagnostic station used at PENTATRAP. Each station is equipped with a Faraday cup (FC) to measure the ion beam current and a two inch multi-channel plate (MCP) detector with phosphor screen (PH) to monitor the size and position of the ion beam.

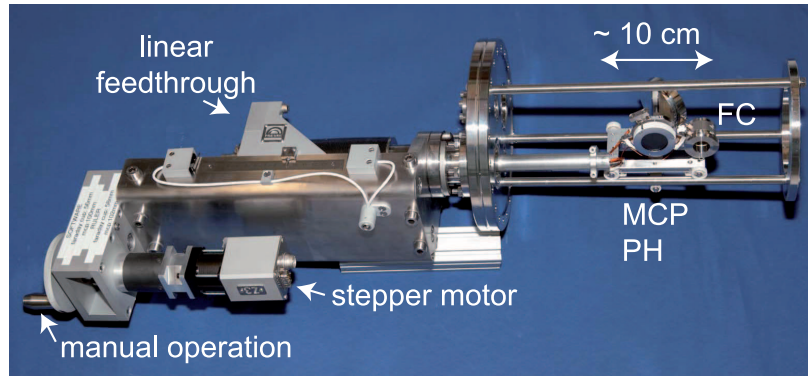


Figure 4.2: Beam diagnostic system (KVI for HITRAP design) consisting of a Faraday cup (FC) and a multi-channel plate (MCP) detector with attached phosphor screen (PH).

4.3 Superconducting magnet system

PENTATRAP utilizes a commercial 7 Tesla, actively shielded (shielding factor >100) superconducting magnet with a vertical bore and an inner diameter of 160 mm (Fig. 4.3(a)). In the cold-bore “bucket-type” cryostat, the same helium reservoir is used to cool the magnet’s superconducting coils as well as the Penning-trap assembly. The spatial homogeneity of the magnetic field $\Delta B/B$ is in the order of a few ppm in the central 1 cm^3 volume. The ions’ oscillation amplitudes will not exceed

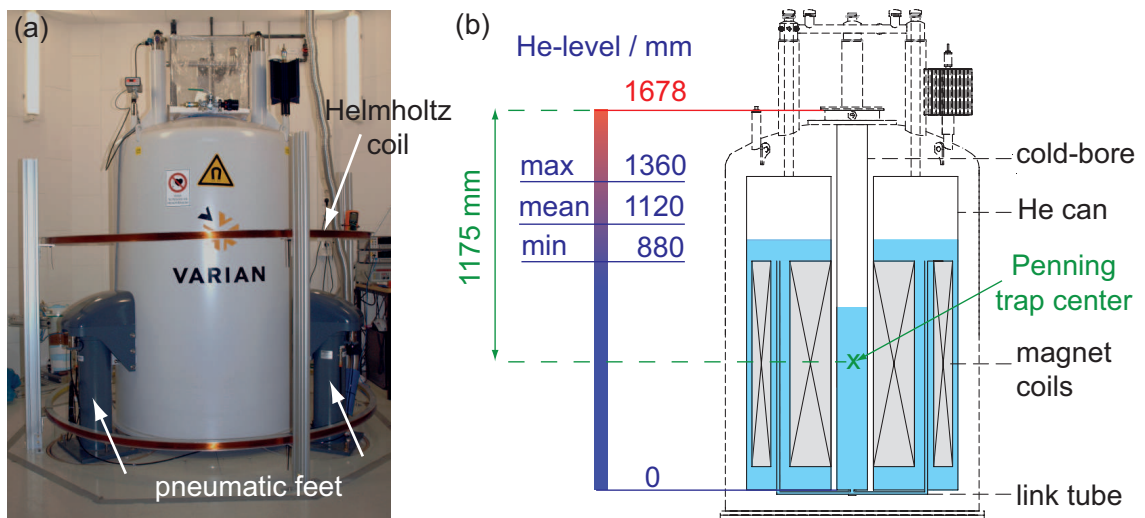


Figure 4.3: (a) Photograph of the PENTATRAP magnet and its installation in the temperature stabilized and pressure regulated room. The magnet is installed on vibrationally damped feet and Helmholtz coils are placed around it. (b) Sectional view of the PENTATRAP magnet with indication of the maximum, mean and minimum liquid helium levels. After complete magnetization a small link tube was opened allowing the liquid helium to flow into the bore where its level can be controlled by pressure regulation.

a few ten μm [87]. In the total trap volume, defined by a cylinder of 2.5 mm radius and 120 mm length along the axis of the bore tube, the maximal spatial homogeneity amounts to about 25 ppm (see Chap. 6). The magnetic field gradient in the region of the traps will be flattened by compensation coils wound around the trap chamber.

A stabilization system is planned to improve the overall temporal stability of the magnetic field $\Delta B/B \cdot 1/\Delta T$ to at least a few ten ppt per hour. It has already been shown that such stabilities can be reached [137]. In the following, the main characteristics of the stabilization system are presented.

A main feature is the stabilization of the pressure and level in the liquid helium reservoir of the superconducting magnet. In case the pressure fluctuates in the helium reservoir, the temperature of the helium will fluctuate and thus the magnetic susceptibility of the used materials will change as well. The fluctuating magnetic susceptibility will change the magnetic field and therefore the eigenfrequencies of the ion. Since for the Penning traps high purity copper was chosen (see Sec. 7.3), the temperature dependence of the magnetic susceptibility of copper with different grades of purity is shown in Fig. 4.4. The temperature dependence scales with the amount of copper impurities. The helium level control will be based on the stabilization of the resonance frequency of a tuned circuit which is placed partially in liquid helium. The pressure stabilization is based on a differential pressure measurement. The pressure in a temperature-stabilized gas vessel is compensated to the helium gas pressure in the bore of the magnet. Attainable values for the level and the pressure stabilities are estimated to be in the 0.1 mm and μbar range, respectively. For details concerning the setup of the pressure and level stabilization system, which is part of the PhD thesis of Ch. Böhm, it should be referred to [140].

Moreover, in order to reduce external influences on the magnetic field, the magnet

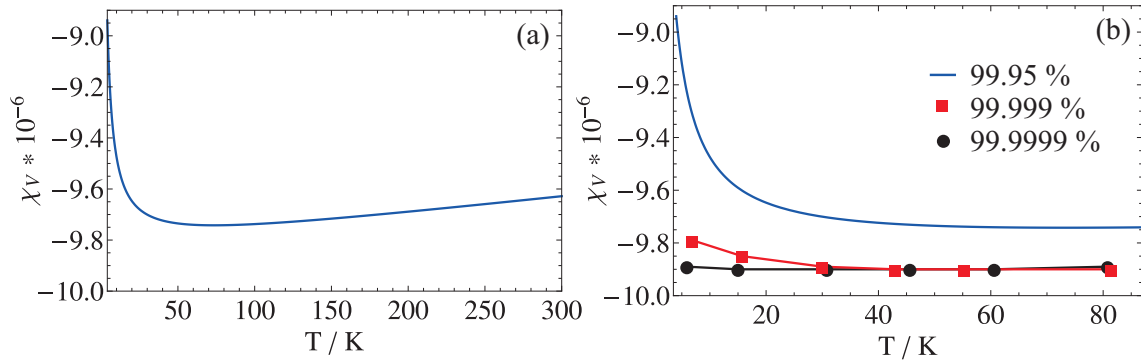


Figure 4.4: Temperature dependence of the magnetic susceptibility of copper with different grades of purity. The solid blue line shows the dependence for 99.95% oxygen free copper (a). The displayed function is replotted using the fit parameters given in [138]. In (b) the temperature range from 4 K to 80 K is zoomed in. The red rectangles correspond to 99.999% and the black circles to 99.9999% oxygen free electronic copper, where the values were taken from [139]. The very high purity copper is diamagnetic over the whole temperature range, but a small amount of iron impurity causes a paramagnetic contribution which is higher at around 4 K. In [138] the increase in magnetic susceptibility at 4 K of high purity copper with the addition of iron as an impurity is determined to $\Delta\chi_V = 1.00 \cdot 10^{-7}[\text{Fe}]$. The iron content [Fe] is in atomic ppm.

is positioned in a vibration-damped, temperature-stabilized and pressure-regulated room. The temperature stabilization system is presented in Chap. 7. The peak-to-peak variation of the temperature over one day is specified below 0.1 K. The magnet is equipped with three anti-vibration pneumatic pads and rests on a vibration-damped, 70 cm thick cushion made of concrete. The vibration amplitude of the cushion is lower than 1 μm . An aluminum housing around the magnet will be installed for shielding the magnet against stray electric and high-frequency magnetic fields.

Furthermore, the vertical component of large-scale, low-frequency magnetic fields will be compensated via a control system based on a fluxgate magnetometer and a pair of Helmholtz coils positioned around the magnet [137]. The setup of the system and first test measurements are discussed in detail in Chap. 7.

4.4 The cryogenic assembly

The part of the system which is inserted into the bore of the magnet and thereby cooled to a temperature of 4 K is called the cryogenic assembly (see Fig. 4.5). It

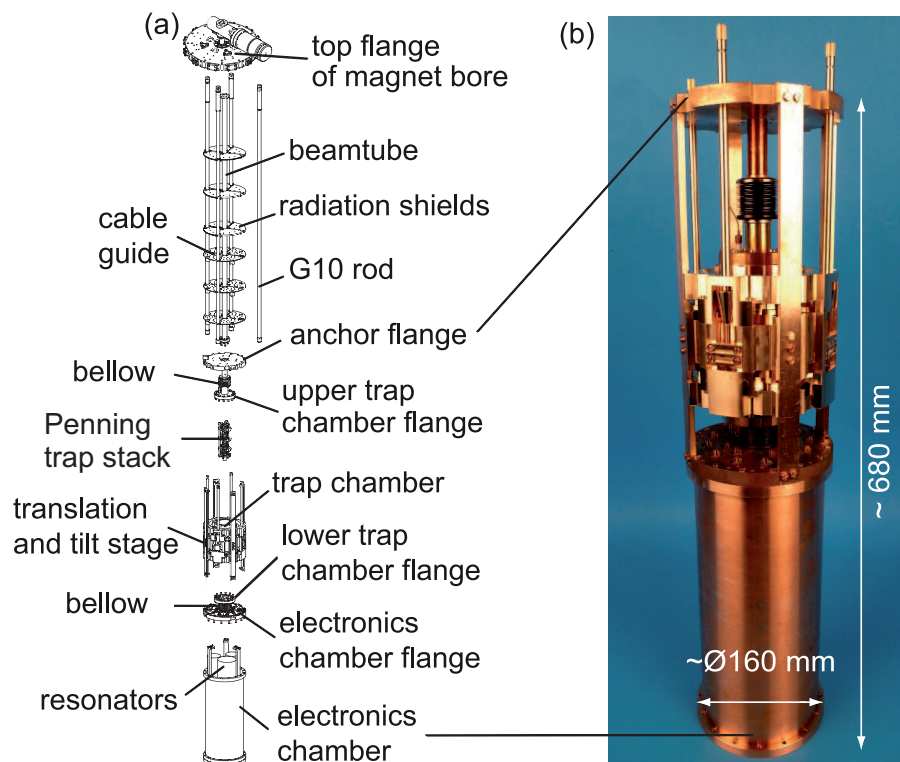


Figure 4.5: (a) Exploded assembly-drawing of the cryogenic assembly of PENTA-TRAP with close to 1200 components in total. Main components are the trap chamber with the Penning-trap stack inside, a translation and tilt stage outside, and the electronics chamber including resonators and amplifiers. An anchor flange will fix the vertical position of the system. To avoid heat transfer, several radiation shields as well as fiber glass rods (G10) are installed. (b) Photograph of a fraction of the cryogenic assembly.

consists of two joined copper vacuum chambers for the trap and the electronics, which are connected to the warm beamline at the top of the magnet with a one meter long DN16 stainless steel tube. The trap chamber, containing a stack of five cylindrical traps, is mechanically connected to the electronics chamber below and the stainless steel tube above with two flexible titanium bellows. In combination with a translation and tilt stage, this enables an independent adjustment of the angular ($\pm 1^\circ$) and horizontal (± 2.2 mm) positions of the trap tower with respect to the axis of the magnetic field. The setup and cryogenic tests of the device are covered later in Chap. 7. Despite the open system, an ultra-high vacuum of better than 10^{-13} mbar in both chambers will be achieved through cryo-pumping at the 4 K surface and by using charcoal absorbers in both chambers (see Chap. 7). Since the electronics chamber houses “in-vacuum” cryogenic resonators and amplifiers (see Fig. 4.5), a direct coupling of the resonators to the trap electrodes is provided.

Materials were chosen thoroughly with respect to appropriate mechanical properties. On the one hand matching thermal expansion coefficients of the materials are required. The thermal expansion of the used materials is shown later in Fig. 7.11. On the other hand materials with low magnetic susceptibilities are chosen for the ion trap apparatus to minimize magnetic field inhomogeneities in the Penning trap volume (see Tab. 4.3). The perturbation of the magnetic field $\Delta B(\rho, z)$ (see Eq. (2.20)) depends on the coefficients B_l . These coefficients can be obtained via integration over radially symmetric rings, which are defined by uniformly distributed dipoles with the magnetization dipole moment M per unit volume [53]. Thereby, M is defined as $M = \chi_V \cdot H$, where χ_V is the volume magnetic susceptibility and H the magnetic field strength. Thus, the perturbation of the magnetic field directly depends on the

Table 4.3: Magnetic susceptibilities of different materials at 4.2 K which are used in the PENTATRAP setup. The value for 99.999% pure Cu is for cold drawn, etched and annealed copper [141]. The value of sapphire is taken from [142] and corresponds to a crystal orientation perpendicular to the c-axis. The remaining values are taken from [141] (see references therein). ETP stands for “Electrolytic Tough-Pitch”. The relation between χ_V and the molar magnetic susceptibility is given by $\chi_{\text{mol}} = M \cdot \chi_V / \rho$, where M is the molar mass and ρ the density.

material	χ_V (SI units)
99.999% pure Cu	$-8.67 \cdot 10^{-6}$
Ti-6%Al-4%V	$-8.27 \cdot 10^{-6}$
phosphor bronze A (94.8%Cu-5%Sn-0.2%P)	$-5.56 \cdot 10^{-6}$
brass, free-cutting (61.5%Cu-35.4%Zn-3.1%Pb)	$-0.14 \cdot 10^{-1}$
sapphire Al_2O_3	$0.25 \cdot 10^{-6}$
ETP copper	$2.53 \cdot 10^{-5}$
G10CR	$5.34 \cdot 10^{-4}$
beryllium copper (Cu-2%Be)	$1.82 \cdot 10^{-3}$
stainless steel 316 LN	$0.11 \cdot 10^{-1}$
stainless steel 316	$0.16 \cdot 10^{-1}$

magnetic susceptibility of the materials in use. The magnetic induction B is given by $B = \mu_0(H + M) = \mu_0(1 + \chi_V)H$, where μ_0 is the permeability of the vacuum. For paramagnetic material ($(1 + \chi_V) > 1$) the magnetic field is strengthened by the presence of the material. Alternatively for diamagnetic material ($(1 + \chi_V) < 1$) the magnetic field is weakened.

Considering the foregoing the trap chamber, as well as the electronics chamber are made of oxygen-free, high thermal conductivity (OFHC) copper with a purity greater than 99.99%. The bellows are made of titanium grade 2, which remains flexible at 4 K. The components of the translation and tilt device (see Fig. 4.5) are made of phosphorous bronze (CuSn8). Special, electrical non-magnetic copper feed-throughs without any nickel alloy, which is the standard brazing material, are used (see Chap. 7).

Moreover, the assembly is constructed such that the heat load on the liquid helium bath of the magnet is kept as small as possible. Thus, materials having low thermal conductivities are used. To this end, fiber glass (G10) tubes are used to actuate the translation and tilt device. Furthermore, the one meter long and comparably small stainless steel tube is constructed for the connection of the anchor flange to the top flange on the magnet. For thermal insulation, highly polished aluminum radiation shields are installed as well. The temperature dependence of the thermal conductivity of materials used at PENTATRAP is plotted in Fig. 4.6. The thermal conductivities are also of importance for the construction of the so-called “warm-bore” device in Chap. 6.

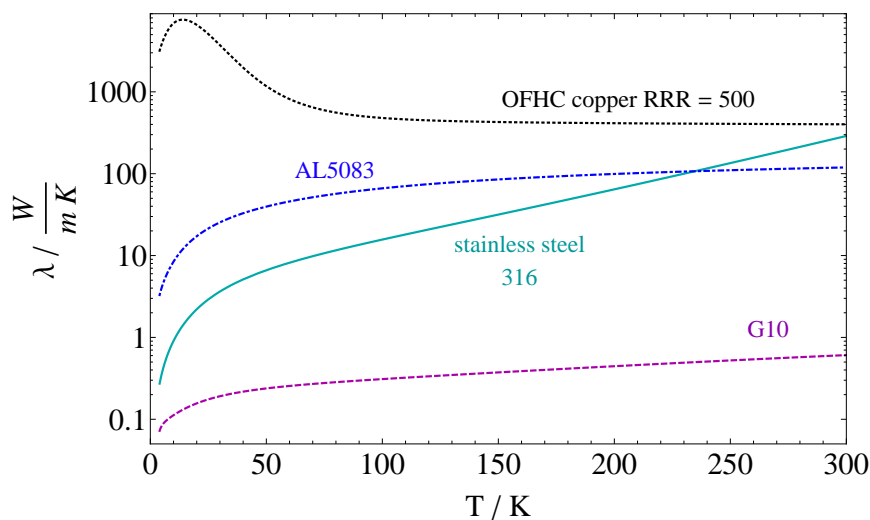


Figure 4.6: Thermal conductivity λ of various materials as a function of the temperature T . The shown curves are fit curves given at the homepage of the National Institute of Standards and Technology (NIST) [143]. The fitted values of copper are taken from [138], the values of aluminum from [144], the values of fiber glass epoxy G10 from [145, 146, 147] and those of stainless steel from [144, 148]. The fit function of copper is $\log_{10} \lambda = (a + cT^{0.5} + eT + gT^{1.5} + iT^2)/(1 + bT^{0.5} + dT + fT^{1.5} + hT^2)$ and the fit function for the other elements is $\log_{10} \lambda = a + b(\log_{10} T) + c(\log_{10} T)^2 + d(\log_{10} T)^3 + e(\log_{10} T)^4 + f(\log_{10} T)^5 + g(\log_{10} T)^6 + h(\log_{10} T)^7 + i(\log_{10} T)^8$, where $a-i$ are the coefficients of the fit.

4.5 Penning traps

A stack of five identical, cylindrical, orthogonalized and compensated five-electrode traps comprises the heart of PENTATRAP (see Fig. 4.7 and Tab. 4.4). The compensation of the traps provides a harmonic electric potential in the traps' central regions by tuning the applied voltages. The orthogonalization of the traps makes the axial oscillation frequency of the particle less sensitive to the correction voltage. In general, the electrostatic potential of a Penning trap can be expressed throughout a Taylor expansion [59], and the influence of the electric field coefficients on the ion modes can be determined as done for the cylindrical trap in [58]. For the analysis of the electrostatic potential and the elaborate design studies of the five traps of PENTATRAP, see [61, 80], in which image charge effects, mutual influence of the trapping potential of the adjacent traps, ion-ion interaction between two ions stored in different traps and the influence of machining tolerances on the performance of the traps are considered. A main part of the thesis presented here was the installation of the Penning-trap stack which is covered in detail in Chap. 7.

Measurements of the cyclotron frequencies of ions of interest will be performed

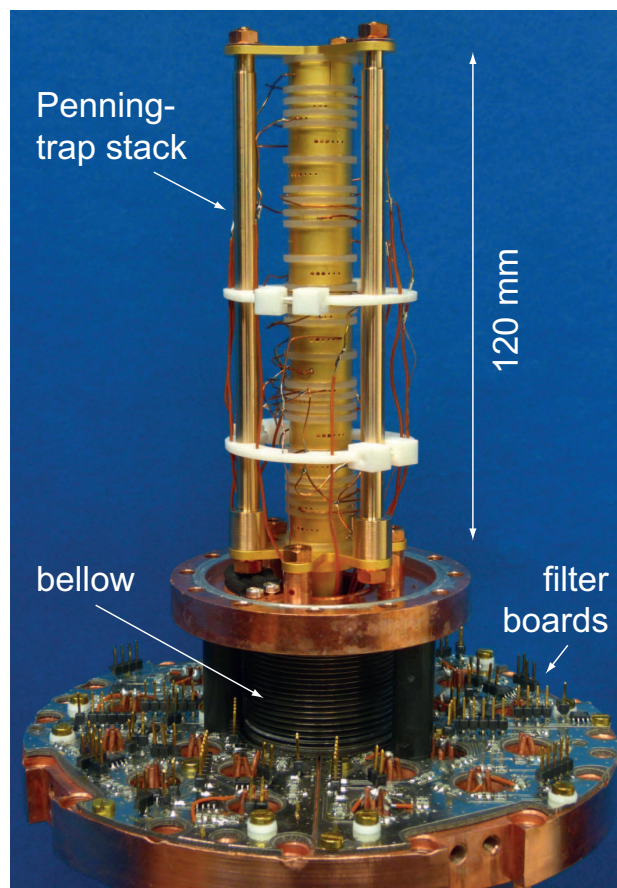


Figure 4.7: Photograph of the Penning-trap assembly mounted at the lower trap chamber flange. One of the titan bellows and the filter boards (for details see [80, 149]), which are placed on top of the electronics chamber flange, are visible. The installation of the Penning-trap stack is covered in detail in Chap. 7.

Table 4.4: Main trap parameters of a single trap. The dimensions of the Penning trap electrodes as well as the dependence of the axial frequency on the ratio $TR = V_C/V_0$ (tuning ratio) of the correction V_C and the ring voltage V_0 are shown. In the case of a vanishing fourth order expansion coefficient of the electric field, the tuning ratio is 0.881. A measure of the influence of the correction voltage on the axial frequency compared to the influence of the ring voltage is the term d_2/c_2 , with $d_2 = \partial c_2/\partial TR$. For more details, especially the uncertainties of the last two values, see [61].

Parameter	Value
overall length	24 mm
length of endcap electrode	7.040 mm
length of correction electrode	3.932 mm
length of ring electrode	1.457 mm
inner radius	5 mm
gaps between electrodes	0.15 mm
$ \Delta\nu_z/\Delta TR $	$< 2.5 \text{ Hz/mUnit}$
d_2/c_2	< 0.01

in the three inner traps, labeled 2-4 in Fig. 4.8, whereas the outer traps 1 and 5 will serve for ion storage, and in some cases, for monitoring magnetic field fluctuations or for the detection of fluctuations of the voltage source. The measurement procedure and individual functions of the particular traps are discussed in detail in Sec. 4.9.

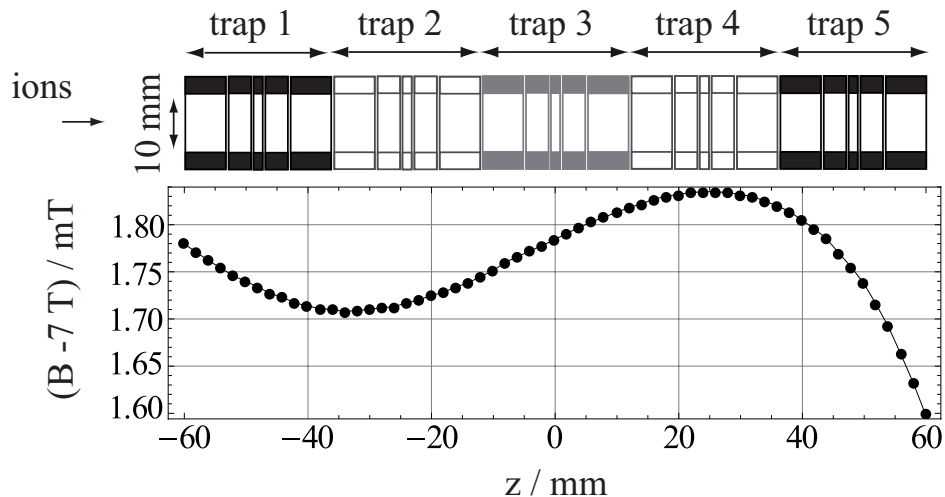


Figure 4.8: (a) Schematic of the five-trap setup. The lower graph shows the magnetic field along the z -axis. The total length of the trap is constrained by the homogeneous region of the magnet (see Chap. 6). The error bars are smaller than the size of the symbols.

4.6 Ion detection

The detection method was already explained in Chap. 2. Here, the main experimental features are outlined. PENTATRAP aims to address a broad spectrum of q/m ratios. Therefore, axial tank circuits are the main detection circuits in the inner traps 2, 3 and 4 (see Fig. 4.9). Different charge-to-mass ratios can then be brought into resonance with the circuits by simply changing the trapping voltage (see Eq. (2.4)) and the radial frequencies ν_{\pm} will be measured via their coupling to the axial tank circuit as discussed in Chap. 2. The inner traps will be equipped with cyclotron tank circuits whose resonance frequencies can be tuned to a specific q/m ratio. In the outer traps 1 and 5 (see Fig. 4.9) the fluctuations of the magnetic field can be monitored by a direct measurement of ν_{+} of, e.g., He^{+} ions. Here, the main detection circuit is the cyclotron tank circuit, and the axial tank circuit will serve, e.g., for measurements of fluctuations of V_0 or for the ion preparation.

The main features of the detection system are outlined in the following. For more details concerning the setup and the characterization of the amplifiers and the resonators it should be referred to the PhD theses of C. Roux [80] and A. Dörr [149]. The superconducting toroidal coil is made of a few hundred (≈ 800) niobium-titanium windings around a teflon torus and is placed in a cylindrical housing made of high-purity OFHC-copper. An unloaded quality factor of > 5000 has been measured. The amplifier has a common-source input stage with high input impedance and extremely low equivalent input noise (see Sec. 2.4). The field-effect-transistors (FETs) used for the amplifiers are based on GaAs. The common-source amplifiers have a high input resistance better than $10\text{ M}\Omega$ and provide an amplification higher than 10 dB at cryogenic temperatures. The system will be operated at $\nu_z \approx 600\text{ kHz}$. The cyclotron detection system is designed for the detection of ions with m/q values between about 4.0 u/e and 4.5 u/e corresponding to resonance frequencies ν_{+} between about 24 MHz and 27 MHz. The cyclotron detection coil has solenoidal geometry and copper windings. Unloaded quality factors of a few thousands have been realized.

Figure 4.9 schematically shows a planned configuration of the detection circuits. For manipulating the eigenmotions of the stored ions, an axial and radial dipolar excitation will be possible in each trap. Moreover, the design allows for a mode coupling via a quadrupolar excitation. The DC-voltages for the Penning trap and amplifier supply voltages will be filtered at room temperature as well as at 4.2 K. The ion signal has to be amplified again at room temperature. Therefore, four cyclotron room temperature amplifiers with subsequent mixers (*ZFL-500LN* and *ZAD6+* from *Mini-Circuits*), as well as four axial room temperature amplifier boards with included down converters (*AF-DC-c* from *Stahl Electronics*) are situated on the magnet's top flange.

4.7 The highly stable voltage source

The main experimental features to achieve the required precision are a 4K environment, a stable magnet system (see Sec. 4.3) and fast measurement cycles (see Sec. 4.9) to reduce the effect of magnetic noise. Furthermore, a stable voltage source to achieve $\Delta\nu_z/\nu_z \leq 10^{-9}$ to measure ν_c on a 10^{-11} level by means of the PNA tech-

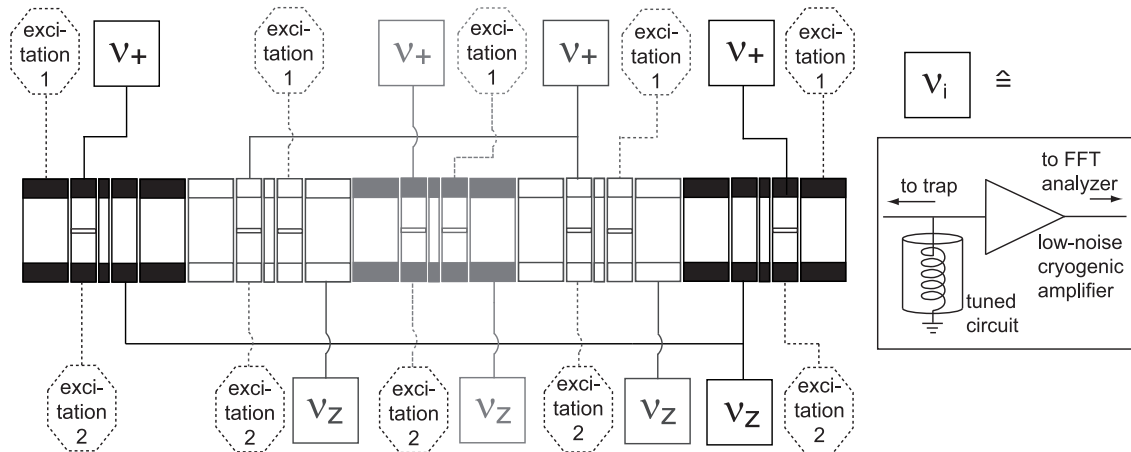


Figure 4.9: Sketch of a proposed cryogenic detection and excitation system for PEN-TATRAP consisting of four axial and four radial tank circuits with high- Q inductors. Low-noise cryogenic amplifiers will complete the cryogenic detection system. Each trap will be connected to two excitation lines to apply dipolar as well as quadrupolar excitations. The position of the segmented electrodes is shown.

nique (see Sec. 2.4) is required. Therefore, even when ν_z is taken as the average over many measurements, the ring voltage must be stable on a level of a few parts in 10^8 over a few minutes. There are no commercial voltage sources available which fulfill this requirement for a voltage range from 0 to -100 V. To this end, the electronics workshop at MPIK in collaboration with the Physikalisch-Technische Bundesanstalt Braunschweig (PTB), Germany, is currently developing a highly stable voltage source covering a voltage range between 0 and -100 V. Design parameters are a voltage stability of $< 4 \cdot 10^{-8} / (10 \text{ min})$, a resolution of $< 10 \mu\text{V}$ and a temperature stability of $< 4 \cdot 10^{-7} / \text{K}$. The voltage source will provide 25 channels and will be LabVIEW controlled. A ramping option for the ion transport and a precision mode for the frequency measurements is planned. The setup of the voltage source is part of the PhD thesis of Ch. Böhm. For more details it should be therefore referred to [140].

4.8 The control system

The LabVIEW-based control and data taking system for the different measurement sequences is based on the GSI Control System (CS) framework [150, 151]. Whereas the original framework is developed to maintain the Time-of-Flight Cyclotron Resonance detection technique [152], the further development for PEN-TATRAP maintains the FT-ICR detection technique within our specific setup. Thus, it is possible to control the ion sources (see Chap. 8), the ion optics and the diagnostics. Due to the flexibility of the new system, it is ensured to change settings, to include new running schemes and to directly replace damaged parts without stopping the whole experiment. Future plans include the implementation of the control of the highly stable voltage source, the implementation of the pressure and level stabilization systems of the superconducting magnet (see Sec. 4.3), and the extension by an “on-line”

data analysis system. For more details it should be referred to the PhD thesis of M. Goncharov [153], which comprises the setup of the PENTATRAP CS system.

4.9 Measurement procedure

PENTATRAP is the first Penning-trap experiment using a stack of five Penning traps for high-precision mass measurements in one setup. Since the effect of magnetic field fluctuations and drifts generally increases with time, it is indispensable that both the measurement of the frequency ratio and the particle preparation are done fast. An application of an FT-ICR measurement principle where two ions are stored simultaneously in one trap and drifts consequently cancel out since they affect the ions in the same way, is not applicable in our case. The perturbation due to the Coulomb interaction of the highly charged ions would increase the systematics and would make a high-precision mass measurement impossible. A solution is the use of a set of Penning traps, assuming that the temporal variation in the magnetic field is largely common to the different traps. Moreover, with a set of five Penning traps a variety of measurement schemes is possible to determine mass ratios.

A measurement scheme of first choice implies the usage of traps 3 and 4 (see Fig. 4.8) to measure the cyclotron frequencies of two ionic species simultaneously. The measurement sequence is carried out as follows (see Fig. 4.10): First, ions with the same charge state and with masses m_1 , m_2 and m_1 are loaded into traps 2, 3 and 4, respectively (Fig. 4.10(a)). The cyclotron frequencies of the ions $\nu_c(m_2)^{(1)}$ and $\nu_c(m_1)^{(1)}$ in traps 3 and 4 are measured simultaneously, and the ratio of their frequencies $R^{(1)} = \nu_c(m_2)^{(1)}/\nu_c(m_1)^{(1)}$ is determined according to Eq. (2.2) to be $R^{(1)} = m_1/m_2 \cdot B_3^{(1)}/B_4^{(1)}$, where $B_3^{(1)}$ and $B_4^{(1)}$ are the magnetic field strengths in trap 3 and 4 averaged over this measurement. After the measurement is completed, the ions are adiabatically transported into the adjacent traps (Fig. 4.10(b)), so that trap 2 becomes empty, traps 3 and 4 are loaded with the ions with mass m_1 and m_2 . The ratio of the cyclotron frequencies is measured again, $R^{(2)} = \nu_c(m_2)^{(2)}/\nu_c(m_1)^{(2)} = m_1/m_2 \cdot B_4^{(2)}/B_3^{(2)}$, where $B_4^{(2)}$ and $B_3^{(2)}$ are the magnetic field strengths in trap 4 and 3, averaged over the second measurement period. The square root of the product $R^{(1)}$ and $R^{(2)}$ yields the m_1/m_2 ratio, assuming the ratio of the magnetic field strengths is time-independent. Thus, unavoidable temporal magnetic field fluctuations common to traps 3 and 4 do not affect the mass ratio. In this measurement scheme, trap 2 and 5 are used to store ions, which are temporarily not measured. In this approach, trap 1 can be used for a long-term monitoring of magnetic field fluctuations or as a reference for the voltage source. To this end, the cyclotron frequency of a permanently stored ion with mass m_3 can be monitored during the measurement cycle.

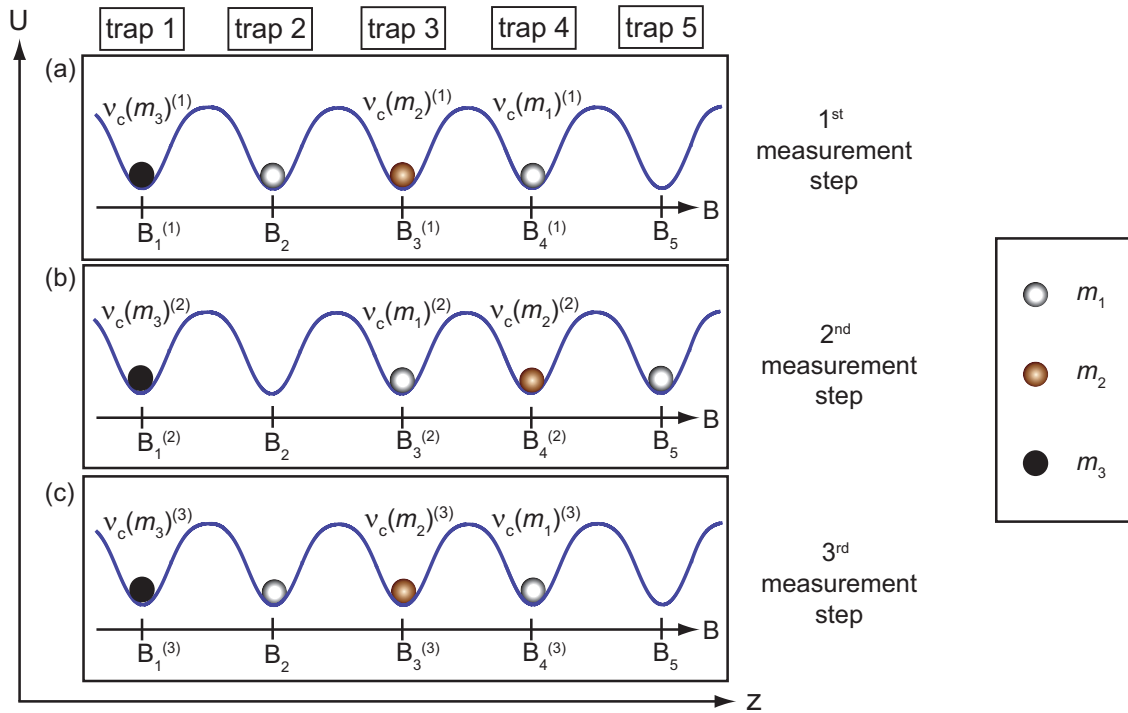


Figure 4.10: Proposed measurement scheme of first choice. The potential wells are shown as a solid blue line. Two ions with mass m_1 are shown as grey balls, the ion with mass m_2 as a brown ball and the permanently stored ion with mass m_3 as a black ball. (a) In step 1, three ions with mass m_1 , m_2 and m_1 are loaded into traps 2, 3 and 4, respectively. The cyclotron frequencies are measured in trap 3 and 4. (b) In step 2 the ions are moved one trap further to the right and again the cyclotron frequencies of the ions are measured in trap 3 and 4. (c) The ions are moved back to the initial position and the same measurement as in (a) is performed again. Trap 1 can be used for a longterm monitoring of the cyclotron frequency of the ion with mass m_3 . These cycles will be repeated several times.

Chapter 5

Simulations of the ion transport and capture in the Penning traps

The objective of this chapter is to describe the simulation studies of the ion capture in the Penning traps. The ion beam parameters preset by the performance of the Heidelberg-EBIT were used. Furthermore, the transport of a single ion between two traps was investigated. The simulations were carried out using the program SIMION[®], version 8.0, which allowed to calculate electromagnetic fields and the trajectories of charged particles in those fields. For this the configuration of the electrostatic electrodes, their voltages, the particles' initial conditions and the magnetic field had to be defined.

5.1 Operating principles of Simion[®]

An introduction in the operating principles of SIMION[®] based on [136] is given in a listed form. For a more detailed explanation please refer to the user's manual [136].

electrode geometry A fixed 3D electrode array geometry is defined in a geometry file. In the potential array, which is an array of points forming an equally-spaced cubic grid¹, all points are allocated to a potential and a type, i.e., non-electrode or electrode. Potential arrays can be used to define both electrostatic and magnetic field. In the following simulations the magnetic field strength was assumed to have a fixed value of 7 T since the magnetic field gradient on-axis along the Penning traps and the considered electrodes is only around a few 100 μ T. A scaling factor is defined in the geometry file, which translates the internal and fixed coordinates used in the .gem file to external coordinates used in the potential array. This scaling factor can be increased to raise the number of grid points and to gain a higher spatial resolution. Finally, the number of grid points is limited by the RAM of the computer.

field calculation SIMION[®] solves the Laplace equation to obtain the potential of the grid points. For that purpose, a finite difference method with the aim to attain the best estimate of the voltages for the points outside of the electrodes

¹The uniform grid is a limitation of the program, since it is not possible to increase the density of grid points near edges or vertices, which leads to inaccurate field calculations.

is used. Once the fields are found by an iterative method, the trajectories of the charged particles are computed.

computation of the trajectories This is done by first determining the electrostatic and magnetic forces for the current position and velocity of the ion. In order to predict the position and velocity at the next time step, these forces are used to compute the current ion acceleration. The accuracy of the trajectory calculation is increased by adjusting the time steps. The user has the possibility to influence the obtained accuracy via the Trajectory Quality (*TQual*) control panel. To this end, SIMION[®] contains several algorithms to improve the accuracy while minimizing the number of integration steps, e.g., to efficiently approach a boundary. For the numerical integration of the ion trajectories in three dimensions, a standard fourth-order Runge Kutta method is used.

5.2 Ion injection into the drift tube

Close to the Penning traps, just before the ions enter the Penning trap stack, a drift tube electrode is situated (see Fig. 5.1). With this electrode the energy and the length of the ion bunch will be reduced to guarantee efficient trapping in the Penning traps. In a first step the properties of the ion bunch after entering the drift tube were investigated for different voltages U_{DT} applied to the drift tube electrode. Moreover, the obtained parameters were used as start parameters to further simulate the injection into the Penning traps and the capture therein. The geometry of the Penning trap stack, the fastening plates, the drift tube and the surrounding vacuum chamber and beam tube used for the simulation are shown in Fig. 5.1.

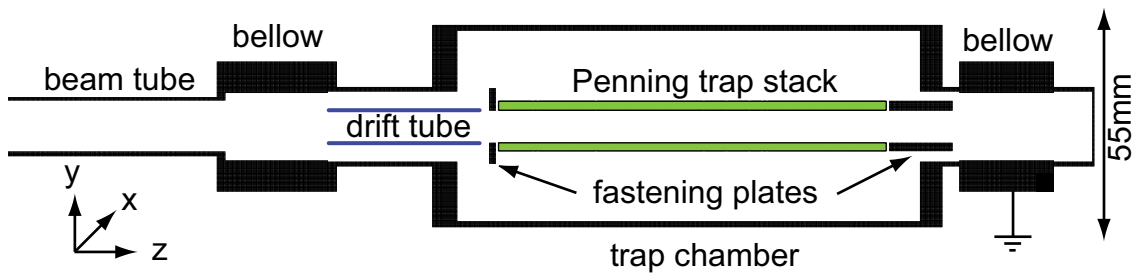


Figure 5.1: Simplified geometry used in the simulations according to the file shown in App. A. Ions entered from the left side. All black parts were grounded and the vertical surface at the right end side was used to define a terminating condition. The single Penning trap electrodes are for simplicity not shown in this sketch.

A bunch of 1000 ions with a charge-to-mass ratio of $0.25 e/u$ was defined, which corresponds to a bunch of, e.g., ${}^4\text{He}^+$ or ${}^{187}\text{Re}^{47+}$ ions. The ions were flying in z -direction (see Fig. 5.1). The initial positions of the ions were described by a cylinder distribution with its center at a point on the z -axis before the ions were subject to the potential of the drift tube. The cylinder had a radius r of 0.25 mm and a length l of 49.11 mm. The beam radius at a specific axial point could be determined from the radial beam emittance ϵ and the beam's divergent angle from this radius. The beam emittance, which is the area surrounded by the phase space ellipse (see

Table 5.1: Summary of the parameters describing the ion bunch before it enters the drift tube and when it is inside the drift tube at $U_{\text{DT}} = 195 \text{ V}$. The values of ϵ can be compared by normalizing both to the mean ion velocity in z -direction. At the initial conditions a normalized value of $1.7 \cdot 10^6 \pi \cdot \text{mm} \cdot \text{mrad} \cdot \text{m/s}$ and at $U_{\text{DT}} = 195 \text{ V}$ a value of $1.6(2) \cdot 10^6 \pi \cdot \text{mm} \cdot \text{mrad} \cdot \text{m/s}$ is obtained. For the detailed description of the ion bunch and the definition of the parameters see text. The value given in brackets for the kinetic energies specifies the energy width.

parameters		initial	$U_{\text{DT}} = 195 \text{ V}$
charge-to-mass ratio	q/m (e/u)	0.25	0.25
ion number	N_{ion}	10000	9263
bunch radius	r (mm)	0.25	0.17(6)
bunch length	l (mm)	49.11	7.98(9)
time length	τ (ns)	500	549(6)
mean kinetic energy	E_{rad} (eV)	0.6(4)	0.6(4)
	E_z (eV)	199.4(4)	4.4(4)
maximum angles	α ($^\circ$)	± 4.0	$\pm 36(1)$
	β ($^\circ$)	± 4.0	$\pm 36(1)$
emittance	ϵ ($\pi \cdot \text{mm} \cdot \text{mrad}$)	≈ 17.5	107(12)

e.g. [154]), was chosen to be $17.5 \pi \cdot \text{mm} \cdot \text{mrad}$, which was estimated considering the performance of the Heidelberg-EBIT ($3 \pi \cdot \text{mm} \cdot \text{mrad}$ at $7 \text{ keV} \cdot \text{Z}$ axial kinetic energy). The total kinetic energy was set here to $200 \text{ eV} \cdot \text{Z}$, since the upper drift tube can reduce the mean axial kinetic energy E_z of the beam from a few $\text{keV} \cdot \text{Z}$ to a few hundred $\text{eV} \cdot \text{Z}$. The beam length l was calculated to $l = v_z \cdot \tau$, where $v_z = (2E_z/m)^{1/2}$ was the ion's velocity and τ the bunch length in time. The value of τ was estimated to be 500 ns at this position in the beam line. The velocity of the ions was defined by a uniform angle distribution characterized by an azimuth ($\alpha \in [-4^\circ, 4^\circ]$) and an elevation angle ($\beta \in [-4^\circ, 4^\circ]$), which resulted from the maximum radial and axial energy components as well as from the total kinetic energy. The parameters of the ion bunch before the ions experienced the potential of the drift tube are summarized in Tab. 5.1.

In this part of the simulation the geometric resolution of the drift tubes' diameter (10 mm) and length (47.80 mm) was around $\pm 0.02 \text{ mm}$. The effect of the time quality factor on the obtained bunch length was checked which led to the choice of the highest value for the actual simulation. The velocity components and the time of flight of 1000 ions flying one after another were recorded in the center of the drift tube². Gaussian distributions were fitted to the velocity and time-of-flight distributions. The bunch length was defined as the product of the mean axial velocity \bar{v}_z and three times the σ width of the time distribution. For different drift tube voltages the bunch lengths are shown in (Fig. 5.2(a)). It was proven that the

²This approach neglects the effect of ion-ion interactions, which will be present in case all 1000 ions will start simultaneously.

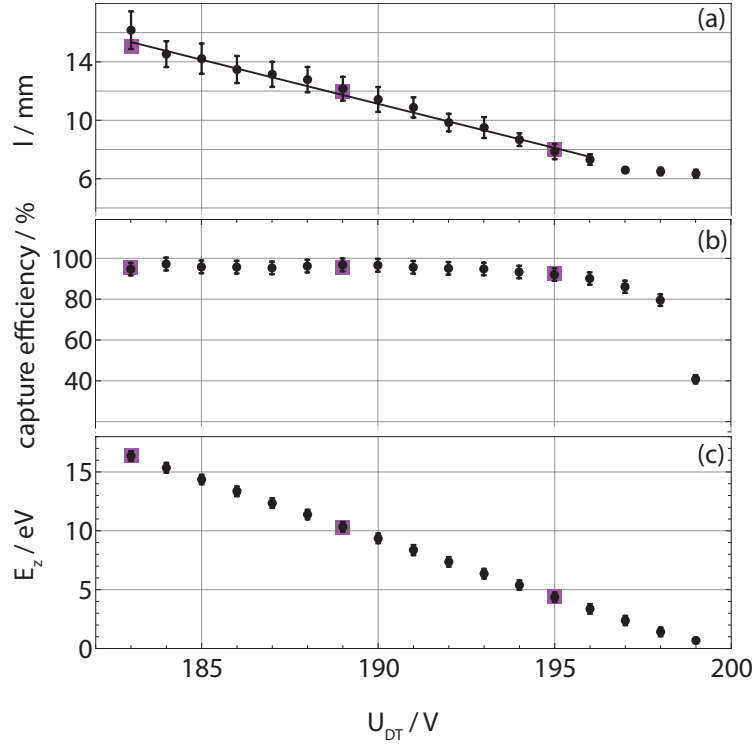


Figure 5.2: (a) Bunch length for different drift tube voltages. The black points were obtained by considering 1000 ions. The magenta rectangles are the values obtained by a cross check using a higher ion number of 10000. The kinetic energy and the length of an ion bunch can be reduced with an efficiency of about 90 % by employing the drift tube (b). In (c) the mean axial kinetic energy of the ions in the center of the drift tube is shown. For the considered drift tube voltages the radial kinetic energy was in the range of 0.6(4) eV. The error bars result from the uncertainty of the fit.

drift tube design allows to bunch 90% of the ions (Fig. 5.2(b)). The bunch length was reduced to a sixth compared to the start length at a voltage of $U_{DT} = 195$ V. A linear fit to the bunch lengths gave $l = -0.60(3) \text{ mm/V} \cdot U_{DT} + 126(6) \text{ mm}$. At $U_{DT} = 199$ V the trapping efficiency was only about 40 % (see Fig. 5.2(b)) since the amount of ions which reached the drift tube center decreased with increasing drift tube voltage. As a cross check a higher ion number of 10000 was chosen for few selected values of U_{DT} (see magenta rectangles in Fig. 5.2). The obtained parameters were in good agreement with the parameters obtained for 1000 ions.

For the following simulation the parameters listed in Tab. 5.1 at $U_{DT} = 195$ V obtained from the flight of 10000 ions were used. Figure 5.2(c) shows, moreover, the mean axial energy of the ion bunch versus the drift tube voltage. The radial energy was in the order of 0.6(4) eV for the used settings. The energy transfer from radial to axial energy caused by a declination of electrostatic and magnetic field with respect to each other was not investigated.

5.3 Ion injection into the trap stack

A sketch of the planned ion injection scheme is shown in Fig. 5.3. The simulation of the bunch properties has been described in Sec. 5.2. Here, the injection scheme will be shortly explained. In a first step the ion bunch with a well-defined axial energy is released out of the drift tube and is injected into the Penning-trap stack (Fig. 5.3 (b)). For this purpose the drift tube voltage is ramped down to a negative value. At this point, it might be worth mentioning, that the drift tube is field free. Thus, the potential can be changed without affecting the ion cloud, as long

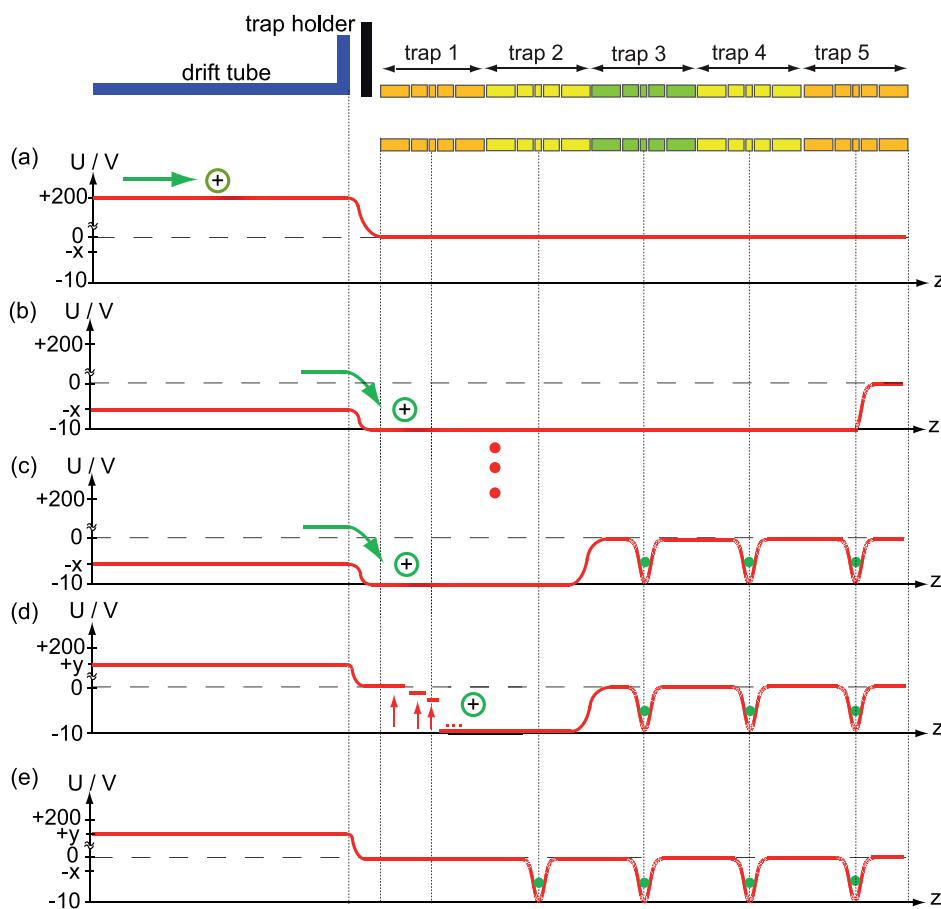


Figure 5.3: Sketch of the ion injection principle. First the ion bunch passes the drift tube where its length and kinetic energy are reduced (a) (see Sec. 5.2). The voltage of the drift tube is reduced to a negative value ($-x$ V) to inject the ion bunch with a well-defined energy into the Penning trap stack (b). Thereby, all Penning trap electrodes are at a negative potential, except the outer endcap electrode of trap 5 which is grounded. Then the traps 3-5 are successively loaded (c). Intermediate steps are not shown, but are illustrated in the following for loading trap 2. After the ion bunch enters the volumes of traps 1-2, the drift tube potential is fast switched up to a positive value ($+y$ V) to confine the ion bunch. Afterwards the Penning-trap electrodes are successively raised up beginning with the upper endcap electrode of trap 1 to slowly move the ion bunch towards trap 2 (d). Then the storage potential is applied at trap 2 and the procedure of reducing the cloud to a single ion can be started. In the end single ions are trapped in traps 2-5 (e).

as the cloud is in the tube. All Penning trap electrodes are at negative potential except the last endcap electrode at the end of the trap stack. This electrode is grounded to avoid a loss of the ion bunch in axial direction. In order to be still able to carry out a fast ion exchange between adjacent traps (see Sec. 4.9), generally maximal four traps have to be loaded with two ion species in an alternating way. First, the traps 3-5 are successively loaded starting with trap 5 (Fig. 5.3 (c)). By means of the loading of trap 2 the trapping process is illustrated in more detail in Fig. 5.3 (d). After the ion bunch enters the trap volumes of traps 1 and 2, which are put on negative potential, the drift tube voltage is fast switched up to confine the bunch. The drift tube can be switched faster than the Penning-trap electrode, since the supply voltages of the Penning-trap electrodes are first filtered³. A high filter capacity of about 3 nF increasing the reachable minimum rise time can be thus avoided. Since the ion passage time through traps 1-2 is shorter than, e.g., through traps 1-3, the drift tube voltage has to switch up faster in the first than in the later case. Thus, the first case is studied in the following. In order to trap the ions finally in trap 2, the electrodes of trap 1 are slowly successively ramped up starting with the upper endcap electrode. Finally, the storage potential can be applied at trap 2 and the procedure of preparing a single ion can be started (see Fig. 5.3(e)). In case contaminant ions are present, a single q/m range must be first isolated. Therefore, e.g., the SWIFT (Stored Waveform Inverse Fourier Transform) [155] cleaning can be applied. Thereby the axial amplitudes of unwanted ions are excited. When the trap voltage is afterwards lowered to a minimum value, the unwanted ions are not trapped anymore.

Another possibility for loading the Penning traps would be the option to transport a cloud of two ion species into the Penning traps, to store the cloud in one trap and to prepare from this reservoir the needed ions for the other traps. The ion cloud could consist of Re and Os ions which are produced at the Dresden-EBIT3. Since these ions needed for β -decay studies have a similar q/m value, the simultaneous ejection from the Dresden-EBIT3 and passage through the Wien filter could be investigated. Thereby, the effect of ion-ion interactions should be kept in mind.

5.3.1 Examination of the electrostatic potential

The exact shape of the electrostatic potential sketched in Fig. 5.3 (c) is shown in Fig. 5.4. In this example the electrodes of traps 1 and 2 were set to the capture potential $U_{\text{Capture}} = -10$ V, U_{DT} was set to -5 V and traps 3 and 5 are supplied with storage potentials, respectively. A sufficiently high potential well, which prevents ions to reach trap 3, was realized in case the right endcap of trap 2 was grounded (see black solid line in Fig. 5.4). In order to avoid a short time of flight through a deep potential, which makes the capture process more difficult, U_{Capture} was set to -10 V in the following simulation. Besides, first measurements will be performed with a voltage source which can deliver 0 V to -14 V (see Sec. 4.7). On the other hand the potential should not be made too shallow, since then the axial kinetic energy E_z of the ions could be high enough to allow them to escape. In Fig. 5.4 the relevant energies are labeled. The sum of E_z and the potential energy gained at the

³The new power supply for the Penning traps is currently under construction [140]. Rise times of few hundred milliseconds at a supply voltage of about 80 V are present specifications.

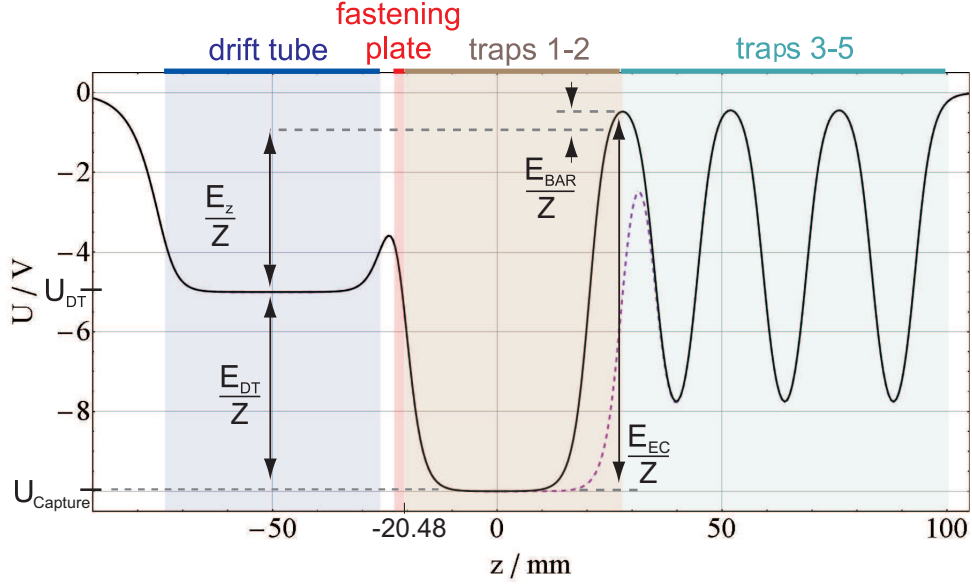


Figure 5.4: The electrostatic potential at a drift tube potential of $U_{DT} = -5$ V and a capture potential $U_{Capture} = -10$ V, which is seen by a Z -fold charged ion flying along the z -axis, is shown. In the traps 3-5 ions were stored at the trapping potential (here $V_0 = -10$ V). The right endcap electrode of trap 2 was grounded to create a sufficiently high potential well (black solid line), which is defined by the potential energy E_{EC} . The purple dashed potential behavior is expected in case this electrode is set to $U_{Capture}$. E_z is the initial axial kinetic energy, E_{DT} the potential energy gained at the drift tube and $E_{BAR} = E_{EC} - E_z - E_{DT}$.

drift tube E_{DT} must be smaller than E_{EC} , which is the height of the potential well to trap 3. An energy relation can be expressed by

$$E_z + E_{DT} = E_{EC} - E_{BAR}. \quad (5.1)$$

Here, the energy E_{BAR} should be positive to assure a capture. Several investigations of the electrostatic potential were performed:

- The influence of the grounded trap holder (or fastening plate) on the potential shape for different voltages applied to the drift tube electrode was examined. Therefore, Fig. 5.5 shows a zoom of Fig. 5.4. The potential at the time when the drift tube was raised in order to “close” the potential can be analyzed by means of this graph as well. The drift tube voltage should not be raised to high positive values, but rather to a value near ground potential to create a potential well approximately as high as the one to trap 3. It should be noted that the drift tube voltage should be increased only when all ions from the bunch have left it. Else particular the slow ions will gain energy, which might allow them to leave the traps in z -direction.
- The potential at $z = -20.48$ mm (see Fig. 5.4) where the ion reaches the first electrode of trap 1 was simulated to investigate the influence of various settings of U_{DT} and $U_{Capture}$ (see Fig 5.6) on the potential. A high positive drift tube voltage should be avoided, since then the potential will be more distorted in

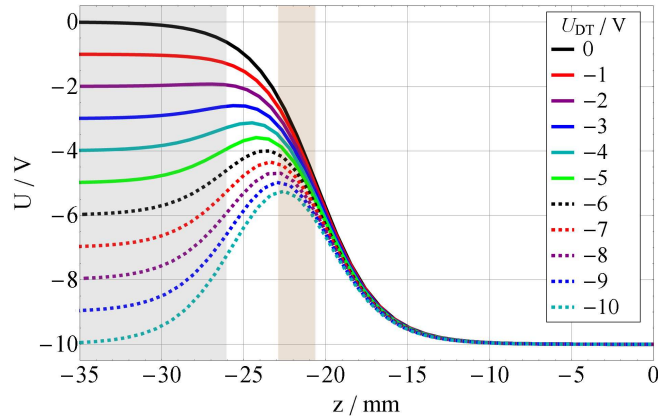


Figure 5.5: Shown is the influence of the drift tube voltage on the electric potential for a grounded fastening plate of the Penning-trap stack (see Fig. 5.1). In this example the traps 1 and 2 were at -10 V and the drift tube voltage was changed. The origin of the z -axis is the same as in Fig. 5.4. Depending on the negative drift tube voltage, the ions have to overcome a small potential well when entering the trap stack. Additionally, it can be seen that a switching of the drift tube voltage to ground potential is sufficient to confine the ions in the trapping volume. The position of the fastening plate is indicated by a brown shaded background and that of the drift tube by a gray shaded background.

direction of trap 1. For $U_{\text{Capture}} = -10\text{ V}$ and $U_{\text{DT}} = 40\text{ V}$ the potential seen by the ions at the start of trap 1 is close to zero. For this setting the dependence of the potential on the radial coordinate was checked. The gradient at a radial position ρ ($dU(\rho)/d\rho$) was estimated from the simulated data to about $-400\text{ mV/mm}^2 \cdot \rho$. For comparison the gradient in the center of the Penning trap given through the trap geometry is about $300\text{ mV/mm}^2 \cdot \rho$.

- The deformation of the storage potential of trap 1 in case 195 V are applied at the drift tube was analyzed (see Fig. 5.7). A shift of the center of about 0.25 mm is visible. The harmonic coefficient of the trapping potential C_2 (see Chap. 2), which theoretical value is $14.96(7) \cdot 10^{-3}/\text{mm}^2$ [61], increased by about $2 \cdot 10^{-3}/\text{mm}^2$. It is obvious that in case the first Penning trap is used for frequency measurements of a stored ion no voltage should be applied at the drift tube.

5.3.2 Investigation of the time of flight

After the potential situation was investigated, the ion capture in the traps was simulated. The parameters redefining the ion bunch inside the drift tube are summarized in Tab. 5.1. The ion bunch was defined in the same way as it was done in Sec. 5.2: The source positions of the ions were defined by a cylinder distribution characterized by its center as well as its radius r and length l . The velocity format of the ion bunch was defined by a uniform angle distribution characterized by α , β and E_z .

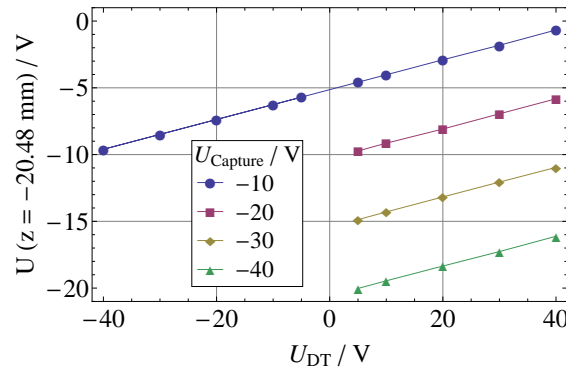


Figure 5.6: The potential at the position where the ion enters Penning trap 1 ($z = -20.48$ mm in Fig. 5.4) influenced by different drift tube voltages U_{DT} is shown. For $U_{DT} = -U_{\text{Capture}}$ the potential is about $0.4 \cdot U_{DT}$ at this point. The errors are in the 0.1 V range.

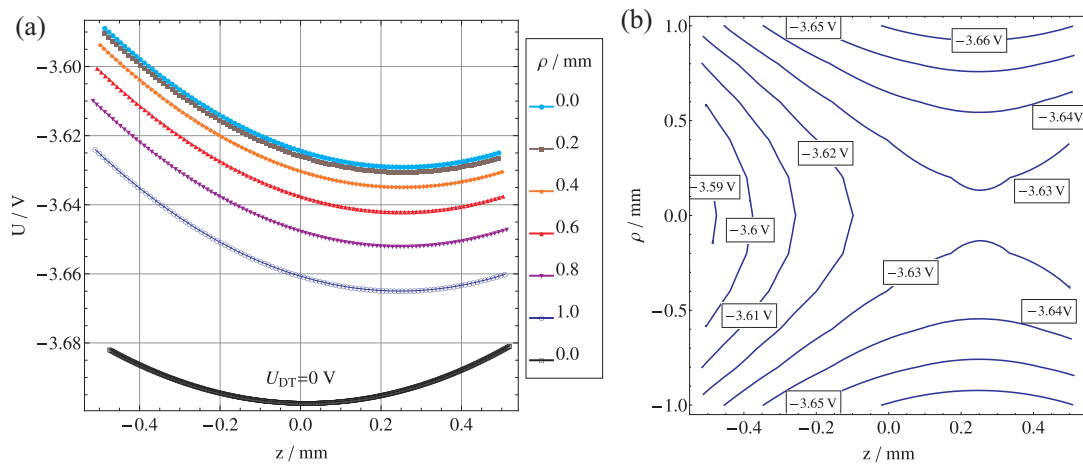


Figure 5.7: Distortion of the Penning-trap potential (here $V_0 = -5$ V) at a voltage of 195 V applied to the drift tube. As expected the harmonic potential is affected. Here, the origin of the z -axis is the center of trap 1. In (a) the potential is shown along the z -axis at different radial positions ρ and (b) shows the contour plot of this simulated data.

The Lua⁴ code implemented for adjusting the drift tube voltage and for providing a termination condition is shown in App. A. A sketch of the timing scheme is shown in Fig. 5.8. The switch time of the drift tube voltage Δt_S was set to a value of 100 ns which can be realized with the *Behlke* switch in use and U_{Capture} was set to -10 V. In a first step the time after which the drift tube voltage should be raised up again Δt_{TOF} was determined. Therefore, the mean time of flight of the ion bunch was determined at both crossings of the plane $z = 0$ (see Fig. 5.4). Δt_{TOF} was taken as the sum of the obtained mean time of flights. The results are shown in Fig. 5.9(a). In general, Δt_{TOF} should decrease with a higher voltage U_{DT} applied at the drift tube since then the kinetic energy of the ion bunch is higher. For $U_{DT} < 0$ V the ions are slowed down by the potential well formed by the trap holder. The ions

⁴The programming language Lua (from Portuguese: lua, “moon”) is a multi-paradigm scripting language.

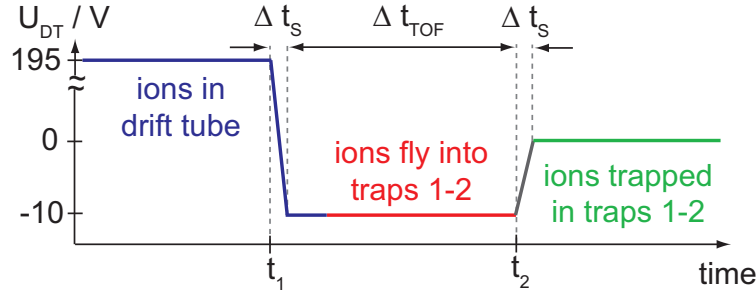


Figure 5.8: Example of a used timing scheme of the pulsed drift tube. After the axial kinetic energy and the length of the ion bunch were reduced the drift tube voltage was switched down at time t_1 to a negative value and the bunch was ejected towards the Penning traps. The time needed to switch the voltage is called Δt_S . Then, after a waiting time of Δt_{TOF} , the voltage was switched up again at time t_2 to confine the ion bunch.

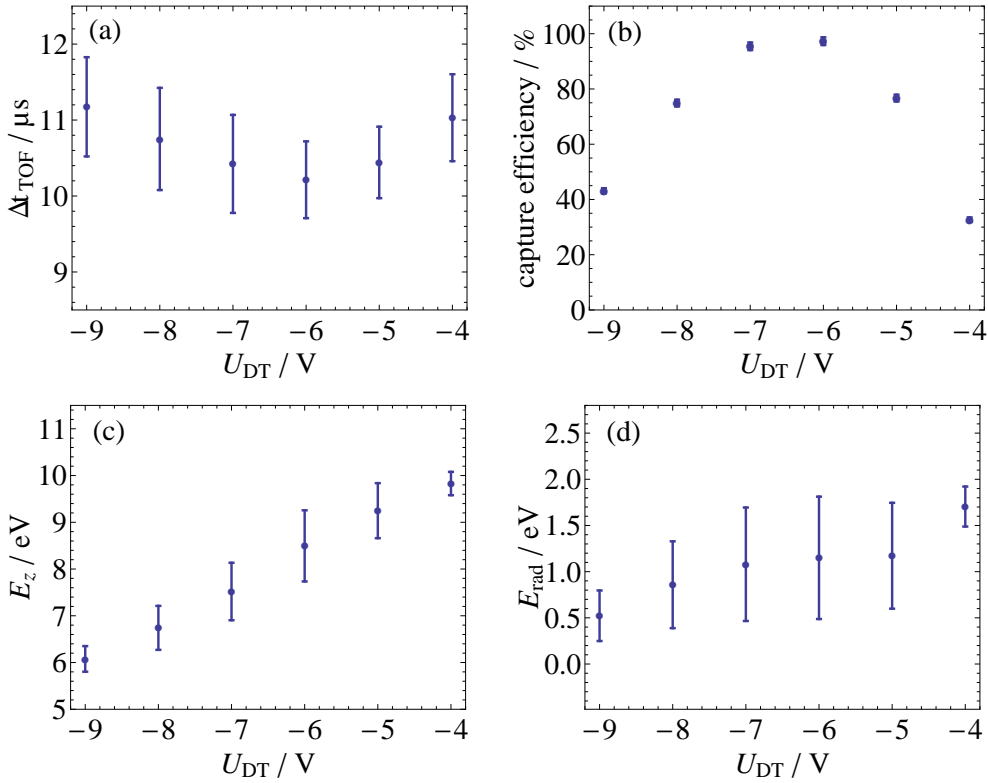


Figure 5.9: Simulated data for the capture of the ion bunch at $U_{\text{Capture}} = -10 \text{ V}$ (see Fig. 5.8). In (a) the time after which the drift tube voltage should be raised up again Δt_{TOF} to confine the ion bunch is shown. Δt_{TOF} is calculated as the sum of the two mean time of flights at the twice crossing of the plane $z = 0$ (see Fig. 5.4). In (b) the capture efficiency, in (c) the mean axial and in (d) the mean radial kinetic energy of the ion bunch at $z = 0$ is shown. The error bars in (a), (c) and (d) represent the time width and the energy widths of the ion beam, respectively, obtained from the standard deviation of the fit. 1000 ions are taken into account for each data point. For the discussion see text.

have to overcome this potential well to reach the Penning traps (see Fig. 5.5). The potential well is higher the lower U_{DT} . Therefore, the number of trapped ions decreased for low values of U_{DT} since not all ions did have enough energy to overcome the potential well (see Fig. 5.9(b)). For $U_{DT} > -6$ V the simulated values of Δt_{TOF} increased again since the ions experience the potential flank of the capture potential at a different position. Moreover, the ions with sufficient kinetic energy can escape in axial direction towards trap 3. Therefore, the number of trapped ions decreased again for high values of U_{DT} . Moreover, the trap content of trap 3 gets contaminated since in trap 3 a different ion species is stored than in trap 2. This case should be prevented.

Concluding, trapping of an ion bunch in traps 1 and 2 by switching the drift tube voltage was possible. For the studied example, the optimum value of U_{DT} would be about -7 V to guarantee a most efficient trapping of the ion bunch. In Fig. 5.9(c-d) the mean axial and radial energy of the ion bunch are shown. The obtained mean axial kinetic energy was as expected the sum of the initial axial kinetic energy and E_{DT} . A radial energy of about 1 eV with a width of about 0.5 eV was obtained for a capture efficiency higher than 80%. For the slow ion bunch at $U_{DT} = -9$ V the ions with high radial energy were not captured. Thus, the value itself and the width were reduced.

5.4 The ion transport between the traps

In this section the adiabatic transport between two neighboring Penning traps is covered. Generally, for an adiabatic transport in axial direction the relation $1/\nu_z \ll t_T$ must be fulfilled, where t_T is the time needed for the total transport. Hence, the ramping of the voltages must be sufficiently slow and the voltage level must be kept constant during the transport to avoid an axial or radial energy gain of the ions. A gain of axial energy can be efficiently cooled after the transport, since the cooling time constant (see Eq. (2.37)) of the axial mode is in the millisecond range (see Chap. 2). However, the cooling time constant of the cyclotron mode is in the range of 10 to 100 seconds (see Chap. 2) and is thus more critical in the context of achieving fast measuring cycles. Moreover, a gain of energy can lead to an unwanted ion loss. In case the ion gained too much radial energy it might hit the surfaces of the Penning-trap electrodes. Moreover, the ion follows the electrostatic minimum of the trap rather than the magnetic field lines during an adiabatic transport. This might lead to an increase of the radial amplitude in case the electrostatic and mechanical center do not coincide. Such a deviation can be caused by patch potentials on the electrode surfaces.

In the following, it was checked whether thermally distributed ions reach the second trap and their axial and radial kinetic energy after the transport were determined.

5.4.1 Possible timing schemes

First, a timing scheme of the trapping voltages was chosen. At PENTATRAP we seek for fast measurement cycles, therefore a scheme with a minimum of four time steps was analyzed. In Fig. 5.10 a sketch of the scheme is given. It is characterized by

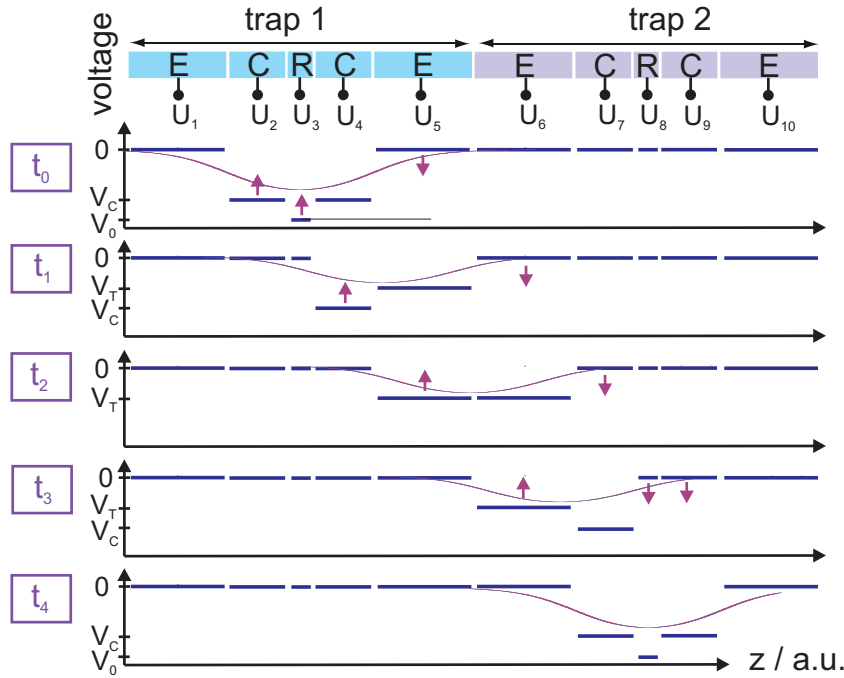


Figure 5.10: Sketch of the timing scheme used for the simulation of the ion transport. The scheme consists of four steps. At t_0 a single ion was stored in trap 1, where the voltage of the ring (R) electrode U_3 were at V_0 and the voltages of the correction (C) electrodes U_2 and U_4 were at V_C . Since the ring (1.457 mm) and the correction electrode (3.932 mm) were in the sum shorter than the endcap (E) electrode (7.040 mm), U_2 and U_3 were simultaneously ramped up to 0 V and the voltage at the endcap U_5 was ramped down to V_T . The value of V_T was adjusted to keep the potential depth on a similar level, even in between the time steps shown here, and to maintain a more or less harmonic potential during the transport. At t_1 the voltage U_4 was raised up to 0 V and the voltage at the endcap electrode of the next trap U_6 was ramped down to V_T . At time t_2 the voltage at U_5 was raised up and U_7 was lowered to V_C . At time t_3 U_6 was raised up and U_8 and U_9 were lowered to the trapping potentials V_0 and V_C , respectively. At t_4 the trapping voltage was applied at trap 2.

a ramping of the ring electrode together with the neighboring correction electrode. The artificially elongated electrodes realized through the simultaneous ramping of the two electrodes are on the one hand a disadvantage of this scheme, since it is more difficult to keep the electrostatic center close to the mechanical one. On the other hand this scheme manages the transport with four ramping steps, which makes the transport as fast as possible. An alternative scheme characterized by successively ramping the voltages would require in total six steps. The scheme would be: ramp the first electrode up, leave the second on its potential and ramp down the voltage of the third electrode. It was checked, if the transport could be theoretically realized with four steps. Nevertheless, it must be proven experimentally as well, since for instance the effect of patch potentials cannot be checked with SIMION[®]. For the voltages applied at the respective time steps and the movement of the position of the potential minimum see Fig. 5.11(a). A symmetric scheme was chosen and the voltages were adjusted to keep the potential depth on a similar level, even in between

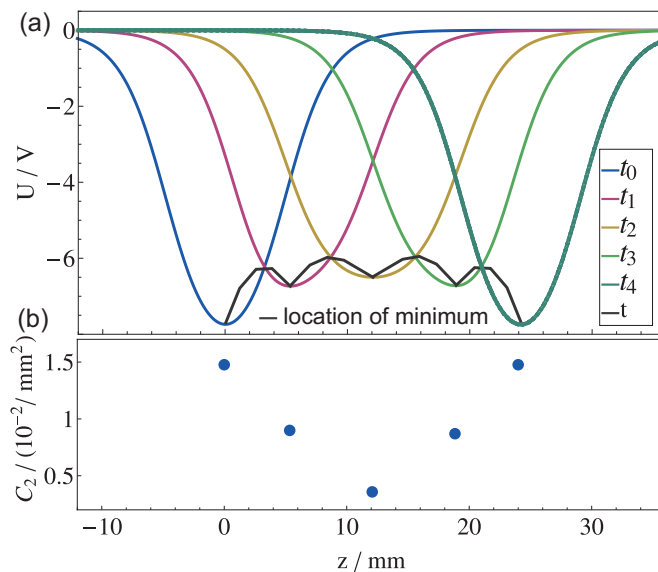


Figure 5.11: Shape of the electric potential in axial direction during the transport. In (a) the potential at the different time steps introduced in Fig. 5.10 is shown. The black curve shows the location of the potential minimum at t_0 - t_4 and intermediate time steps. A symmetric scheme was chosen to simplify the process. In (b) the C_2 parameter characterizing the harmonic potential is shown. The errors are estimated to be in the 1% range due to symmetry considerations. For discussion see text.

the time steps, and to maintain an adequate harmonic potential during the transport (see Fig. 5.11(b)).

5.4.2 Variation of the ramping times

At the beginning of the transport a velocity distribution of the ions whose transport was simulated was chosen. Hence, the realistic case of Maxwell-Boltzmann distributed ions was approximated by a Gaussian distribution. The Gaussian velocity distribution is an implemented function which can be directly chosen on the user interface for the definition of the ion beam properties. Using this approximation small velocities are overestimated and high velocities are underestimated. For a single velocity direction v_i the Maxwell-Boltzmann distribution is given by

$$f(v_i) = \sqrt{\frac{m}{2\pi k_B T}} \exp\left[-\frac{mv_i^2}{2k_B T}\right], \quad (5.2)$$

with k_B the Boltzmann constant, m the ion mass and T the temperature. The mean velocity of the Gaussian distribution was set as the most probable velocity of the Maxwell-Boltzmann distribution. The mean axial energy is defined by the mean squared velocity in z -direction $\langle v_z^2 \rangle$ and is given as $E_z = k_B T_z = \frac{1}{2} m \langle v_z^2 \rangle$.

In the simulations described in the following 100 ions with $q/m = 0.25 e/u$, a mean energy of 0.36 meV and a standard deviation of the energy distribution of 0.36 meV corresponding to a thermal energy at 4.2 K started in the center of the trap. The radial start amplitudes were set to zero, since they are a few μm for a previously cooled magnetron mode, which is smaller than the geometrical resolution of the electrodes. Here, the geometrical resolution of a single grid point was

± 0.02 mm, which was limited by the RAM of the computer. Thus, the limitation of the geometrical resolution was reflected in the obtained energies. The energies were stored at the ideal geometrical center of the Penning trap which could deviate from the electrostatic center. For the used potential depth the potential energy of an ion, which was shifted by 0.02 mm from the potential minimum, was 0.06 meV being 17% of the mean ion energy. Therefore, the errors in the determination of the mean ion energy and of the width of the energy distribution were estimated to be at least about 25% considering also the low statistics of 100 ions. It should be mentioned that the needed simulation time was very long, e.g., about one week for 100 ions and better statistics would have been extremely time consuming to achieve. The velocity components in the radial directions were set to zero, to determine the energy transfer into the radial mode after the transport. This was of course an artificial situation which cannot be realized in the experiment and the energy transfer from the radial into the axial direction was not accounted for. Later, in Sec. 5.4.5, the results obtained for a three-dimensional thermal velocity distribution of the ions will be presented. It was proven that the ion transport for the voltage settings of $V_0 = -10.00$ V, $V_C = -8.81$ V and $V_T = -6.86$ V was possible for the chosen ramping times (see Fig. 5.12). In case the electrodes were ramped in $10 \mu\text{s}$ the start direction of the ions got relevant. For this setting $1/\nu_z$ is $1.7 \mu\text{s}$ being in the same order of magnitude as the ramping time. In general, ramping times smaller $100 \mu\text{s}$ should be avoided.

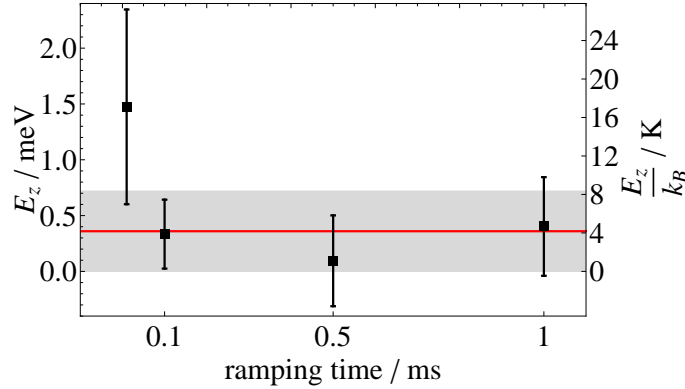


Figure 5.12: Axial energy gain of ions with charge-to-mass ratio of $0.25 e/u$ depending on the ramping time of the voltage of one electrode. The total transport cycle thus took four times the ramping time shown here. The ions started in $+z$ -direction. The first point on the left is for a ramping time of one electrode of $10 \mu\text{s}$. For this setting the ions gain a factor 4 more energy in axial direction and the energy distribution is broadened by a factor 2.5. Since $1/\nu_z$ is here $1.7 \mu\text{s}$, ramping times lower $100 \mu\text{s}$ should be avoided. The red line and the gray shaded area represent the mean energy and the standard deviation of the energy distribution at start. The values shown here are obtained by a fit to the energy distribution in the final state and the error bars represent the standard deviation σ of the fit. The errors of E_z and σ are estimated to be at least 25%, due to the reasons explained in the text.

5.4.3 Introduction of imperfections

So far an ideal situation of the potentials, especially of the supply voltages has been considered. In reality the axes of the magnetic and the electrostatic field can be tilted relative to each other. The case of patch potentials cannot be checked with SIMION[®]. The ramping voltages show noise due to the voltage source and they cannot be changed in an infinitely short time due to filtering of the trap voltages. Moreover, the ramping profile was assumed so far to raise and fall linear. Experimentally the shape is, however, characterized by the shape of trap voltage filter responses which is $V_0 \cdot \exp[-t/\tau]$, where τ is the filter time constant.

First, for a ramping time of 1 ms the angle between the electrostatic and the magnetic field was varied to introduce a coupling between magnetic and electrostatic field (see Fig. 5.13). To analyze the effect of different start directions of the ions, the ion distribution was started in positive and negative z -direction, respectively. Simulating one data point took approximately one week, thus higher ramping times were hardly realizable. A tilt was introduced, since in case of an adiabatic transport the ions will follow the electrostatic center of the Penning traps rather than the magnetic field lines, which causes a radial shift of the center of the ion motion. Experimentally, in the worst case some surface potentials can distort the electrostatic potential and in particular shift its center. Thus, the ions might move to a large radial position and get lost on the surface of an electrode. An expected increase of the radial kinetic energy with increasing angle was observed. The energy transfer tends to be higher for ions which started in negative axial direction. This indicates that the final ion distribution was not independent from the initial conditions.

Furthermore, a time uncertainty of the start of each individual electrodes' ramp-

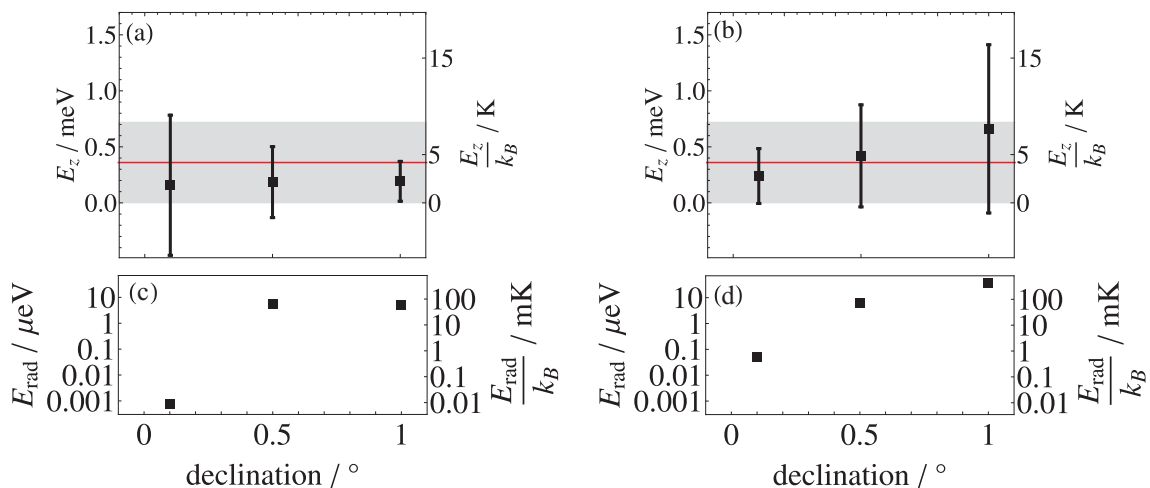


Figure 5.13: Axial and radial energy gain depending on the tilting angle of the Penning trap electrodes with respect to the magnetic field. The axial energy in the second trap for ions starting in $+z$ -direction (a) and for ions starting in $-z$ -direction (b) is shown. The error bars represent the standard deviation of the energy spectrum. In (c) and (d) the radial energy is shown for the two starting directions, respectively. Here, the standard deviation σ of the energy distribution is not shown to have a better overview. It is in the range of the value itself resulting from the fit. The errors of E_z and σ are about 25% (see text).

ing time was introduced (see Tab. 5.2). For example t_0 (see Fig. 5.10) was set to $t_0(1+\delta t/100\cdot\zeta)$, where ζ was a uniformly distributed random variable between one and zero and δt was set to 10. Thus, the ramping of each individual voltage could start in an intervall of $1\text{ ms}_{-0}^{+0.1\text{ms}}$ after the ramping was triggered. The results are shown in Tab. 5.2. The shown error bars represent, as in the previous graphs, the standard deviations of the fitted energy distributions. With the introduced time uncertainty the transport was still possible.

Table 5.2: Results obtained introducing a time uncertainty δt in % of the start and stop times of the applied ramping voltage. θ is the angle between the tilted electric and magnetic field. δt is the percentage of the ramping time which the voltage of each electrode can start maximum later to ramp after the ramping is triggered. For this purpose, uniformly distributed random variables are generated. For the data shown here the ramping of each individual voltage can start in an intervall of $1\text{ ms}_{-0}^{+0.1\text{ms}}$ after the ramping is triggered. Again a distribution of ions starting in positive and negative z -direction is considered. The values shown here are obtained by a fit to the energy distribution in the final state and the given errors represent the standard deviation σ of the fit. The errors of E_z and σ are at least about 25%. For the explanation see text.

start direction	$\theta / ^\circ$	$\delta t / \%$	$E_z \pm \sigma / \text{meV}$	$E_{\text{rad}} \pm \sigma / \mu\text{eV}$
+z	0.1	0	0.16 ± 0.63	< 0.01
		10	0.04 ± 0.04	0.38 ± 0.87
-z	0.1	0	0.24 ± 0.25	0.05 ± 0.06
		10	0.04 ± 0.04	0.03 ± 0.17

5.4.4 Choosing a shallow trap depth

A shallow trap depth of $V_0 = -1\text{ V}$ was chosen, which corresponds to an axial frequency ν_z of 190 kHz. The ramping time of each individual voltage was set again to 1 ms. On the one hand the voltage change per time was here smaller, but on the other hand $1/\nu_z$ was larger than for a trap depth of $V_0 = -10\text{ V}$. The obtained mean axial energy after the transport increased by about a factor 25. Moreover, it is worth mentioning that the transport at a shallow trap depth is more sensitive on patch potentials. Both facts imply the application of a deep potential depth for ion transport. Nevertheless, it should be kept in mind that the total transport time increases for ramping the voltage over a larger range.

5.4.5 Choosing a three-dimensional start distribution

A three-dimensional Gaussian distribution of the start velocities was considered for a thermal temperature of 4.2 K. The distribution was adapted from a Maxwell-Boltzmann distribution analog as it was done in the one-dimensional case. In each spatial direction an energy of $1/2k_B T$ corresponding to 0.18 meV was assumed. For a trap depth of -10 V and a declination angle $\theta = 0.1^\circ$ a mean axial energy of 0.09 meV

with a standard deviation of the energy distribution of 0.10 meV and a mean radial energy of 0.13 meV with a standard deviation of 0.37 meV was obtained after the transport. The values were obtained by fits to the energy distributions and the errors are at least 25%. In the experiment a declination angle smaller $\theta = 0.1^\circ$ will be realized (see Sec. 2.2.2). The energy gain in axial as well as in radial direction did not increase.

In conclusion, everything looks promising for our ion transport, since additional care was taken to minimize patch potentials on the electrode surfaces (see Sec. 7.3). It should be noted that for first basic studies the use of SIMION[®] was adequate. However, it turned out that for more accurate and detailed studies a more powerful program should be used. An alternative would be the use of the program SIMBUCA [156], which is a graphic card based ion trajectory program being a factor 1000-10000 faster than CPU based programs. Unfortunately, there was not enough time within this thesis for further studies.

Chapter 6

Magnetic field investigations

In the following chapter the characterization of the magnetic field at PENTATRAP is addressed. At the beginning of this thesis the whole experimental room in the basement was empty. Only the temperature stabilization facility and the installation of the gas and power supplies were finished. Thus, a task within this work was to assist in the Europe-wide call for tender for our new magnet and after arrival perform measurements in order to characterize the magnetic field. A description of the 7-T magnet was already given in Chap. 4. Here, the first measurements of the magnetic field at PENTATRAP are presented and the design of the dewar dedicated to these measurements is addressed. The effect of the determined magnetic field inhomogeneities on the ion frequencies, the change of the magnetic field due to the magnetization of the trap material itself, as well as the earth's magnetic field in the lab is analyzed.

6.1 The earth's magnetic field and investigations of distortions

In order to present the results in chronological order, the long-term measurement of the vertical earth's magnetic field in the lab is discussed first. At that time the superconducting magnet was not yet delivered. As a fortunate coincidence the Heidelberg-EBIT was not in operation allowing us to carry out measurements, which were not influenced by the fringe field of the superconducting Heidelberg-EBIT magnet. This magnet can produce a maximum magnetic field in the EBIT's trapping volume of 9 T at 2.5 K. Figure 6.1(a) shows the vertical earth magnetic field over several days around Christmas time 2009 measured with a flux-gate magnetometer, which is presented in detail later in Chap. 7. The field decreased during these twelve days by 0.1 μT and day-night fluctuations have been observed. Figure 6.1(b) shows the magnetic field in the magnet room during one night, when there was less environmental interference than during daytime. Here, the absolute variation of the magnetic field was in the order of a few nT.

Additional, elaborate studies of disturbing factors on the magnetic field like, e.g., the Heidelberg-EBIT or the movement of the ceiling crane were performed (see Fig. 6.2). The measurement of the vertical magnetic field in the basement lab during the power-up of the Heidelberg-EBIT showed the sensitivity of PENTATRAP

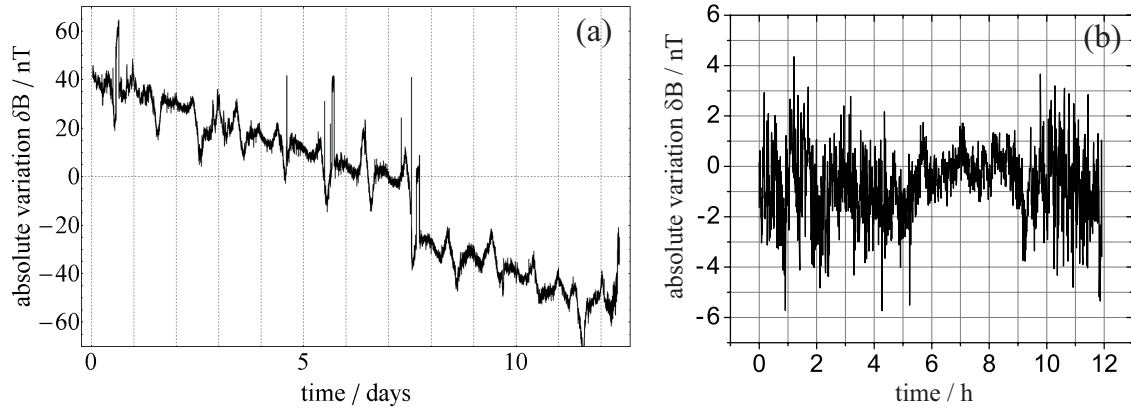


Figure 6.1: (a) Vertical earth magnetic field over several days measured in the laboratory. Day-night fluctuations are clearly visible. (b) Zoom into (a) showing the fluctuations at a single night. In both cases, the field was measured with a fluxgate magnetometer (see Chap. 7.2). For a better overview the errors are not included. They scale with the measured output voltage of the fluxgate sensor. For the values shown in (a) the errors are smaller than 1.5 nT and for the values shown in (b) they are smaller than 0.1 nT.

on the increase and decrease of the current of the superconducting EBIT magnet (see Fig. 6.2(a)). An increase from 0 A to 50 A causes an increase of about $2 \mu\text{T}$ and an increase up to the maximum current of 76.24 A causes an increase of about $3 \mu\text{T}$. Considering a screening factor of approximately 100 of our magnet, still 30 nT and thus a relative magnetic field increase $\Delta B/B$ of about $4 \cdot 10^{-9}$ results in the Penning traps. In the future, when high-precision mass measurements on ions delivered from the Heidelberg-EBIT will be carried out, this is of no concern, since then the Heidelberg-EBIT settings remain fixed during a measurement cycle. In the meantime, when we plan to perform measurements with ions delivered from the small Dresden-EBIT3, care should be taken that PENTATRAP is not disturbed by these comparably large magnetic field jumps. A fluxgate stabilization system is ready to be installed to compensate the vertical component of low-frequency magnetic field disturbances. Therefore, a control system based on a flux-gate magnetometer and a pair of Helmholtz coils positioned around the magnet was built up (see Chap. 7.2). In Fig. 6.2(b) other environmental influences, such as the movement of the 25 t and 10 t bridge cranes, the roof of the EBIT lab and the elevator in the building are shown. The biggest disturbance with $0.2 \mu\text{T}$ is caused by the movement of the 25 t heavy duty bridge crane inside the building above the Penning-trap laboratory.

6.2 The homogeneous magnetic field region

Knowledge of the magnetic field in the five trap regions is of fundamental interest, since magnetic field imperfections influence the ion's motion. The motional frequencies get energy dependent, which results in frequency shifts and broadened detection signals. In the starting phase of the experimental setup stored ions were

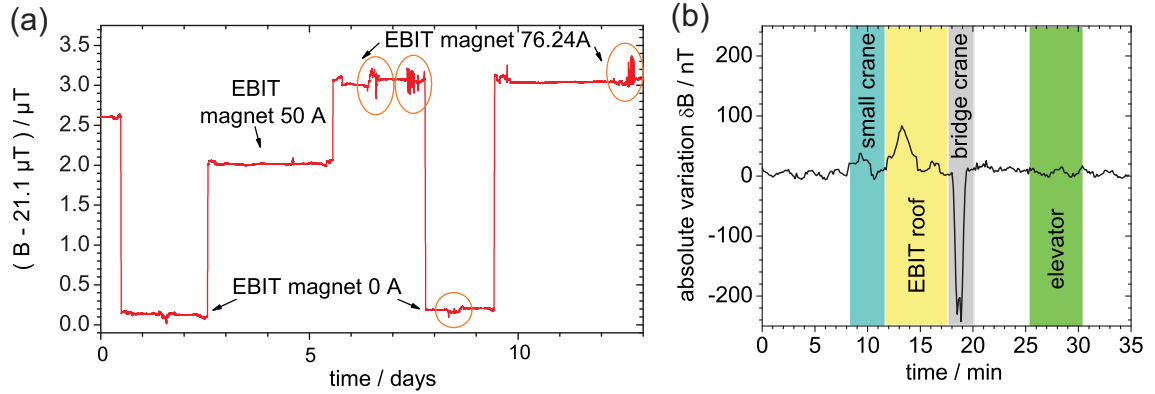


Figure 6.2: (a) Influence of the Heidelberg-EBIT magnet on the vertical magnetic field measured in the PENTATRAP lab. Depending on the current running through the superconducting coils of the EBIT's magnet, the additional magnetic field is in the order of 2-3 μT . In the encircled areas high voltage tests were performed at the Heidelberg-EBIT. (b) Examination of environmental influences, such as the movement of several cranes, the roof of the EBIT lab, and the elevator in the building during a standard working day. The fields were measured with a fluxgate sensor. For a better overview the errors are not included. The errors of the absolute magnetic values shown in (a) are in the order of 1 μT . For the absolute variation δB shown in (b) the errors are below 5 nT.

not available to examine the magnetic field of the Penning traps via a frequency measurement of the stored ion. Therefore, a Nuclear Magnetic Resonance (NMR) probe was used for the field measurements in the homogeneous central magnet region. Our probe (model number 8 of the teslameter *PT2025* from *Metrolab*) [157] comprises a small glass tube with an active sample volume with a diameter of 4 mm and a length of 4.5 mm filled with D_2O . The detection principle is based on the detection of induced transitions between the energy levels of the nuclei in the static magnetic field. To induce the transitions an alternating magnetic field is applied perpendicular to the static magnetic field via a flat modulation coil wound around the glass tube. Moreover, this coil is part of an LC circuit which is coupled to an rf amplifier. The modulation frequency is varied. In case the coil is driven to its resonance frequency the deuterons continuously absorb energy from the alternating field, since transitions from lower to higher states are more frequent and the thermal equilibrium populations re-establish. Thus, the Q -value of the coil is slightly reduced. Every time the frequency is close to the nuclear resonance frequency associated with the static magnetic field, an absorption signal appears in the resonance circuit.

6.2.1 The warm-bore device for NMR measurements

Since the NMR probe employs a small deuterium filled volume to carry out the field measurement, the probe must be held at temperatures above 273.15 K. Therefore, a dewar was built which is put into the cold-bore of the magnet and provides inside a temperature of about 300 K and a standard pressure of 1 bar (see Fig. 6.3). In the following this setup it is referred to as 'warm-bore' system. It is realized by

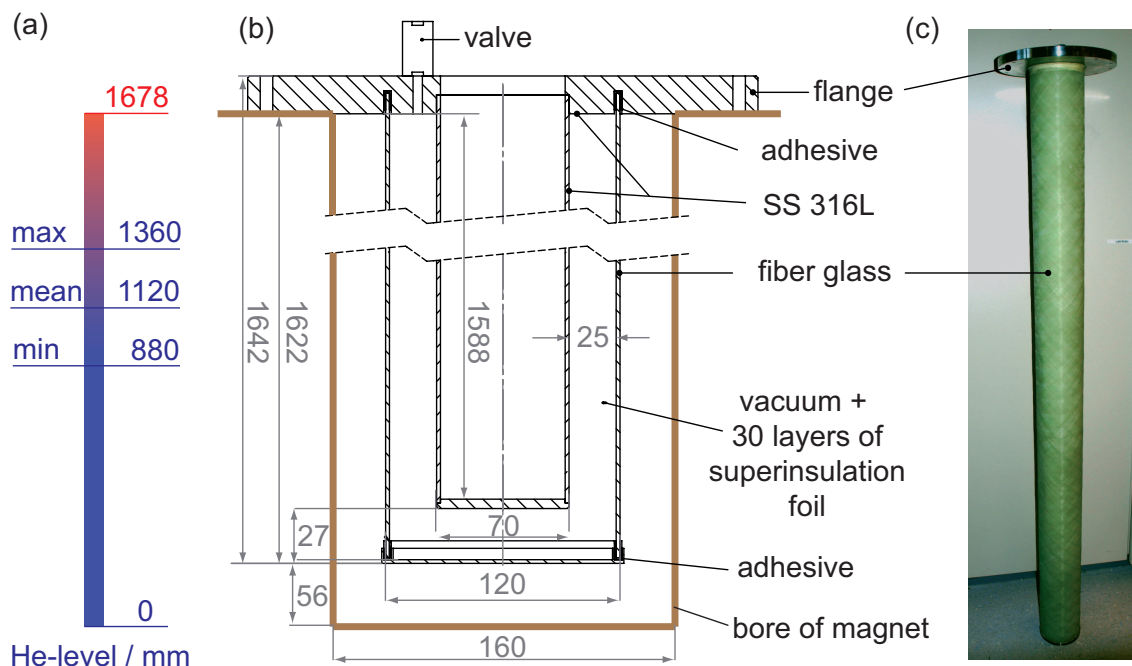


Figure 6.3: (a) Liquid helium level in the cold-bore of the magnet. (b) Technical drawing of the fiber glass epoxy dewar used for the NMR measurements. The double-walled tube consists of an inner stainless steel tube and an outer fiber glass epoxy tube, in order to minimize the heat transport from 4 K to 300 K. In the volume between these tubes 30 layers of superinsulation are placed in the vacuum to reduce the heat load by thermal radiation. (c) Photograph of the assembled device. Dimensions are given in mm.

a double-walled tube with an inner stainless steel (316L) and an outer fiber glass epoxy tube providing low thermal conductivity. The space between the tubes is pumped and 30 layers of superinsulation foil are wrapped around the inner tube in a proper way to minimize radiation heat transfer. The superinsulation foil *Coolcat 2* from *RUAG space* consists of ten layers of double sized aluminized and perforated polyester films interleaved with polyester spacers. The fiber glass tube is from *CG TEC GmbH* and is made out of Glasroving with epoxy resin, a winding angle of $\pm 45^\circ$ and an additional mat of fibers inside for a leak-proof device. A similar trademark produced in the US is called G10. First the epoxy *EP21TCHT-1* from *Master Bond Inc.* was used as adhesive. This adhesive characterized through high thermal conductivity was directly available at our institute. However, it turned out that the device was not vacuum tight using this probably not flexible enough epoxy. In case the contraction rates at cryogenic temperatures are dissimilar, the adhesive area can become stressed on a cool down process and can crack. The difference of radial contraction of glass fiber and stainless steel is estimated to be in the order of 0.1 mm. Afterwards, the epoxy *2850KT* from *Stycast, Catalyst 9* was used and the glued surface was enlarged. Before the adhesive joint was made, a full detergent clean to remove any traces of grease and pollutants was carried out. These improvements finally lead to a leak-proof device under cryogenic conditions. It is recommended that the tube is put dehumidified into the magnet, since an absorption of humidity of the fiber glass tube will take place, which will stress the material by a cool-down

process.

An estimation of the heat load is indispensable, in order to determine the heat power dissipated by the dewar and the resulting helium consumption. Three mechanisms must be taken into account:

1. The thermal conduction along the tube from 4 K to 300 K.
2. The thermal radiation between the two cylinders.
3. The cooling of the tube by the evaporating helium.

The thermal heat conduction \dot{Q}_C can be calculated as (see textbook e.g. [158])

$$\dot{Q}_C = \frac{A}{L} \int_{4K}^{300K} \lambda(T) dT, \quad (6.1)$$

where $\lambda(T)$ is the temperature-dependent thermal conductivity, L the length from the mean helium level to the upper magnet flange and A the cross-section area of the fiber glass tube material. See Fig. 4.6 in Sec. 4.4 for a plot of the thermal conductivity of the glass fiber epoxy G10. The integral is solved using the fit equation given in [143] leading to a thermal conductivity of 0.61 W. In case the minimum and maximum helium levels are considered, 0.43 W and 1.1 W are obtained, respectively. The volume current I_V of the vaporized helium per added heat power is given as

$$I_V = \frac{1}{\rho(T)} \frac{\Delta m_{\text{He}}}{\Delta t} = \frac{1}{\rho(T)} \frac{\dot{Q}}{H(T)}. \quad (6.2)$$

Thereby, it is neglected that with a falling helium level the geometrical distances between the warm and the cold end and therewith over Eq. (6.1) the heat conduction is changed. The latent heat of vaporization of liquid ^4He at 4.2 K is given as $H(T) = 20.78 \text{ J/g}$, and the density of liquid ^4He at 4.2 K at the saturated vapor pressure is given as $\rho(T) = 0.105 \text{ g/cm}^3$. Both values are taken from [159]. With Eq. (6.2) the amount of liters of vaporized helium per day η

$$\eta = 4.58 \cdot 10^{-4} \left[\frac{\text{m}^3}{\text{s} \cdot \text{W}} \right] \cdot \dot{Q} [\text{W}] = 39.6 \left[\frac{1}{\text{d} \cdot \text{W}} \right] \cdot \dot{Q} [\text{W}], \quad (6.3)$$

and the percentage of the vaporized helium refill volume of the magnet per day $\tilde{\eta}$

$$\tilde{\eta} = 17.2 \left[\frac{\% \text{He}}{\text{d} \cdot \text{W}} \right] \cdot \dot{Q} [\text{W}] \quad (6.4)$$

can be calculated. Here, units which are convenient in the daily lab routine are used. Finally, for an added heat power of 0.61 W a helium consumption of 24.31/d or a loss of 10.5 % of the helium refill volume per day is obtained.

The heat transfer by thermal radiation between the stainless steel and the fiber glass epoxy tube can be calculated by [141]

$$\dot{Q}_R = \sigma \cdot \frac{A_1}{\frac{1}{\epsilon_1} + \frac{A_1}{A_2} \left(\frac{1}{\epsilon_2} - 1 \right)} (T_2^4 - T_1^4), \quad (6.5)$$

assuming long and concentric cylinders with lengths much longer than their diameters. Here, σ is the Stefan-Boltzmann constant, A_1 and A_2 are the surfaces of temperature T_1 and T_2 , respectively. ϵ_1 and ϵ_2 are the emissivities of the two bodies given as (for a derivation see, e.g., [160])

$$\epsilon \approx \sqrt{\frac{16\pi\epsilon_0 c}{\sigma_0 \lambda}}, \quad (6.6)$$

where ϵ_0 is the permittivity of the vacuum and c the speed of light. σ_0 is the electrical conductivity which can be calculated via the Wiedemann-Franz-Lorenz law [161] from the thermal conductivity [143]. λ is the wave length of the thermal radiation, which is according to Wien's displacement law $9.7\ \mu\text{m}$ at $300\ \text{K}$ and $690.0\ \mu\text{m}$ at $4.2\ \text{K}$. For \dot{Q}_R a value of $1.19\ \text{W}$ is obtained resulting in a helium consumption of $47.1\ \text{l/d}$ or a loss of $20.5\ \%$ of the helium refill volume per day.

So far the effect of the radiation shields, which reduce the amount of the transferred thermal radiation, is not considered. To give an estimation Eq. (6.5) is multiplied by a factor $1/(N+1)$, where N is the number of superinsulation layers [141]. Thus, the thermal radiation is reduced to $0.04\ \text{W}$, and the helium consumption is $1.6\ \text{l/d}$ or $0.7\ \%$ He per day provided that the quality of the vacuum between the two tubes is sufficient and the aluminized layers of the superinsulation are not in direct contact with each other.

Whereas the thermal conduction along the tube and the thermal radiation between the two cylinders can be estimated straightforward, the description of the cooling of the fiber glass epoxy tube by the evaporating helium is more complicated. The heat load on the liquid helium bath causes the helium to evaporate and to transport the released energy away. At the lower part of the bore the helium gas is considered to be colder than the fiber glass tube. It follows that the tube is pre-cooled, which will cause in turn a change of the heat load due to thermal conduction and radiation. The changing heat load again will affect the amount of evaporating helium. As can be seen, the whole process has to be computed iteratively. Moreover, the thermal conduction at the contact of the gas and the solid state body has to be accounted for. Furthermore, the helium is pushed during the lowering of the tube into the outer reservoir of the magnet (see Fig. 4.3). This will cause a permanent increase of the helium level in the first hours in case the pressure in the magnet's main bore is relieved over a pressure relief valve allowing the helium to slowly flow back.

The warm-bore was first tested in a liquid nitrogen dewar. A pressure of $7 \cdot 10^{-5}$ mbar was reached and the temperature inside the warm-bore was recorded (see Fig. 6.4). After 18 hours the temperature decreased below $5\ ^\circ\text{C}$ denoting the time intervall in which NMR measurements can be performed. Later in the cold-bore of the magnet the temperature decrease was much faster limiting the measurement time to only 3-5 hours. During a first test the helium consumption was $10.6\ \text{l/d}$. The helium consumption was lower than the expected value of $\dot{Q}_{\text{total}} = \dot{Q}_C + \dot{Q}_R = 25.9\ \text{l/d}$. It should be kept in mind that the pre-cooling due to evaporating helium was not considered in this value. However, during the first measurement run the helium consumption increased ($66.9\ \text{l/d}$) and an even larger consumption was observed during the second measurement run ($123.31\ \text{l/d}$). This might be explained by a vacuum leak at $4.2\ \text{K}$

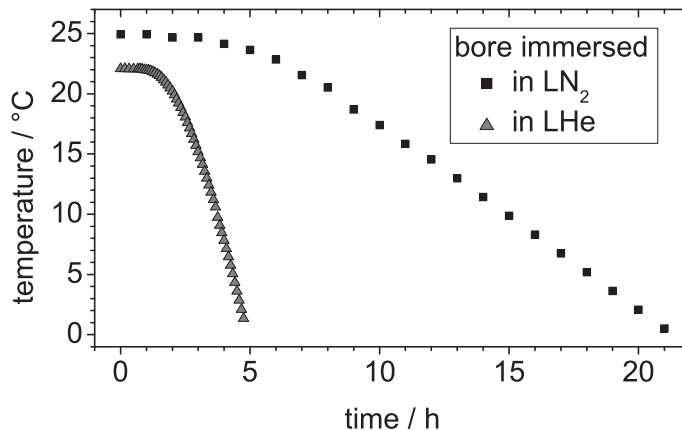


Figure 6.4: Temperature decrease inside the warm-bore. At the first test measurement with the bore immersed into liquid nitrogen a start pressure of $3 \cdot 10^{-4}$ mbar was reached after pumping the device over night. After cooling the bore down in a liquid nitrogen dewar, the pressure decreased to $7 \cdot 10^{-5}$ mbar. The error bars are too small to be visible in this graph. For discussion see text.

(probably at the adhesive joint) destroying the effectiveness of the superinsulation. Moreover, at the later cool-downs the temperature decrease inside the warm-bore was even larger than it was at the first cool-down. The fast cool-down inside the warm-bore hampers us to carry out long-time measurements to study the temporal magnetic field stability. The temperature dependence of the NMR probe's accuracy is given as $0.05 \text{ ppm}/^\circ\text{C}$, which causes shift of about 0.75 ppm for the temperature change of 15°C during our measurement.

In case a new NMR measurement is required, it might be considered to change the design of the warm-bore device. The position of the glued joint should be changed to a more favorable location above the liquid helium level to prevent a direct 'shock' by the cool-down process. However, this of course has the disadvantage that the heat transfer through a longer stainless steel tube would be higher. Another design would be therefore to completely avoid the use of fiber glass and to implement a bellow below the flange and artificially enlarge the way for the heat transport. Furthermore, aluminum should be used instead of stainless steel to obtain a lower magnetic susceptibility of the apparatus. It should be mentioned that the company carried out their measurements with a double-walled stainless steel tube. Thereby, the bore of the magnet was at cryogenic temperatures, but not filled with liquid helium (see Fig. 4.3). Avoiding glass fiber in the design would be advantageous as well, since fiber glass shows a temperature dependence of the magnetic susceptibility at cryogenic temperatures. On the accuracy level of the performed NMR measurement this temperature dependence however should not be critical.

6.2.2 Measurement of the magnetic field on-axis

For the magnetic field measurements in the homogeneous central region of the superconducting magnet, an NMR teslameter *PT2025* from *Metrolab* was used [162]. Magnetic field measurements on-axis were performed as long as the NMR-probe locked, i.e. as long as the magnetic field gradient is smaller than $0.5 \text{ ppm}/\text{mm}$, which

is the required homogeneity for the probe model number 8 in use [157]. The result of this measurement and, for comparison, the data provided by the magnets supplier after installation are shown in Fig. 6.5. The discrepancy between the measured data and the specified data motivated us to perform a second measurement. As can be seen by means of Fig. 6.5 none of our two measurements is consistent with the seven points measured by the supplier. A measurement of more data points by the supplier would have been preferable to carry out a more meaningful comparison. The deviation of our measurements at the outer edges is due to the fact that not exactly the same z -positions could be found in the two runs. A little variation in the probe position causes a difference in the magnetic field value due to the given inhomogeneity. The positioning of the probe can be realized with an estimated uncertainty of 0.5 mm in all spatial directions and the error in the determination of the magnetic field is 1 μ T.

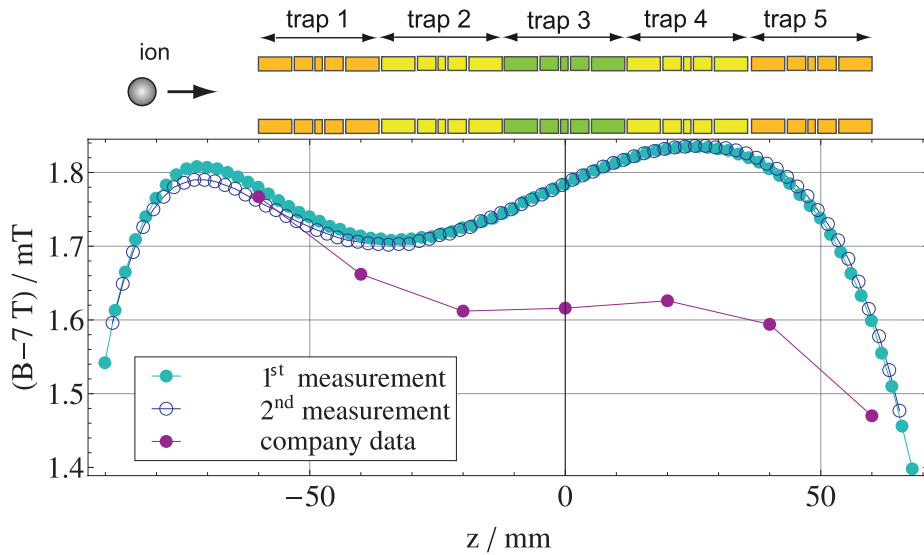


Figure 6.5: Magnetic field amplitude as a function of the distance from the magnet's center measured with an NMR-probe. The field values were measured twice and as long as the magnetic field gradient was small enough for the use of the NMR-probe. The data provided by the magnet's supplier after installation is shown in comparison and the locations of the Penning traps are sketched at the top. The error bars are smaller than the point size.

At the start of both measurements, before the warm-bore was inserted into the cryostat, the helium level was at 80 %. Thus, systematic uncertainties due to different levels and resulting different temperature trend along the fiber glass tube, which cause different magnetic susceptibilities of the materials, are omitted. The nitrogen levels during both measurements were at a level of about 45 % and 80 %, respectively.

6.2.3 Influence of the determined magnetic field inhomogeneities on the eigenfrequencies

As discussed in Sec. 2.2.2 field imperfections cause the motional frequencies to get energy dependent. First, the non-secular distortion due to B_1 is regarded. The

magnetic moment due to the radial motion of the ion depends on the reduced cyclotron energy E_+ and couples to the magnetic field gradient B_1 . As a consequence the mean position of the ion in axial direction is shifted. Since the net force in axial direction caused by the magnetic field gradient must be compensated by the electrostatic field gradient the shift in axial direction Δz is given as [163]

$$\Delta z = -\frac{B_1}{C_2} \cdot \frac{1}{2mV_0\omega_+} \cdot E_+. \quad (6.7)$$

Thus, the mean magnetic field experienced by the ion is changed and consequently ω_+ . The modified cyclotron frequency is depending on E_+ and the shift is given as [163]

$$\frac{\Delta\omega_+}{\omega_+} \simeq -\frac{1}{m\omega_z^2} \left(\frac{B_1}{B_0}\right)^2 E_+. \quad (6.8)$$

Furthermore, the ion will see a mean magnetic field depending on the axial energy owing to the B_2 term. Thus, a shift of ω_+ depending on E_z results. Moreover, a linear z -dependent force will occur due to a coupling of the magnetic moment caused by the radial ion motion to the magnetic bottle. This force adds to the electrostatic force from the trapping potential. Thus, the axial frequency shifts by

$$\frac{\Delta\omega_z}{\omega_z} \simeq \frac{B_2}{B_0} \frac{1}{m\omega_z^2} E_+. \quad (6.9)$$

For the multipole expansion of the magnetic field see Eq. (2.20). Additionally, as a result of the different magnetic field at the changed cyclotron radius the modified cyclotron frequency is shifted again. Thus, the total shift is given as

$$\frac{\Delta\omega_+}{\omega_+} \simeq \frac{B_2}{B_0} \frac{1}{m\omega_z^2} \left(-\left(\frac{\omega_z}{\omega_+}\right)^2 E_+ + E_z \right). \quad (6.10)$$

Both Eq. (6.9) and (6.10) neglect the small contribution due to the magnetron energy since the magnetron energy is commonly much smaller than the axial and modified cyclotron energies. For the complete expression of the frequency shifts of all three eigenfrequencies see Eq. (2.21). Terms higher than B_2 cause frequency shifts with non-linear energy dependence, especially B_4 leads to a small change in the tuning ratio [163].

Considering the foregoing the magnetic field values in the trap regions are fitted in order to determine the B_0 , B_1 and B_2 coefficients and, thus, the energy dependent frequency shifts. To this end, a third order Polynomial fit is used to fit the magnetic field in the trap regions in an interval $z = \pm 12$ mm. The results are listed in Tab. 6.1.

The energies in the different ion modes, which depend on the measurement method, influence the shift of the eigenfrequencies. First the mean value of both measurements is taken to calculate the resulting frequency shift of ω_c (see Fig. 6.6) for a bolometric detection of ω_+ using the axial double-dip detection technique. In this case the radial energy is connected via Eq. (2.29) and Eq. (2.30) to the thermal axial energy. With Eq. (6.9) and Eq. (6.10) neglecting the small contribution of the magnetron frequency and energy the shift of ω_c is dominated by the $\Delta\omega_+$ shift due to E_z , resulting in [164]

$$\frac{\Delta\omega_c}{\omega_c} \simeq \frac{B_2}{B_0} \frac{1}{m\omega_z^2} \langle E_z \rangle. \quad (6.11)$$

Table 6.1: Obtained fit parameters for a third order polynomial fit to the magnetic field in the five trap regions shown in Fig. 6.5. Additionally, the parameters obtained for a fit of the magnetic field minimum are given. The errors are the standard errors from the fit.

location	run	B_0	$B_1/\frac{\mu\text{T}}{\text{mm}}$	$B_2/\frac{\text{nT}}{\text{mm}^2}$
trap 1	1	7.0017332(3)	-3.059(51)	60.0(11.0)
	2	7.0017202(2)	-2.727(46)	91.2(10.2)
trap 2	1	7.0017170(4)	1.616(65)	58.2(14.1)
	2	7.0017149(6)	1.972(136)	35.3(33.6)
trap 3	1	7.0017849(3)	3.088(61)	-7.0(13.1)
	2	7.0017850(0)	3.238(66)	-16.3(16.3)
trap 4	1	7.0018350(2)	2.138(344)	-109.7(6.4)
	2	7.0018355(2)	3.751(359)	-93.6(8.3)
trap 5	1	7.0017546(4)	-8.584(72)	-331.0(15.6)
	2	7.0017618(5)	-8.132(100)	-277.5(23.1)
minimum	1	7.0017088(3)	-0.006(59)	95.6(10.6)
	2	7.0017020(4)	0.088(90)	136.3(19.8)

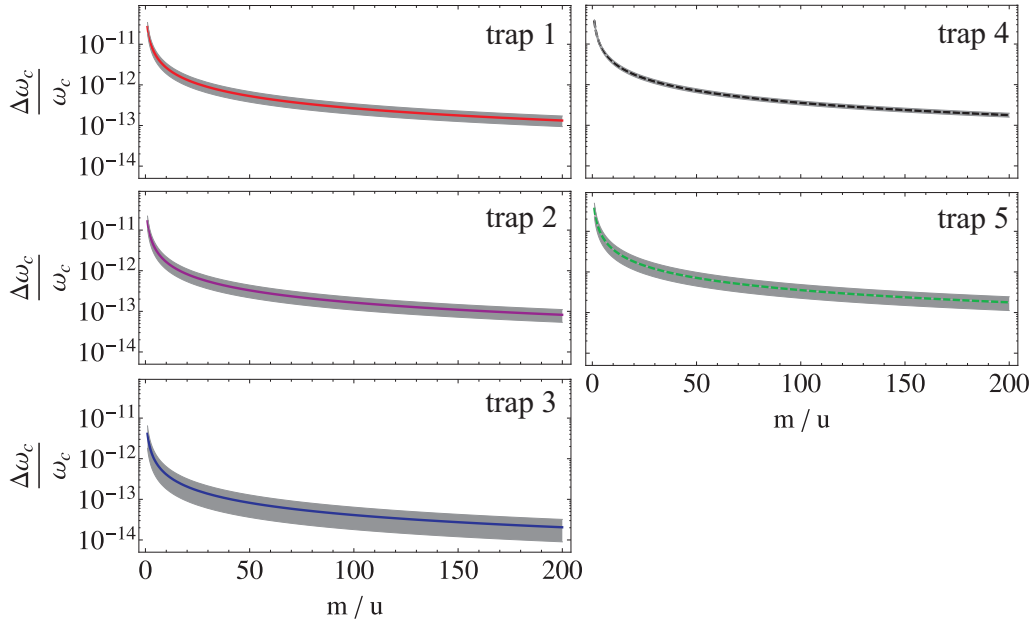


Figure 6.6: Dependence of the absolute value of the frequency shift $\Delta\omega_c/\omega_c$ on the ion mass due to the magnetic bottle term B_2 in each of the five traps for a bolometric detection of ω_+ at $\langle E_z \rangle = 4.2$ K using the axial double-dip technique (see Eq. 6.11). An axial frequency of $\omega_z = 2\pi \cdot 600$ kHz is considered. For a fixed $\langle E_z \rangle$ and ω_z the axial radius is directly connected to the mass of the ion: $\langle E_z \rangle = 1/2 \cdot m \omega_z^2 \rho_z^2$. The gray bands are the error bands resulting from the fit to the measured data (see Tab. 6.1). For a better overview, the expected thermal energy fluctuations are not included in the graph.

For the five traps the dependence of $\Delta\omega_c/\omega_c$ on the axial radius ρ_z considering an axial frequency of 600 kHz is shown in Fig. 6.6. For the whole mass range, the shift in each trap is below 10^{-11} . For heavy ions associated with a small axial radius the shift decreases, thus, for $^{187}\text{Re}^{47+}$ the thermal axial radius is about 5 μm and the shift in the central trap is only $2.2(3.4)\cdot 10^{-14}$. To illustrate the small contribution of B_1 to the modified cyclotron frequency shift compared to the contribution of B_2 , both shifts are calculated according to Eq. (6.8) and Eq. (6.10) for each trap and a bolometric detection (see Fig. 6.7).

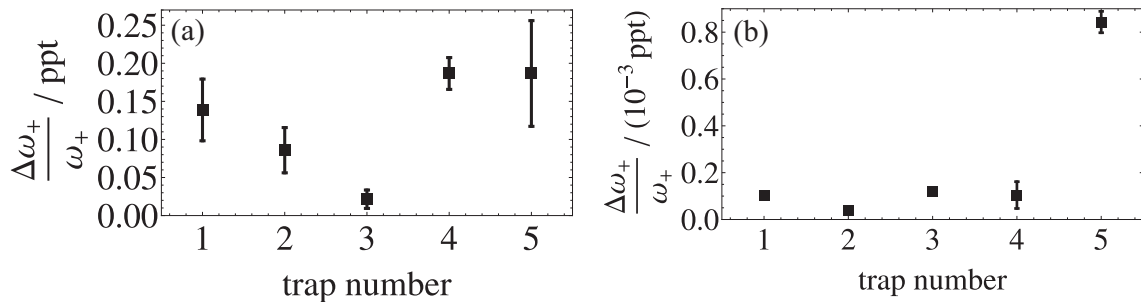


Figure 6.7: Absolute value of the frequency shift of ω_+ due to B_2 (a) and B_1 (b) for the double-dip technique. Both shifts are calculated according to Eq. (6.8) and Eq. (6.10) for a $^{187}\text{Re}^{47+}$ ion and an axial detector working at $\omega_z = 2\pi \cdot 600$ kHz and a temperature of 4.2 K. The errors are resulting from the fit to the measured data (see Tab. 6.1).

Ultimately, we plan to perform the measurement of ω_+ via the PNA method (see Sec. 2.4). This method is faster than the double-dip technique and therefore less sensitive to magnetic and electric field fluctuations. Secondly, it allows to carry out cyclotron measurements with substantially smaller cyclotron amplitudes than the PNP method reducing the energy-dependent systematic shift due to the B_2 term. At the start of a measurement cycle the cyclotron mode is directly cooled via the cyclotron tank circuit. Thus, e.g., for $^{187}\text{Re}^{47+}$ the temperature T_+ can be reduced from around 190 K for an indirect cooling via the axial tank circuit as applied in the double-dip method to around 4.2 K. The cooling is necessary, since the initial cyclotron energy defines the required excitation energy of the rf pulse which is applied to define the starting phase. For our example of a $^{187}\text{Re}^{47+}$ ion ρ_+ at $T_+ = 4.2$ K is 0.11 μm . To realize a phase resolution of 10° the ion should be excited to only 0.65 μm . This would be below the value of $\rho_+ = 0.76$ μm for an indirect axial sideband cooling of ν_+ and far below the amplitude needed for the PNP method. Comparing the radius of 0.11 μm with the one of 0.76 μm at the axial double-dip method shows that thermal fluctuations are reduced. Considering for the PNA method a thermal axial energy, the resulting shift of ω_+ due to B_2 (Eq. (6.10)), which is dominated by the contribution of the axial energy, is nearly the same as for bolometric detection at a thermal axial energy (see Fig. 6.7(a)). An advantage of the PNA method is that feedback cooling can be applied to further decrease the axial energy without any restrictions in the signal-to-noise ratio.

A low-charged ion such as $^4\text{He}^+$ having the same charge-to-mass-ratio should be excited to 4.44 μm employing the PNA method and considering a phase resolution of 10° . This again emphasizes the advantage of highly-charged ions, since lower ampli-

tudes are needed which reduces the distortion due to magnetic field inhomogeneities. Compared to Fig. 6.7(a) $\Delta\omega_+/\omega_+$ is here in the range of (1-12) ppt considering a thermal axial energy.

The benefit of the PNA method is that smaller line widths are obtained and the statistical noise is reduced. At a bolometric detection the lineshape is limited by thermal fluctuations of the ion when coupled to the thermal bath of the detector. In contrast, with the PNA method phase fluctuations of the starting phase lead to fluctuations of the ion's radius. Since we plan to perform mass-ratio measurements, frequency shifts, which did not depend on radius fluctuations, would ideally cancel out assuming the same magnetic field behavior in each trap.

6.2.4 Examination of the spatial homogeneity

For the determination of the spatial homogeneity in a cylindrical volume including all five traps several circles with a radius of 2.5 mm were probed at different positions along the z -axis and the magnetic field values were measured with the NMR-probe in 30° steps (see Fig. 6.8). The difference of the maximum and minimum magnetic field value in the measured cylinder volume is divided by the mean value of the measured values on-axis to calculate the spatial homogeneity $\Delta B/B$. Due to the fact that the probe failed to lock in the boundary area, the measurement was carried out for consistency twice. In a volume comprising the inner three Penning traps $\Delta B/B$ is determined to be $<25(1)$ ppm at the first and $<24(1)$ ppm at the second

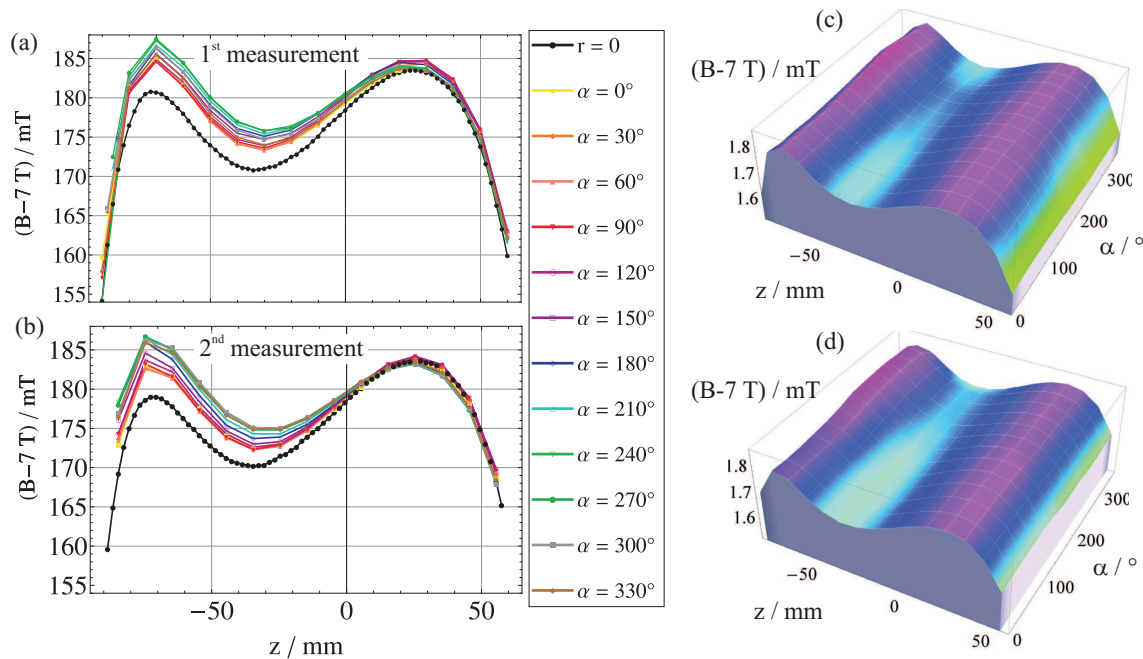


Figure 6.8: Magnetic field values measured in a cylinder with radius 2.5 mm and length 120 mm comprising the five Penning traps. The NMR probe failed to lock for points at the edge of the boundary area. Therefore, the spatial homogeneity considering the length of the three inner traps is determined to 25(1) ppm for the first (a) and 24(1) ppm for the second measurement (b). In (c) and (d) the corresponding three dimensional plots of the data are shown to provide a better visualization.

measurement.

The magnetic field was additionally probed at circles with a radius of 5 mm at different positions along the z -axis (see, e.g., Fig. 6.9(a)). In the central 1 cm^3 volume the spatial homogeneity of the magnetic field $\Delta B/B$ is determined to $<7(1)$ ppm, which is significantly larger than the value of 0.7 ppm specified by the supplier in the quotation. Compared to this volume the ions' oscillation amplitudes are much smaller and will not exceed a few ten μm [87]. Thus, the spacial homogeneity seen by the ions is much smaller than 7 ppm. It was checked, if a shift of the center of the third Penning trap to the minimum of the magnetic field would result in a lower spatial homogeneity in the central 1 cm^3 volume. A homogeneity of $\Delta B/B < 6(1)$ ppm would be obtained, which lies within the errors of the previously determined homogeneity. The values used to calculate this value are illustrated in a three-dimensional plot in Fig. 6.9(b).

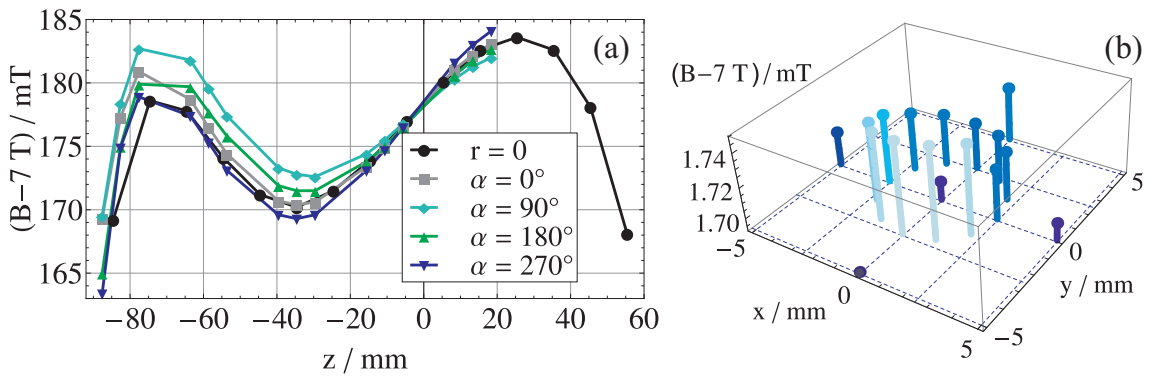


Figure 6.9: (a) Spatial homogeneity in a cylinder with radius 5 mm comprising the Penning traps. (b) Three-dimensional representation of the data used to calculate $\Delta B/B$ in a 1 cm^3 volume at the minimum of the magnetic field on-axis.

6.2.5 Magnetization of the trap materials

Not only the inhomogeneous field of the magnet itself but also the magnetization of the used trap materials cause a change of the magnetic field and thus will affect the eigenfrequencies of the stored ions. Choosing appropriate materials the effect can be minimized. The perturbation of the magnetic field, which is given in Eq. (2.20), depends on the coefficients B_l (see also Sec. 4.4). The program Suszi [165] calculates these coefficients to obtain the perturbation (see also Chap. 4). Therefore, the magnetic susceptibilities of the used materials must be provided. The value of OFHC copper having 99.999% purity at 4.2 K is taken from [141] and is $-8.67 \cdot 10^{-6}$ (in SI units the magnetic susceptibilities is dimensionless). The value of sapphire depends on the crystallographic axis (c -axis), here the higher value for a orientation perpendicular to the c -axis is chosen ($0.25 \cdot 10^{-6}$) [142]. A polynomial of third order is fitted to the data in the range ± 2.5 mm. A B_2 term of $B_2 = 19.39(4)\text{ nT/mm}^2$ is obtained (see Fig. 6.10). The value is in the same order of magnitude than the B_2 value obtained in Sec. 6.2.3 for the central trap (see Tab. 6.1). Since the outer traps will experience an asymmetrical modification of the magnetic field a future task would be to simulate the magnetization of the complete trap stack and the adjacent support structure with a more powerful and faster program like, e.g., COMSOL[®].

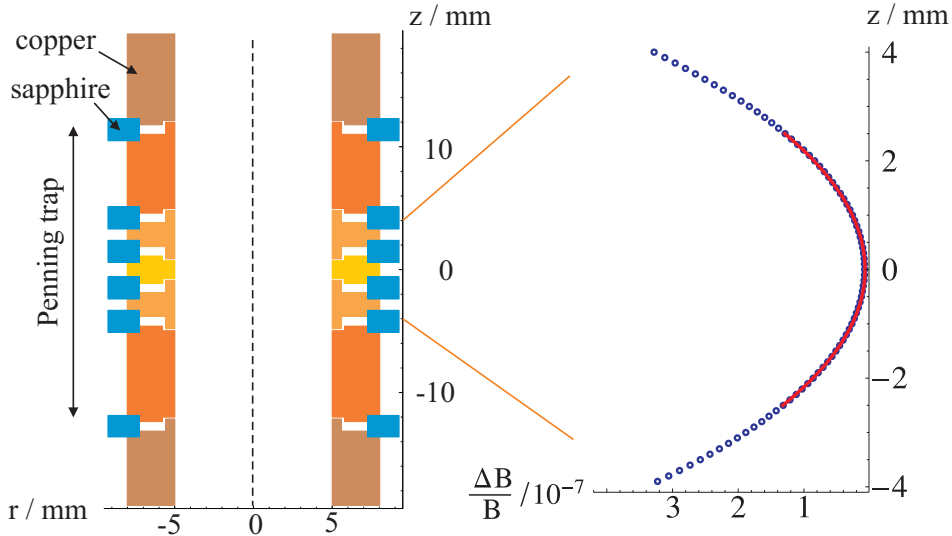


Figure 6.10: On the left the trap geometry used for the simulation of the magnetic field change inside the trapping volume due to a magnetization of the trap material itself is shown. The program Suszi [165] is utilized to calculate the additional field on the z -axis, which is the magnetic field axis. The fitted values are shown on the right yielding $B_2 = 19.39(4) \text{ nT/mm}^2$. The red curve is the polynomial fit of third order to the simulated data in the range $\pm 2.5 \text{ mm}$.

6.3 Magnetic field measurements outside the Penning trap

The magnetic field on axis through the magnet's bore is measured with the Hall probe *STF71-1808-05-T* and the associated Teslameter *7010* from *Sypris Bell*. The measured values together with the data provided by the supplier are shown in Fig. 6.11. The field profile is of interest to determine the magnetic field gradient and strength. This knowledge is necessary for the ion transport and for the location and the design of the electronics, for example to design a magnetic shielding of a planned SQUID detector [166] or to determine the influence of the magnetic field on the quality factor of the superconducting rf resonators [79]. The field on the z -axis of the magnet can be described by a Helmholtz coil pair model as a superposition of the field created by j coils at positions p_i , with lengths l_i and radii r . For the following fit it was sufficient to choose a fixed radius r , but in general it can be varied as well. The number of windings N_i , the currents running through the coils I_i and the vacuum permeability μ_0 are linked with the variables k_i via $k_i = \mu_0/2 \cdot I_i N_i$. Consequently the magnetic field B_z^{Hcoil} can be expressed as summation of the fields of Helmholtz coils being spaced by r

$$B_z^{\text{Hcoil}} = \sum_{i=1}^j \left(B_z^{\text{coil}}\left(z + p_i + \frac{r}{2}, r, l_i, k_i\right) + B_z^{\text{coil}}\left(z + p_i - \frac{r}{2}, r, l_i, k_i\right) \right). \quad (6.12)$$

Here, the field created by a single cylindrical coil is

$$B_z^{\text{coil}}(\tilde{z}, r, l, k) = \frac{k}{l} \left[\frac{\frac{l}{2} - \tilde{z}}{\sqrt{\left(\frac{l}{2} - \tilde{z}\right)^2 + r^2}} + \frac{\frac{l}{2} + \tilde{z}}{\sqrt{\left(\frac{l}{2} + \tilde{z}\right)^2 + r^2}} \right]. \quad (6.13)$$

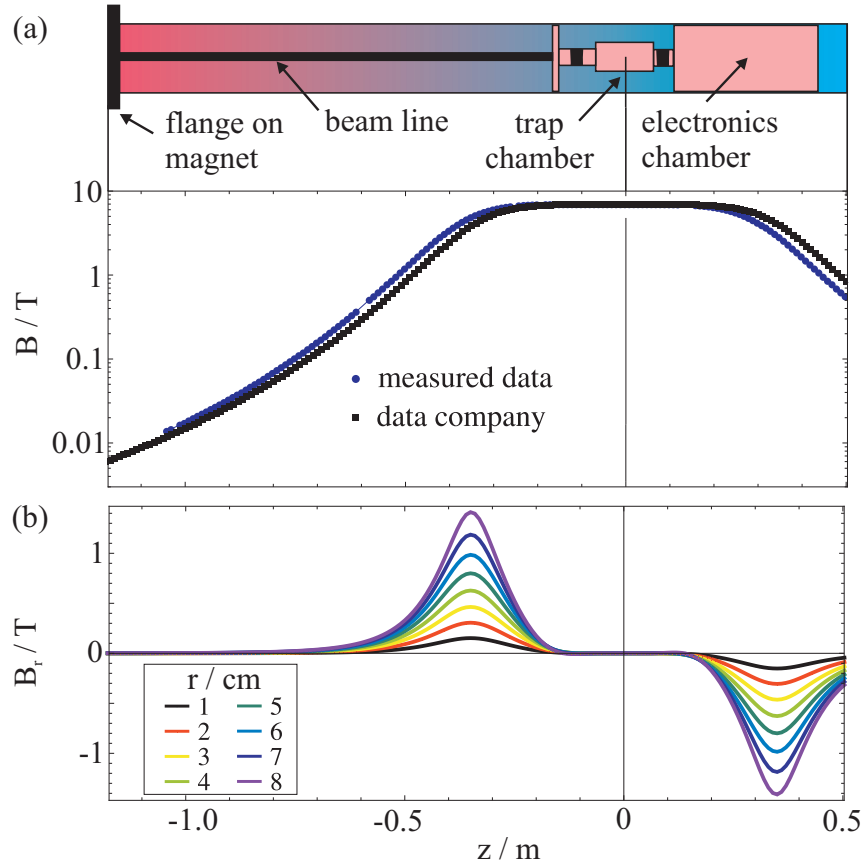


Figure 6.11: (a) Magnetic field on axis through the magnet's bore and a sketch of the location of the cryogenic components at PENTATRAP. The measured values as well as the data provided by the company are shown. Both curves are fitted using a Helmholtz coil pair model. The shapes of the curves agree within the error bars, however, the position along the z -axis is shifted. In (b) the radial component of the magnetic field is shown according to the data provided by the supplier. At a radius of 1 cm the ratio of B_r/B_z is $1.4 \cdot 10^{-6}$ at $z = 1$ cm and $5.7 \cdot 10^{-6}$ at $z = 6$ cm. Due to the NMR-probe design it was not possible to re-measure these values. Nevertheless, they are shown for the sake of completeness.

The fit result of the measured data considering $j = 3$ coils is shown in Tab. 6.2. They can be used to calculate the on-axis magnetic field at any position. A fit to the suppliers data shows that both fits agree within the error bars except for an offset in the parameters p_1 , p_2 and p_3 , which indicates a shift along the z -axis. For a comparison with the company data see [167].

The fringe field of the superconducting magnet is shown in Fig. 6.12. Knowledge of it is important for the positioning of the flux-gate sensor used for the magnetic field stabilization system (see Sec. 7.2) and for the positioning of sensitive electronic components in the lab. The shape of the fringe field (see Fig. 6.12(a)) indicates that the magnet does not only consists of a simple cylindrical coil rather of a complex coil system employing shim coils.

Table 6.2: Fit parameters which are obtained by fitting the measured magnetic field on the magnet's vertical axis with the function given in Eq. (6.12).

K_1 / Tm	K_2 / Tm	K_3 / Tm	L_1 / m	L_2 / m	L_3 / m
1.08(2)	-0.03(1)	0.26(2)	0.686(2)	0.8(1)	1.00(1)
p_1 / m	p_2 / m	p_3 / m	r / m		
0.0355(8)	-0.19(6)	0.027(5)	0.0800(9)		

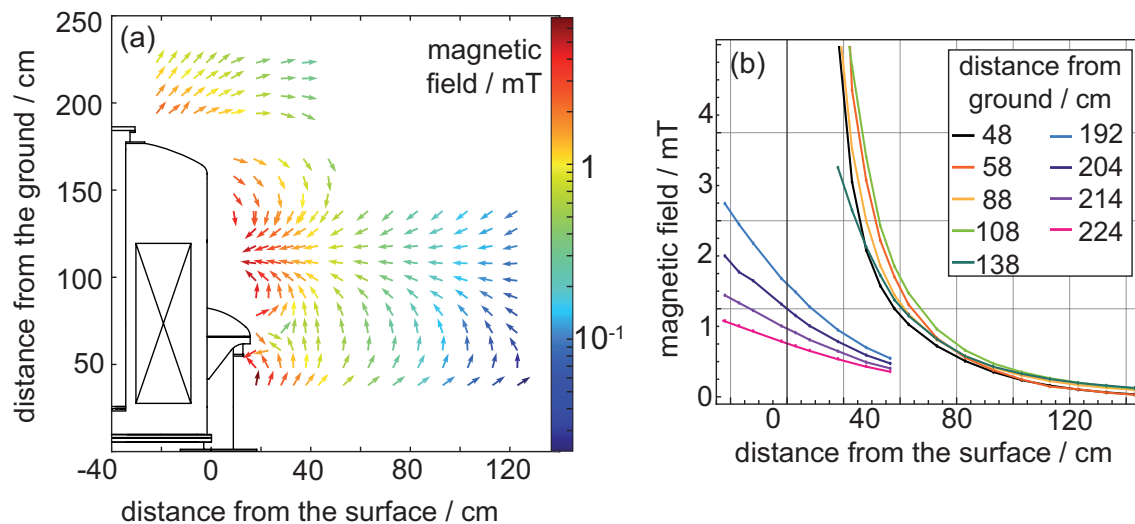


Figure 6.12: Fringe field of the superconducting magnet. The graphs are taken and adapted from [167]. (a) shows the maximum field component including the direction in a vertical plane. In (b) the vertical magnetic field in dependence of the distance from the magnet's surface is shown for different heights.

Chapter 7

Commissioning of PENTATRAP

During the thesis work presented here, a major task was the setup of the world-wide unique Penning-trap experiment PENTATRAP. The commissioning and testing of this instrumentally challenging experiment is covered in this chapter. First, the characterization of the temperature stabilization system of the laboratory (Sec. 7.1) and the setup and testing of the magnetic field compensation system (Sec. 7.2) are addressed. For the investigation of the magnetic field see Chap. 6. Further, the assembly of the highly tolerated Penning traps with their well prepared surfaces (Sec. 7.3), and the first test of the cryogenic translation and tilt system (Sec. 7.4) are presented. Finally, the first installation of the cryogenic assembly, the cabling of the Penning traps (Sec. 7.5) and the first cooling down of the experiment (Sec. 7.6) are highlighted.

7.1 The temperature stabilization of the laboratory

The commercial temperature stabilization system of the laboratory, specified to guarantee a peak-to-peak variation of the temperature over one day below 100 mK, is provided by the company *Siemens* [168]. It consists of two individual air supply facilities¹ which can be controlled via the building services. Together with an aluminium housing being placed around the magnet, and containing on its inside two electric heaters, a control circuit is realized (see Fig. 7.1). Two temperature sensors are located outside and one is located inside the aluminum housing. It is worth mentioning that the temperature sensors used by *Siemens* are not calibrated. The temperature near the magnet can be regulated, since the temperature in the laboratory T_2 is kept colder than the temperature inside the aluminium housing T_1 . The specified values of T_1 range from +25 °C to +27 °C and T_1 is recommended to be 3 °C higher than T_2 [168]. In this mode the facility is operating in a circulating air operation. In another mode, called “Spülbetrieb” (flushing mode) on the user control interface, both air supply facilities are running simultaneously. A shutter to the surrounding air is opened and the cooling systems are running on maximum power.

¹In case of a failure of one facility the remaining facility can take over operation for safety reasons. During normal operation both facilities change operation in a weekly rhythm. Thus, roughly the same wear of both facilities is achieved.

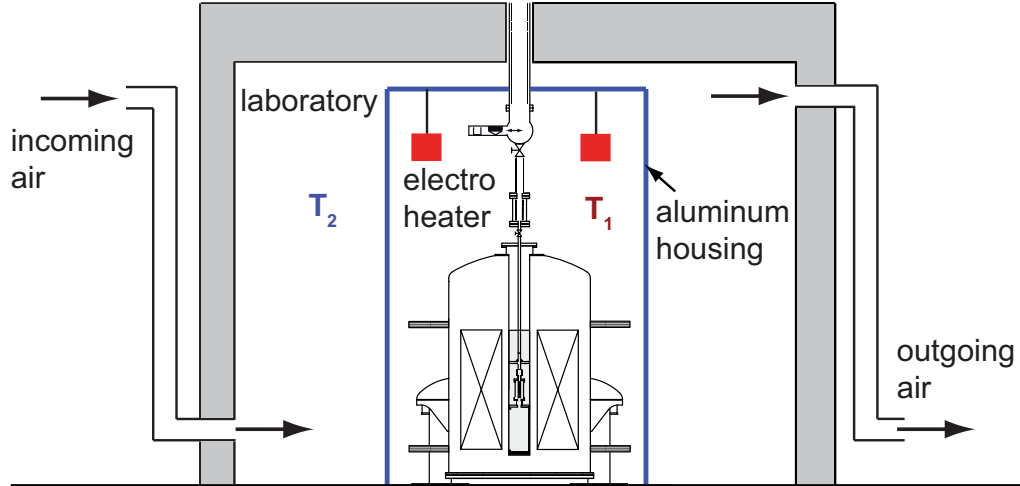


Figure 7.1: Sketch of the temperature stabilization system in the laboratory. The temperature inside the aluminum housing placed around the magnet is regulated. The temperature T_2 in the laboratory is adjusted by the air supply system. Inside the aluminum housing electric heaters are used to regulate the temperature T_1 , where T_1 is recommended to be 3°C higher than T_2 . The system is controlled via the building services.

This mode is needed to compensate high heat developments in the laboratory. In case this mode is chosen all doors of the laboratory should be opened.

All temperature measurements were carried out before the magnet was delivered, since for the magnet's delivery the laboratory wall was removed and is still not being built up again. The first long-term measurements of the temperature in the laboratory showed a shift of the mean temperature in the laboratory of about 0.6 K depending on the air supply system, although the nominal temperatures of both systems were set equal. Moreover, during the operation of one facility called "Zuluftanlage 1" a drift of 0.2 K and a higher standard deviation of about 40 mK compared to a value of about 15 mK for the second facility were observed over approximately 5 days. The temperature offset was resulting from the assignment of each air supply facility to one specific temperature sensor placed at different positions outside the aluminum housing. Such a temperature jump is unwanted during the measurement. Thus, the system was improved in such a way that the mean value of both temperatures is now used to regulate both facilities. Figure 7.2 shows the measured temperature T_1 over about three weeks after the improvement of the setup as well as the overlapping Allan deviation [169] calculated from these values. For a time slice of one day, the Allan deviation is about 0.02 K . However, the measurement was carried out with almost no electrical power load in the laboratory. The increase for small time slices is mainly due to the resolution of the temperature sensor (PT100 class 1/10B). For the resistance measurement the multimeter *8508A* from *Fluke* was used.

The temperature stability in dependence of the nominal temperature values set in the two areas and the resulting heater power of the electric heaters were studied. In general the temperature fluctuations were reduced in case the power of the heaters were zero. For the chosen settings and considering time intervals smaller than one

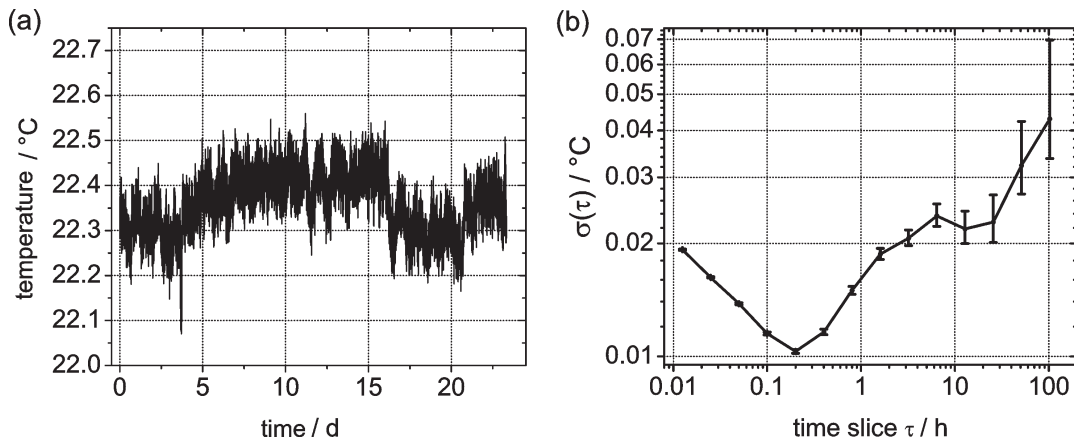


Figure 7.2: Temperature behavior over approximately three weeks in a closed volume around the PENTATRAP magnet (a) and the resulting overlapping Allan deviation (b) calculated with AlaVAR 5.2 [170]. Figure taken from [1].

day the obtained standard deviations lie between 4 mK and 17 mK. Considering the maximum and minimum values to calculate the temperature stability, the obtained values are higher than the specified 100 mK.

7.2 The fluxgate system for the stabilization of the magnetic field

The magnetic field distortions analyzed in Sec. 6.1 motivate the setup of a magnetic field stabilization system. Disturbing factors on the magnetic field originate, e.g., from the Heidelberg-EBIT or the movement of the ceiling cranes. The system is dedicated for the compensation of low-frequency vertical magnetic field distortions, which are uniformly distributed in the complete laboratory area. Main components of the system are a fluxgate sensor, a Helmholtz coil pair and the control electronics. The setup and the commissioning of the system is described and first test measurements are presented.

7.2.1 Principle of operation and setup of the fluxgate system

To measure the magnitude and direction of constant or low-frequency magnetic fields a fluxgate sensor is used. For our tasks a fluxgate sensor provides a sufficient measurement range, which is commonly between about 0.1 nT and 0.1 mT [171]. Employing this sensor weak magnetic fields can be measured with a resolution of better 0.1 nT. In general, fluxgate sensors have a simple mechanical setup and require a temperature stable setup. Usually the sensitivity on temperature changes is 30 ppm/°C [171].

The working principle is based on the saturation property of a core of high magnetic permeability, which is periodically magnetically saturated in both polarities. To this end an excitation coil is wound around the core to which an, e.g., sinusoidal

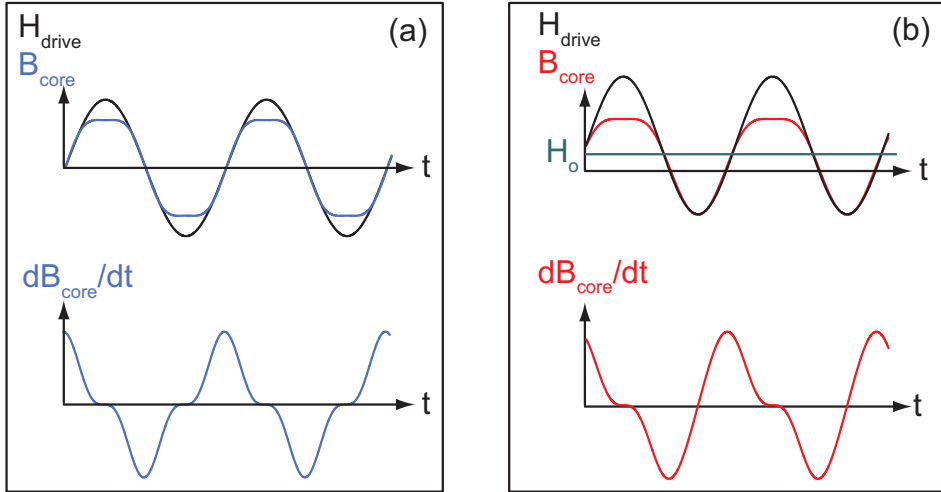


Figure 7.3: Signal shapes of the fluxgate detection principle without (a) and with (b) external field H_0 . The magnetic B-field in the core B_{core} and the associated H-field drive H_{drive} are shown in the upper graphs. The magnetic field intensity \vec{H} and the flux density \vec{B} are linked via the magnetic permeability of the core μ to $\vec{B} = \mu\vec{H}$. In the lower graphs the time derivation of B_{core} is shown. This signal is proportional to the induced voltage signal in the sense coil. Further explanations are given in the text.

excitation current is applied. The magnetic field to be measured produces a high flux through the core due to its high permeability. In case the core is saturated the core permeability μ drops to the vacuum permeability. The flux changes are detected by the voltage induced in a second coil named sense coil. A sketch of the signal shapes is shown in Fig. 7.3. Due to Faraday's law the voltage signal at the sense coil is proportional to the magnetic field. For a constant pickup coil area and neglecting the basic induction term ($\propto dH(t)/dt$) the induced voltage V_i is [171]

$$-V_i = NA\mu_0 H \frac{d\mu(t)}{dt}, \quad (7.1)$$

with N being the number of turns of the coil, A the cross-sectional area of the core, μ_0 the magnetic field constant and H the magnetic field in the sense coil. The name "fluxgate" is originating from the fact that the core is gating flux in and out of the sense coil. The frequency of the sense voltage is twice the frequency of the excitation, thus the detection at the second harmonic of the excitation frequency is generally carried out. Therefore, the read out electronics typically employs a lock-in filter that filters the amplitudes of the second harmonic of the small induced signal. For a more detailed overview the reader is referred to [171]. A classic description of the fluxgate is given in [172].

At PENTATRAP a ring-core fluxgate is used consisting of a toroidal ring-core, a toroidal drive coil and a solenoidal sense coil. A sketch of the sensor and a photograph of the ring-core fluxgate used at PENTATRAP is shown in Fig. 7.4. To understand the working principle, the ring core can be divided into two half-cores (see dashed line in Fig. 7.4(a)). In case of a present external field the two associated voltages induced in the sense coil are phase shifted such that the excitation is canceled while the signal voltages are combined. A ring-core geometry is advantageous

for realizing low-noise sensors [171].

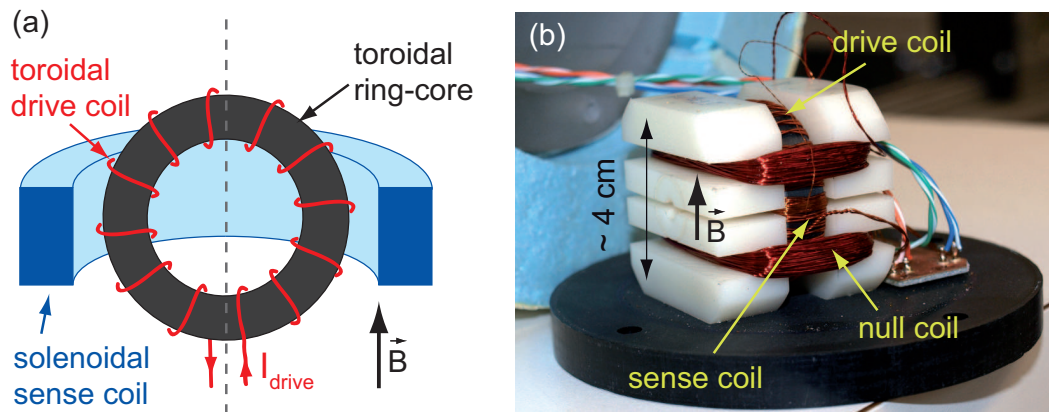


Figure 7.4: (a) Sketch of a ring-core fluxgate (sectional view) consisting of a highly permeable toroidal ring-core, a toroidal drive coil and a solenoidal sense coil. A current I_{drive} is applied to drive the core periodically into magnetic saturation. The flux changes are then detected over the induced voltage in the sense coil. (b) Photograph of the fluxgate in use at PENTATRAP.

In Fig. 7.5 a sketch of the magnetic field stabilization system at PENTATRAP is shown. To correct for the fluctuations which are commonly distributed in the laboratory area, a current through the Helmholtz coil pair is generated. This current is proportional to the current required to cancel the variations in the magnetic field at the location of the fluxgate. The product of the compensation factor of the Helmholtz coil pair, which is estimated to be approximately a factor 100 [137], and the self-shielding factor of the magnet, which is roughly a factor 100 as well (see Sec. 7.2.3), gives an overall shield factor of about 10000. It is worth mentioning that a similar system is currently put into operation at the THE-trap experiment [173].

The detailed setup of the system and the associated control electronics is shown

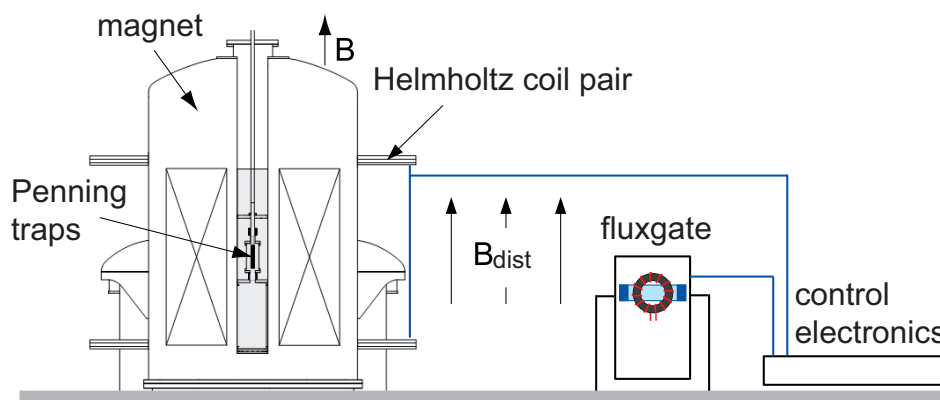


Figure 7.5: Sketch of the magnetic stabilization system. Distortions in the vertical magnetic field B_{dist} are detected by a fluxgate sensor. A current, which is generated by the control electronics, is supplied at the Helmholtz coil pair. Thus, a magnetic field with the same magnitude and the opposite direction of the distortion will be created at the location of the Penning traps. The distance of the fluxgate sensor to the outside margin of the magnet is approximately 1 m.

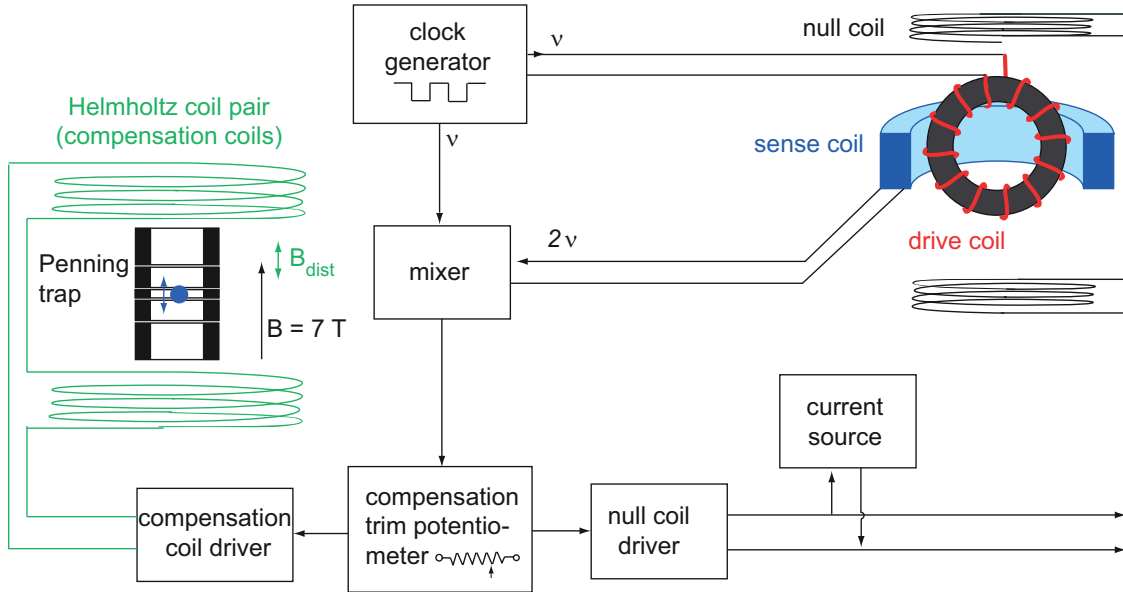


Figure 7.6: Simplified block diagram of the complete fluxgate stabilization system. For details see text.

as a simplified block diagram in Fig. 7.6. In order to increase the measuring range, which is limited by the complete saturation of the core, a null coil is positioned around the ring-core. The null coil generates an offset magnetic field enabling measurements of magnetic fields which would otherwise drive the coil into saturation. The compensation field can be regulated by adjusting a resistance (R_{adj}) at the null coil driver. The clock generator sets the frequency of the drive coil. At the mixer the amplitude of the second harmonic of the induced voltage signal in the sense coil is extracted. Therefore, the signal is multiplied with the 90° shifted excitation frequency and afterwards amplified. The obtained output voltage is proportional to the amplitude of the second harmonic. It is possible to read out the final voltage signal for monitor reasons. At the compensation trim potentiometer the voltage is divided between the inputs of the compensation coil (Helmholtz coil pair) driver and the null coil driver. The division ratio can be adjusted via the chosen potentiometer setting, which thus controls the current applied at the respective coil. Values between 0 and 10 can be set on the front side of the electronics box. The adjustment of the division ratio is necessary to compensate the feedback of the field of the Helmholtz coil pair on the fluxgate sensor. The null coil driver is connected to a current source, which supplies the null coils with the required current. Changing the shunt resistance of the current source allows us to adjust the offset magnetic field. The fluxgate coils and a part of the electronics is placed in a temperature stabilized polystyrene cylinder to reduce temperature drifts of the induced voltage since the magnetic permeability of the core is sensitive to temperature changes.

7.2.2 Commissioning and characterization of the fluxgate system

Prior to the setup of the complete fluxgate system the calibration of the fluxgate sensor was carried out to assign the measured output voltage to an absolute mag-

netic field value. This was necessary for the amplitude determination of magnetic field distortions in the laboratory, which were already presented in Sec. 6.1. The magnitude of the distortions determine the magnetic field range which should be compensated by the system. For the calibration in the vertical earth magnetic field the fluxgate and a Hall probe were probed one after another in the vertical field and the obtained values were compared. It should be noted that the calibration depends on the setting of the compensation trim potentiometer. For a setting of 8 used for the measurements presented in Chap. 6 a conversion factor of $(-1.61 \pm 0.02) \mu\text{T}/\text{V}$ is obtained. The calibration was carried out in the absence of the stray field of the Helmholtz coil pair which will create a feedback and will affect the absolute value of the conversion factor. In the vertical earth magnetic field and for a setting of 8 a resolution of the fluxgate sensor of better 5 nT was estimated.

For the stabilization system a Helmholtz coil pair needs to be adapted to the existing feedback electronics. Since the coil radius was fixed by the space between the magnet and the aluminum housing a radius of 0.9 m was chosen. The number of turns was defined by the maximum field strength, which should be compensated by the control electronics and additionally keeping in mind the total weight of the coil. Each coil consists of 589 windings of 0.4 mm diameter copper wire. Thus, the system is capable to compensate distortions in the range of about $\pm 10 \mu\text{T}$ maximum amplitude limited due to the fixed maximum output voltage of $\pm 15\text{V}$ of the electronics. The frames of the coils were bended aluminum u-profiles fabricated by the company *Schuster* in Mannheim. They were mounted on aluminum profiles screwed on the concrete floor. The u-profiles and the coil windings were insulated against each other by a layer Makrolon[®] foil. For stability reasons each layer of coil windings was covered with a special wire enamel. The axial magnetic field B_z in the center of the Helmholtz coil pair in dependence of the applied current as well as the axial and radial dependence of B_z measured with the Teslometer 7010 from *Sypris Bell* are shown in Fig. 7.7. For a perfectly aligned Helmholtz coil pair with respect to the magnetic field axis and for a spatially constant screening factor of the magnet the influence of the radial and axial gradient of B_z on the ion motion in the Penning trap can be neglected. In a volume of $\pm 5\text{mm}$ around the central trap the maximum change of B_z in axial and radial direction is expected to be below a few hundredth ppt in both directions assuming a screening factor of 100. The change of B_z on the z -axis from the trap center to the end of the trap stack is expected to be a few tens ppt. Nevertheless, the real distortion of the magnetic field should be investigated as soon as stored ions are available.

The radial behavior of B_z (Fig. 7.7 (c)) indicates the ideal radial location of the fluxgate which would be at the zero crossing point of B_z . Placed at this point, the fluxgate would not experience the stray field of the Helmholtz coil pair and a feedback effect would be avoided. In the experiment this is difficult to realize due to the comparable large gradient of B_z in that region. The fluxgate should be positioned in a region where B_z is negative, which means at distances larger than about 110 cm. The z -position of the fluxgate is set to 60 cm above the ground floor since here the magnetic field points into the same direction ($+z$ -direction) as it does in the Penning trap (see Fig. 6.12).

The adjusting of the fluxgate is realized by a gimbal mounting (see Fig. 7.8). Two gimbals allow for a declination of maximum $\pm 10^\circ$ in 0.1° steps in the x - and y -planes.

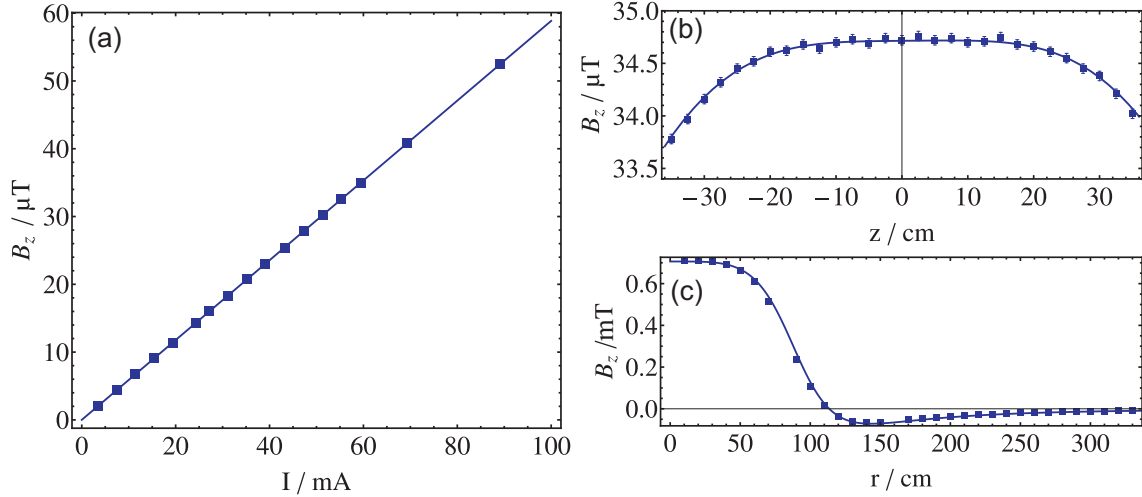


Figure 7.7: Measured characteristics of the Helmholtz coil pair. (a) The axial magnetic field B_z in dependence of the applied current I at the center of the Helmholtz coil pair. From the fit a slope of $0.5886(4) \mu\text{T}/\text{mA}$ is obtained. (b) Measured axial magnetic field B_z along the z -axis of the Helmholtz coil pair and fit (see Eq. (6.13)) to the data. Here, a current of 59.3 mA is applied. (c) Radial dependence of B_z at $z=0$. The measured values and the numerically calculated expected dependence are shown. Here, the current through the coils is set to 1.2 A to gain a better signal-to-noise ratio. In graphs (a) and (c) the error bars are too small to be visible.

By means of a threaded rod a radial translation of $\pm 5 \text{ cm}$ towards the magnets center is feasible. Once the final position of the fluxgate in the laboratory was chosen the fluxgate was declinated and translated in such a way that the measured z -component of the magnetic field was maximized to obtain the best signal-to-noise ratio. Afterwards the null coil was adjusted in such a way that ideally the magnetic field without distortions corresponds to 0 A current flowing through the Helmholtz coil pair. At the chosen location of the fluxgate the magnetic field was 0.1 mT , which led to a shunt resistance of the current source of $733(5) \Omega$. The final setup of the compensation system and the location of the components in the laboratory are shown in Fig. 7.9.

7.2.3 Operating tests of the fluxgate system

During the setup of the compensation system a determination of the screening factor of the magnet was carried out. To this end considerably higher currents in the range of $1\text{-}3 \text{ A}$ than the maximum current of about 20 mA usually applied at the Helmholtz coil pair positioned around the magnet. High currents were required to create a magnetic field in the order of a few μT inside the superconducting magnet. This field strengths can be resolved by an NMR probe (the same probe that is used in Sec. 6.2.2) located in the homogeneous center of the magnet. The ratios of the external to the internal detected magnetic fields and a linear fit to the data lead to a screening factor of 90 ± 55 . The large uncertainty is due to a lack of measurement time (see Sec. 6.2.1). The effect of time-dependent processes, e.g., the change of the outer magnetic field in time or the reaction time of the magnet on magnetic

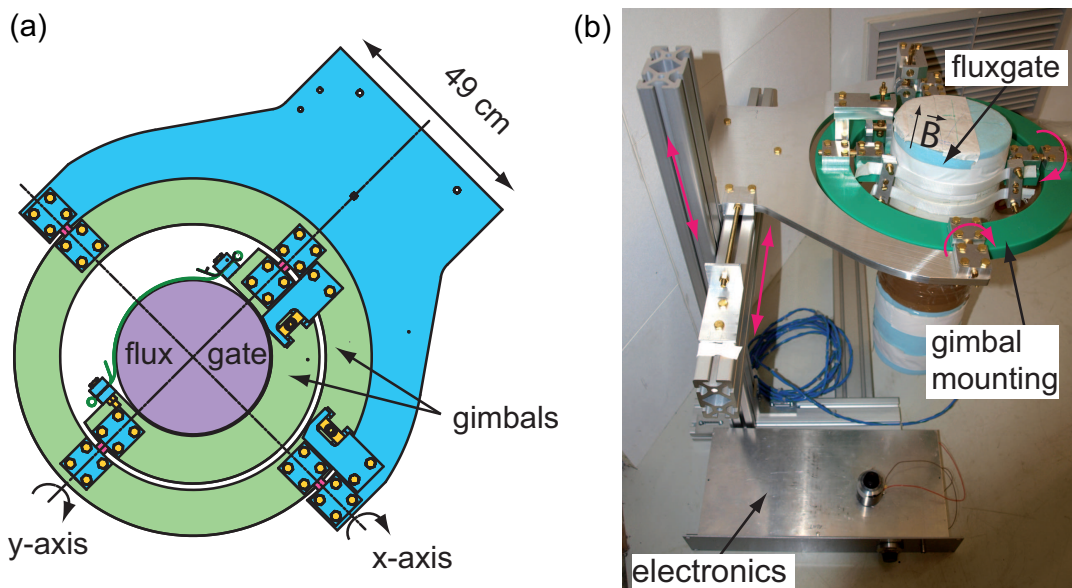


Figure 7.8: (a) Technical drawing of the gimbal-mounted fluxgate. Shown is the top view on the system. The two gimbals allow us to declinate the fluxgate in x - and y -direction. The x -direction is here radially pointing towards the magnet's center. Additionally, a translation towards the magnet is possible as well as an adjustment of the height of the fluxgate. In (b) a photograph of the final assembly is shown. The red arrows indicate the moving directions.

field changes could not be studied. The measurement should be repeated as soon as stored ions are available. Nevertheless, the obtained value is in agreement with the specified value of above 100.

At the stage of development the use of a stored ion as a magnetic field sensor was not possible and other high-resolution sensors like a SQUID detector were not available. Thus, an alternative to test the functionality of the system was needed. Therefore, the experimental setup shown in Fig. 7.10(a) was arranged. The PEN-TATRAP fluxgate (fluxgate 1) was positioned at its final destination close to the superconducting magnet and the Helmholtz coil pair was positioned in the corridor in front of the laboratory with a second fluxgate sensor (fluxgate 2) placed in its center. In this configuration fluxgate 2 served just as a magnetic field sensor and it was not connected to the open loop electronics. The heavy duty bridge crane was moved on the first floor creating almost the same magnitude of magnetic field distortion in the complete experimental area (see Fig. 6.2). The aim was to adjust the open loop electronics such that the ratio of the magnetic field distortion B_{dist} to the compensation field B_{comp} generated by the Helmholtz coil pair was -1. Thereby, B_{dist} was measured with fluxgate 1 and B_{comp} with fluxgate 2. For a coarse adjustment the resistor R_{adj} was changed. The fine adjustment was carried out via a trim potentiometer. For different settings of R_{adj} the ratio of $B_{\text{dist}}/B_{\text{comp}}$ was determined. The results are shown in Fig. 7.10(b). Since the crane did not arrive at the same time at both fluxgate locations, the different time shapes of the signals were accounted for. More details concerning the signal shapes can be found in [167]. To obtain one data point the crane was moved two times through almost the complete accelerator hall. This procedure was required to calibrate the two fluxgates against

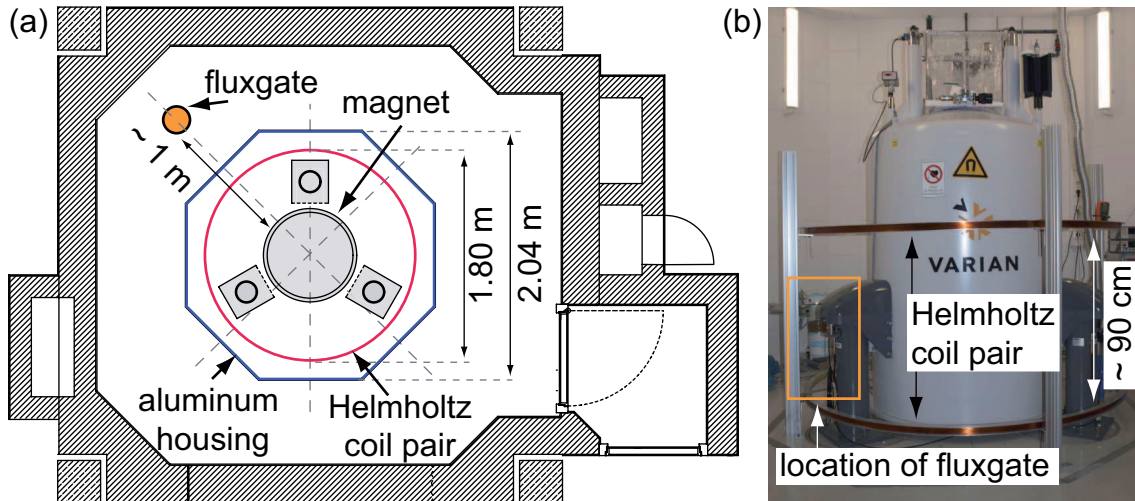


Figure 7.9: In (a) the PENTATRAP laboratory and the positioning of the fluxgate and the Helmholtz coil pair is sketched. (b) Photograph of the fluxgate setup in the laboratory. The position of the fluxgate sensor is indicated.

each other without the Helmholtz coil pair connected. A ratio of -1 was obtained for a resistance of 3.4(5) k Ω keeping in mind that the feedback of the Helmholtz coil pair on fluxgate 1 was not present in this configuration. Due to the limited access to the crane, only three settings were checked. Nevertheless, it was shown that the system is working in principle and that it is ready for first studies employing stored ions in its final configuration.

In the future the performance of the system should be quantified. In case it is not capable to compensate all present distortions improvements are required. For example the control electronics could be digitized such that it could be controlled

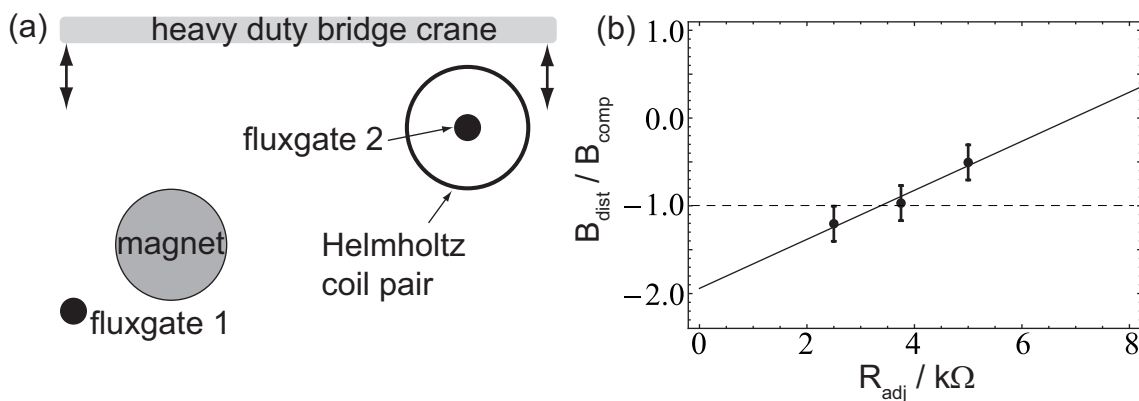


Figure 7.10: Top view of the setup for determining the compensation factor (a) and measurement results including a linear fit to the data (b). The heavy duty bridge crane was moved over the shown setup. Fluxgate 1 was connected to the electronics and measured the distortion B_{dist} . Fluxgate 2 was used to measure the compensated magnetic field in the center of the Helmholtz coil pair B_{comp} . For different settings of the resistance R_{adj} , which adjusts the compensation strength, the ratio B_{dist}/B_{comp} was determined. For further discussions see text and [167].

via the PENTATRAP control system. This would facilitate the adjustment procedure of the system. Additionally, the effect of the pneumatic bearing and thus the movement of the magnet with respect to the Helmholtz coil pair should be investigated. A perspective would be the use of three fluxgate sensors for a triangulation measurement. However, this would require a more space-saving setup since the space in the laboratory is limited. It should be noted that a change to commercial fluxgate sensors is challenging. To obtain a resolution of better 1 nT with a sensor with, e.g., fullscale ± 1 mT and an output voltage of ± 10 V, voltage changes of a few $\mu\text{V}/\text{nT}$ need to be resolved. Common multimeters are not fast enough to measure this voltage changes on the required time scales and an adequate amplifier is required. The use of high temperature superconductors as magnetic field sensors is not possible since a cryostat is needed whose use is not compatible with the present laboratory space.

7.3 The setup of the Penning-trap stack

The setup of the five-Penning trap stack dedicated to high-precision mass measurements is described. The physical requirements for the Penning-trap electrodes are extreme: low magnetic susceptibilities of the materials in use, well-prepared surfaces, high tolerances and suitability for use at cryogenic temperatures. After the electrodes' lengths of the compensated and orthogonalized Penning traps were determined [61], the next step was to determine the three-dimensional shape of the electrodes and to finally put them into practice.

7.3.1 The mechanical construction of the Penning traps

As far as possible a symmetrical design of the Penning-trap setup was chosen. Thus, the ring electrode (see Fig. B.4) and the correction electrode (see Fig. B.5) were symmetrical designed, which means that it does not matter which side of the electrode faces the following electrode. For the endcap electrodes a symmetric (see Fig. B.6) and an asymmetric (see Fig. B.7) electrode are required. The asymmetric design results from an introduced edge such that from the ion's point of view the insulators are not visible. This was done to avoid charge accumulation on the insulators and to avoid that the ion experiences the potential of a charged insulator (see Fig. B.2). The edge additionally made it possible to enlarge the distance between two following electrodes by removing material behind it. Thus, the electric capacity measured between two electrodes was reduced.

In order to keep influences on the magnetic bottle term small, low magnetic susceptibility materials were used for the traps. Thus, the electrodes were made of $>99.999\%$ purity OFHC copper, and the insulators between them of sapphire (Al_2O_3). The technical drawing of the sapphire ring, which is tolerated by $1\ \mu\text{m}$ is shown in Fig. B.3. In the final Penning-trap setup the slits between the electrodes seen by the ion are 0.15 mm. Sapphire balls with 1 mm diameter were used as insulators between the two halves of a splitted electrode. In the final setup the radial spacing of the electrodes is 0.16 mm. The balls have a deviation from a perfect shape of at most $0.5\ \mu\text{m}$.

Additionally, the thermal shrinkage of the Penning-trap electrodes at 4.2 K was accounted for. The tolerances of the electrodes are so high ($\pm 5 \mu\text{m}$) that the shrinkage due to the cooling from 300 K to 4.2 K, which is in the order of a few μm depending on the electrode's length, should be accounted for. At 4.2 K the thermal expansion $\Delta L/L = (L_{293\text{K}} - L_T)/L_{293\text{K}}$, where $L_{293\text{K}}$ is the length at 293 K and L_T the length at a temperature T , of copper [174] and gold [175] is almost identically -0.324% . In Fig. 7.11 the temperature dependence of the thermal expansion of copper and sapphire is shown. At 4.2 K $\Delta L/L$ for sapphire is -0.079% [176]. In Fig. 7.12 a sketch of the Penning trap including the relevant lengths, which were adjusted to consider the thermal expansion at cryogenic temperatures, are shown. The calculated dimensions are given in Tab. 7.1.

The trap stack is fixed on the bottom and the top by two fastening plates which are mechanically joined by three rods made of CuSn8 (see Fig. B.2). The difference in shrinkage of the rods compared to the Penning-trap stack is about 0.25-0.3 mm. It is absorbed by annealed disk springs of beryllium copper (Cu98%-Be2%) each having a thickness of 0.125 mm and a maximum deflection of ≈ 0.3 mm.

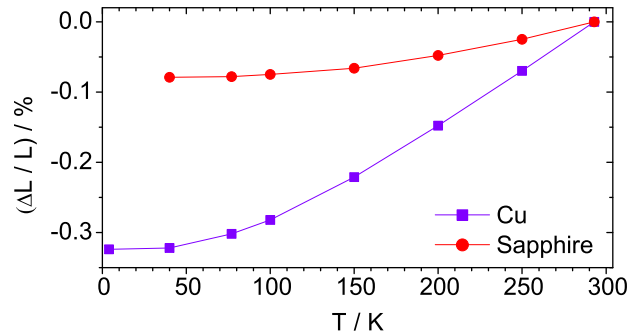


Figure 7.11: Thermal expansion $\Delta L/L = (L_{293\text{K}} - L_T)/L_{293\text{K}}$ of copper and sapphire (parallel to the c-axis) at cryogenic temperatures. $L_{293\text{K}}$ is the length at 293 K and L_T is the length at the temperature T . The values given in [141] are replotted. [141] refers for the copper values on [174] and for the sapphire values on [176].

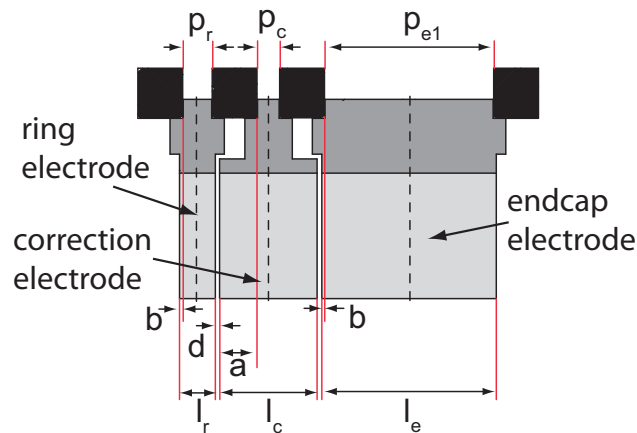


Figure 7.12: Sketch of the Penning trap defining the parameters for which the thermal shrinkage from 293 K to 4.2 K was calculated. Only the three symmetrical electrodes of the Penning trap are shown for simplicity.

Table 7.1: Dimensions of the Penning-trap electrodes at 4.2 K and at 293 K. For the definition of the parameters see Fig. 7.12. Just as in the case of the symmetrical endcap electrode, the length of the outer surface of the asymmetrical endcap electrode is named p_{e2} . The errors of the nominal sizes at 293 K are ≤ 0.001 mm assuming an error of 5 % of the thermal shrinkage of copper and sapphire.

parameter	nominal size at 4.2 K / mm	nominal size at 293 K / mm
l_r	1.457	1.462
l_c	3.932	3.945
l_e	7.040	7.062
p_r	1.173	1.178
p_c	0.916	0.921
p_{e1}	6.756	6.778
p_{e2}	5.390	5.408
a	1.508	1.512
b	0.142	0.142

7.3.2 The manufacturing process of the Penning traps

The manufacturing of the Penning-trap electrodes consisted of several steps:

1. Manufacturing of the copper electrodes and the sapphire parts.
2. Dimensional check of the delivered parts.
3. Splitting of some electrodes via wire-electro discharge machining.
4. Acid cleaning of the electrodes.
5. Polishing of the inner surfaces.
6. Gold plating of the electrodes.
7. Dimensional check of the final electrodes.
8. Laser welding of the copper pins on the outer surface.

The trap electrodes were fabricated by the company *Blum CNC* in Heidelberg with a tolerance of about $\pm 2 \mu\text{m}$. After step 1 the important lengths of the ring electrode and the associated planes and sphericities were measured by the company *Zeiss* in Oberkochen. They are able to attain measuring uncertainties between (1-2) μm depending on the measure. It should be remarked that at this level of measuring uncertainty the thermal expansion of copper was considered. All measures were within the tolerances given at the technical drawing and even more accurate. The given form- and positional tolerances and the measurement report of the manufacturer could be verified. The splitting of the electrodes was carried out at the *Institut für Mikrotechnik (IMM) Mainz* via wire-electro discharge machining.

The sapphire products were fabricated by the company *Saphirwerk Industrieprodukte AG* in Switzerland. A quality check of the highly tolerated sapphire rings was

carried out at *Zeiss* as well. Besides of the length tolerances the form- and positional tolerances were checked². The evenness of the sapphire's horizontal contact surfaces with the electrodes was within the expectations (between 0.1 μm -0.3 μm). Moreover, the axial runout and the circularity of the inner plane, which touches the electrodes radially and which is necessary for the exact radial positioning of the traps, was measured (see Fig. 7.13). The cylindrical circularity of the shown example is 1.66 μm .

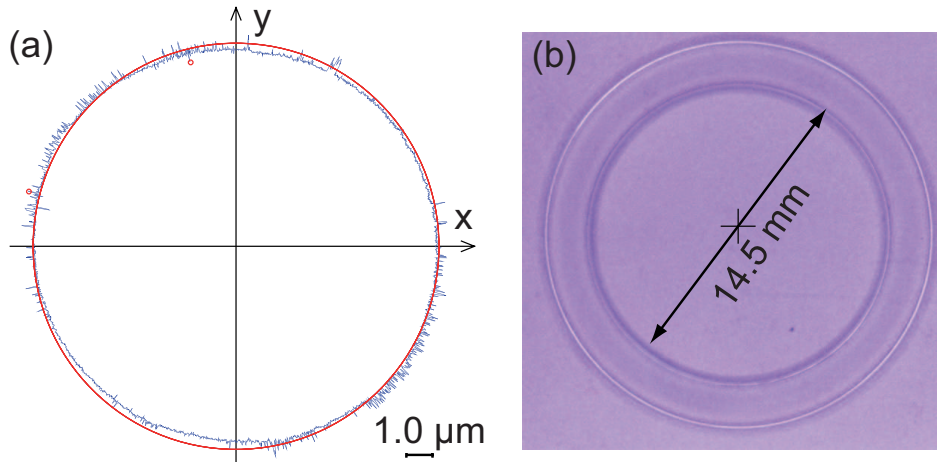


Figure 7.13: (a) Circularity of the sapphire ring measured along one edge at the diameter of 14.5 mm. The picture is extracted from the measurement report from *Zeiss*. The least square circle (red) and the measured 4629 data points (blue) are shown. The spacing of the maximum and the minimum circle through the data points is 0.95 μm . (b) Photomicrograph of the sapphire ring showing no visible edges or distortions.

Since copper oxidates after a few hours in air, the surfaces of the electrodes were first cleaned from existing oxidations and were afterwards coated. Therefore, acid cleaning of the Penning traps was carried out. Prior to the etching process the electrodes were cleaned in an ultrasonic bath with acetone. The darkening of a polished rose-colored copper plate at air is due to the creation of the auburn monovalent copper oxide Cu_2O . In case Cu_2O is heated the black-colored bivalent CuO is formed at air. It can be solved from the surface by using acid sulfur:



To solve Cu_2O hydrogen peroxide is added to the solution:



A basic condition of the cleaning process is to avoid to much detachment of the surface, since the high tolerances of the electrodes should not be destroyed. The solution 1 consisting of 1 % H_2SO_4 and 3 % H_2O_2 and the solution 2 consisting of 10 % H_2SO_4 and 0.35 % H_2O_2 were tested. Solution 1 is used for cleaning and passivation of copper surfaces to remove surface radioactivity and prevent oxide formation

²For a description of the form- and positional tolerances see e.g. [177].

in low-background experiments [178]. Solution 2 is, e.g., used at a Mainzer Penning-trap experiment to etch the electrodes [179]. To systematically check the surface detachment, several small and identical copper disks of the trap material were subjected for varying times and temperatures to the solutions. The results obtained at room temperature are shown in Fig. 7.14. An increase of the temperature of solu-

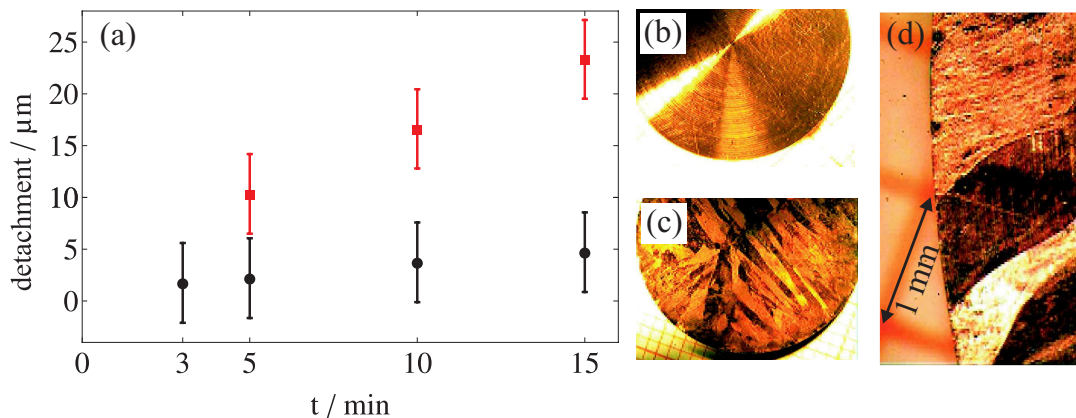


Figure 7.14: Surface detachment due to acid cleaning at room temperature and photomicrographs of test copper samples. The samples were immersed for varying times in the solution 1 consisting of 1 % H_2SO_4 and 3 % H_2O_2 (red rectangles) and the solution 2 consisting of 10 % H_2SO_4 and 0.35 % H_2O_2 (black disks) (a). In (b) a picture of the untreated sample having a diameter of about 2 cm and a thickness of about 0.5 mm is shown. (c) Sample after being immersed for 15 min in solution 1 and (d) sample being immersed for 15 min in solution 1 at a higher resolution. Independent of the method the grain boundaries become visible.

tion 2 from 20 °C to 55 °C lead to an increase of the detachment from 2.2(3.8) μm to 3.7(3.8) μm in case the probe is immersed for 5 min in the solution. The large error bars are due to the large uncertainty obtained by measuring the diameter and thickness of the probes with a scale caliper. A high concentration of hydrogen peroxide in solution 1 is responsible for the better solution of Cu_2O and thus the higher surface detachment. Finally, it was decided to use solution 2 at room temperature and to subject the electrodes only a few minutes to the acids. In Fig. 7.15(a) the surface of a very oxidized ring electrode and in Fig. 7.15(b) the surface after being etched is shown. Although the surface roughness of the electrodes is far below $R_z^3 = 6.3 \mu\text{m}$ specified in the technical drawing it is necessary to polish them to remove the fine rills created during the machining at the numerically controlled lathe (see Fig. 7.15(a)-(b)). In order not to pollute the surface again with other chemicals, natural Vienna polishing chalk mixed with distilled water was used as polishing agent. The polishing was carried out using a rotating cotton bud which was fixed at a dremel. An approximately fifty times enlargement of the polished surface is shown in Fig. 7.15(c).

Patch potentials on the electrode surfaces have to be avoided since they influence the electric storage potential seen by the ion. A random distribution of regions with fixed crystal orientation on the surface can be present and the work function will

³Denoting the distance between the lowest depression and the highest elevation of the surface in μm . For the detailed definition it should be referred to [177]

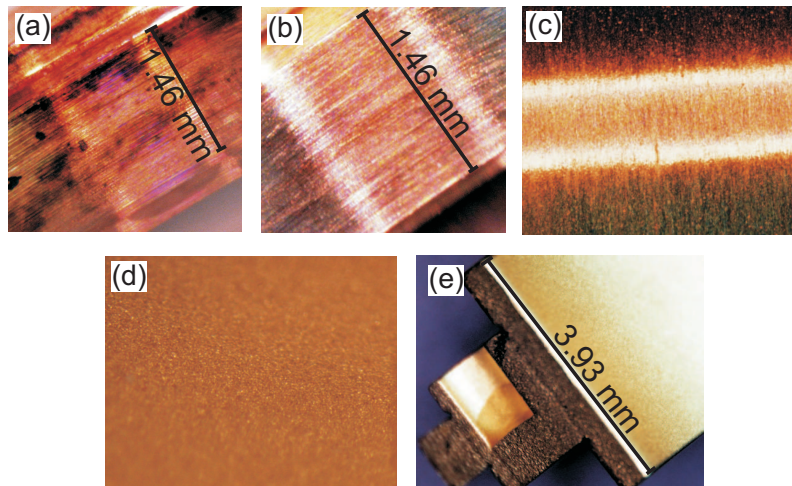


Figure 7.15: Photomicrograph of the surfaces at the different processing steps. (a) Very oxidized inner surface of a ring electrode. This electrode was lying a few weeks at air. Prior to the acid cleaning the processed Penning-trap electrodes were much less oxidized. (b) Etched surface of a ring electrode. In (c) and (d) an about fifty-fold enlargement of the polished surface and the gold-plated surface are shown, respectively. In (e) a part of a gold-plated and splitted correction electrode is shown. Here, the gold deposition at the cutting edge of the electrode and the splitted bore hole for the sapphire ball are visible.

vary between these regions [180]. Thus, an ion will see a changing potential when passing near the surface. Therefore, to reduce the effect of patch potentials, the trap electrodes were galvanically gold-plated. A 20 μm thin layer of pure gold, containing no organic or inorganic additives that are commonly used to enhance shine, was chosen. Galvanic companies reported to us that a layer thickness greater (4-5) μm is required to obtain a closed surface. Generally, a nickel barrier coat is placed between the copper and the gold layer to prevent diffusion of the gold into the copper. Since nickel has a high magnetic permeability, it was not applicable at PENTATRAP. To this end we chose only a thick layer of gold. The plating was carried out at the company *Umicore Galvanotechnik*. To avoid oxidation during the transport, the electrodes were sent under a nitrogen protective atmosphere. The lengths of some electrodes after the gold-plating were cross checked by the mechanics workshop at the MPIK. At the galvanic processing a tolerance of better than $\pm 3 \mu\text{m}$ was realized. In total the tolerance of the final electrodes is about 5 μm .

To further improve the coating with regard to patch potentials an alternative would be the use of an amorphous coating material. A dispersion of colloidal graphite in water called *Aquadag* from *Acheson* is a possible candidate. However, the application of the dispersion with μm precision is a challenging task. Furthermore, some long-term projects would be the investigation of sputtering gold or carbon on the surfaces.

In a last step the trap pins were attached. 0.5 mm thick and about (2-3) cm long 99.9999% pure copper pins were laser-welded to the electrodes. For a better handling during the laser-welding process, they were stuck in holes in the outer surfaces of our cylindrical electrodes. The holes have a diameter of 0.5 mm and a depth of 1mm. Laser welding has the big advantage compared to the soldering of

the pins that less heat is transferred during the process on the electrodes. Too much heat transfer might cause a distortion of the electrodes and should be minimized since the electrodes are highly tolerated. Another benefit of laser-welding is that the position of the bond can be adjusted very precisely. This is necessary especially for the correction electrodes, which have a height of the outer surface of only 1.138 mm (see Fig. B.5). In contrast, the flow of the solder cannot be controlled so precise. The welding was carried out at the *Schweißtechnische Lehr- und Versuchsanstalt (SLV) Mannheim* employing a Nd:YAG (Neodymium-doped Yttrium Aluminum Garnet)-laser. A pulse duration of 14.5 ns and a power of 1500 W was set. It is worth mentioning that the gold surfaces reflected the laser light and that a carefully tuning of the laser power and position was required (see Fig. 7.16(a)). In Fig. 7.16(b) a photomicrograph of a laser-welded pin is shown.

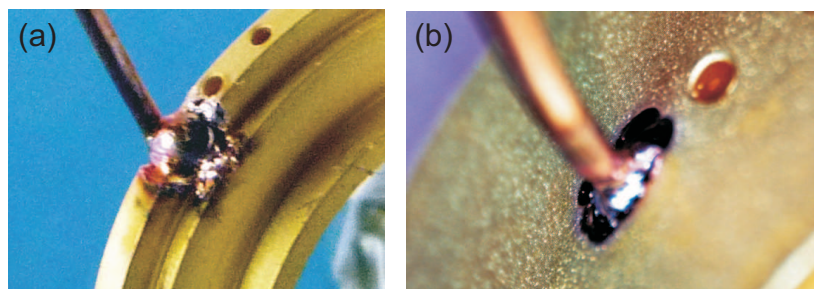


Figure 7.16: (a) Photograph of a destroyed correction electrode in case the laser power was chosen to high. The outer surface of the correction electrode is the smallest of the four electrode types. Thus, it was most challenging to carry out the laser welding at this electrode. (b) Photomicrograph of a perfectly laser-welded trap pin. The copper pin is coalesced with the electrode.

7.3.3 Assembly of the Penning traps

As soon as all trap components were available the trap tower was assembled. As an example a photograph of a finished endcap electrode is shown in Fig. 7.17(a). The tight fitting of some parts necessitated the use of liquid nitrogen to cool the electrodes and the sapphire rings prior to assembly. Thus, the assembly was eased since the copper electrodes shrank more than the sapphire. Figure 7.17(b) shows the view inside an assembled Penning trap and the 0.15 mm slits between the electrodes.

The arrangement of the electrodes was chosen such that the center three traps each had two splitted correction electrodes which were turned by 90° on the horizontal plane against each other. With this arrangement axial and radial dipolar excitations and especially effective quadrupolar coupling (see Sec. 2.3) can be applied. Due to a loss of electrodes during the manufacturing process, the outermost traps were equipped in a different way. This is at first not critical since so far in these traps no high precision measurements are aimed for. Penning trap 1 (the topmost) employs one splitted correction and one splitted endcap electrode and Penning trap 5 one splitted correction electrode. The final setup is shown in Fig. 7.17(c). Nevertheless, new electrodes are already ordered and it is planned to build a four-fold segmented correction electrode. This would provide the possibility to perform even octupolar excitations.

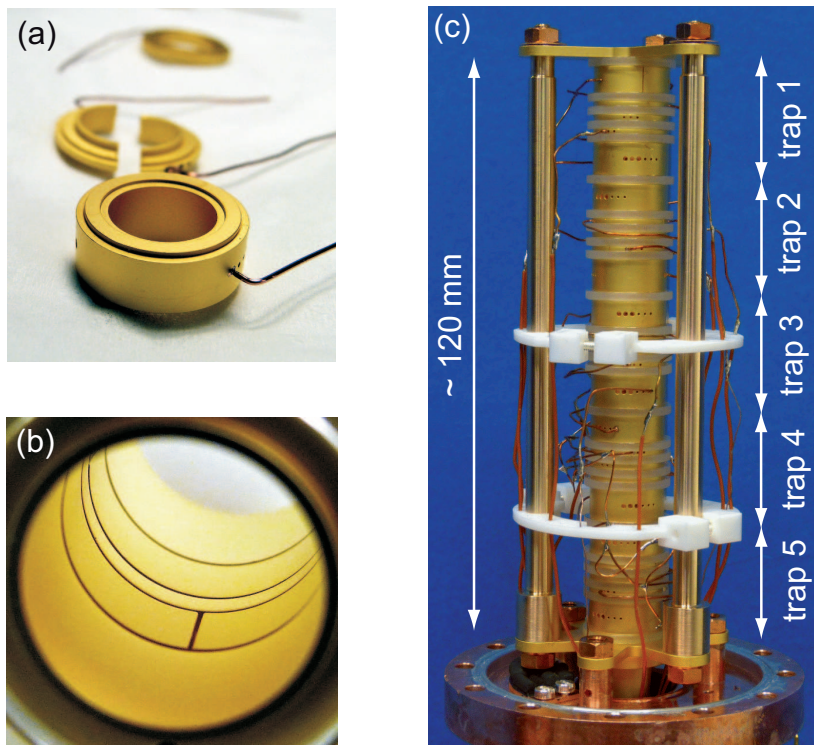


Figure 7.17: (a) Photograph of a finished endcap electrode. (b) View inside an assembled five-electrode Penning trap. The 0.15 mm spacers between the electrodes are visible. (c) Photograph of the assembled Penning-trap tower mounted on the lower flange of the trap chamber. The first cabling is described in Sec. 7.5

7.4 The setup of the translation and tilt system

A technically very challenging component of PENTATRAP is the translation and tilt system. The challenge was to set up a system which consists of low magnetic susceptibility materials and which works at cryogenic temperatures. The system was designed in collaboration with the engineering design office at the MPIK and should permit the adjustment of the traps' horizontal and angular positions with respect to the magnetic field. It was constructed to compensate for a maximum declination of $\pm 1^\circ$ and a maximum translation of ± 2.2 mm at 4.2 K. For the adjustment procedure it is not required to remove the cryogenic assembly out of the magnet.

7.4.1 The mechanical construction of the translation and tilt system

A photograph of the mounted system is shown in Fig. 7.18 (a) and the assembly drawing can be found in App. B. The trap chamber can be adjusted independent from the beamline and the electronics chamber since it is decoupled by means of two bellows. An eccentric fixes the position in the magnet's bore. A complex structure realizing the translation and tilt is arranged around the trap chamber. Similar to a gimbal mounting the trap chamber is hanging in two rings which are located equally spaced above and below the Penning-trap center. The declination axes of the rings are turned by 90° against each other. Each ring is moved by two slides that slide

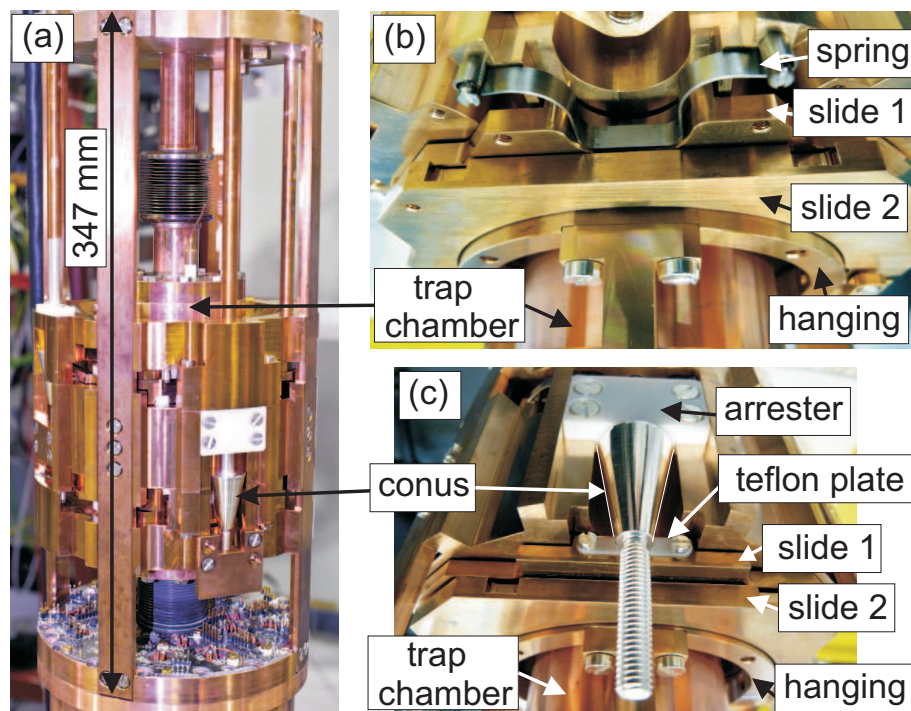


Figure 7.18: (a) Photograph of the completely mounted translation and tilt system. (b) Photograph of the return spring pushing slide 1 and (c) photograph of the conus contacting slide 1 at the opposite side. The slide moves the hanging of the trap and thus its position. Slide 2 is acutated along the axis which is 90° tilted. For the detailed explanation of the system see text.

perpendicular to each other. In turn, each slide is moved by means of a conus that can be operated from the top of the magnet. At the opposite side of the conus a return spring is located. This spring is necessary to exert a reset force on the slide. Photographs of the spring and the conus contacting the slide are shown in Fig. 7.18(b) and Fig. 7.18(c), respectively. A sketch illustrating the basic working principle is given in Fig. 7.19.

All parts of the mounting structure as well as the rings, the slides and the conis were made of phosphorous bronze (CuSn8). Titanium grade 2, which remains flexible at 4.2K, was used for the bellows. The slides are running on small teflon pads to keep the friction small and to guarantee a smooth running. The titanium grade 2 return springs are leaf springs, where the shape and the thickness are individually adapted to guarantee a reset force at cryogenic temperatures. The conis were silver plated and they contact small teflon pads to avoid fretting and stiff actuating. Fiber glass (G10) tubes being glued to the CuSn8 joints with the adhesive *EP21TCHT-1* from *Master Bond Inc.* are used to actuate the conis and thus the translation and tilt device. At the magnet's top flange a scale is sitting which allows the user to read out the actual position of the conus. The travelling distance is ± 11 turns.

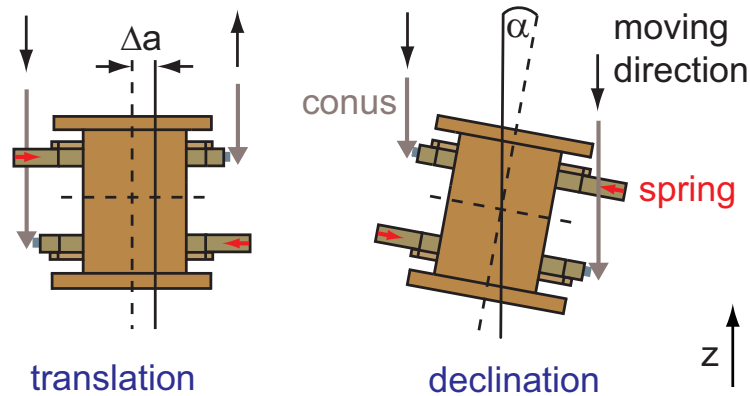


Figure 7.19: Sketch of the working principle of the translation and tilt stage. The black arrows indicate the moving direction of the conis. The small red arrows indicate the location of the return springs. Left side: trap translation by the distance Δa in x -direction for turning a conus downwards and the opposed one upwards. Right side: trap declination by the angle α for turning both conis in the same direction.

7.4.2 Test of the translation and tilt system at room and cryogenic temperatures

A functionality test of the translation and tilt system was carried out at 293 K and at 77 K. The thermal expansion of the used materials will change from 293 K to 77 K by about 80 %-90 % compared to the expansion from 293 K to 4.2 K. This can be seen, e.g., in Fig. 7.11 showing the thermal expansion of copper. Due to the small shrinkage from 77 K to 4.2 K, the shrinkage at 4.2 K will not differ dramatically from that at 77 K. Therefore, if the system is working at 77 K, it is concluded that the system is also working at 4.2 K. However, it is very crucial to avoid the freezing of the system by water ice or at 4.2 K by oxygen ice.

The experimental setup shown in Fig. 7.20(a) has been built up. Instead of the Penning trap a device consisting of a holding stucture, a teflon plate, Light-Emitting Diodes (LEDs) and a 0.1 mm thick taut wire was arranged in the trap chamber. The holding structure allowed for the arrangement of a thin wire such that a cross could be realized whose center coincides with the Penning-trap center. Behind the teflon plate, which had two small holes, five SMD (Surface Mounted Device) LEDs were placed. Additional, a cross was drawn at the plate's center. The LEDs were needed to light the interior space through the slightly transparent teflon plate and to make the holes visible as small light dots. At the magnet's top flange a Charge-Coupled Device (CCD) camera was fixed. Thus, the movement of two crosses with respect to each other was investigated in case the conis were operated. For a translation of the trap chamber, the crosses moved in the same direction. A declination of the system caused the crosses to move against each other. The second light dot was just used for calibration reasons.

The system was pumped down to a pressure of about 10^{-6} mbar at ambient temperature. For the test at 77 K it was lowered into a dewar filled with liquid nitrogen. Therefore, short G10 tubes were constructed to fit the cryogenic insert into the dewar. A photograph showing the complete system hanging over the dewar is given in Fig. 7.20(b). The used coordinate system and the respective location of

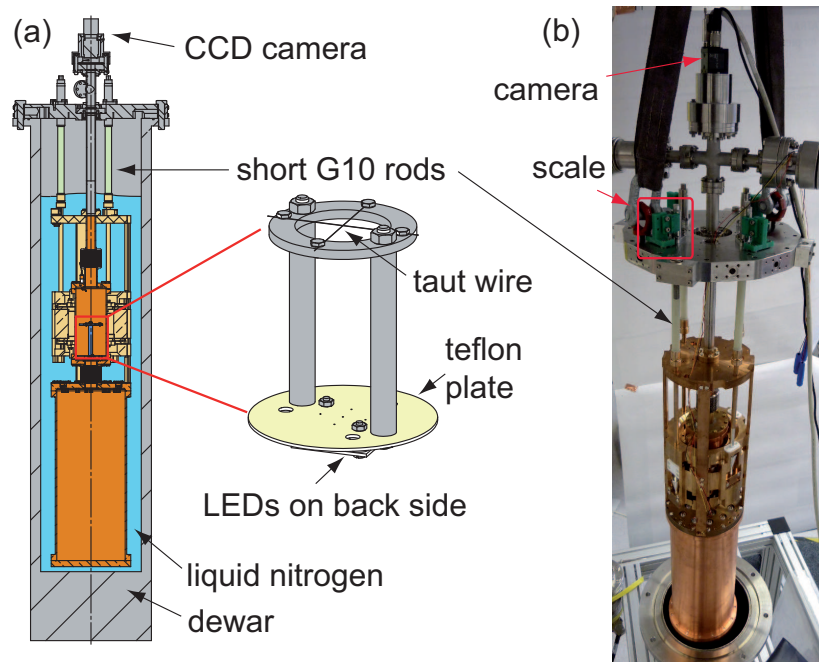


Figure 7.20: Experimental setup used for the test of the translation and tilt system. (a) sectional view of the experimental setup and zoom at the mounting inside the trap chamber. (b) photograph of the experiment hanging over the dewar filled with liquid nitrogen. The red rectangle borders the scale where the position of the conus was read out. Further details are given in text.

the conus is specified in Fig. 7.21. In Tab. 7.2 the moving direction of the conus is assigned with the resulting displacement of the trap for a pure translation and a pure declination of the trap. An exemplary camera picture is shown in Fig. 7.22(a). In the evaluation of the cryogenic test, the thermal shrinkage of the used materials was accounted for. The thermal expansion of the aluminum distance pieces and the teflon plate was considered.

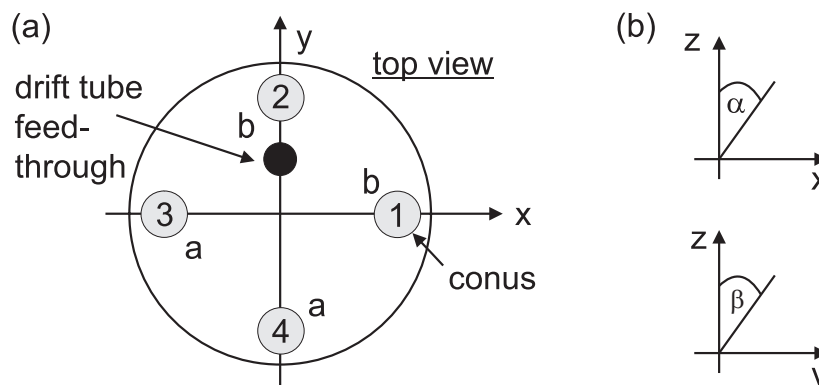


Figure 7.21: (a) Definition of the coordinate system and locations of the conus. The position of the drift tube feedthrough is shown to ease the assignment of the conus in the experiment. Additionally, it is indicated where the conus actuate the trap: the letter “a” stands for above and the letter “b” stands for below the Penning-trap center. In (b) the declination angles are defined.

Table 7.2: Operating of the conis and the resulting movement of the trap for the simple cases of a pure translation and a pure tilt. The arrow downwards and upwards indicates the downward and upward movement of the conus, respectively. The angles α and β are defined in Fig. 7.21.

conus 1	conus 2	conus 3	conus 4	trap movement
↑	0	↓	0	translation in +x
↓	0	↑	0	translation in -x
0	↑	0	↓	translation in +y
0	↓	0	↑	translation in -y
↓	0	↓	0	tilt by $+\alpha$
↑	0	↑	0	tilt by $-\alpha$
0	↓	0	↓	tilt by $+\beta$
0	↑	0	↑	tilt by $-\beta$

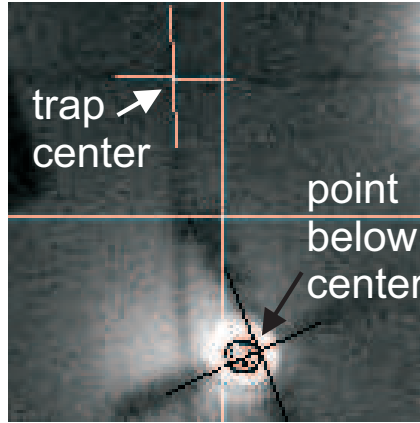


Figure 7.22: Example of a camera picture used for the evaluation. The location of the two crosses, which represent the trap center and the second reference point below the center, are retraced. Their distance to the fixed center of the camera system (large cross) is measured using the computer program GIMP.

Figure 7.23 and Fig. 7.24 show the measurement results obtained at room temperature and at 77 K. Dashed rectangles border the areas which are expected to be addressed. The errors are originating from the pixel resolution and the measuring uncertainties determining the dimensions of the assembly. At room temperature the central position was several times successfully readjusted after the actuation of the conis. The system is working with almost the same features at cryogenic temperatures as at room temperature. In general, the translation could be realized as expected (Fig. 7.23(a) and Fig. 7.24(a)). At 77 K the addressed points are slightly shifted to negative x -values, which might be explained with a not carefully set zero position. The declination of the system only worked properly in positive directions (Fig. 7.23(b) and Fig. 7.24(b)).

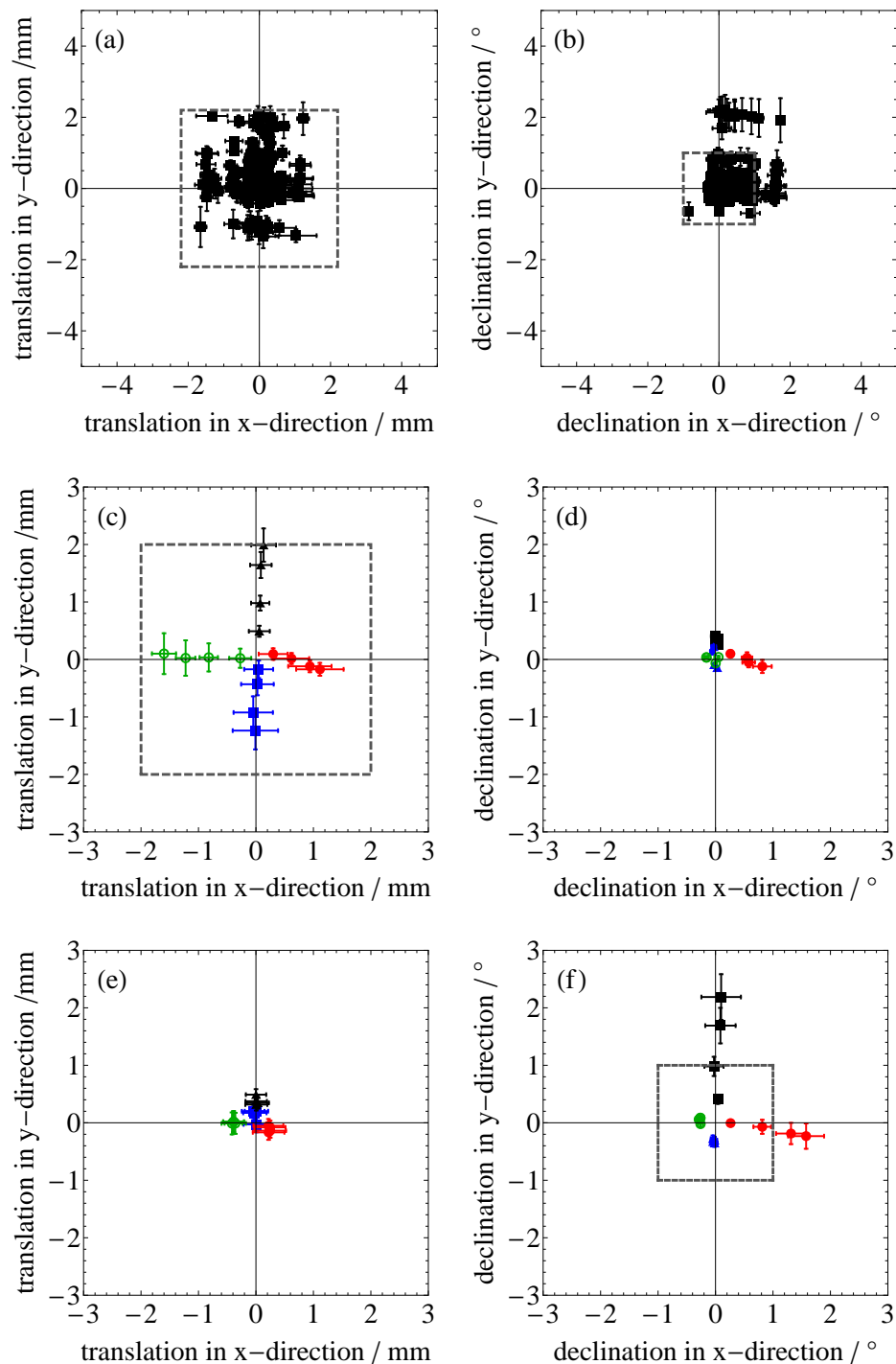


Figure 7.23: Measurement results of the translation and tilt system's functionality tests at 293 K. In (a) and (b) the translation and declination, respectively, calculated from all addressed points are shown. All possible combinations with $0, \pm 3, \pm 6, \pm 9$ and ± 11 turns, where the absolute values for two opposite conis are kept equal, were chosen. In (c) and (d) the trap was just translated and in (e) and (f) the trap was just declinated in the respective direction and the observed movements are shown. Here, only two opposite conis were moved and the orthogonal conis were set to the zero position. For further details text.

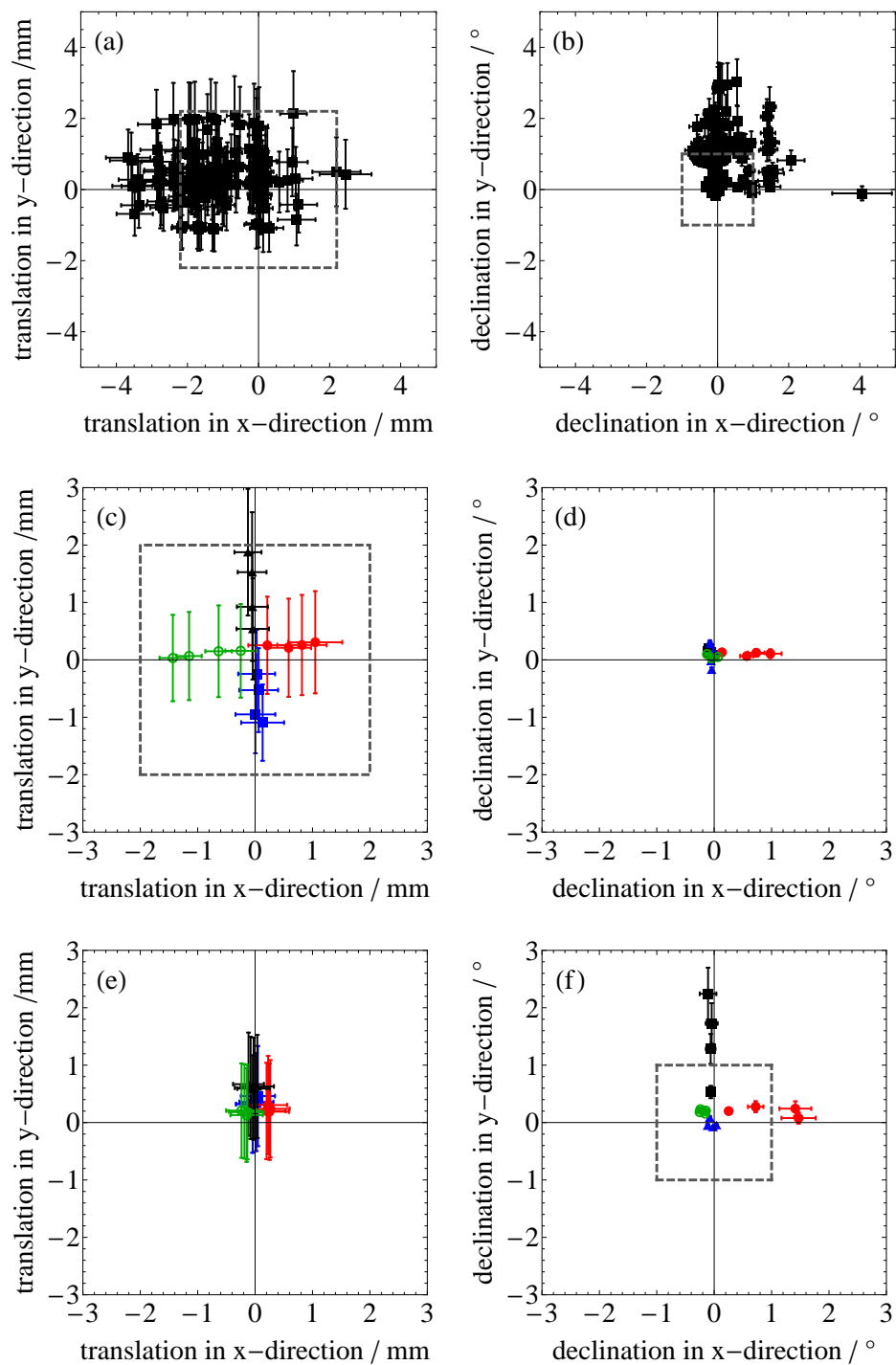


Figure 7.24: Measurement results of the translation and tilt system's functionality tests at 77 K. (a)-(f) Show the same graphs as shown in Fig. 7.23 obtained for the measurements at room temperature.

In case a pure translation is expected in a single direction, the system behaves nearly as expected for both temperatures (Fig. 7.23(c)-(d) and Fig. 7.24(c)-(d)). In case a pure declination is expected in a single direction, the declinations in negative directions failed (Fig. 7.23(e)-(f) and Fig. 7.24(e)-(f)). This is the situation when two opposed coni are moved upwards and both springs should push to realize the tilt. It is assumed that the springs are too weak in their interplay. For a pure translation only one spring needs to push, here both springs are needed to create a force on the chamber. Depending on the result of a cross-check measurement, the spring force of the titan springs should be increased.

Finally, the successful setup of the translation and tilt system and the demonstration of the cryogenic functionality was an important step during the setup of PENTATRAP. With a comparably simple test setup (e.g., a laser setup would have been a lot more complicated to put into practice) the behavior of the system was systematically tested. It should be noted, that the used test assembly is sensitive on misalignment errors. Moreover, it is time-consuming, since every picture is read out manually. As soon as stored ions are available, the system will be investigated again, especially the declination behavior should be of course cross-checked. The optimization of the misalignment angle θ is carried out by maximizing the axial frequency for a fixed trapping voltage, see Sec. 2.2.2.

7.5 First installation of the cryogenic part and Penning-trap cabling

So far the Penning-trap setup (Sec. 7.3) and the translation and tilt system (Sec. 7.4) have been addressed. In this section the remaining components and the first complete assembly of the cryogenic components as well as the cabling of the Penning traps are described.

7.5.1 Installation of the cryogenic components

The by far mechanically most sensitive part of PENTATRAP - apart from the Penning traps - is the so-called feedthrough flange. It consists of the cryogenic-electronics chamber flange and the lower Penning-trap chamber flange which were both welded to a titanium bellow. In the electronics chamber flange twenty four-pin feedthroughs are located. They are needed to cover the high demand of electric lines for the Penning trap and the complete detection system. Special custom made feedthroughs with low magnetic susceptibility from the company *Kyocera* were used. Their insulator is made of oxide ceramic Al_2O_3 , and the pins and the outer jacket are made of OFHC copper. For the connection of the ceramic to the copper a special Ag-Cu brazing material was used to keep the magnetic susceptibility of the product small. The brazing material has a melting temperature of 780°C . The company guarantees for a handling of the feedthroughs up to a maximum temperature of 300°C . Three possible fixations of the feedthroughs at the flange were investigated:

1. Indium sealing: The feedthroughs were pressed by little plates, which were screwed at the copper flange, on indium wire. The cover plates were positioned

evenly and the fastening screws tightened.

2. Soldering: All feedthroughs were soldered simultaneously on a heating plate. Thereby, the heat transfer was realized employing a copper disk with a hole pattern. For soldering the solder *Castolin 157* with the flux material *Lavar 21* was used at a temperature between (220-240) °C.
3. Welding: One after the other the feedthroughs were welded in. The precision mechanics at our institute reported to us that temperatures were locally a factor 2-3 larger than during the soldering process.

For testing the indium sealing at room and cryogenic temperatures, a special test setup was built. Due to the limited space on the electronics chamber flange, it was difficult to arrange the cover plates and the associated screws. Thus, the created force on the indium sealing was probably not uniformly distributed leading to a non successful test. It is worth mentioning that care must be taken not to crack the feedthroughs by applying too much force on them. Thereupon, the feedthroughs were welded in the first feedthrough flange. However, after the welding process some feedthroughs were not vacuum-tight. They were drilled out and afterwards new feedthroughs were soldered in. Currently, a second feedthrough flange is equipped with all feedthroughs being soldered in. A photograph of the complete feedthrough flange is shown in Fig. 7.25(a) and a photograph of a single feedthrough is shown in Fig. 7.25(b).

Further components of the cryogenic assembly which were built up are the custom-made absorbers to improve cryo pumping. The material of choice is charcoal providing a large surface on which the residual gas particles cryo-condensate. The cryosorption scales with the surface which is usually between (1000-2000) m²/g large and the pore size distribution [181]. At PENTATRAP the cryopumps were realized

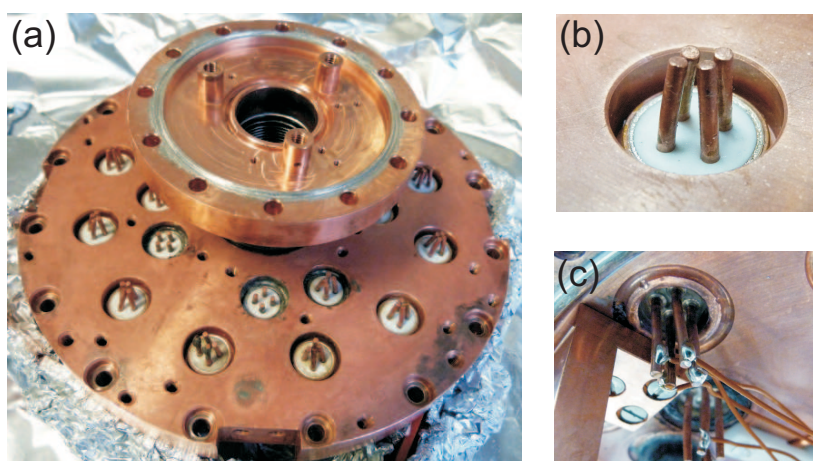


Figure 7.25: (a) Photograph of the feedthrough flange consisting of the electronics chamber flange equipped with twenty four-pin feedthroughs and the lower Penning-trap chamber flange. Both flanges are welded to the same titan bellow. (b) Photograph of the 4-pin feedthrough and (c) photograph of the indium soldered wire at the feedthrough pins.

by charcoal pellets glued on OFHC copper plates. The pellets, model *RB* from the company *Norit*, have a diameter of 3 mm. Due to the limited space, no higher and sophisticated arrangement of the charcoal providing an even larger surface was built up. As adhesive *Stycast 2850FT* with *catalyst 9* was used. It provides good thermal conductivity, since the heat transferred by the condensed particles should be transported away. Prior to the assembly in the respective chamber the charcoal absorbers should be backed out under vacuum. After being cooled down to room temperature, they should be built in quickly. The heating is necessary to remove gas particles deposited during the storage at room temperature. Limited by the maximum operating temperature of the adhesive, a heating temperature of up to $+130\text{ }^{\circ}\text{C}$ can be chosen. This temperature corresponds with the approximate temperature needed for a complete regeneration given in [181]. At PENTATRAP one cryo pump is located at the bottom of the electronics chamber (see Fig. 7.26(a)) and one in the Penning-trap chamber (see Fig. 7.26(a)).

Before the Penning traps were built in the trap chamber the copper parts of the feedthrough flange were carefully cleaned. In a first step they were degreased with acetone and the dirt from the surface was removed. Afterwards, they were deoxidized with citric acid and finally rinsed with deionized water. Thus, on the one hand it is avoided that dirt can attain the Penning-trap volume. On the other hand the careful cleaning of the electronics chamber flange surface is needed to guarantee a proper electric ground connection of the filter boards.

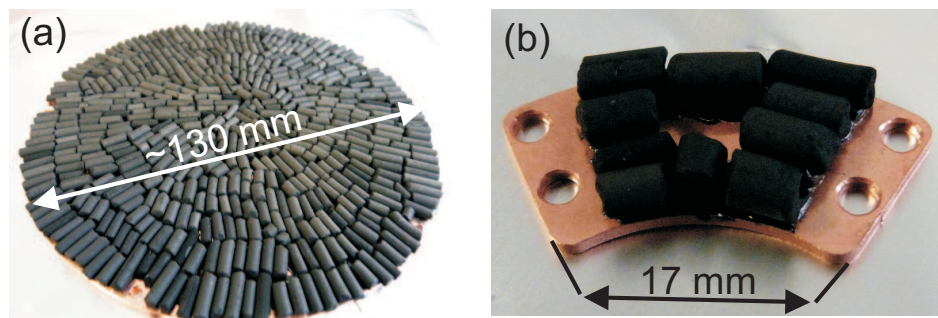


Figure 7.26: Photographs of the charcoal absorbers. (a) Large absorber placed in the electronics chamber and (b) small absorber placed in the Penning-trap chamber. Both consist of charcoal pellets glued on a copper disc.

7.5.2 First cabling of the Penning traps

In the first simplified Penning-trap setup only traps 2 and 3 (counted from the top) were foreseen for frequency measurements. In this setup one endcap electrode is connected to an axial detection system, respectively. In each trap one splitted correction electrode is used for the excitation of the ion movement. The electrodes of trap 1 are only connected to permit the transport to the lower traps 2-3. The electrodes of traps 4-5 were all connected with each other and were grounded.

For the voltage supply lines of the Penning trap and the axial amplifiers teflon insulated copper wire, and for the signal lines cryo-coax cables were chosen. Standard lead solder was used for the connections to the trap pins, the resonators, the amplifiers and the filter boards. For the connection to the feedthrough pins we tested a

special indium solder (In52Sn48) and the associated flux *Indium TACFlux012* (see Fig. 7.25). This solder allowed us to solder at only around 180 °C, due to its low melting point of around 118 °C. In comparison the widely-used lead solder Sn60Pb39Cu1 has a melting point of (183-190) °C. By choosing a low soldering temperature the thermal stress on the feedthrough is minimized. However, this procedure was very time-consuming, since every single pin needed to be cleaned separately prior to the soldering. For the cleaning the same cleaning procedure as carried out for the feedthrough flange was applied. Moreover, some practice is needed to realize a good soldering joint, since the solder did not wet the pins very well. For the future, we therefore plan to employ plug connectors to ease and speed up the process. A photograph of the cabled setup is shown in Fig. 7.27(a). Later, outside the vacuum for connections between the cryogenic and the room temperature region manganin wires will be used for the supply lines and cryo-coax cables for the signal lines. At first, the cabling outside the vacuum was not carried out. The lowering and lifting procedure, the helium consumption, and the obtained vacuum should be investigated first. In case these tests failed, all time-consuming cablings were in vain.

Finally, all cryogenic components were assembled. In Fig. 7.27(b) a picture of the setup ready to be lifted into the cryogenic magnet is shown. The location of the polished aluminum radiation shieldings as well as the so-called “cryo-cotton” placed between them are indicated. The cotton was fixed with absorbent gauze

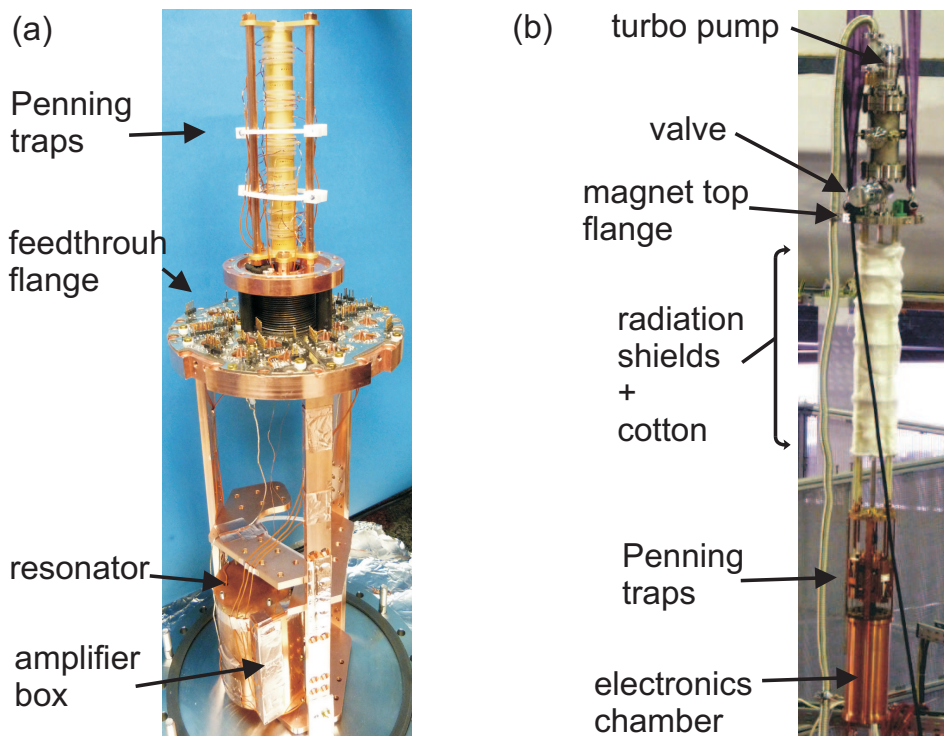


Figure 7.27: (a) Photograph of the first cabled setup of the Penning traps. In this first test setup only two traps were foreseen for frequency measurements. The traps were each connected to an axial detection system. (b) Photograph of a part of the PENTATRAP experiment hanging on the heavy-duty crane in the accelerator hall. The assembly was maneuvered over the superconducting magnet and lowered into its cold bore.

which is usually used in medicine. The cotton should slow down the helium flow, and hinder the flow of warm ambient air into the cold-bore during the lifting of the experiment. Thus, the condensation of the warm ambient air at the cold surfaces should be reduced. This is favorable, since liquid oxygen can freeze out and can accumulate at the homogeneous center of the magnet due to its paramagnetism. So far a pressure at room temperature of a few 10^{-7} mbar was achieved employing the turbo pump *TURBOVAC SL 80 H* from *Oerlikon Leybold Vacuum* placed on top of the assembly (see Fig. 7.27(b)). In the future the final setup will be connected to the NEG-coated beamline, which is pumped by a more powerful turbo pump and an ion getter pump, and much lower pressures will be realized.

7.6 First cool down of the experiment in the superconducting magnet

The successful setup of the cryogenic parts of PENTATRAP was addressed in Sec. 7.5.2, the first lowering and lifting test of the experiment is described in this section. During the tests some technically challenging problems arose:

- The accumulation of air in the bore of the magnet and the problems arising from that.
- The tilting of the cryogenic insert during the lifting of the experiment.

The partially freezing of the bore due to the accumulation of paramagnetic oxygen ice at the homogeneous center of the magnet is critical (see Fig. 7.28(a)). On the one hand the experiment might not fit into the cold bore any more. On the other hand, in case the ice accumulates after the experiment is lowered in the magnet, the experiment might freeze to the ice making in a worst-case scenario a lifting impossible. Therefore, we removed all disturbing ice in the bore prior to the lowering of the experiment. The used ice-removing tool made of aluminum is shown in Fig. 7.28(b). It has a sharp edge with which the ice was broken and shoveled. The small container was used to transport the ice out of the magnet. Moreover, the flow of warm ambient air into the cold-bore and at the cold experiment's surface during the lifting procedure was hindered. For this purpose a plastic tube was fixed at the magnet's top flange and held tight around the experiment during the lowering. In the volume between the tube and the experiment helium gas was permanently let in via a gas inlet. *Nowoflon* FEP foil was found to be the foil material of choice, since it can stand the cold temperatures. The joint of the foil is made employing thermo-impulse sealing at the company *Koch Membranen*. A few more techniques had been tested which will be addressed in [140].

During the first lowering of the experiment we found out that the outer diameter of the cryogenic insert (158 mm) was chosen to large compared to the diameter of the bore (160 mm). Therefore, material was removed, apart from the translation and tilt stage, to realize an overall diameter of below 156 mm. Additionally, the lower electronics chamber flange was removed and instead the bottom plate was directly welded to the chamber. After this modifications the system was fitting into the magnet. A picture of the experiment's lifting through the ceiling is shown in

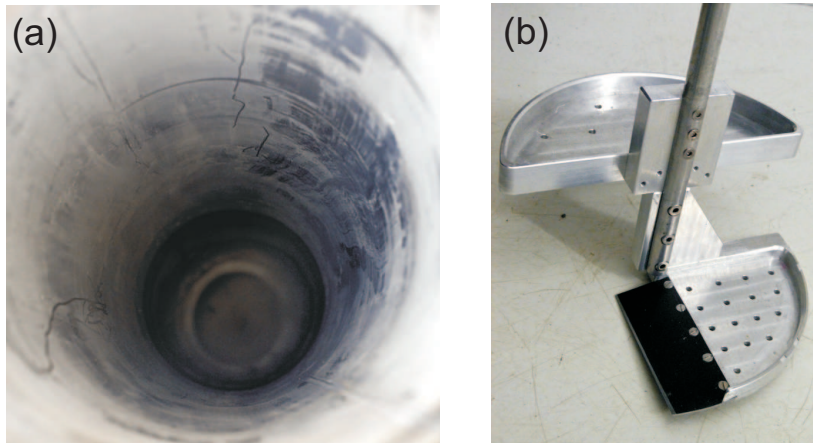


Figure 7.28: (a) Photograph of paramagnetic oxygen ice in the cold bore of the magnet. The ice was accumulated in the homogeneous center, since there the magnetic field strength is maximal. (b) Tool used to remove the ice from the bore. The tool was operated from the top of the magnet.

Fig. 7.29. Thereby, the experiment is hanging on the 10 t ceiling crane in the first floor of the accelerator building. Currently another improvement of the setup is under development. During the lifting of the experiment a tilting of the cryogenic insert with respect to the magnet's axis occurred. As a result the cryogenic insert scratched at the magnet's bore and undesired stress at the small CF 16 flange located at the magnet's top flange occurred. Thus, an advanced hanging structure at the

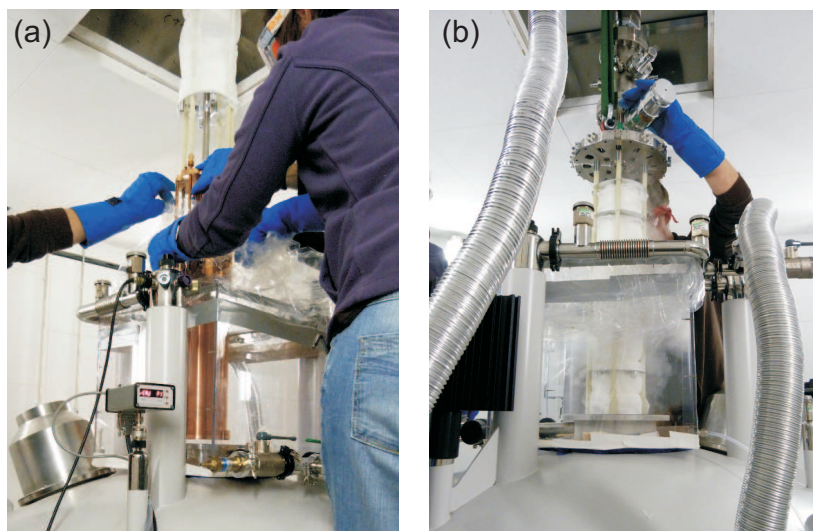


Figure 7.29: Photographs of the first lowering of the experiment in the superconducting magnet. In (a) the experiment is directly hanging over the magnet's bore. Here, everything is prepared to start the cooling process. In (b) the experiment is already lowered in the magnet up to the radiation shields. For the whole procedure at least five people are needed. One person is operating the crane and two guide the experiment and take care directly at the magnet. The fourth person is controlling that the experiment properly passes the ceiling. For safety reasons a fifth person is standing in the accelerator hall.

crane is developed to allow for a better adjustment of the experiment with respect to the magnet's bore. Moreover, a bellow is installed below the magnet's top flange to minimize the stress on the CF 16 flange.

Chapter 8

The PENTATRAP-EBIT

In this chapter the commissioning of the PENTATRAP-EBIT and first production studies of highly-charged ions are presented. The utilized commercial EBIT is called in the following Dresden-EBIT3. In Sec. 8.1 the Dresden-EBIT3 and in Sec. 8.2 the measuring setup in the accelerator hall are described in detail. The commissioning and the characterization of the EBIT (Sec. 8.3) and charge breeding studies of xenon ions (Sec. 8.4) are addressed. Later, in Sec. 8.5 the first ion production studies of highly-charged rhenium and osmium ions for β -decay studies, and in Sec. 8.6 the complete charge breeding studies are summarized.

8.1 The setup of the Dresden-EBIT3

The commercial EBIT employed at PENTATRAP is operated at room temperature [182]. It has a compact design and is additionally equipped with a Wien filter for a selection of the mass-to-charge ratio of the produced ions. The different elements are presented in the following.

A main component is the cathode, it emits the electron beam which is required for the radial confinement and the stepwise ionization of the ions. The emitting cathode material consists of a metal alloy containing cerium and iridium and has a radius of $r_c = 0.5$ mm. Thereby, the maximum heating current is 2.0 A and a maximum electron beam current of about 50 mA can be achieved. The temperature at the cathode is approximately 2000 K. It is worth mentioning, that the cathode is a very sensitive device. During the commissioning of the EBIT mechanical stress on the outer feedthrough should be avoided. The mounting of the cathode wire can be easily bent resulting in a misalignment of the emitting direction with respect to the central axis of the EBIT. A photograph of the cathode is shown in Fig. 8.1(a).

For the axial compression of the electron beam a permanent SmCo magnet and soft iron components are used. A magnetic field strength of 0.25 T is realized on-axis. The electrostatic potential required for the axial confinement of the ions is applied at three drift tubes. A photograph of them is shown in Fig. 8.1(b). The complete electrode arrangement including also the cathode, the collector and the extractor is sketched in Fig. 8.2. Neglecting space charge effects, the electrostatic potential experienced by the ions in the EBIT volume is given by

$$V_{\text{appl}} = |U_C| + |U_A| \quad (8.1)$$

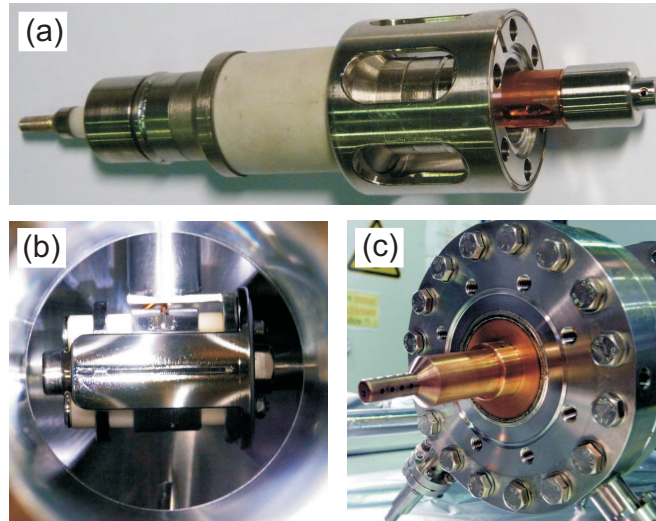


Figure 8.1: (a) Photograph of the dismounted cathode which will be mounted at a CF16 flange for operation. The ions are emitted at the right side. (b) Photograph of the trap drift tubes having a length of 20 mm. The photograph is taken through the opening of a removed CF40 flange. (c) Photograph of the water-cooled electron collector being fixed at a CF100 flange. All components shown here were purchased at the company *DREEBIT GmbH*.

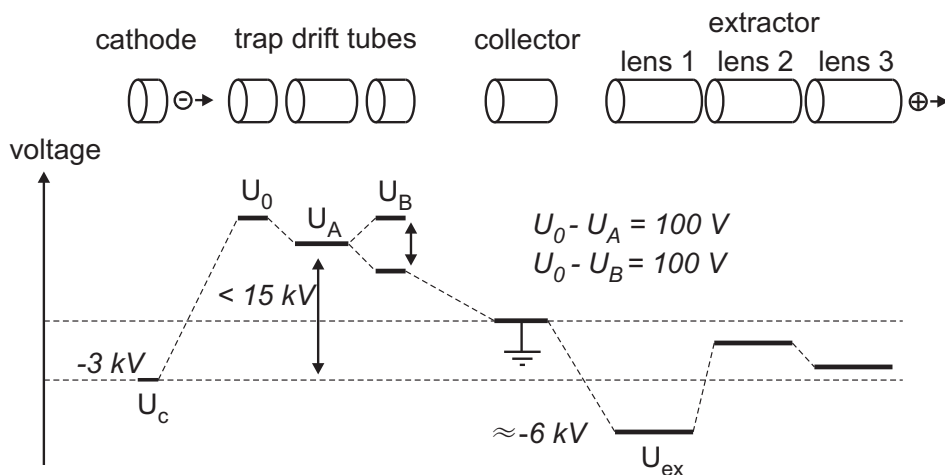


Figure 8.2: Sketch of the electrode arrangement and the applied potentials at the Dresden-EBIT3. At the top of the picture the electrodes consisting of the cathode, the trap drift tubes, the electron collector and the three extraction lenses are sketched. The length from the cathode to the end of the extractor is about 500 mm. At the bottom of the picture the associated potentials and the recommended voltage settings are included. The ions will be confined, in case the voltage U_A at the central drift tube is lower than the voltage at the outer electrodes U_0 and U_B . By lowering the voltage of the outer trap drift tube U_B by a few tens volt with respect to U_A the confinement time in the EBIT can be changed. The voltage applied at lens 1 U_{ex} should be lower than the voltage applied at the cathode U_C to extract the ions and to deflect them like an einzel lens. The shown value of U_{ex} is just an example. It will be adjusted in the particular measurements. More details are given in the text.

(see also Eq. (3.3)), where $U_C = -3\text{ kV}$ is the voltage applied at the cathode and U_A is the voltage applied at the central drift tube electrode. The maximum value of V_{appl} , which can be achieved with the Dresden-EBIT3, is about 15 kV . It is worth mentioning that the electron beam energy, which defines the ionization energy, is notated in the following as $E_e = e \cdot V_{\text{appl}}$. However, the value of E_e is reduced by the radial space charge potential of the electron beam (see Fig. 3.6). This notation is chosen, since we are at first glance not interested in the exact value of E_e but rather in the created charge states for a fixed applied voltage. The ion energy is given as $E_i = q \cdot U_A$. The confinement time of the ions in the EBIT can be adjusted by fast lowering or rising the voltage at the outer drift tube U_B . For the measurements presented later a voltage difference $U_B - U_A$ of 50 V was chosen. It should be noted that for all measurements presented in Chap. 8 the trap depth of the EBIT was set to the recommended setting of $U_A - U_0 = -100\text{ V}$ [182].

The electrons are collected at the water-cooled and grounded collector. The extractor is used to extract the ions, since the extractor lenses 1-3 can be utilized as an einzel lens. A photograph of the mounted EBIT and the Wien filter is shown in Fig. 8.3.

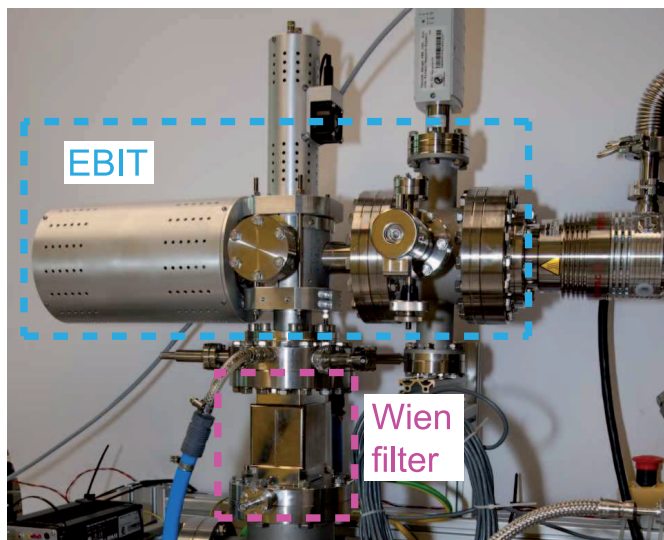


Figure 8.3: Photograph of the Dresden-EBIT3 setup. Behind the Dresden-EBIT3 the Wien filter is directly located.

A component of the EBIT supply structure is the so-called EBIT Power Control (EPC) unit [182]. It is a safety switching device controlling the pressure in the EBIT and the cooling of the collector. The interlock circuit of the device is connected to the pressure measurement and control unit *Maxi Gauge* from *Pfeiffer*, which reads out the pirani vacuum gauge at the EBIT. Moreover, a water flow meter from *Kobold* and a controlled water valve from *Bürkert* are integrated in the interlock circuit. The closed cooling water circulation is provided by a laser cooler *P500* from *Termotek*. In case the pressure rises above 10^{-7} mbar or the water flow is interrupted the cathode heating and potential is switched off.

For the gas inlet into the EBIT an all-metal control valve *UDV 146* and the associated controller *RVG 050C* both from *Pfeiffer* are implemented. The pressure

gauge measures the actual pressure in the EBIT and gives a signal to the controller, which in turn regulates the gas dosing valve to sustain the set pressure. In front of the control valve the gas connection sketched in Fig. 8.4 was arranged. This setup was used for the production of metal ions via the MIVOC (Metal Ions from the Volatile Compounds) technique [183]. A reservoir filled with the powder of the volatile metal compound of interest was evacuated to the vapor pressure of the compound. Thus, metal ions and molecular fragments evaporate which are then let into the EBIT volume for ionization. Later in Sec. 8.5 the method is used for the creation of rhenium and osmium ions. In case the valve to the reservoir and the pump are closed, gaseous species of interest can be fed into the EBIT via a connection to a pressure can or a pressure cylinder. Thereby, a pressure-reducing valve should be connected prior to the pressure can or cylinder.

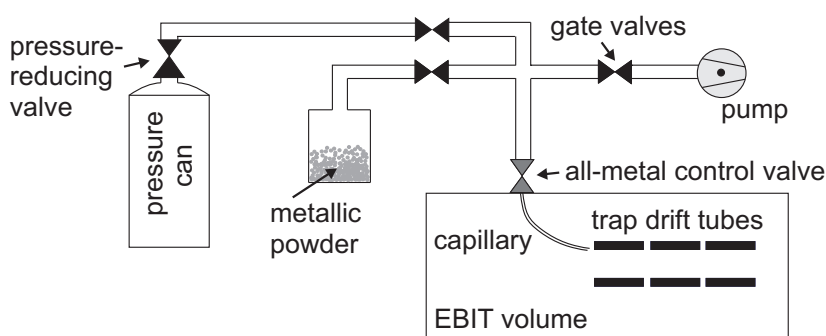


Figure 8.4: Sketch of the EBIT gas connection used for the production of metal ions via the MIVOC (Metal Ions from the Volatile Compounds) technique [183]. The indicated metallic powder is the volatile metal compound of interest. First, the gate valve in front of the pump is opened and the volume up to the other gate valves is evacuated to keep the residual gas background small. Then, e.g., the gate valve in front of the reservoir of the compound is opened. In case the reservoir is evacuated to the vapor pressure of the compound, metal ions evaporate which are then let into the EBIT volume via a small capillary. Moreover, the connection to a pressure can providing gaseous species of interest is indicated. The gas flow is regulated with the all-metal control valve located directly at the EBIT.

8.1.1 The Wien filter

A photograph of the Wien filter is shown in Fig. 8.5. The $\vec{E} \times \vec{B}$ filter separates the ions with respect to their velocities. Thereby, the electric \vec{E} and the magnetic \vec{B} fields are orthogonal to each other. In case the ion velocity is orthogonal to the fields, the ions of interest with the velocity $v_{\text{Wien}} = E/B$ pass the Wien filter and the remaining ion species are deflected. The main components of the used Wien filter are a 0.52 T permanent magnetic yoke, two opposed electrodes which can be supplied with ± 1 kV, respectively, and an entrance and separation aperture [184]. The total length of the Wien filter from its entrance aperture to its separation aperture is 153 mm. The drift distance from the end of the magnet to the separation aperture is 50 mm. Depending on the aperture size the resolution is between 20-100 [184]. For Kr^{20+} ions, an aperture of 1 mm and an ion start potential of 11 kV allowed a

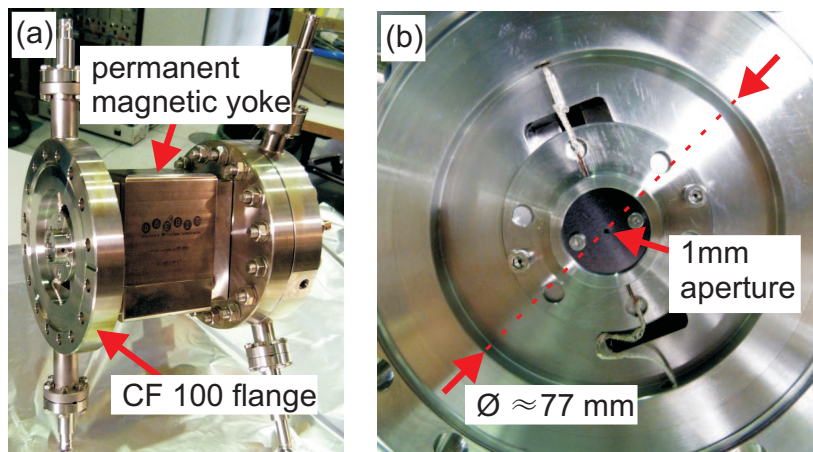


Figure 8.5: Photographs of the Wien filter. (a) Overall view showing the mounting for the strong permanent magnetic yoke. (b) 1 mm aperture of the Wien filter. It can be changed to 0.5 mm or 1.5 mm.

resolution of 40 [184]. The resolution can be increased to 80 for a smaller aperture of 0.5 mm with the consequence of a loss in beam intensity.

8.2 The measurement setup in the accelerator hall

An overview of the PENTATRAP setup in the accelerator hall is shown in Fig. 8.6. The location of the Dresden-EBIT3 and the Heidelberg-EBIT are indicated in the photograph. The highly-charged ions which are produced at the Dresden-EBIT3 are guided through the beamline towards the Penning traps located in the basement.

The beamline components and the detectors employed for the following EBIT measurements are sketched in Fig. 8.7. The ions were detected at two positions in the beamline (see also Chap. 4). The first detector (detector 1) was located behind the Wien filter and the second one (detector 2) in the basement above the superconducting magnet. The drift distance of the ions from the EBITs trapping region to the detector was about 0.5 m and about 2 m, respectively. Ion optical elements such as steering electrodes used for an adjustment of the beam position and drift tubes used for a focussing of the ion beam were installed in the beamline. The voltages applied at the EBIT drift tubes and at the optical elements placed in the beamline were provided by the *CAEN* power supply main board *SY2527*.

A sketch of the detection setup and the signal processing steps are given in Fig. 8.8. The ion signal was detected by a two inch MCP detector from *El-Mul Technologies* and subsequently amplified using the fast-timing pre-amplifier *VT120* from *Ortec*. Further, the signal was processed by a Constant Fraction Discriminator (CFD) and a TTL-to-NIM converter before the Multi-Channel Scaler (MCS) determined the time-of-flight spectrum. During the data acquisition time t_{DAQ} , i.e. when the voltage U_{B} was lowered, the time-of-flight spectrum was recorded with the MCS card *MCS-pci* from *Ortec*. After U_{B} was raised up, the ions were confined for the time t_{conf} in the EBIT. Both switches sketched in Fig. 8.8 were from *Behlke* (model *GHTS A*). Their trigger was provided by a Pattern Pulse Generator (PPG). For the PPG an arbitrary waveform generator *AG33250A* from *Agilent* was used.

The starting trigger pulse of the MCS was delayed by a few hundred nanoseconds related to the pulse of switch 1 which opens the traps. Thus, the noise of switch 1 distorting the MCS spectrum was cut off. A pulse width of 50 ns was chosen for the

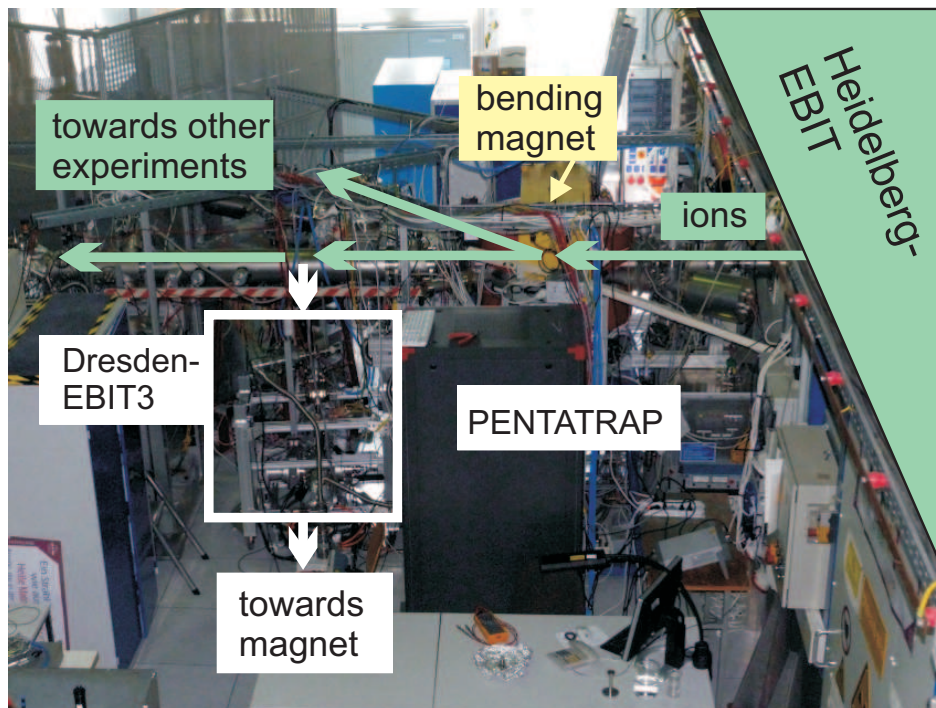


Figure 8.6: Photograph of the PENTATRAP setup in the accelerator hall and the location of the two EBITs. Ions created at the Dresden-EBIT3 will pass the PENTATRAP beamline to the Penning-trap electrodes which are located in the superconducting magnet in the basement. Highly-charged ions created at the Heidelberg-EBIT are guided to the respective experiment by employing a bending magnet. The connection of the PENTATRAP beamline to the present beamline of the Heidelberg-EBIT is currently under construction.

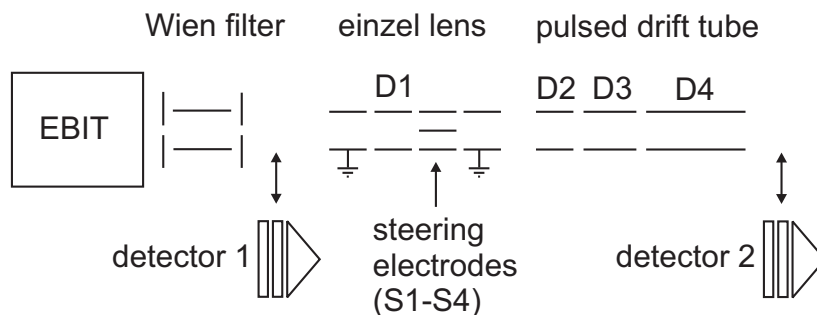


Figure 8.7: Sketch of the beamline components utilized for the EBIT measurements. After the ions were created in the EBIT and the respective mass-to-charge ratio was chosen with the Wien filter they were detected either at detector 1 or 2. Both detectors consists of a Faraday cup and an MCP detector with phosphor screen (see Sec. 4.2). Detector 1 is situated approximately 0.5 m and the detector 2 approximately 2 m below the EBIT drift tubes. Steering electrodes allow for an adjustment of the beam position and drift tubes for a focussing of the beam.

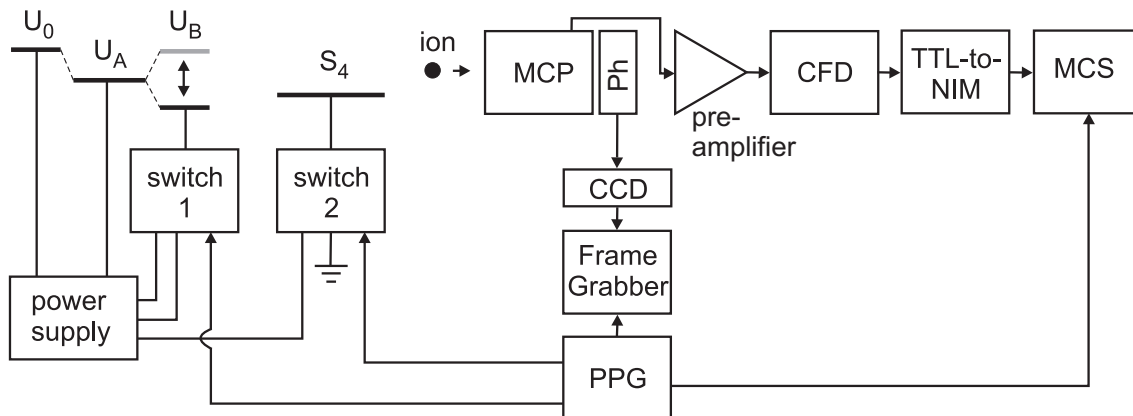


Figure 8.8: Sketch of the detection setup and the signal processing steps. The ion signal is detected with an MCP detector and afterwards amplified using a fast pre-amplifier. A Constant Fraction Discriminator (CFD), a TTL-to-NIM converter precede the Multi-Channel Scaler (MCS) with which the time-of-flight spectrum is recorded. Switch 1 is used to switch the drift tube electrode which sets the ion confinement time. Switch 2 is connected to a segment of the steering electrode in order to deflect the ion beam when the trap is closed. Thus, the background can be reduced. Switch 1 and 2, the start pulse of the MCS and the frame grabber PC card attached to the CCD camera are triggered by a Pattern Pulse Generator (PPG). The CCD camera is connected to the Phosphor screen (Ph).

pulse triggering switch 1. Further noise reduction was realized for the detection at detector 2. Here, one segment of the steering electrode was switched (switch 2) to deflect the beam when the EBIT was closed. The pictures taken with the CCD camera and the associated frame grabber *mvHyperion-CLE* from *Matrix Vision* allowed us to optically check and to optimize the beam position. The frame grabber was also triggered by the PPG such that pictures were only recorded when the EBIT was opened.

The voltages which were supplied by the *CAEN* power supply, the camera software and the MCS were controlled via the *PENTATRAP* Control System (CS). For a detailed description it should be referred to the PhD thesis of M. Goncharov [153]. With the CS it was possible to automatically scan the Wien filter voltage and to store the time-of-flight spectrum of the current Wien filter setting. Moreover, the Wien spectrum (sums of the counts of the time-of-flight spectra versus the corresponding Wien filter voltages) could be directly read out.

8.3 First characterization of the EBIT parameters

A first step of the EBIT commissioning was the characterization of the cathode in use. The characteristic increase of the heating voltage U_{heat} and of the emitted cathode current I_e with increasing applied heating current I_{heat} is shown in Fig. 8.9. It is recommended to not exceed a heating current of 2.0 A. In the following the cathode potential was always set to $U_C = -3\text{ kV}$. The supply of the cathode is part

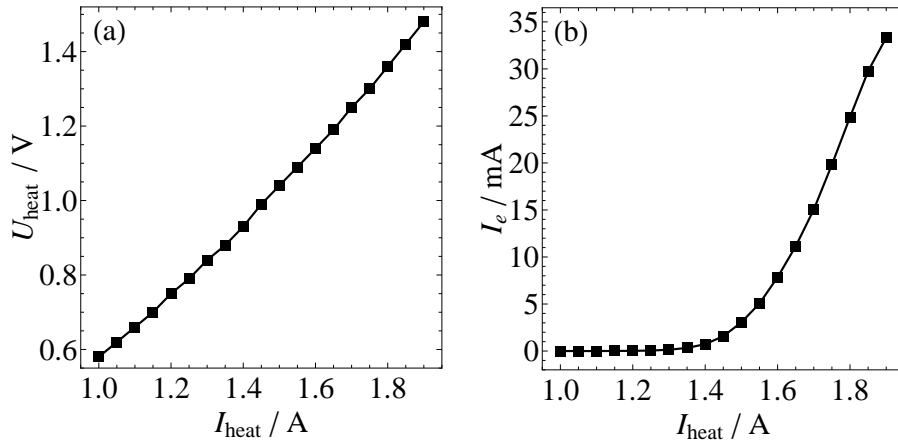


Figure 8.9: Characteristics of the cathode in use at the Dresden-EBIT3. In (a) the dependence of the heating voltage U_{heat} and in (b) the dependence of the emitted cathode current I_e on the applied heating current I_{heat} is shown. The cathode was at a potential of -3 kV. The maximum heating current should not exceed 2.0 A. Error bars are too small to be visible.

of the purchased EBIT equipment. The emitted cathode current can be read out with a $10 \mu\text{A}$ resolution. Concerning the stability of the cathode no information is provided in the manual. It should be remarked that the emitted electron beam current depends on the vacuum.

A further task was the calibration of the applied Wien filter voltage U_{Wien} to the respective mass-to-charge ratio of those ions which can pass the Wien filter. The calibration was carried out with argon ions. Therefore, natural argon gas, which was directly available at the institute, was let into the EBIT. Since natural abundant argon consists to 99.6% of the most abundant isotope ^{40+}Ar , the measured argon lines are not broadened and the gas was considered to be monoisotopic in the calibration. The Wien filter voltage was scanned and the ions were detected at the MCP detector. In Fig. 8.10 spectra used for the calibration are shown. Here, in addition the confinement time of the ions in the EBIT was changed. With the ion confinement time the ionization factor can be adjusted and thus the mean charge state. The argon peaks occurring in the Wien filter spectra were fitted with a Gaussian distribution. The assignment of the peaks was done by comparing the measured spectra with the ones taken during the acceptance test at the supplier. Considering the electron binding energies the expected mass-to-charge ratios were calculated and assigned to the respective voltage (see Fig. 8.11). The obtained values were fitted using the equation

$$\frac{m}{q} = \left(\frac{\kappa_{\text{Wien}}(U_A)}{U_{\text{Wien}} - U_{\text{offset}}(U_A)} \right)^2 \quad (8.2)$$

to obtain the calibration factors $\kappa_{\text{Wien}}(U_A)$ and $U_{\text{offset}}(U_A)$. It should be mentioned that the calibration depends on the electron beam energy E_e and therefore on the voltage U_A . The calibration was carried out for two settings of U_A , which was sufficient for the first charge breeding measurements. In Tab. 8.1 the obtained parameters are listed.

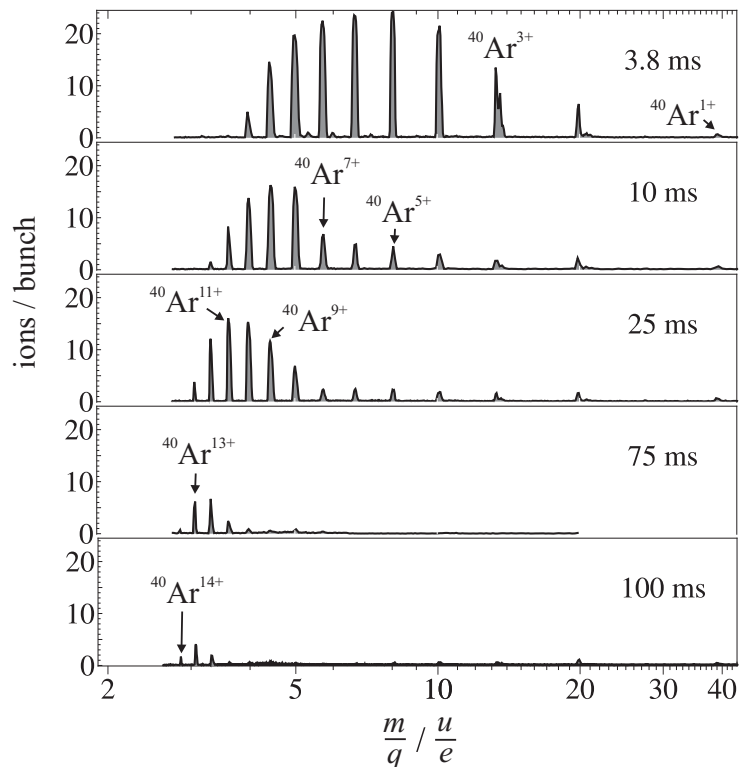


Figure 8.10: Wien filter scans of argon ions stored for different confinement times in the EBIT. The spectra were used for the calibration of the Wien filter. Therefore, the peak maxima were assigned to the theoretically expected mass-to-charge ratios and fitted with the function given in Eq. (8.2). Here, the x -coordinates are already transformed in units of m/q . The mean charge state can be adjusted by changing the ion confinement time in the trap. The settings were $U_A = 2.9$ kV and $I_e = 18.00$ mA.

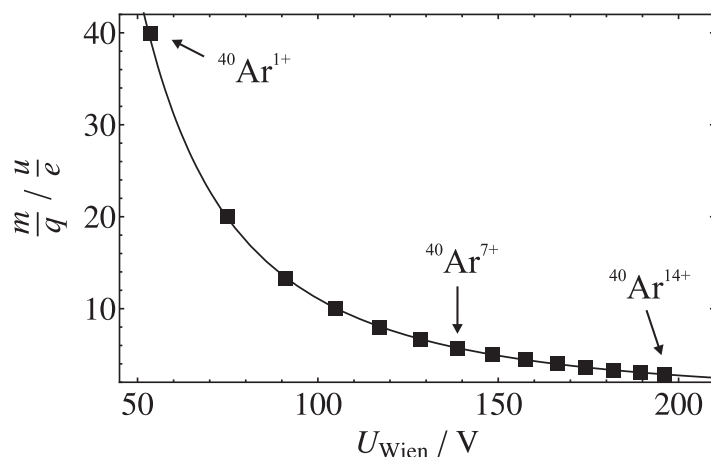


Figure 8.11: Assignment of the Wien filter voltage to the respective mass-to-charge ratio. The m/q ratios were calculated considering the electron binding energies and assigned to the determined peak maxima of Fig. 8.10. The settings were $U_A = 2.9$ kV and $I_e = 18.00$ mA. The points were fitted using Eq. (8.2). Error bars are smaller than the data points.

Table 8.1: Obtained calibration factors of the Wien filter. Argon ions were used to determine the factors $\kappa_{\text{Wien}}(U_A)$ and $U_{\text{offset}}(U_A)$ of Eq. (8.2). For further details see text.

U_A / kV	U_{offset} / V	κ_{Wien} / ($\text{V} \cdot \sqrt{\text{m/q}}$)
2.9	+0.899(11)	329.93(3)
5.9	-2.800(60)	416.69(17)

Currently, the power supply boards of the Wien filter *A1737P* and *A1737N* from *CAEN* were used up to ± 250 V. Therefore, the minimal addressable mass-to-charge ratio was 1.75 u/e for $U_A = 2.9$ kV and 2.72 u/e for $U_A = 5.9$ kV, respectively. The minimal stepwidth of the positive and the negative applied Wien filter voltage could be set to 0.05 V steps and the accuracy of the set voltage versus the output voltage is stated to $\pm 0.3\%$ by the supplier. The power supply boards *A1526P* and *A1526N* from *CAEN* were used for the supply voltage of the trap electrodes and the lenses. Their resolution is about 1 V and the accuracy of the set voltage versus the output voltage is specified to $\pm 0.3\% \pm 1$ V. Moreover, it is worth mentioning that the ion count rate shown in Fig. 8.10 and the ones shown in the following spectra are the measured count rates at the respective MCP detector. In the energy range of operation the efficiency of the MCP is about 30% to 40% for singly charged ions and reaches an efficiency of about 60% to 70% for highly charged ions limited by the open area ratio.

Several residual gas spectra were taken between the different measurements presented later. Here, an example spectrum is shown (see Fig. 8.12). In case heavy highly charged ions are created in the EBIT, the comparable light and low charged residual gas ions are not bound any more in the EBIT. Their peaks vanish whereas new peaks of the higher charged ions occur.

8.4 Charge breeding of xenon ions

To test the functionality of the EBIT, prior to the use of some special and expensive monoisotopic gases, studies of the charge breeding of xenon ions were performed by means of natural xenon gas which was let into the EBIT. Compared to the spectra of argon shown in Fig. 8.10 the lines of the xenon ions in the Wien filter spectrum shown in Fig. 8.13 are broadened. This is due to the presence of various isotopes in the xenon gas. The most abundant stable isotopes of xenon are: ^{129}Xe (26.4%), ^{131}Xe (21.29%), ^{132}Xe (26.9%), ^{134}Xe (10.4%) and ^{136}Xe (8.9%). By increasing the ion confinement time in the trap the mean created charge state increased as can be seen in Fig. 8.13 (see also Fig. 8.10). For $t_{\text{conf}} = 3.8$ ms the maximum count rate at the MCP was obtained for the creation of $^{\text{nat}}\text{Xe}^{12+}$, whereas for $t_{\text{conf}} = 100$ ms already a much higher charge state of 30+ showed the maximum count rate. With the chosen electron beam energy of 5.9 keV the maximum attainable charge state is 43+, since the electron binding energy of the $3s^1$ electron is about 3.3326 keV. To remove the $2p^6$ electron already 7.6600 keV are required. Both values are taken from [113]. The confinement times set in Fig. 8.13 were chosen to short to produce

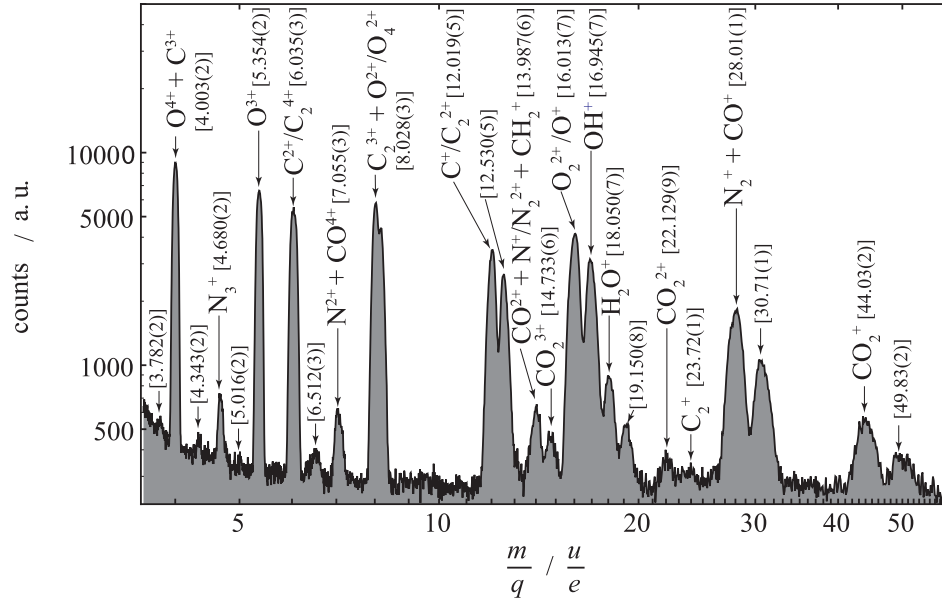


Figure 8.12: Example of a residual gas spectrum taken at $E_e = 7.9$ keV, $I_e = 22.00$ mA and $t_{\text{conf}} = 100$ ms. By changing the Wien filter voltage different mass-to-charge ratios are selected. The peaks are assigned to the most probably created ions and the determined mass-to-charge ratio of the peak maximum is shown in brackets. An extreme value distribution was fitted to the peaks. The given errors represent the errors of the fit.

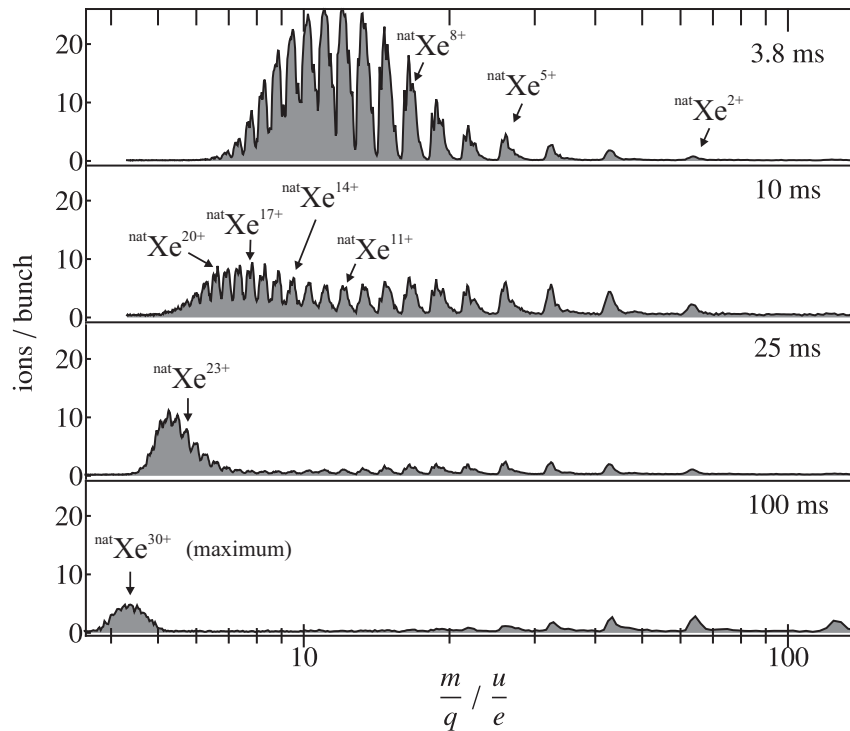


Figure 8.13: Wien filter scans of xenon ions for different confinement times in the EBIT. U_A was set to 2.9 kV and the ion beam current was 18.50 mA. For further discussions see text.

the charge state $43+$. For longer confinement times the ion beam current should be increased as well in order to get higher count rates.

For another performance test the Wien filter voltage was fixed at a mass-to-charge ratio of interest and the ion confinement time in the trap was varied. Thereby, the electron beam energy as well as the ion beam current remained constant as well. Here, a higher electron beam energy of 7.9 keV was set. Thus, the maximum attainable charge state was $45+$. To remove the $2p^5$ electron 7.8899 keV and to remove the $2p^4$ electron 8.1439 keV are needed [113]. The Wien filter voltage was set such that the mass of the most abundant isotope ^{132}Xe was chosen. Graphs of the charge state evolution of highly charged ^{132}Xe ions are shown in Fig. 8.14. A description of the evolution of the ion densities in the EBIT is presented in Sec. 3.4.3. The full rate equation is given in Eq. (3.28). The rates of electron ionization and radiative recombination processes are proportional to the electron current density and to the cross sections of the respective processes. Thereby, the cross sections depend on the electron beam energy. As can be seen in Fig. 8.14 higher charge states are produced at longer confinement times. In case frequency measurements of xenon ions will be performed in the Penning trap, the optimum confinement time for a selected mass-to-charge ratio can be determined by means of such a spectrum. It should be remarked that the spectra and the charge state distribution shown in Fig. 8.13 and Fig. 8.14, respectively, are detected at detector 1. Due to the short drift length, a full width half maximum (FWHM) of the recorded time of flight of about $0.75\text{ }\mu\text{s}$ was obtained.

For comparison the charge state evolution of $^{40}\text{Ar}^{10+}$ and $^{40}\text{Ar}^{13+}$ at an electron

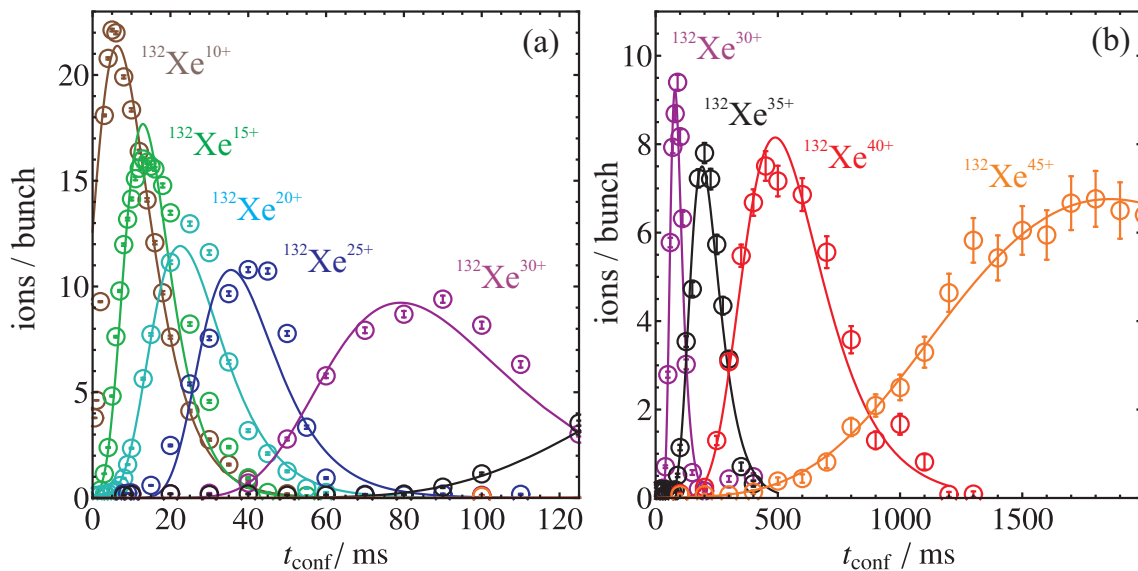


Figure 8.14: Charge state evolution of the charge states $10+$ to $45+$ in intervals of five for ^{132}Xe at $E_e = 7.9\text{ keV}$ and an electron beam current of 18.50 mA . For different confinement times t_{conf} in the EBIT ions of fixed mass-to-charge ratio are detected at the MCP and the count rate is determined. In (a) the evolution of the charge states $10+$ to $30+$ and in (b) the evolution of the charge states $30+$ to $45+$ is shown. The data were fitted with an extreme value distribution and the error bars are denoting the statistical error.

beam energy of 7.9 keV and an ion beam current of 18.50 mA is shown in Fig. 8.15. Whereas in Fig. 8.14 the pure charge state evolution of xenon ions was measured, here a charge balance of argon and oxygen was observed. Since the chosen mass-to-charge ratios of $^{40}\text{Ar}^{10+}$ and $^{40}\text{Ar}^{13+}$ are similar to the mass-to-charge ratios of $^{16}\text{O}^{4+}$ and $^{16}\text{O}^{5+}$, respectively, two peaks occur at a fixed U_{Wien} . In contrary to the charge state evolution of highly charged xenon ions, the maximum count rate of the detected argon ions remains almost constant, independent of the selected charge state. The same applies for the maximum count rate of the oxygen ions. The lower count rate of oxygen is due to the fact that light ions with low charge states leave the trap first (see Sec. 3.4.3).

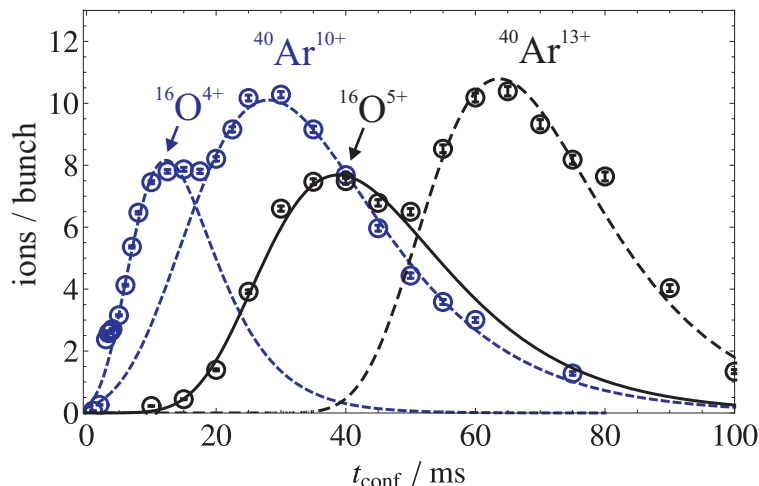


Figure 8.15: Measured charge balance of argon and oxygen ions created in the Dresden-EBIT3. The maximum count rate of the respective ion species did not change with the selected charge state. E_e was 5.9 keV and an electron beam current of 18.50 mA was chosen. The data were fitted with an extreme value distribution. The statistical errors are included.

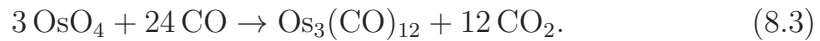
8.5 Rhenium and osmium ions for first β -decay measurements

An important step was the creation of highly charged rhenium and osmium ions needed for first mass measurements related to the field of neutrino physics. As outlined in Chap. 1, the Q -value determination of the β -decay of rhenium $^{187}\text{Re} \rightarrow ^{187}\text{Os} + e^- + \bar{\nu}_e$ is a major aim of PENTATRAP. Therefore, it is advantageous that the production of the mother and daughter nuclides of the process can be realized in a straightforward way. As it turned out, the MIVOC technique [183] is the production technique of first choice for the creation of these metal ions.

Metallocenes with low saturated vapor pressure at room temperature are candidates for the MIVOC technique. Bis(cyclopentadienyl)-compounds of the transition metals are called metallocenes (see textbooks, e.g., [185]). They consist of a doubly charged metal cation and two singly negatively charged cyclopentadienyl anions. The most prominent example is ferrocene. Further metallocenes of the iron group

are ruthenocene and osmocene. For the creation of highly charged osmium ions we therefore sublimated bis(cyclopentadienyl)osmium ($C_{10}H_{10}Os$) [186] and fed it into the EBIT as shown in Fig. 8.4. Due to the easy availability and the cheap price we firstly tested a natural osmium compound. The total mass of the compound is 320.24 u. However, for the β -decay studies the isotope ^{187}Os is required. There are two possible solutions:

1. Continuing the use of natural osmocene and selection of the isotope ^{187}Os in the Penning trap. Due to the different m/q ratios contaminating isotopes can be removed in the Penning trap (see Sec. 5.3). A disadvantage is the low natural abundance of ^{187}Os of only 1.96 %. The most frequent natural abundances are 40.78 % (^{192}Os), 26.26 % (^{190}Os), 16.15 % (^{189}Os) and 13.24 % (^{188}Os).
2. Since so far no company offering a custom synthesise of enriched osmocene has been found, a prospective would be the sublimation of enriched triosmiumdodecacarbonyl $Os_3(CO)_{12}$ compounds. The procedure would be to produce enriched osmiumtetroxid (OsO_4) and to perform the chemical reaction



Since osmium-tetroxid sublimes at room temperature it might be a possible candidate as well, however, it is very toxic.

The natural abundance of rhenium is more favorable concerning the creation of ^{187}Re ions, since the two stable isotopes are ^{185}Re (37.4 %) and ^{187}Re (62.6 %). For the production of highly charged rhenium ions the volatile compound tricarbonyl(cyclopentadienyl)rhenium ($C_8H_5O_3Re$) was evaporated and inserted into the EBIT. The total mass of the compound is 335.25 u. It should be remarked that rhenium(VII)-oxide (Re_2O_7), which is another possible volatile compound, was not tested due to its toxicity. In general, a variety of inorganic compounds with low saturated vapor pressure can be selected and tested [187].

Several systematic studies of the production of highly charged osmium and rhenium ions were performed. The gas inlet of the evaporated osmocene compound into the trapping region of the EBIT was studied (see Fig. 8.16). For a closed gas dosing valve a residual gas spectrum similar to the spectrum shown in Fig. 8.12 was detected. By gradually opening the valve a broad peak appeared at m/q values around 300 u/e. This peak is assigned to the creation of molecular fragments of osmocene. Simultaneously the peaks at $m/q < 10$ u/e, which are assigned in Fig. 8.12 to low charged carbon or oxygen ions, disappeared and a broad peak at about $m/q = 6$ u/e was being created. The newly occurring broad distribution of detected ions is assigned to created highly charged osmium ions. The center is at about $^{nat}Os^{32+}$. Due to the limited resolving power and the presence of multiple isotopes, the single peaks could not be resolved.

In a next step the part of the spectrum showing the created highly charged osmium ions is further investigated. Wien filter scans with different electron beam currents were performed. The remaining EBIT parameters stayed constant ($t_{conf} = 100$ ms, $I_e = 7.9$ keV). As can be seen by means of Fig. 8.17(a) higher charge states were detected at the MCP for higher electron beam currents. Moreover, the ion

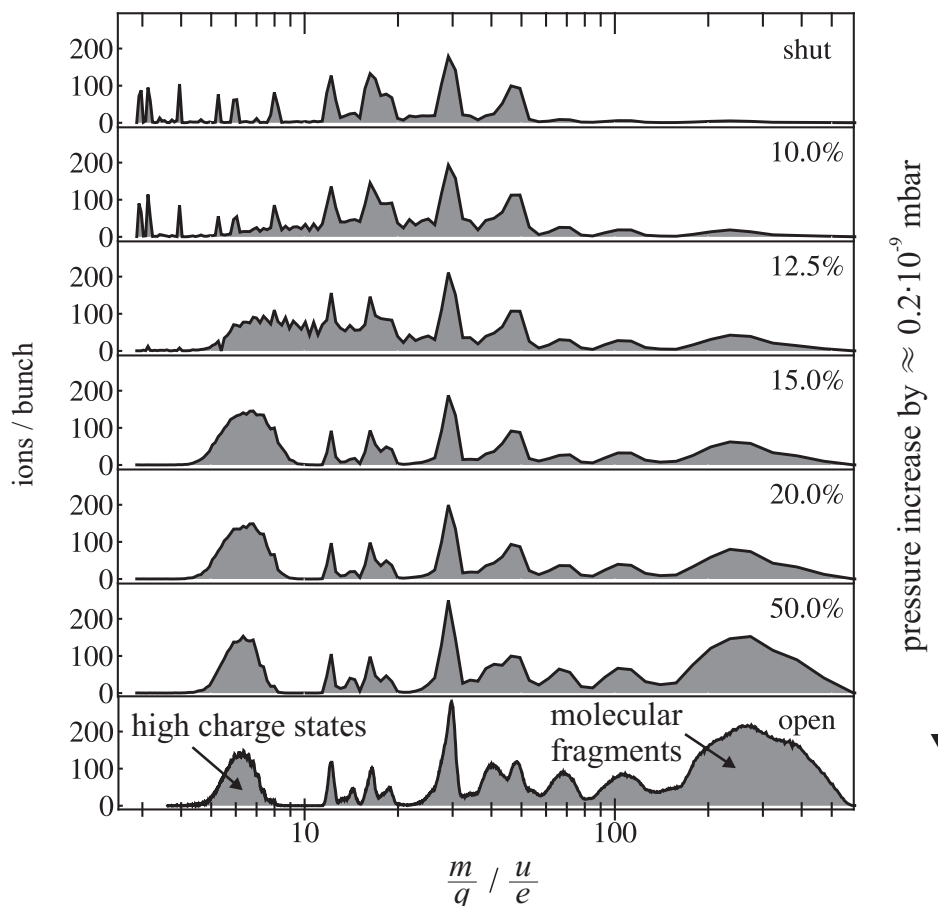


Figure 8.16: Gas inlet of natural abundant osmocene into the EBIT. The spectrum at the top shows the residual gas spectrum. From top to bottom the gas dosing valve to the EBIT was gradually opened. For m/q ratios greater than about 60 u/e molecular fragments of the evaporated compound appeared from step to step in the spectra. Simultaneously a broad peak which was assigned to highly charged osmium ions was appearing at a m/q ratio of about 6 u/e. The resolution was not high enough to resolve the single charge states of the natural abundant osmium ions. The pressure in the EBIT increased from a completely closed to a completely opened valve by $0.2 \cdot 10^{-9}$ mbar. The EBIT settings were $t_{\text{conf}} = 100$ ms, $I_e = 30.00$ mA and $E_e = 7.9$ keV.

count rate increased with the electron beam current. A high electron beam current is related to a high electron beam density, which is directly proportional to the full rate (see Eq. (3.28)) describing the evolution of the charge state distribution. It is worth mentioning that the maximum realizable ion beam current is specified to 50 mA [182]. We worked only up to about 30 mA which is the operating range assuring long cathode lifetimes [188].

Furthermore, Wien filter scans with varying ion confinement times were taken, whereby the ion current was fixed to 30.00 mA and the electron beam energy stayed at 7.9 keV. The results of the study are shown in Fig. 8.17(b). A stepwise increase of the ion confinement time from 0.1 s to 0.8 s led to the creation of higher charge states. With a further increase up to 1 s and 2 s no gain of produced charge states was realized. Since the behavior of rhenium ions in the charge breeding process is

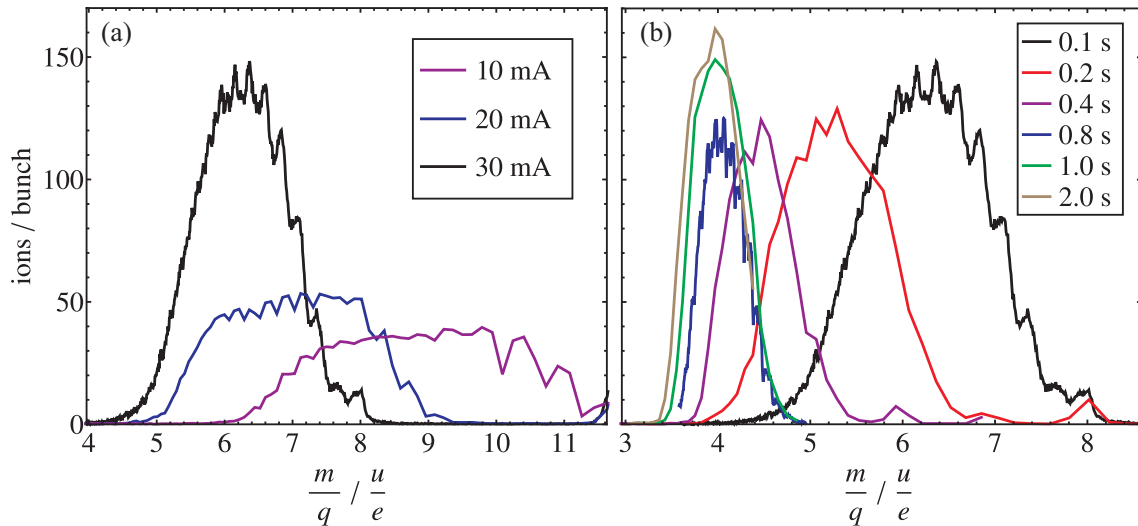


Figure 8.17: Studies to optimize the creation of highly charged osmium ions. (a) variation of the ion beam current for a fixed confinement time of 100 ms. (b) variation of the ion confinement time for a fixed electron beam current of 30.00 mA. In both graphs the electron beam energy was 7.9 keV. The black colored spectra in each of the figures are identical. Note, the x -axes in (a) and (b) are not identical. The blue colored spectrum in (b) is shown in Fig. 8.20(b) including the assignment of the peaks. For further discussion see text.

quite similar to that of osmium, the systematic studies presented till now are just shown for osmium. It should be noted that a variety of spectra were taken and here only a selection of the most evident ones is presented.

As an example of a systematic study covering the creation of highly charged rhenium ions, the evolution of high charge states of ^{187}Re is shown in Fig. 8.18. For long ion confinement times in the EBIT the count rate of the charge states 45+ and

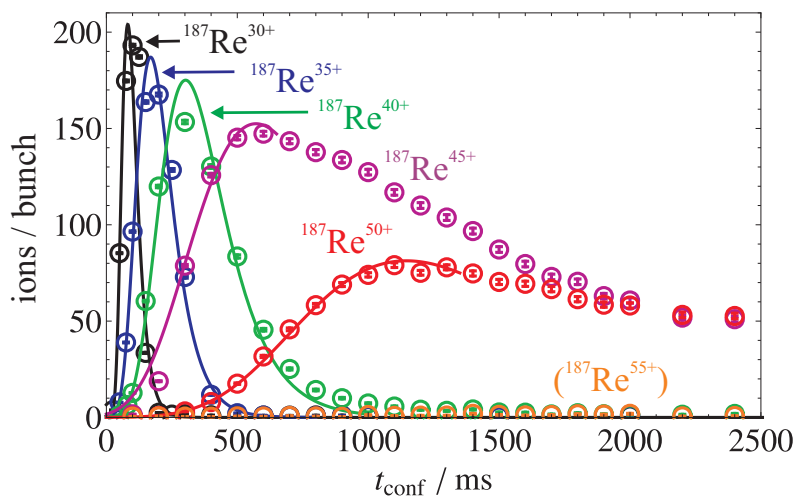


Figure 8.18: Charge state evolution of the charge states 30+ to 50+ in intervals of five of ^{187}Re at $E_e = 7.9$ keV and an electron beam current of 30.33 mA. For a fixed Wien filter voltage the ions were detected at the MCP. An extreme value distribution was fitted to the data and the errors represent the statistical error.

50+ are in saturation. The charge state 55+ could not be produced.

Moreover, it should be pointed out that the measurements presented in Sec. 8.5 were carried out using detector 2 (see Fig. 8.7). It was successfully proved that decelerated ions could be focussed and detected shortly above the PENTATRAP magnet. As an example the time-of-flight distribution of differently charged rhenium ion bunches, which are recorded at detector 2, are shown in Fig. 8.19. The ion beam energy was 4.9 kV·q. For the charge state 44+ an optimized puls width (FWHM) of about 2.5 μ s was determined.

Concluding, the production of osmium and rhenium ions with natural abundances with charge states up to about 50+ has been demonstrated (see Fig. 8.20). Since osmium and rhenium differ only by one atomic number, the expected attainable mass-to-charge ratios in the EBIT are similar. Considering the chosen electron beam energy of 7.9 keV the maximum theoretically achievable charge states are 66+ and 65+, respectively [113]. That these high charge states were not detected might be due to a too low count rate at the MCP, a not sufficiently low vacuum behind the Wien filter, or low overlap factors of the electron and the ion beam (see Chap. 3).

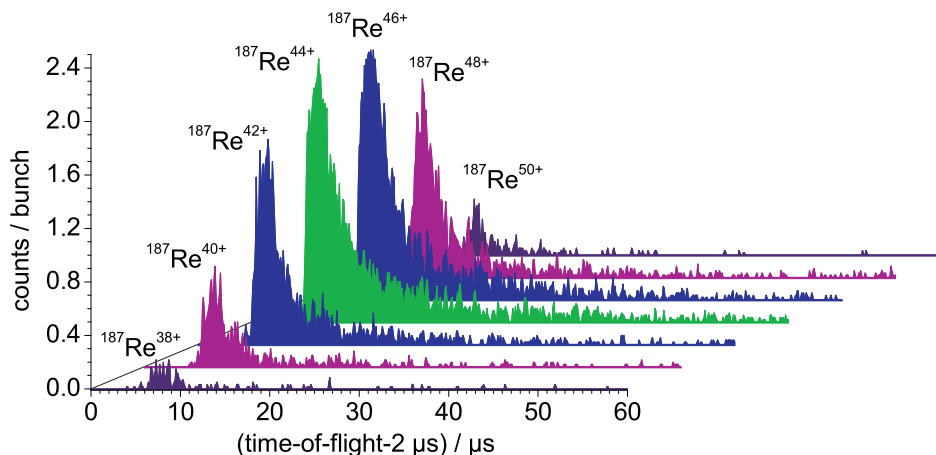


Figure 8.19: Time-of-flight spectra of differently charged rhenium ion bunches at detector 2. The m/q ratio at the Wien filter was chosen such that ^{187}Re ions were extracted. Nevertheless, contributions from other rhenium isotopes can be present. Here, the ions were confined for 500 ms in the EBIT. An electron beam current of 37.0 mA and an electron beam potential of 7.9 keV were set. The offset of 2 μ s was only introduced for signal processing purposes.

8.6 Summary of the charge breeding studies

First successful charge breeding studies of highly charged argon, xenon, osmium and rhenium ions were performed. A summary of the reached charge states and the corresponding ion confinement times is shown in Fig. 8.21. In Fig. 8.21(a) a higher electron beam energy ($E_e = 7.9$ keV) than in Fig. 8.21(b) ($E_e = 5.9$ keV) was chosen. Osmium data were not included, since they are in the same order of magnitude as the rhenium data. The electron beam currents were between 18.00 mA and 20.00 mA. The figures show that higher charge states were bred for longer ion confinement times in the EBIT. The rate equation describing the population of charge states

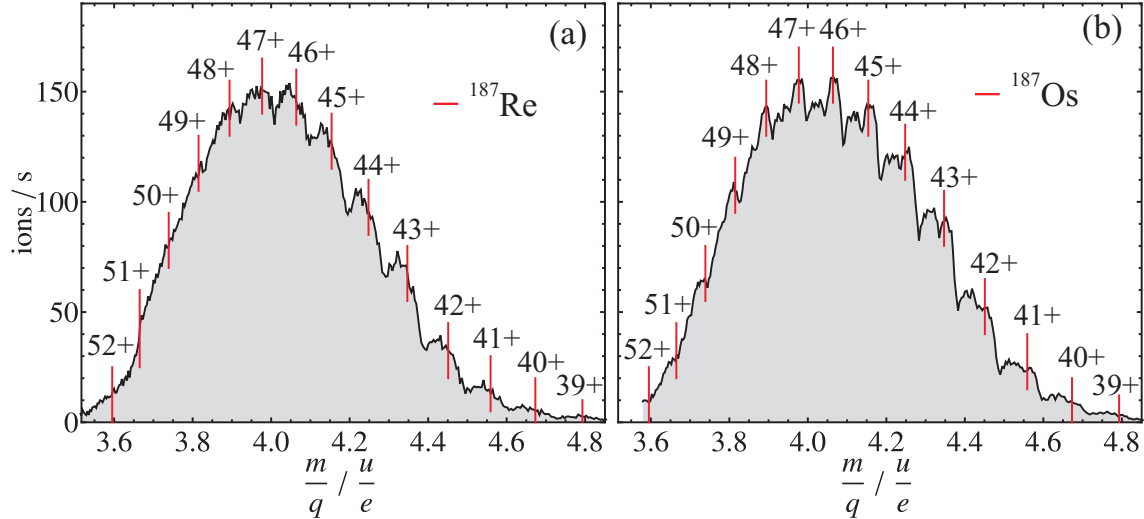


Figure 8.20: Count rate of Re ions (a) and Os ions (b) extracted from the Dresden-EBIT3 and detected with a multi-channel plate detector for different mass-to-charge ratios. In both cases the setup was operated with a trapping time of 800 ms, an electron current and energy of 30.00 mA and 7.9 keV, respectively. Osmium ions as well as various types of molecular fragments were produced by sublimation of osmocen $\text{Os}(\text{C}_5\text{H}_5)_2$ before the gas was fed into the trapping volume and ionized. For the creation of rhenium ions the compound $(\text{C}_8\text{H}_5\text{O}_3\text{Re})$ was sublimated. Both compounds had natural abundances of osmium and rhenium, respectively. In the spectrum, the resolving power was not high enough to resolve the different isotopes. It was possible to create charge states of Re and Os up to 50+. The red vertical lines indicate the position of the m/q values of the isotopes ^{187}Os and ^{187}Re which are of interest for the β -decay studies.

is directly proportional to the ion beam current density and to the cross sections of the respective processes which are dependent on the electron beam energy (see Eq. (3.28)). By means of these figures the optimum ion confinement time for the production of a required charge state of a nuclide can be chosen.

The addressable mass-to-charge ratios in the Penning trap depend on the supply voltage of the Penning trap electrodes V_0 and the resonance frequency of the axial detection circuit ν_0 (see Eq. 2.4 and Fig. 8.22). For a fixed frequency of the axial detection circuit different m/q values can be brought into resonance with the detection system by changing V_0 . The voltage V_0 required to address the charge states of the ions produced so far with the EBIT is shown in Fig. 8.22(a) for $\nu_0 = 600$ kHz and in Fig. 8.22(b) for $\nu_0 = 400$ kHz. In order to be able to address first ions in the trap with the commercial voltage source from *Stahl electronics*, the axial resonator should be tuned to 400 kHz instead to the planned 600 kHz. In the future, a highly stable voltage source (see Chap. 4) will be covering the voltage range from 0 to -100 V.

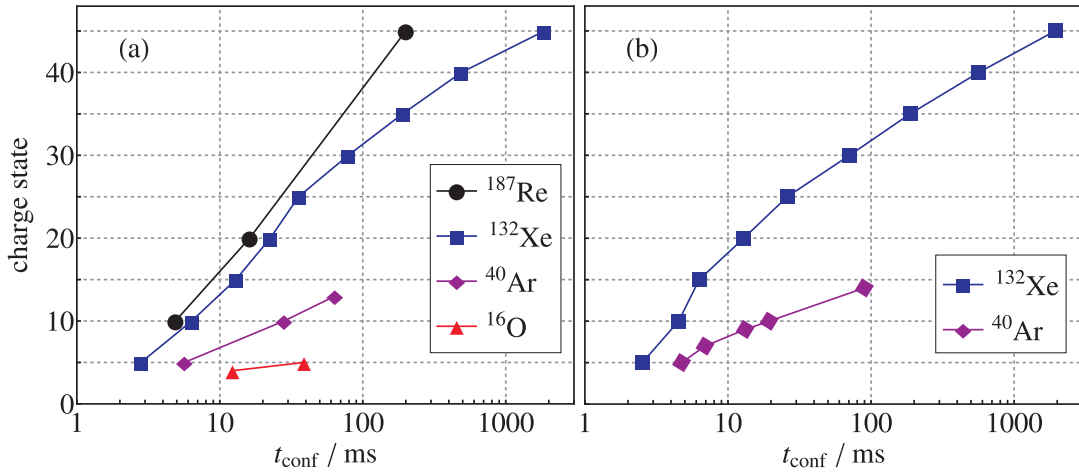


Figure 8.21: Summary of the charge breeding studies. In (a) a higher electron beam energy ($E_e = 7.9 \text{ keV}$) than in (b) ($E_e = 5.9 \text{ keV}$) was used. The electron beam current I_e was set almost constant. For argon and oxygen 18.00 mA, for xenon 18.50 mA and for rhenium 20.00 mA was set. The error bars of t_{conf} , which are too small to be visible, are the fit errors from the fit of the extreme value distribution to the charge state evolution. For example see Fig. 8.14 for the fitted xenon data. The error of q is also not visible and results from the accuracy with which the Wien filter voltage of the respective m/q ratio can be set.

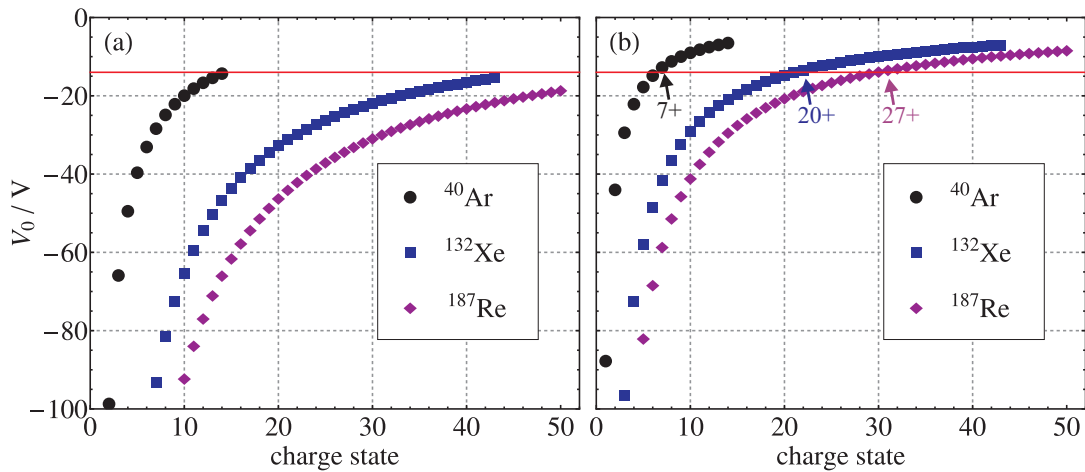


Figure 8.22: Addressable mass-to-charge ratios in the Penning trap for frequency measurements at a fixed axial frequency. Depending on the applied storage potential V_0 in the Penning trap different mass-to-charge ratios can be brought in resonance with the axial detection circuit. In (a) an axial frequency of $\nu_0 = 600 \text{ kHz}$ and in (b) an axial frequency of 400 kHz is considered. The solid line indicates the minimum output voltage (-14 V) of the available voltage source from *Stahl electronics*.

Chapter 9

Conclusion and outlook

In the context of this thesis, the installation of PENTATRAP was started and considerably put forward. PENTATRAP is a novel five-Penning-trap mass spectrometer aiming for an accuracy of up to a few parts in 10^{12} for mass ratios of long-lived highly charged nuclides up to uranium. Main features of PENTATRAP are a multi-trap configuration enabling fast and simultaneous frequency measurements, highly sensitive cryogenic non-destructive detection systems, and the access to highly charged ions via two EBITs.

Prior to the setup, ion trajectory simulations using SIMION[®] were carried out. Here, the work involved the simulation of the injection of an ion bunch into the Penning traps. It was shown that the kinetic energy and the length of an ion bunch can be reduced with an efficiency of about 90 % by employing a drift tube such that subsequent efficient trapping in the Penning traps is guaranteed. Thereby, the start parameters of a bunch of ions with a charge-to-mass ratio of 0.25 e/u and a mean axial kinetic energy of about 200 eV were estimated considering the performance of the Heidelberg-EBIT. It was successfully simulated that the ion bunch can be captured with an efficiency of a few tens percent in the Penning trap volume by switching the applied voltage at the drift tube.

Furthermore, the adiabatic transport of the single ions, which had a kinetic energy corresponding to a thermal energy at 4.2 K, between two traps was analyzed. A ramping scheme consisting of four steps was introduced and the feasibility was successfully simulated. Ramping times longer than 100 μ s of the individual voltages for a trap depth of -10 V should be chosen. Imperfections like a tilted trap with respect to the magnetic field or uncertainties in the start trigger of the respective voltages were investigated. For future studies it is recommended to use a more powerful and faster program like COMSOL[®] in order to simulate the effect of patch potentials. The results of the performed simulations may help to find the optimum ramping scheme in the experiment and to serve as input parameters for tests of the ramping option of the new developed highly stable voltage source.

At the beginning of this thesis only the infrastructure of the experimental room of PENTATRAP was present. A task within this work was to assist in the procurement of the new magnet and after arrival to perform first measurements in order to characterize the magnetic field. The measurements carried out with an NMR-probe in the homogeneous center of the cold bore magnet required the design of a special dewar. Utilizing this dewar room temperature conditions for the sensitive

NMR-probe measurements were assured. The specifications of the supplier could be partly confirmed. The effect of the determined magnetic field inhomogeneities on the ion frequencies and the change of the magnetic field due to the magnetization of the trap material itself were calculated. Moreover, the earth's magnetic field in the lab was mapped and distortions were analyzed. Further investigations of the magnetic field will proceed as soon as stored ions in the Penning traps are available. Then, a more accurate B_2 determination can be performed and the temporal stability of the magnetic field can be investigated.

In the context of this thesis, a multitude of operational tests were performed. For example, the new temperature stabilization facility of the PENTATRAP lab was characterized. Here, the obtained results look promising. A next step would be to perform functional tests of the system with operation of the magnet and the complete running experiment in parallel. One of the requirements to continue the tests is that one of the lab's walls, which was removed for the magnet's delivery, has to be built up. This wall is needed for the operation of the temperature stabilization system.

Another task within this work was to put a system dedicated for the compensation of magnetic field fluctuations into operation. This system consists of a pair of Helmholtz coils positioned around the superconducting magnet and a fluxgate sensor for the detection of the magnetic field. First successful functionality tests were carried out. Further steps concerning the adaption to the PENTATRAP experiment will require the detection of stored ions.

Moreover, instrumentally challenging components of the experiment were designed, built, assembled and tested: the highly tolerated Penning traps with their well prepared surfaces, the cryogenic translation and tilt system as well as the rest of the cryogenic assembly. These tests and the complete setup of the components performed and presented in this thesis, finally allowed the first cool down of the experiment. Currently some vacuum leaks at the feedthrough flange, which is located in the liquid helium, are being repaired. The vacuum leaks probably arise due to a non carefully welding process. In the near future, a simplified one-trap-setup is planned for first performance tests making the demounting and cabling process at the beginning much faster.

A further main task of this thesis was the successful commissioning of another very important component namely the small PENTATRAP-EBIT. First ion production studies of highly-charged ions were carried out. Therefore, the PENTATRAP-EBIT and the measuring setup in the accelerator hall were installed. The performance of the EBIT was firstly tested using argon ions and charge breeding studies of xenon ions were performed. A highlight was the production of highly-charged rhenium and osmium ions up to charge state 50+ employing the MIVOC technique. It was demonstrated that these ions, which are required for high-precision mass measurements with applications in neutrino physics, can be produced in a straightforward way as soon as they are needed for first frequency measurements. It was shown that the produced ions can be focussed and detected at an MCP positioned close to the magnet. Next steps comprise the ion injection into the superconducting magnet and the demonstration of the capture of the ions in the Penning trap stack.

Currently, tests focussing on the creation of highly-charged erbium ions are ongoing. A proceeding would be a more systematic investigation of the time-of-flight

width of the ion bunch at the MCP close to the magnet. This was temporally not feasible, since every time the cryogenic assembly is lowered into the cold bore of the magnet the beamline and the EBIT have to be dismantled. Further prospects are the search for new volatile compounds, which are of physical interest, and the creation of monoisotopic osmocene. Eventually, evaporative cooling can be contemplated to reach higher charge states as far as the ion production is not limited by the electron beam energy. The connection to the Heidelberg-EBIT is currently in the design and manufacturing phase. A new PhD student recently started on this project.

Concluding, in the last years a huge step towards the full operation of PENTA-TRAP was done. In general, the whole team put a lot of effort into the realization of PENTATRAP, e.g., in the context of the setup of the detection electronics, the designing of a new stable voltage source, the programming of the control system or the installation of the helium level and pressure stabilization. It looks promising that latest end of the year and in the next PhD thesis performed at PENTATRAP a first ion signal of stored ions can be presented. As soon as first ions are trapped and detected systematic studies of the Penning traps such as the characterization of the harmonicity and the orthogonality as well as of the magnetic field inhomogeneities will follow. In the future, there is much work to be done keeping in mind that we have five Penning traps and therefore hopefully not the fivefold trouble. For example, the capability of the stabilization systems to minimize external influences on the ions and the ion transport between the traps will be studied.

All this operational tests will lead to a first Q -value measurement of the ^{187}Re β^- -decay within the next years. Thereby, it is aimed to determine the Q -value of ^{187}Re and ^{187}Os with a precision of much better than 1 eV. Hence, together with a calorimetric measurement, the electron neutrino mass can be probed at a sub-eV level.

Appendix A

Geometry files and *LUA* codes

The geometry files used for the SIMION[®] simulations (Fig. A.1 and Fig. A.2) as well as the Lua code for pulsing down the drift tube (Fig. A.3 and Fig. A.4) are shown. The codes were used for the simulations, which are described in Chap. 5.

```

1  pa_define(8575,850,1,Cylindrical,Y,Electrostatic,1)
2  locate(0,0,0,25){
3  ;
4  ;-----
5  ; Penning Traps
6  ;-----
7  ;-----
8  ; Monitor Trap      1
9  ;-----
10     ;upper endcap electrode (M1ue)
11     e(1) {Fill {within_inside_or_on {Box(154.560,5,161.600,8)}}};
12     ;upper correction electrode (M1uc)
13     e(2) {Fill {within_inside_or_on {Box(161.750,5,165.682,8)}}};
14     ;ring electrode (M1r)
15     e(3) {Fill {within_inside_or_on {Box(165.832,5,167.289,8)}}};
16     ;lower correction electrode (M1lc)
17     e(4) {Fill {within_inside_or_on {Box(167.439,5,171.371,8)}}};
18     ;lower endcap electrode (M1le)
19     e(5) {Fill {within_inside_or_on {Box(171.521,5,178.560,8)}}};
20     ;-----
21     ; Preparation Trap      1
22     ;-----
23     ;upper endcap electrode (P1ue)
24     e(6) {Fill {within_inside_or_on {Box(178.710,5,185.750,8)}}};
25     ;upper correction electrode (P1uc)
26     e(7) {Fill {within_inside_or_on {Box(185.900,5,189.832,8)}}};
27     ;ring electrode (P1r)
28     e(8) {Fill {within_inside_or_on {Box(189.982,5,191.439,8)}}};
29     ;lower correction electrode (P1lc)
30     e(9) {Fill {within_inside_or_on {Box(191.589,5,195.521,8)}}};
31     ;lower endcap electrode (P1le)
32     e(10) {Fill {within_inside_or_on {Box(195.671,5,202.710,8)}}};
33     ;-----
34     ; Precision Trap
35     ;-----
36     ;upper endcap electrode (PCue)
37     e(11) {Fill {within_inside_or_on {Box(202.860,5,209.900,8)}}};
38     ;upper correction electrode (PCuc)
39     e(12) {Fill {within_inside_or_on {Box(210.050,5,213.982,8)}}};

```

Figure A.1: Geometry file of the Penning-trap stack, the pulsed drift tube and the surrounding vacuum chamber (part 1). For historical reasons the five traps are named here monitor, preparation and precision trap.

```

40         ;ring electrode (PCr)
41         e(13) {Fill {within_inside_or_on {Box(214.132,5,215.589,8)}}};
42         ;lower correction electrode (PClc)
43         e(14) {Fill {within_inside_or_on {Box(215.739,5,219.671,8)}}};
44         ;lower endcap electrode (PCle)
45         e(15) {Fill {within_inside_or_on {Box(219.821,5,226.860,8)}}};
46         ;-----
47         ; Preparation Trap          2
48         ;-----
49         ;upper endcap electrode (P2ue)
50         e(16) {Fill {within_inside_or_on {Box(227.010,5,234.050,8)}}};
51         ;upper correction electrode (P2uc)
52         e(17) {Fill {within_inside_or_on {Box(234.200,5,238.132,8)}}};
53         ;ring electrode (P2r)
54         e(18) {Fill {within_inside_or_on {Box(238.282,5,239.739,8)}}};
55         ;lower correction electrode (P2lc)
56         e(19) {Fill {within_inside_or_on {Box(239.889,5,243.821,8)}}};
57         ;lower endcap electrode (P2le)
58         e(20) {Fill {within_inside_or_on {Box(243.971,5,251.010,8)}}};
59         ;-----
60         ; Monitor Trap            2
61         ;-----
62         ;upper endcap electrode (M2ue)
63         e(21) {Fill {within_inside_or_on {Box(251.160,5,258.200,8)}}};
64         ;upper correction electrode (M2uc)
65         e(22) {Fill {within_inside_or_on {Box(258.350,5,262.282,8)}}};
66         ;ring electrode (M2r)
67         e(23) {Fill {within_inside_or_on {Box(262.432,5,263.889,8)}}};
68         ;lower correction electrode (M2lc)
69         e(24) {Fill {within_inside_or_on {Box(264.039,5,267.971,8)}}};
70         ;lower endcap electrode (M2le)
71         e(25) {Fill {within_inside_or_on {Box(268.121,5,275.160,8)}}};
72         ;-----
73         ; Pulsed Drift Tube
74         ;-----
75         e(26) {Fill {within_inside_or_on {Box(101.19,5,148.99,5.5)}}};
76         ;-----
77         ; Trap Holder Top
78         ;-----
79         e(27){Fill {within_inside_or_on {Box(152.13,5,154.41,12)}}};
80         ;-----
81         ; Trap Holder Bottom
82         ;-----
83         e(28){Fill {within_inside_or_on {Box(275.31,5,298.35,8)}}};
84         ;-----
85         ; Trap Chamber (Ground)
86         ;-----
87         e(29){Fill {within_inside_or_on {Box(0,8,66.04,9.5)
88                 within_inside_or_on {Box(66.04,8,68.84,20.5)}
89                 within_inside_or_on {Box(68.84,10.5,101.24,20.5)}
90                 within_inside_or_on {Box(101.24,11,104.04,20.5)}
91                 within_inside_or_on {Box(104.04,11,134,12.5)}
92                 within_inside_or_on {Box(134,11,142,32)}
93                 within_inside_or_on {Box(142,30,288,32)}
94                 within_inside_or_on {Box(288,11,295,32)}
95                 within_inside_or_on {Box(295,11,300.45,12.5)}
96                 within_inside_or_on {Box(300.45,10.5,330.45,20.5)}
97                 within_inside_or_on {Box(330.45,11,333.05,12.5)}
98                 within_inside_or_on {Box(333.05,11,343.05,12.5)}
99                 within_inside_or_on {Box(342.55,0,343.05,12.5)}}};
100        ;-----
101        }

```

Figure A.2: Geometry file of the Penning-trap stack, the pulsed drift tube and the surrounding vacuum chamber (part 2).

```

1  -----LUA CODE-----
2  -----INVESTIGATION OF THE CAPTURE OF AN ION BUNCH IN THE PENNING TRAP VOLUME-----
3  -----
4  --An ion bunch leaving the pulsed drift tube is injected into the Penning traps. In this
5  --example the bunch should be stored in a potential mainly created by supplying taps 1-2
6  --with -10V. The drift tube voltage is then raised up to store the bunch and to determine
7  --its properties. The parameters describing the bunch were stored when the bunch crosses
8  --the plane at x = 175.04 mm. This plane defines the minimum of the storage potential.
9  --The time after which the drift tube is raised up, is determined in a first step as the
10 --mean time needed to reach this plane.
11
12 simion.workbench_program()
13
14 --definition of the adjustable parameters:
15
16 adjustable DT_start = 195           --potential of the drift tube at start
17 adjustable DT_low = -5              --potential of the drift tube after switching it down
18 adjustable DT_stop = 0              --potential of the drift tube after switching it up
19 adjustable switch_time_start = 0    --setting the start time for the switching process
20 adjustable switch_time_DT_down = 0.1--time for switching down the drift tube
21 adjustable waiting_time = 3.45     --after this time the drift tube voltage is raised up
22 adjustable switch_time_DT_up = 0.1 --time for switching down the drift tube
23
24 --This segment is implemented to adjust the voltage of the drift tube:
25
26 function segment.fast_adjust()
27     if ion_time_of_flight <= switch_time_start then
28         voltage1 = -10 --start trap1
29         voltage2 = -10
30         voltage3 = -10
31         voltage4 = -10
32         voltage5 = -10
33         voltage6 = -10 --start trap 2
34         voltage7 = -10
35         voltage8 = -10
36         voltage9 = -10
37         voltage10 = 0
38         voltage11 = 0 --start trap 3
39         voltage12 = -8.81
40         voltage13 = -10
41         voltage14 = -8.81
42         voltage15 = 0
43         voltage16 = 0 --start trap 4
44         voltage17 = -8.81
45         voltage18 = -10
46         voltage19 = -8.81
47         voltage20 = 0
48         voltage21 = 0 --start trap 5
49         voltage22 = -8.81
50         voltage23 = -10
51         voltage24 = -8.81
52         voltage25 = 0
53         voltage26 = 195 --pulsed drift tube
54         voltage27 = 0 --trap holder top
55         voltage28 = 0 --trap holder bottom
56         voltage29 = 0 --trap chamber

```

Figure A.3: Lua code for pulsing down the drift tube (part 1).

```

57     else
58         local timestep = switch_time_start + switch_time_DT_down + waiting_time
59         if ion_time_of_flight >= switch_time_start then
60             voltage26 = (DT_low-DT_start)*(ion_time_of_flight-switch_time_start)/
61                 switch_time_DT_down+DT_start
62             if voltage26 <= DT_low then
63                 voltage26 = DT_low
64             end
65         end
66         if ion_time_of_flight >= waiting_time then
67             voltage26 = (DT_stop-DT_low)*(ion_time_of_flight-timestep)/
68                 switch_time_DT_up+DT_low
69             if voltage26 <= DT_low then
70                 voltage26 = DT_low
71             end
72             if voltage26 >= DT_stop then
73                 voltage26 = DT_stop
74             end
75         end
76     end
77     end
78     adj_elect26 = voltage26
79 end
80
81 local splat = false
82
83 --The following segment is called on every time-step. It is implemented to cause the
84 --particle to terminate. In case the termination condition is fulfilled at end of current
85 --time-step, then the current time-step is finished but a splat on start of next time-step
86 --is scheduled. In the ideal case the ion crosses the plane x = 175.04 mm two times.
87 --If an ion crosses this plane, the ion number, the time-of-flight, the x,y and z-position
88 --as well as the velocity components in this directions vx, vy and vz are stored.
89 --The data recording settings are set via the user interface of SIMION.
90
91 function segment.other_actions()
92     if splat then
93         ion_splat = -1
94         counter = counter+1
95     end
96
97     --Definition of the termination condition:
98
99     if (ion_time_of_flight >= switch_time_DT_down+2*waiting_time+switch_time_DT_up and
100         ion_px_mm <= 175.04)
101         or ion_px_mm <= 100 --ion escaped towards trap 3
102         or ion_px_mm >= 215 --ion escaped towards drift tube
103         or ion_time_of_flight >= 4*waiting_time then --to set an upper time limit
104             splat = true
105         end
106
107     --Reset local variable 'splat' for next particle:
108
109     if ion_splat ~= 0 then
110         splat = false
111     end
112 end

```

Figure A.4: Lua code for pulsing down the drift tube (part 2).

Appendix B

Technical drawings and photographs of selected components

The assembly drawing of the translation and tilt stage is shown in Fig. B.1. Moreover, the technical drawing of the sapphire ring, the assembly drawing of the Penning-trap stack and the technical drawings of the Penning-trap electrodes are shown (Fig. B.3 and B.4). The drawings are made at the engineering design office of the Max-Planck-Institut für Kernphysik, Heidelberg. Additionally, some photographs are presented (Fig. B.8 and Fig. B.9).

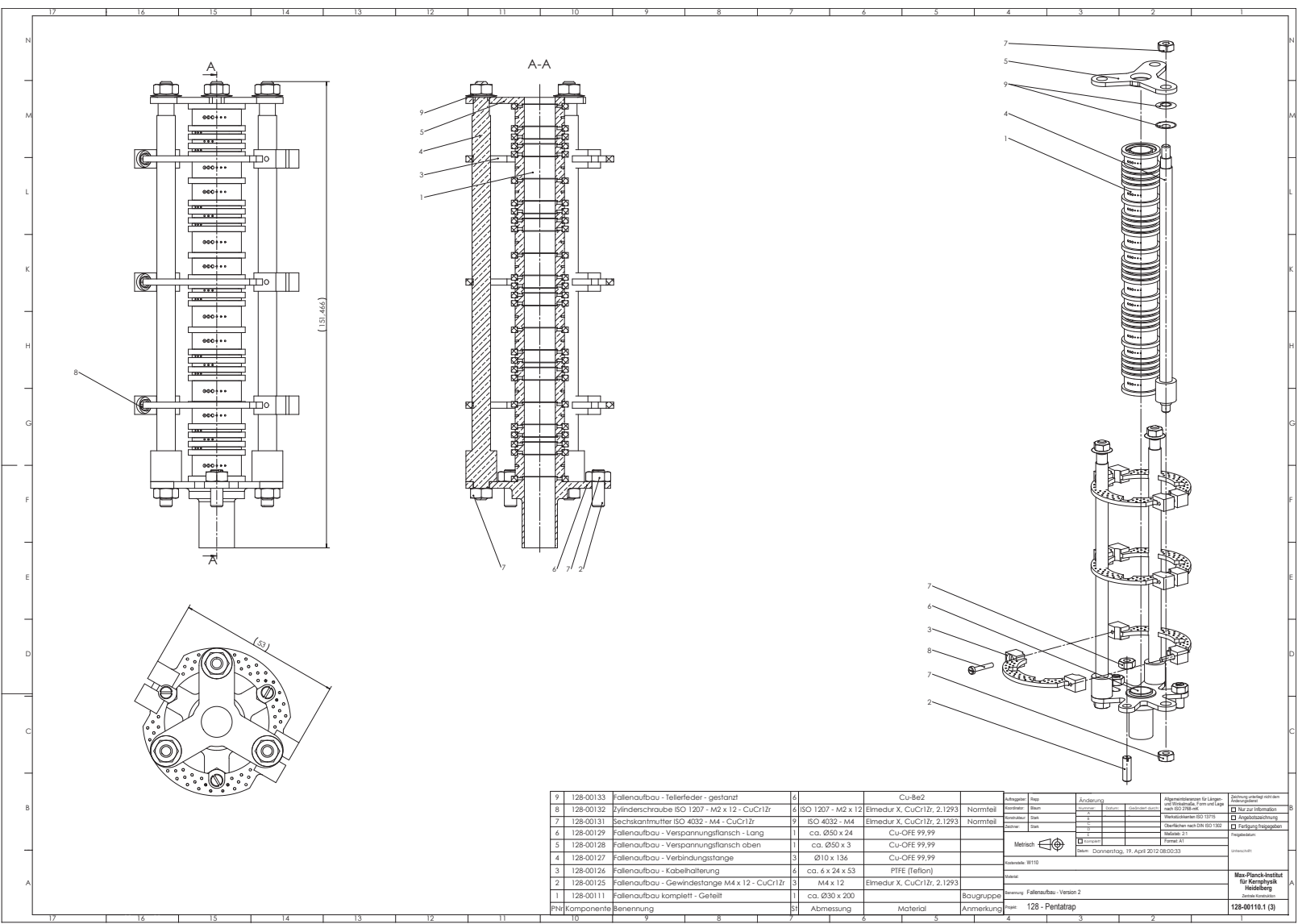


Figure B.2: Assembly drawing of the Penning-trap stack including among others the fixation rods and plates as well as the cable guides.

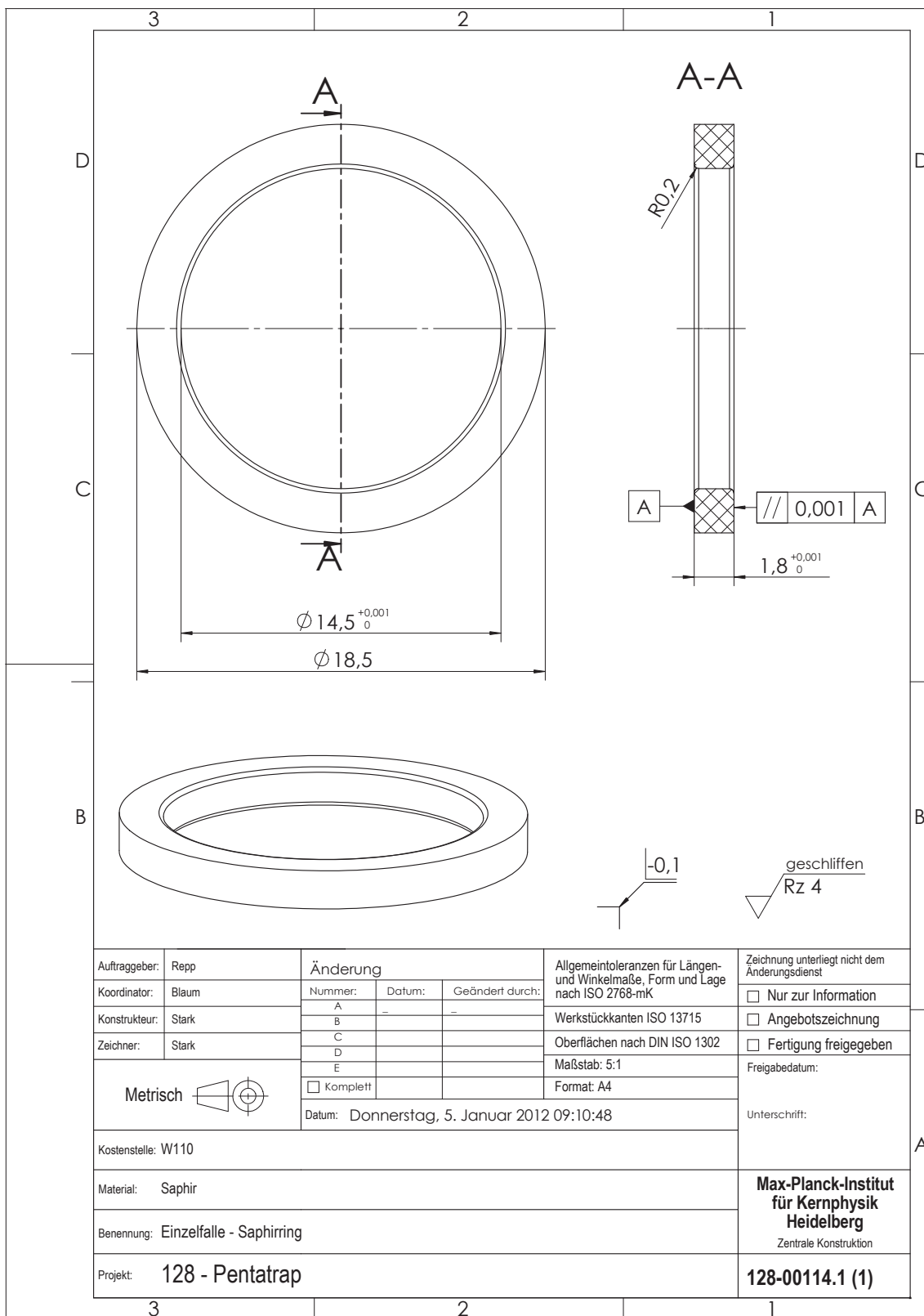


Figure B.3: Technical drawing of the sapphire ring.

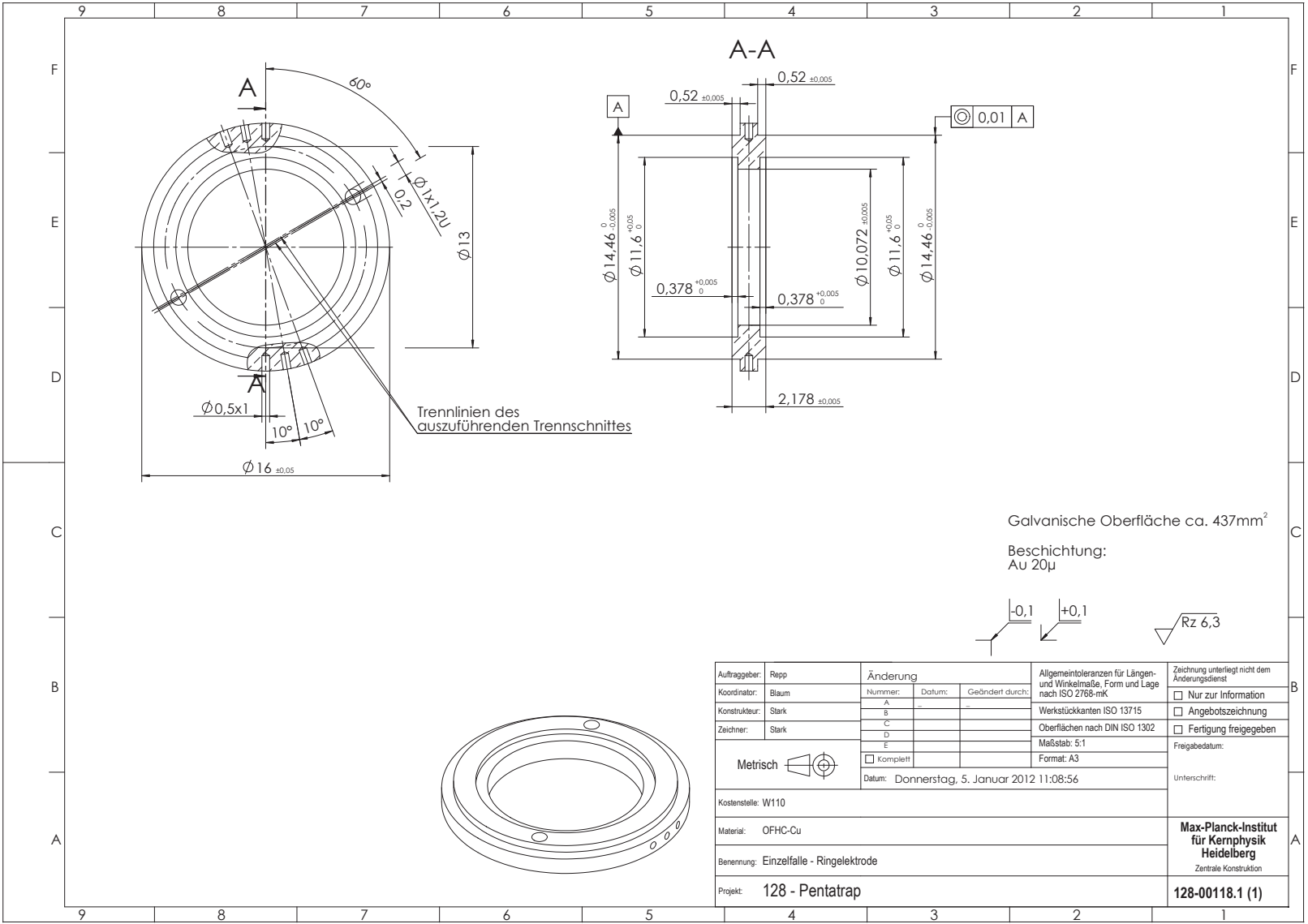
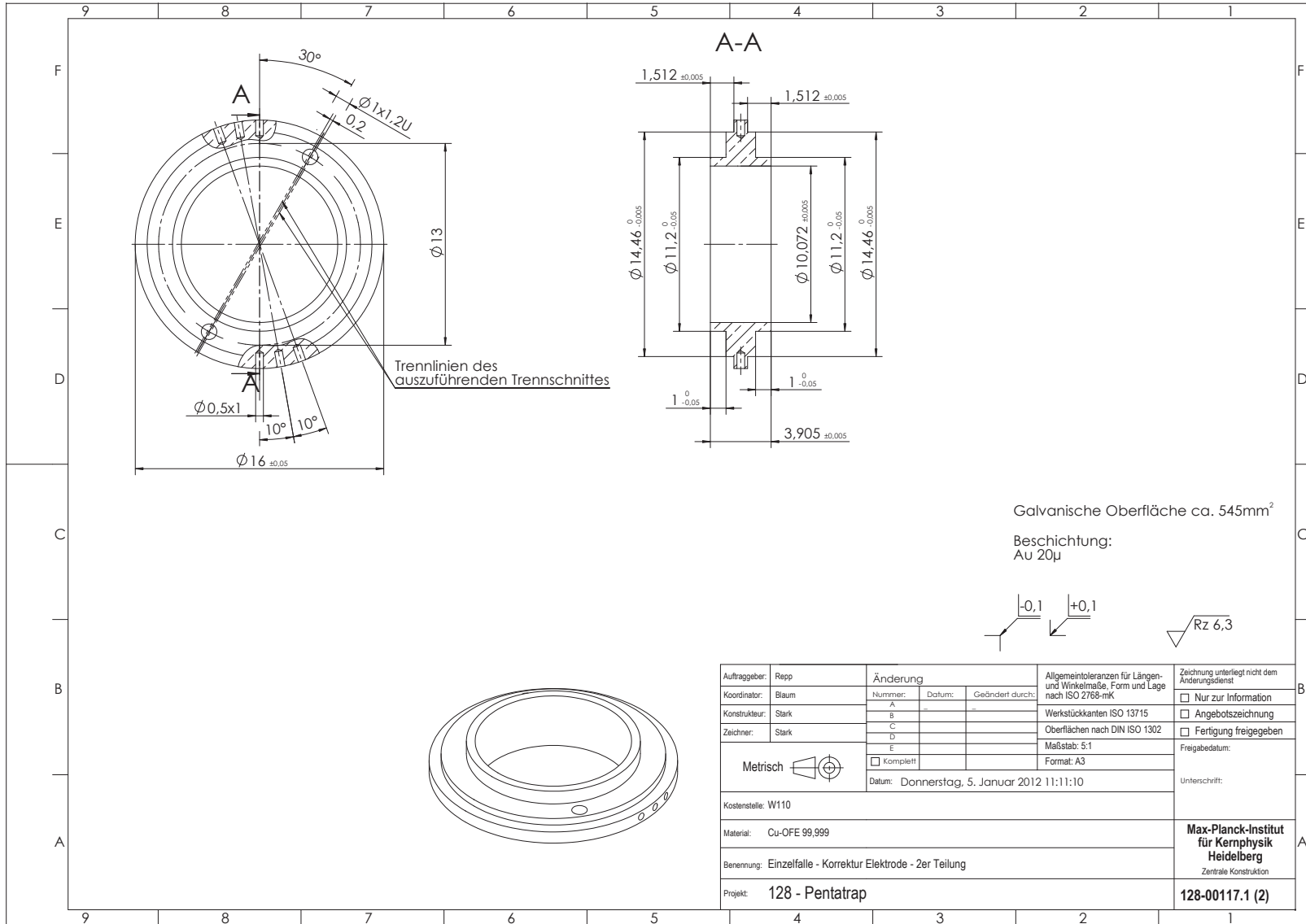


Figure B.4: Technical drawing of the ring electrode.

Figure B.5: Technical drawing of the correction electrode.



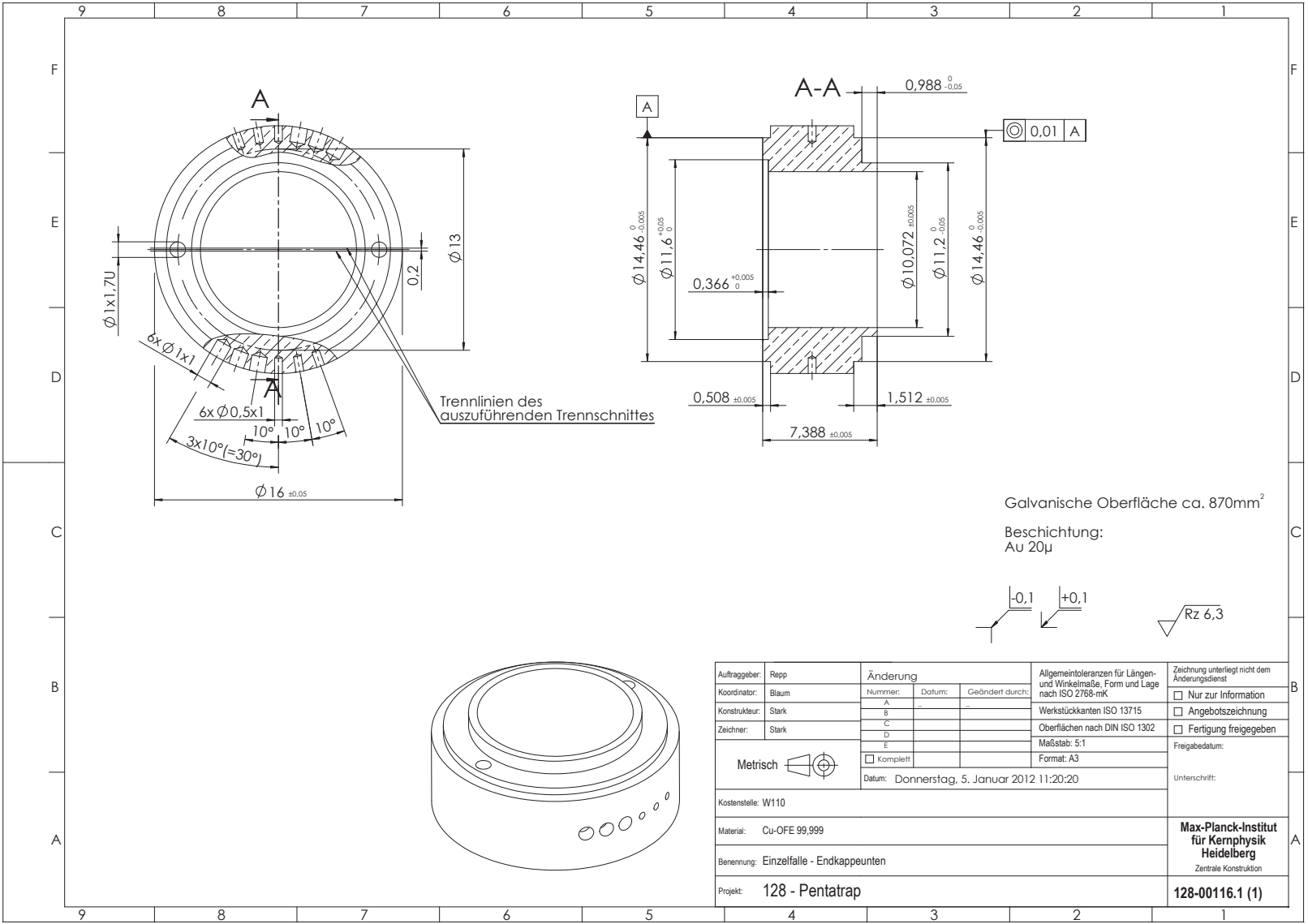
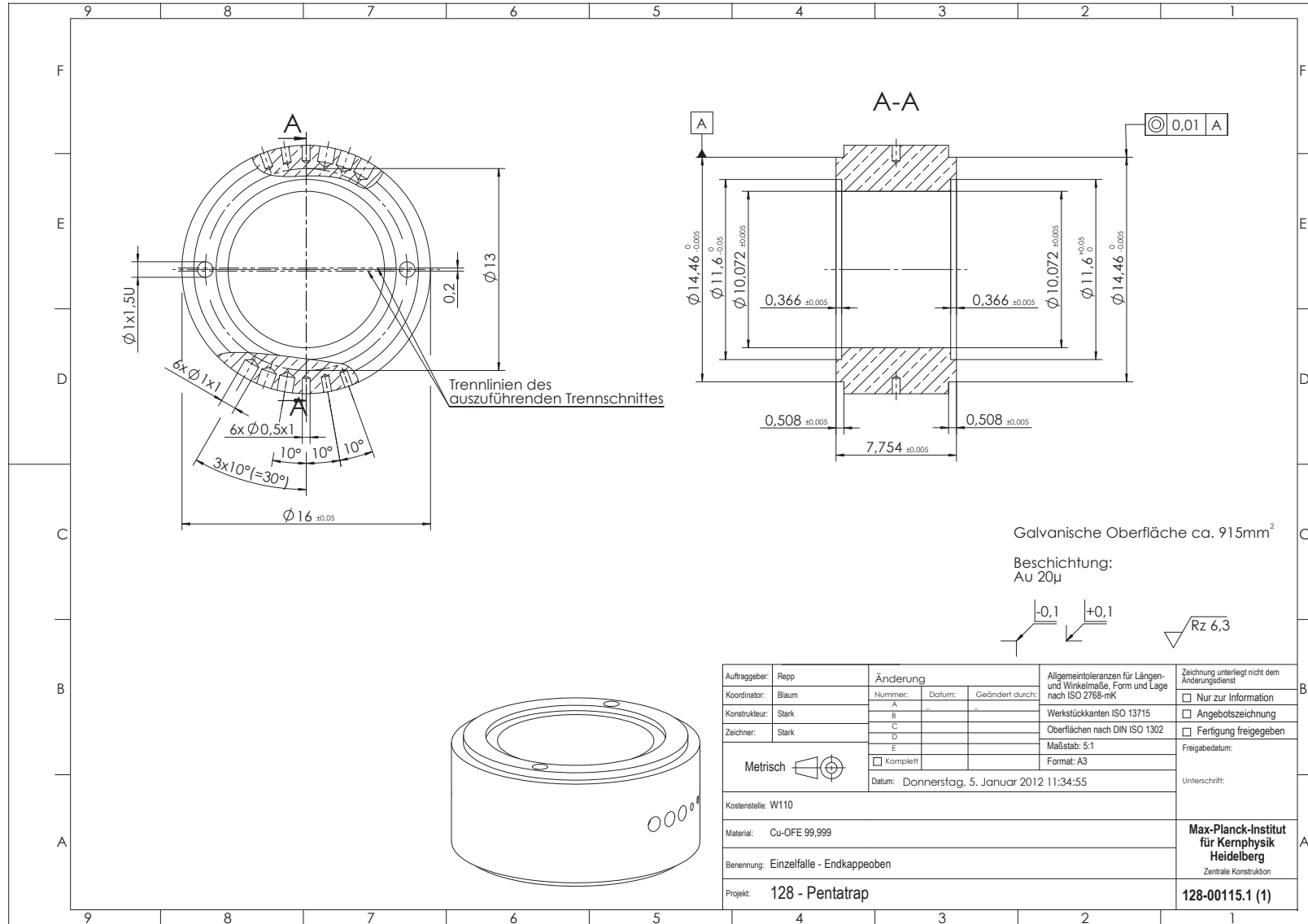


Figure B.6: Technical drawing of the lower endcap electrode.

Figure B.7: Technical drawing of the upper endcap electrode.



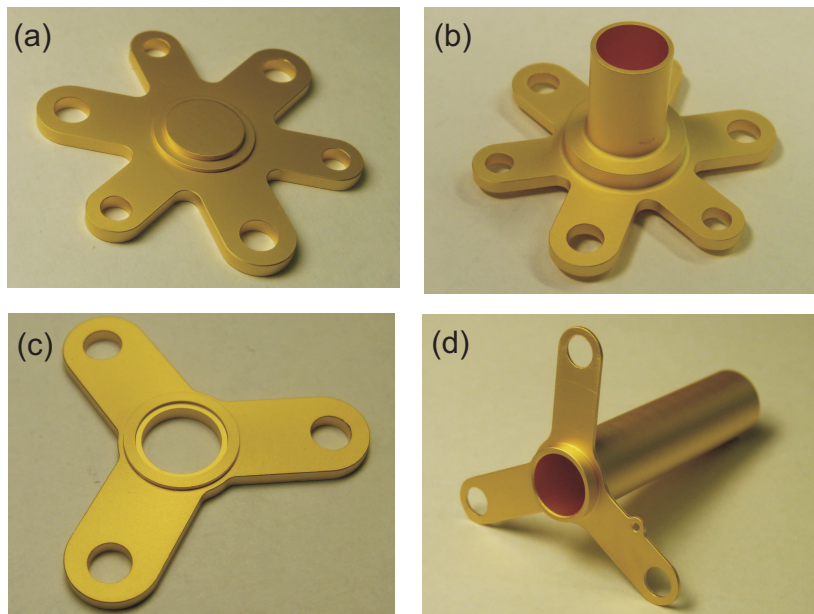


Figure B.8: Photographs of gold and silver plated Penning-trap components. (a) lower fastening plate (part number 128-00129.1) with a closed surface and (b) lower fastening plate (part number 128-00129.2) with a opened surface. The design in (b) is chosen to not deform the electrostatic potential of the lowest Penning trap. In (c) the upper fastening plate (part number 128-00128) and in (d) the drift tube situated above the Penning traps are shown.

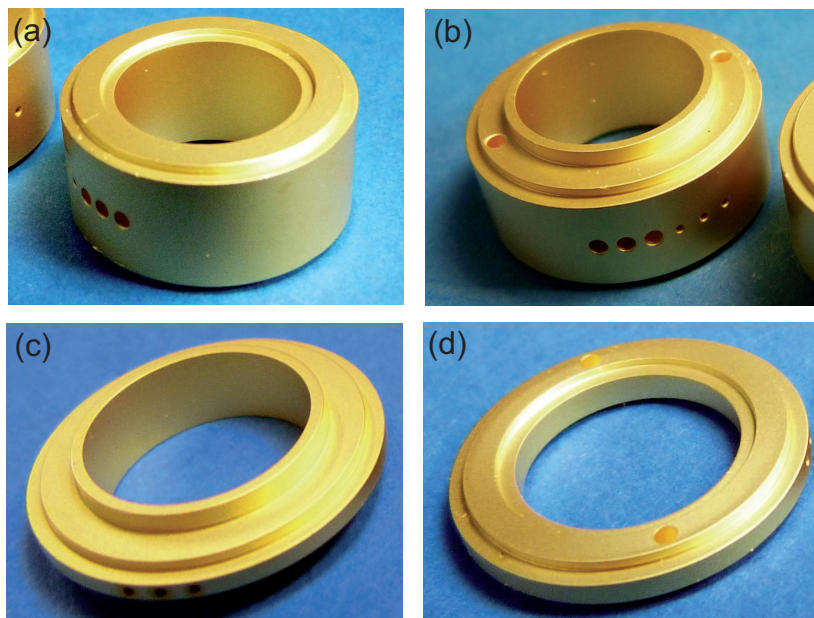


Figure B.9: Photograph of the gold plated Penning-trap electrodes. (a) the symmetric endcap electrode (part number 128-00115, see Fig. B.7), (b) the asymmetric endcap electrode (part 128-00116, see Fig. B.6), (c) the correction electrode (part number 128-00117, see Fig. B.5) and (d) the ring electrode (part number 128-00118, see Fig. B.4).

Bibliography

- [1] Repp, J. et al. (2012) PENTATRAP: a novel cryogenic multi-Penning-trap experiment for high-precision mass measurements on highly charged ions. *Appl. Phys. B*, **107**, 983.
- [2] Blaum, K. (2006) High-accuracy mass spectrometry with stored ions. *Phys. Rep.*, **425**, 1.
- [3] Franzke, B., Geissel, H., and Münzenberg, G. (2008) Mass and lifetime measurements of exotic nuclei in storage rings. *Mass Spectrom. Rev.*, **27**, 428.
- [4] Blaum, K., Novikov, Y., and Werth, G. (2010) Penning traps as a versatile tool for precise experiments in fundamental physics. *Contemp. Phys.*, **51**, 149.
- [5] Lunney, D., Pearson, J., and Thibault, C. (2003) Recent trends in the determination of nuclear masses. *Rev. Mod. Phys.*, **75**, 1021.
- [6] Blaum, K. et al. (2003) Masses of ^{32}Ar and ^{33}Ar for Fundamental Tests. *Phys. Rev. Lett.*, **91**, 260801.
- [7] Kankainen, A. et al. (2010) High-precision mass measurement of ^{31}S with the double Penning trap JYFLTRAP improves the mass value for ^{32}Cl . *Phys. Rev. C*, **82**, 052501.
- [8] Weber, C. et al. (2008) Mass measurements in the vicinity of the rp -process and the νp -process paths with the Penning trap facilities JYFLTRAP and SHIPTRAP. *Phys. Rev. C*, **78**, 054310.
- [9] Dworschak, M. et al. (2008) Restoration of the $N = 82$ Shell Gap from Direct Mass Measurements of $^{132,134}\text{Sn}$. *Phys. Rev. Lett.*, **100**, 072501.
- [10] Elomaa, V.-V. et al. (2009) Quenching of the SnSbTe Cycle in the rp Process. *Phys. Rev. Lett.*, **102**, 252501.
- [11] Hardy, J. and Towner, I. (2009) Superaligned $0^+ \rightarrow 0^+$ nuclear β decays: A new survey with precision tests of the conserved vector current hypothesis and the standard model. *Phys. Rev. C*, **79**, 055502.
- [12] Eronen, T. et al. (2009) Q_{EC} Values of the Superaligned β Emitters ^{34}Cl and $^{38}\text{K}^m$. *Phys. Rev. Lett.*, **103**, 252501.
- [13] Gabrielse, G. et al. (1999) Precision Mass Spectroscopy of the Antiproton and Proton Using Simultaneously Trapped Particles. *Phys. Rev. Lett.*, **82**, 3198.

- [14] Shabaev, V. et al. (2006) QED effects in heavy few-electron ions. *Int. J. Mass Spectrom.*, **251**, 109.
- [15] Stöhlker, T. et al. (2008) Quantum Electrodynamics in Extreme Fields: Precision Spectroscopy of High- Z H-like Systems. *Lect. Notes Phys.*, **745**, 157.
- [16] Rainville, S. et al. (2005) A direct test of $E = mc^2$. *Nature*, **438**, 1096.
- [17] Van Dyck, R. et al. (2004) Ultraprecise Atomic Mass Measurement of the α Particle and ${}^4\text{He}$. *Phys. Rev. Lett.*, **92**, 220802.
- [18] Van Dyck, R. et al. (2006) The UW-PTMS: Systematic studies, measurement progress, and future improvements. *Int. J. Mass Spectrom.*, **251**, 231.
- [19] Rainville, S., Thompson, J., and Pritchard, D. (2004) An Ion Balance for Ultra-High-Precision Atomic Mass Measurements. *Science*, **303**, 334.
- [20] Shi, W., Redshaw, M., and Myers, E. (2005) Atomic masses of ${}^{32,33}\text{S}$, ${}^{84,86}\text{Kr}$, and ${}^{129,132}\text{Xe}$ with uncertainties ≤ 0.1 ppb. *Phys. Rev. A*, **72**, 022510.
- [21] Redshaw, M., McDaniel, J., and Myers, E. (2008) Dipole Moment of PH^+ and the Atomic Masses of ${}^{28}\text{Si}$, ${}^{31}\text{P}$ by Comparing Cyclotron Frequencies of Two Ions Simultaneously Trapped in a Penning Trap. *Phys. Rev. Lett.*, **100**, 093002.
- [22] Schneider, D. et al. (1994) Confinement in a cryogenic Penning trap of highest charge state ions from EBIT. *Rev. Sci. Instrum.*, **65**, 3472.
- [23] Bergström, I. et al. (2002) SMILETRAP – A Penning trap facility for precision mass measurements using highly charged ions. *Nucl. Instr. Meth. Phys. Res. A*, **487**, 618.
- [24] Bergström, I. et al. (2003) High-precision mass measurements of hydrogen-like ${}^{24}\text{Mg}^{11+}$ and ${}^{26}\text{Mg}^{11+}$ ions in a Penning trap. *Eur. Phys. J. D*, **22**, 41.
- [25] Bergström, I. et al. (2001) Present status of the Stockholm electron beam ion source and its scientific program. *AIP Conference Proceedings*, vol. 572, p. 20.
- [26] Hobein, M. and other (2011) SMILETRAP II. *Hyperfine Interact.*, **199**, 141.
- [27] Böhm, S. et al. (2007) First results from the Stockholm electron beam ion trap. *Journal of Physics: Conference Series*, vol. 58, p. 303, IOP Publishing.
- [28] Dilling, J. et al. (2006) Mass measurements on highly charged radioactive ions, a new approach to high precision with TITAN. *Int. J. Mass Spectrom.*, **251**, 198.
- [29] Ettenauer, S. et al. (2011) First Use of High Charge States for Mass Measurements of Short-Lived Nuclides in a Penning Trap. *Phys. Rev. Lett.*, **107**, 272501.

- [30] Froese, M. et al. (2006) A high-current electron beam ion trap as an on-line charge breeder for the high precision mass measurement TITAN experiment. *Hyperfine Interact.*, **173**, 85.
- [31] Gräff, G., Kalinowsky, H., and Traut, J. (1980) A direct determination of the proton electron mass ratio. *Zeitschrift für Physik A*, **297**, 35.
- [32] Wineland, D. and Dehmelt, H. (1975) Principles of the stored ion calorimeter. *J. App. Phys.*, **46**, 919.
- [33] Fukuda, Y. et al. (1998) Evidence for oscillation of atmospheric neutrinos. *Phys. Rev. Lett.*, **81**, 1562.
- [34] KATRIN collaboration, T. (2004) KATRIN Design Report. *Wissenschaftliche Berichte FZKA*, **7090**.
- [35] Nagy, S. et al. (2006) On the Q -value of the tritium beta-decay. *Europhys. Lett.*, **74**, 404.
- [36] Diehl, C. et al. (2011) Progress with the MPIK/UW-PTMS in Heidelberg. *Hyperfine Interact.*, **199**, 291.
- [37] Lobashev, V. et al. (2001) Direct search for neutrino mass and anomaly in the tritium beta-spectrum: Status of “Troitsk neutrino mass” experiment. *Nucl. Phys. B-Proceedings Supplements*, **91**, 280.
- [38] Kraus, C. et al. (2005) Final results from phase II of the Mainz neutrino mass search in tritium decay. *EPJC*, **40**, 447.
- [39] Otten, E. and Weinheimer, C. (2008) Neutrino mass limit from tritium β decay. *Rep. Prog. Phys.*, **71**, 086201.
- [40] Ferri, E. (2011) Direct Neutrino Mass measurements. *Nucl. Phys. B*, **217**, 62.
- [41] Ferri, E. et al. (2012) MARE-1 in Milan: Status and Perspectives. *J. Low Temp. Phys.*, **167**, 1035.
- [42] De Rújula, A. and Lusignoli, M. (1982) Calorimetric measurements of $^{163}\text{holmium}$ decay as tools to determine the electron neutrino mass. *Phys. Lett. B*, **118**, 429.
- [43] Audi, G. (2003) The 2003 NUBASE and Atomic Mass Evaluations. *Nucl. Phys. A*, **729**, 676.
- [44] Ranitzsch, P. et al. (2012) Development of Metallic Magnetic Calorimeters for High Precision Measurements of Calorimetric 187 Re and 163 Ho Spectra. *J. Low Temp. Phys.*, p. 1.
- [45] Eliseev, S. et al. (2011) Resonant Enhancement of Neutrinoless Double-Electron Capture in ^{152}Gd . *Phys. Rev. Lett.*, **106**, 052504.
- [46] Fritioff, T. and other (2006) Precise measurements of ionic masses for QED tests. *Int. J. Mass Spectrom.*, **251**, 281.

- [47] Stöhlker, T. et al. (2006) Ground state Lamb-shift of heavy hydrogen-like ions: status and perspectives. *Hyperfine Int.*, **172**, 135.
- [48] Greene, G. et al. (1991) Test of special relativity by a determination of the Lorentz limiting velocity: Does $E = mc^2$? *Phys. Rev. D*, **44**, R2216.
- [49] Penning, F. (1936) Glow discharge at low pressure between coaxial cylinders in an axial magnetic field. *Physica*, **3**, 873.
- [50] Pierce, J. (1949) *Theory and Design of Electron Beams*. D. van Nostrand Co., New York.
- [51] Dehmelt, H. (1990) Experiments with an isolated subatomic particle at rest. *Rev. Mod. Phys.*, **62**, 525.
- [52] Paul, W. (1990) Electromagnetic traps for charged and neutral particles. *Rev. Mod. Phys.*, **62**, 531.
- [53] Brown, L. and Gabrielse, G. (1986) Geonium theory: Physics of a single electron or ion in a Penning trap. *Rev. Mod. Phys.*, **58**, 233.
- [54] Earnshaw, S. (1842) On the nature of the molecular forces which regulate the constitution of the luminiferous ether. *Trans. Camb. Phil. Soc.*, **7**, 97.
- [55] Porto, J. (2001) Series solution for the image charge fields in arbitrary cylindrically symmetric Penning traps. *Phys. Rev. A*, **64**, 023403.
- [56] Van Dyck, R. et al. (1989) Number dependency in the compensated Penning trap. *Phys. Rev. A*, **40**, 6308.
- [57] Gabrielse, G., Haarsma, L., and Rolston, S. (1989) Open-endcap Penning traps for high precision experiments. *Int. J. Mass Spectrom. Ion Process*, **88**, 319.
- [58] Gabrielse, G. and MacKintosh, F. (1984) Cylindrical Penning traps with orthogonalized anharmonicity compensation. *Int. J. Mass Spectrom.*, **57**, 1.
- [59] Verdú, J. et al. (2008) Calculation of electrostatic fields using quasi-Green's functions: application to the hybrid Penning trap. *New J. Phys.*, **10**, 103009.
- [60] Ulmer, S. (2011) *First Observation of Spin Flips with a Single Proton Stored in a Cryogenic Penning Trap*. Ph.D. thesis, Ruprecht-Karls-Universität Heidelberg.
- [61] Roux, C. et al. (2012) The trap design of PENTATRAP. *Appl. Phys. B*, **107**, 997.
- [62] Kretzschmar, M. et al. (1992) Single Particle Motion in a Penning trap: Description in the Classical Canonical Formalism. *Physica Scripta*, **46**, 544.
- [63] Mitchell, D., Rockwood, A., and Smith, R. (1995) Frequency shifts and modulation effects due to solenoidal magnetic field inhomogeneities in ion cyclotron mass spectrometry. *Int. J. Mass Spectrom. Ion Process.*, **141**, 101.

- [64] Major, F., Gheorghe, V., and Werth, G. (2004) *Charged Particle Traps: Physics And Techniques Of Charged Particle Field Confinement*. Springer.
- [65] Anderson, P. (1962) Theory of Flux Creep in Hard Superconductors. *Phys. Rev. Lett.*, **9**, 309.
- [66] Kellerbauer, A. et al. (2003) From direct to absolute mass measurements: A study of the accuracy of ISOLTRAP. *Eur. Phys. J. D.*, **22**, 53.
- [67] Brown, L. and Gabrielse, G. (1982) Precision spectroscopy of a charged particle in an imperfect Penning trap. *Phys. Rev. A*, **25**, 2423.
- [68] Gabrielse, G. (2009) Why is sideband mass spectrometry possible with ions in a Penning trap? *Phys. Rev. Lett.*, **102**, 172501.
- [69] Cornell, E. et al. (1990) Mode coupling in a Penning trap: π pulses and a classical avoided crossing. *Phys. Rev. A*, **41**, 312.
- [70] Schweikhard, L. and Marshall, A. (1993) Excitation Modes for Fourier Transform-Ion Cyclotron Resonance Mass Spectrometry. *J. Am. Soc. Mass Spectrom.*, **4**, 433.
- [71] Eliseev, S. et al. (2007) Octupolar excitation of ions stored in a Penning trap mass spectrometer-a study performed at SHIPTRAP. *Int. J. Mass Spectrom.*, **262**, 45.
- [72] Ringle, R. et al. (2007) Octupolar excitation of ion motion in a Penning trap-a study performed at LEBIT. *Int. J. Mass Spectrom.*, **262**, 33.
- [73] Liouville, J. (1838) Note sur la Théorie de la Variation des constantes arbitraires. *Journ. de Math. Pures et Appl.*, **3**, 342.
- [74] Itano, W. et al. (1995) Cooling methods in ion traps. *Physica Scripta*, **59**, 106.
- [75] König, M. et al. (1995) Quadrupole excitation of stored ion motion at the true cyclotron frequency. *Int. J. Mass Spectrom. Ion Process.*, **142**, 95.
- [76] Jefferts, S. et al. (1993) Superconducting resonator and a cryogenic GaAs field-effect transistor amplifier as a single-ion detection system. *Rev. Sci. Instrum.*, **64**, 737.
- [77] Shockley, W. (1938) Currents to conductors induced by a moving point charge. *J. of Appl. Phys.*, **9**, 635.
- [78] Stahl, S. (1998) *Aufbau eines Experimentes zur Bestimmung elektronischer g-Faktoren einzelner wasserstoffähnlicher Ionen*. Ph.D. thesis, Johannes Gutenberg-Universität Mainz.
- [79] Ulmer, S. et al. (2009) The quality factor of a superconducting rf resonator in a magnetic field. *Rev. Sci. Instrum.*, **80**, 123302.
- [80] Roux, C. (2012) *In preparation*. Ph.D. thesis, Ruprecht-Karls-Universität Heidelberg.

- [81] Dehmelt, H., Nagourney, W., and Sandberg, J. (1986) Self-excited mono-ion oscillator. *Proc. Nat. Acad. Sci. USA*, **83**, 5761.
- [82] D'Urso, B., Odom, B., and Gabrielse, G. (2003) Feedback Cooling of a One-Electron Oscillator. *Phys. Rev. Lett.*, **90**, 43001.
- [83] Feng, X. et al. (1996) Tank circuit model applied to particles in a Penning trap. *J. of Appl. Phys.*, **79**, 8.
- [84] Djekic, S. et al. (2004) Temperature measurement of a single ion in a Penning trap. *Eur. Phys. J. D*, **31**, 451.
- [85] Stahl, S. et al. (2005) Phase-sensitive measurement of trapped particle motions. *J. Phys. B*, **38**, 297.
- [86] Cornell, E. et al. (1974) Single-Ion Cyclotron Resonance Measurement of $M(\text{CO}^+)/M(\text{N}_2^+)$. *Phys. Rev. Lett.*, **63**, 312.
- [87] Sturm, S. et al. (2011) Phase-Sensitive Cyclotron Frequency Measurements at Ultralow Energies. *Phys. Rev. Lett.*, **107**, 143003.
- [88] Levine, M. et al. (1988) The Electron Beam Ion Trap: A New Instrument for Atomic Physics Measurements. *Physica Scripta*, **T22**, 157.
- [89] Levine, M. et al. (1989) The use of an Electron Beam Ion Trap in the study of highly charged ions. *Nucl. Instrum. Methods B*, **43**, 431.
- [90] Donets, E., Ilushenko, V., and Alpert, A. (1969) Proceedings of the Première Conférence sur les sources d'Ions, INSTN, Saclay, France.
- [91] Donets, E. and Ovsyannikov, V. (1981) Investigation of ionization of positive ions by electron impact. *Sov. Phys. JETP*, **53**, 466.
- [92] Knapp, D. et al. (1993) A high-energy electron beam ion trap for production of high-charge high-Z ions. *Nucl. Instrum. Methods A*, **334**, 305.
- [93] Marrs, R. et al. (1994) Production and Trapping of Hydrogenlike and Bare Uranium Ions in an Electron Beam Ion Trap. *Phys. Rev. Lett.*, **72**, 4082.
- [94] Marrs, R., Beiersdorfer, P., and Schneider, D. (1999) The Electron-Beam Ion Trap. *Physics Today*, **47**, 27.
- [95] Beiersdorfer, P. et al. (1997) Measurements of nuclear parameters of high-Z isotopes performed on a high-energy electron beam ion trap. *Nucl. Phys. A*, **626**, 357.
- [96] Gillaspay, J. (2001) *Trapping highly charged ions: Fundamentals and applications*. Nova Science Publishers, Inc.
- [97] Wolf, B. (1995) *Handbook of ion sources*. CRC.
- [98] Beiersdorfer, P. et al. (2003) Laboratory simulation of charge exchange-produced X-ray emission from comets. *Science*, **300**, 1558.

- [99] Epp, S. et al. (2007) Soft X-Ray Laser Spectroscopy on Trapped Highly Charged Ions at FLASH. *Phys. Rev. Lett.*, **98**, 183001.
- [100] Liang, G. et al. (2009) Extreme-ultraviolet spectroscopy of Fe VI-Fe XV and its diagnostic application for electron beam ion trap plasmas. *The Astrophysical Journal*, **696**, 2275.
- [101] Brenner, G. et al. (2009) On the Transition Rate of the Fe X Red Coronal Line. *The Astrophysical Journal*, **703**, 68.
- [102] Simon, M. et al. (2010) Resonant and Near-Threshold Photoionization Cross Sections of Fe¹⁴⁺. *Phys. Rev. Lett.*, **105**, 183001.
- [103] Fischer, D. et al. (2003) Subshell Resolved Measurements of Single Electron Capture in Slow Ne⁷⁺-Helium Collisions. *Hyperfine Interact.*, **146**, 177.
- [104] Ginzler, R. et al. (2010) Deceleration system at the Heidelberg EBIT providing very slow highly charged ions for surface nanostructuring. *Nucl. Instrum. Methods B*, **268**, 2972.
- [105] Simon, M. et al. (2012) The on-line charge breeding program at TRIUMF's Ion Trap For Atomic and Nuclear Science for precision mass measurements. *Rev. Sci. Instrum.*, **83**, 02A912.
- [106] Ovsyannikov, V. and Zschornack, G. (1999) First investigations of a warm electron beam ion trap for the production of highly charged ions. *Rev. Sci. Instrum.*, **70**, 2646.
- [107] Zschornack, G. et al. (2010) Status report of the Dresden EBIS/EBIT developments. *Rev. Sci. Instrum.*, **81**, 02A507.
- [108] see: <http://www.dreebit.com>.
- [109] Crespo López-Urrutia, J. et al. (2000) First results from the Freiburg electron beam ion trap FreEBIT. *Hyperfine Int.*, **127**, 497.
- [110] Crespo López-Urrutia, J. et al. (2001) First results from the Freiburg Electron Beam Ion Trap FreEBIT. *Physica Scripta*, **T92**, 110.
- [111] Crespo López-Urrutia, J. et al. (2004) Optimization of the charge state distribution of the ion beam extracted from an EBIT by dielectronic recombination. *Rev. Sci. Instrum.*, **75**, 1560.
- [112] Kluge, H. et al. (2008) HITRAP: A facility at GSI for highly charged ions. *Adv. Quantum Chem.*, **53**, 83.
- [113] Rodrigues, G. et al. (2004) Systematic calculation of total atomic energies of ground state configurations. *Atomic Data and Nuclear Data Tables*, **86**, 117.
- [114] Brillouin, L. (1945) A theorem of Larmor and its importance for electrons in magnetic fields. *Phys. Rev.*, **67**, 260.

- [115] Herrmann, G. (1958) Optical theory of thermal velocity effects in cylindrical electron beams. *J. Appl. Phys.*, **29**, 127.
- [116] Fussmann, G., Biedermann, C., and Radtke, R. (1999) EBIT: An electron beam source for the Production and Confinement of highly ionized Atoms. *NATO ASI Series 3 (Proceedings Summer School, Sozopol)*, **67**, 429.
- [117] Vlasov, A. (1968) The vibrational properties of an electron gas. *Soviet Physics Uspekhi*, **10**, 721.
- [118] Currell, F. (2003) *The Physics of Multiply and Highly Charged Ions: Sources, applications, and fundamental processes*. Springer Netherlands.
- [119] Tawara, H. and Kato, T. (1987) Total and partial ionization cross sections of atoms and ions by electron impact. *Atomic Data and Nuclear Data Tables*, **36**, 167.
- [120] Lotz, W. (1967) An empirical formula for the electron-impact ionization cross-section. *Zeitschrift für Physik A*, **206**, 205.
- [121] Uddin, M. et al. (2005) Electron-impact ionization of hydrogen and lithiumlike systems. *Phys. Rev. A*, **72**, 032715.
- [122] Knudsen, H. et al. (1983) Experimental investigation of electron capture by highly charged ions of medium velocities. *Physica Scripta*, **1983**, 101.
- [123] Müller, A. and Salzborn, E. (1977) Scaling of cross sections for multiple electron transfer to highly charged ions colliding with atoms and molecules. *Phys. Lett. A*, **62**, 391.
- [124] Bohr, N. and Lindhard, J. (1954) Electron capture and loss by heavy ions penetrating through matter. *Kgl. Danske Videnskab. Selsk. Mat.-fys. Medd.*, **28**.
- [125] Ryufuku, H., Sasaki, K., and Watanabe, T. (1980) Oscillatory behavior of charge transfer cross sections as a function of the charge of projectiles in low-energy collisions. *Phys. Rev. A*, **21**, 745.
- [126] Abrines, R. and Percival, I. (1966) Classical theory of charge transfer and ionization of hydrogen atoms by protons. *Proceedings of the Physical Society*, **88**, 861.
- [127] Ginzl, R. (2010) *Wechselwirkung niederenergetischer hochgeladener Ionen mit Materie*. Ph.D. thesis, Ruprecht-Karls-Universität Heidelberg.
- [128] Spitzer, L. (1965) *Physics of fully ionized gases*. Interscience Tracts on Physics and Astronomy, New York: Interscience Publication, Wiley.
- [129] Kim, Y. and Pratt, R. (1983) Direct radiative recombination of electrons with atomic ions: Cross sections and rate coefficients. *Phys. Rev. A*, **27**, 2913.
- [130] Bethe, H. and Salpeter, E. (1977) *Quantum mechanics of one-and two-electron atoms*. Plenum Publishing Corporation.

- [131] Andersen, L. and Bolko, J. (1990) Radiative recombination measurements with H- and Li-like ions. *J. Phys. B*, **23**, 3167.
- [132] Shkarofsky, I. and Johnston, M., T. and Bachynski (1966) *The particle kinetics of plasmas*. Addison-Wesley Reading.
- [133] Penetrante, B. et al. (1991) Evolution of ion-charge-state distributions in an electron-beam ion trap. *Phys. Rev. A*, **43**, 4861.
- [134] Lu, X., Watanabe, H., and Currell, F. (2003) Numerical simulation of the charge balance in an EBIT. *Nucl. Instrum. Methods B*, **205**, 234.
- [135] González Martínez, A. et al. (2005) State-Selective Quantum Interference Observed in the Recombination of Highly Charged $\text{Hg}^{75+..78+}$ Mercury Ions in an Electron Beam Ion Trap. *Phys. Rev. Lett.*, **94**, 203201.
- [136] Dahl, D. and Manura, D. (2007) *Manual SIMION 8.0*. Scientific Instruments Services, Inc.
- [137] Van Dyck, R. et al. (1999) Ultrastable superconducting magnet system for a Penning trap mass spectrometer. *Rev. Sci. Instrum.*, **70**, 1665.
- [138] Simon, N., Drexler, E., and Reed, R. (1992) *Natl. Inst. Stand. Technol. Mono. 177, Properties of Copper and Copper Alloys at Cryogenic Temperatures*. U.S. Government Printing Office, Washington, DC.
- [139] Hurd, C. (1966) A magnetic susceptibility apparatus for weakly magnetic metals, and the susceptibility of pure copper in the range 6-300 degree K. *Cryogenics*, **6**, 264.
- [140] Böhm, C. (2013) *in preparation*. Ph.D. thesis, Ruprecht-Karls-Universität Heidelberg.
- [141] Ekin, J. (2007) *Experimental Techniques for Low Temperature Measurements: Cryostat Design, Materials, and Critical-Current Testing*. Oxford University Press.
- [142] Dobrovinskaya, E., Lytvynov, L., and Pishchik, V. (2009) *Sapphire, Material, Manufacturing, Applications*. Springer.
- [143] see: <http://cryogenics.nist.gov/mproprsmay/material%20properties.htm>.
- [144] Mann, D. (1977) *LNG Materials and Fluids*. National Bureau of Standards, Cryogenics Division.
- [145] Veres, H., Thermal Properties Database for Materials at Cryogenic Temperatures. Page: 4.503.
- [146] Hust, J. (1984) *Thermal Conductivity Of Glass Fiber/Epoxy Composite Support Bands For Cryogenic Dewars*. Phase II National Bureau of Standards, Boulder, CO.

- [147] Child, G., Erics, L., and Powell, R. (1973) *Thermal Conductivity of Solids at Room Temperature and Below, Monograph 131*. National Bureau of Standards.
- [148] Touloukian, Y. and Ho, C. (1976) *Thermophysical Properties of Selected Aerospace Materials, Part II: Thermophysical Properties of Seven Materials*.
- [149] Dörr, A. (2014) *in preparation*. Ph.D. thesis, Ruprecht-Karls-Universität Heidelberg.
- [150] Beck, D. and Brand, H. (2003) CS - A Control System Framework for Experiments at GSI. *GSI Scientific Rep.*, p. 210.
- [151] Beck, D. et al. (2004) A new control system for ISOLTRAP. *Nucl. Instrum. Methods A*, **527**, 567.
- [152] Bollen, G. et al. (1996) ISOLTRAP: a tandem Penning trap system for accurate on-line mass determination of short-lived isotopes. *Nucl. Instrum. Meth. A*, **368**, 675.
- [153] Goncharov, M. (2013) *in preparation*. Ph.D. thesis, Ruprecht-Karls-Universität Heidelberg.
- [154] Hinterberger, F. (2008) *Physik der Teilchenbeschleuniger und Ionenoptik*. Springer Verlag.
- [155] Chen, L. et al. (1987) Phase-modulated stored waveform inverse Fourier transform excitation for trapped ion mass spectrometry. *Anal. Chem.*, **59**, 449.
- [156] Van Gorp, S. et al. (2011) Simbuca, using a graphics card to simulate Coulomb interactions in a Penning trap. *Nucl. Instrum. Methods A*, **638**, 192.
- [157] METROLAB INSTRUMENTS (1999) *NMR Teslameter Accessories: 1062 Probes*. Datasheet.
- [158] Baehr, H. and Stephan, K. (2006) *Wärme und Stoffübertrag*. Springer.
- [159] Donnelly, R. and Barenghi, C. (1998) The observed properties of liquid helium at the saturated vapor pressure. *Journal of Physical and Chemical Reference Data*, **27**, 1217.
- [160] Ulmer, S. (2006), Entwicklung eines experimentellen Aufbaus zur Messung des g-Faktors des Protons in einer Penning-Falle. Diploma thesis, Ruprecht-Karls-Universität Heidelberg.
- [161] Franz, R. and Wiedemann, G. (1853) Über die Wärme-Leitungsfähigkeit der Metalle. *Ann. Phys.*, **165**, 497.
- [162] METROLAB INSTRUMENTS (2000) *NMR Teslameters High Precision: PT 2025 Bench Unit*. Datasheet.
- [163] Verdú, J. (2003) *Ultrapräzise Messung des elektronischen g-Faktors in wasserstoffähnlichem Sauerstoff*. Ph.D. thesis, Johannes Gutenberg-Universität Mainz.

- [164] Sturm, S. (2011) *The g-factor of the electron bound in $^{28}\text{Si}^{13+}$: The most stringent test of bound-state quantum electrodynamics*. Ph.D. thesis, Johannes Gutenberg-Universität Mainz.
- [165] Schwarz, S. (1993) *Aufbau und Test einer Laserdesorptionsquelle fuer das CERN-Massensexperiment*. Master's thesis, Johannes Gutenberg-Universität Mainz.
- [166] Dörr, A. (2011), *Setup, test and optimization of detection electronics for high-precision mass measurements at PENTATRAP*. Diploma thesis, Ruprecht-Karls-Universität Heidelberg.
- [167] Rischka, A. (2011), *Aufbau und Charakterisierung eines Systems zur Stabilisierung des Magnetfeldes an PENTATRAP*. Bachelor thesis, Ruprecht-Karls-Universität Heidelberg.
- [168] Siemens (2010) *Funktionsbeschreibung, Projekt: Max-Planck-Institut, Heidelberg Gebäude 16 UG, Neuer Experimentierbereich: PENTATRAP*.
- [169] Allan, D. (1996) Statistics of Atomic Frequency Standard. **54**, 221.
- [170] See: <http://www.alamath.com/> for a program to calculate the Allan deviation.
- [171] Ripka, P. (2001) *Magnetic sensors and magnetometers*. ARTECH HOUSE, INC.
- [172] Gordon, D., Lundsten, R., and Chiarodo, R. (1965) Factors Affecting the Sensitivity of Gamma-Level Ring-Core Magnetometers. *IEEE Trans. Magn.*, **1**, 330.
- [173] Streubel, S. (2013) *In preparation*. Ph.D. thesis, Ruprecht-Karls-Universität Heidelberg.
- [174] Clark, A. (1983) *Materials at low temperatures*. ASM International, Materials Park, OH.
- [175] Corruccini, R. and Gniewek, J. (1961) *Natl. Inst. Stand. Technol. Mono. 29, Thermal Expansion of Technical Solids at Low Temperatures*. U.S. Government Printing Office, Washington, DC.
- [176] Arp, V. et al. (1962) Thermal Expansion of Some Engineering Materials from 20 to 293 K. *Cryogenics*, **2**, 230.
- [177] Fischer, U. et al. (2002) *Tabellenbuch Metall*, vol. 41. Europa-Lehrmittel.
- [178] Hoppe, E. et al. (2007) Cleaning and passivation of copper surfaces to remove surface radioactivity and prevent oxide formation. *Nucl. Instrum. Meth. A*, **579**, 486.
- [179] de Carvalho Rodegheri, C. (2012) *in preparation*. Ph.D. thesis, Johannes Gutenberg-Universität Mainz.
- [180] Camp, J. et al. (1990) Macroscopic variations of surface potentials on conductors. *J. Appl. Phys.*, **69**, 7126.

- [181] Day, C. (2006) Basics and applications of cryopumps. *CAS-CERN Accelerator School and ALBA Synchrotron Light Facility : Course on Vacuum in Accelerators, Platja d'Aro, Spain*, p. 241.
- [182] *DREEBIT GmbH* (2010), Instruction manual Dresden EBIT with Wien filter.
- [183] Koivisto, H., Arje, J., and Nurmi, M. (1998) Metal ions from the volatile compounds method for the production of metal ion beams. *Rev. Sci. Instrum.*, **69**, 785.
- [184] Schmidt, M. et al. (2009) A compact electron beam ion source with integrated Wien filter providing mass and charge state separated beams of highly charged ions. *Rev. Sci. Instrum.*, **80**, 063301.
- [185] Holleman, E. a. W. N., A.F. and Wiberg (1995) *Lehrbuch der anorganischen Chemie*. Walter de Gruyter.
- [186] Fischer, E. and Grubert, H. (1959) Über Aromatenkomplexe von Metallen, XXIX. Di-cyclopentadienyl-osmium. *Chemische Berichte*, **92**, 2302.
- [187] Perry, D. and Phillips, S. (1995) *Handbook of inorganic compounds*. CRC.
- [188] Thorn, A. et al. (2010) Optimization of the electron beam properties of Dresden EBIT devices for charge breeding. *JINST*, **5**, C09006.

Acknowledgements

At this point I would like to thank all the people who supported me during my PhD time in Heidelberg and contributed to the progress of PENTATRAP.

First of all, I would like to thank my supervisor Prof. Klaus Blaum for his support over the years, his confidence put in me and that he always found some time, despite his overfull appointment calendar, for the discussion of arising problems.

Furthermore, I thank PD Dr. Yuri Litvinov for accepting being the second referee of the thesis.

Thanks to Dr. Sergey Eliseev for the support, the corrections concerning this thesis, and the many helpful discussions. Also, I would like to thank the other present and former colleagues at PENTATRAP for their help: Christine Böhm, Andreas Dörr, Mikhail Goncharov, Christian Hökel-Schmöger, Alexander Rischka, Christian Roux and Dr. Sebastian George. Especially I have to thank Christine and Andreas for the accurate proofreading of this thesis and Mikhail for even reading parts during his vacation. Thanks to our technician Ralph Zilly, who always helped solving technical problems.

Thank you, Christine, for your friendship since the first days of our physics studies, the many words of support and all the nice encouraging pictures you draw on the corrections.

Moreover, I would like to thank all colleagues of the Penning-trap groups here in Heidelberg, Mainz and Genf for the good work atmosphere and the fruitful discussions between the different groups. Thanks to all who helped me during my PhD time! Thanks to Sebastian Streubel for the discussions and his help concerning the setup of the fluxgate stabilization system and to Anke Wagner and Crícia de Carvalho Rodegheri for their help related to the preparation of the Penning-trap electrodes. Especially, I would like to thank Dr. Stefan Ulmer and Dr. Sven Sturm, who contributed with their great ideas and knowledge a lot to the progress of PENTATRAP and who always helped with their explanations. Thanks to Sven for the comments to chapter 2. I want to thank Dr. Burcu Cakirli and Dr. Marta Ubieto-Diaz for the small talks during the breaks which always encouraged me a lot.

Thanks to Michael Kamp-Froese and José Crespo López-Urrutia who gave comments to the EBIT theory chapter.

I would like to thank the people from the technical infrastructure who signifi-

cantly contributed to the setup and progress of PENTATRAP.

Especially, I would like to thank the former leader of the precision mechanics workshop Volker Mallinger and his successor Thorsten Spranz as well as his deputy Martin Beckmann for their unbureaucratic and fast treatment of all the special requests, which arised during the commissioning of PENTATRAP. Their ideas and advices in the context of, e.g., material properties or manufacturing steps contributed a lot to the realization of the experiment.

Thanks to the accelerator workshop lead by Karl Hahn for the help during the installation of the experiment in the accelerator building.

Thanks to the engineering design office lead by Thomas Weber for their contribution to the design of PENTATRAP, especially to Annika Stark for implementing a lot of modifications in the CAD model of PENTATRAP.

I would like to thank Mr. Schleinkofer for the uncomplicated and fast laser welding of the trap pins at the *SLV* in Mannheim.

Besonderer Dank gilt meinen Eltern, die mir durch ihre Unterstützung das Studium und somit auch diese Arbeit erst ermöglicht haben. Euch, insbesondere Dir Papa zu deinem 75 Geburtstag, sei diese Arbeit gewidmet! Danken möchte ich auch meinen Geschwistern und deren Familien Thomas, Susanne, Andrea, Stefan, Lukas, Florian, Katharina, Stephan, Katja, Jakob und David sowie meiner Oma Änni, die mich, jeder auf seine Weise, unterstützt und ermutigt haben. Entschuldigt, dass ihr mich die letzten Monate so wenig gesehen habt!

Ganz besonders danke ich meinem Freund Florian für die gemeinsame Zeit hier in Heidelberg und seine Unterstützung. Danke für deine Ermutigungen und deinen Glauben an mich.

